1. Introduction

The Pulse Tube Cryocooler (PTC) is presently one of few options available for providing reliable cryogenic refrigeration for many applications such as re-liquefying liquid helium boil-off in Magnetic Resonance Imaging systems (MRI), cooling commercial and military satellite structures and sophisticated electronics packages, and providing reliable and portable cooling for laboratory applications. In the coming years, it is likely that additional applications will require cryogenic refrigeration and also that these applications will demand improvements in the cooling power, size, and efficiency of these cryocoolers. Unfortunately, present PTCs operate with poor efficiency relative to the Carnot limit (typically much less than 20% of Carnot) and require physically large compressors to drive the system. While there has been more than two decades of research related to PTCs, much is still unknown about how to properly design these systems in order to improve their efficiency and reduce their physical size. PTC systems are typically designed using empirical "rules of thumb" coupled with first-order design models; this approach is primarily due to the lack of sophisticated and predictive models for the PTC components. In order for the PTC to remain an attractive option for future cryogenic refrigeration applications, it is critical that advanced high-order modeling techniques be applied to the design and optimization of these systems.

1.1 Pulse-Tube Cryocooler Cycle

The PTC represents a reliable and efficient method for producing cryogenic refrigeration. There are many variations of the PTC configuration; some examples include the orifice pulse-tube cryocooler (OPTC), the inertance pulse-tube cryocooler (IPTC), and the double-inlet pulse-tube cryocooler (DIPTC). In this work the focus is on the IPTC, as it is the most

widely utilized configuration. In the remainder of this document, the IPTC will be referred to simply as PTC. The PTC configuration is illustrated schematically in Figure 1.1(a).

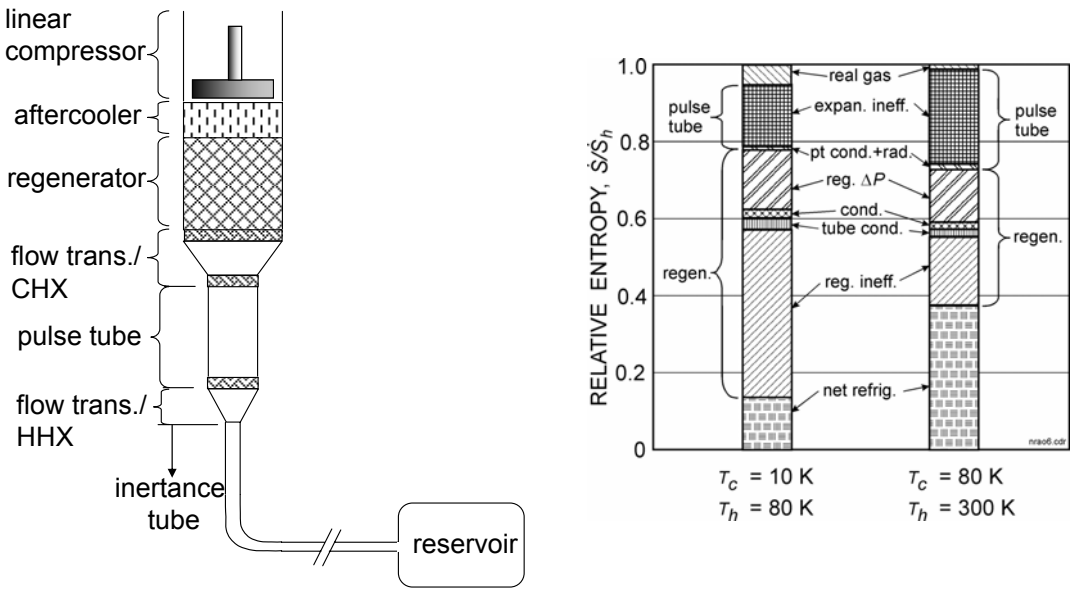

(a) (b)

Figure 1.1: (a) Schematic showing the fundamental components of a pulse-tube cryocooler, and (b) the delineation of the loss mechanisms for a PTC at two operational conditions, from Radebaugh et al. (2007).

The key system components include a pressure wave generator (typically a linear compressor) that mechanically produces an oscillatory pressure wave in the system, an aftercooler that rejects the heat of compression to ambient, a regenerator matrix that acts as a thermal storage medium alternately accepting and giving up energy to the working fluid during the cycle, a cold end heat exchanger that accepts a thermal load from the object to be cooled, a pulse-tube that serves to establish the compliant gas piston that provides thermal isolation between the cold end and the warm ends and therefore allows the transport of energy (as work) up the temperature gradient, a hot heat exchanger that rejects heat to

ambient, and an acoustic inertance network that provides the proper phasing between the pressure and mass flow.

An idealized description of the fundamental processes that occur during the course of a single cycle for a PTC are:

(1-2) The compressor piston moves downward, compressing the working fluid. Due to the compression process, the temperature of the gas rises and the compression heat is rejected to ambient in the aftercooler. Due to the increased system pressure relative to the reservoir pressure, there is a net flow of gas toward the reservoir end of the system. As the gas flows through the regenerator, the regenerator matrix accepts heat from the gas and pre-cools it before it enters the cold end of the pulse-tube. Due to the pressure rise of the working fluid in the pulse-tube section, the temperature of the gas increases. As this heated gas flows through the hot heat exchanger and into the reservoir, there is an additional heat rejection to ambient. Note that due to the net gas flow, the compliant gas piston within the pulse-tube component begins to move along the pulse-tube towards the reservoir volume.

(2-3) During this portion of the cycle, the net gas flow continues until the combination of gas entering the reservoir (i.e., the gas exiting the pulse-tube) coupled with the heat rejection to ambient in the hot heat exchanger is sufficient to cause the system pressure to equilibrate with the mean pressure in the reservoir.

(3-4) The compressor piston moves upward causing the gas in the cold end of the pulse-tube to rapidly expand. This rapid gas expansion causes the temperature of the gas in the cold end of the pulse-tube to become lower than the cold heat exchanger temperature.

(4-5) During this portion of the cycle, the expansion process causes the system pressure to be lower than the reservoir pressure. As a result, a net gas flow develops in the direction of the compressor end of the system. As the gas flows back towards the compressor, the cooler gas in the pulse-tube flows through the cold heat exchanger accepting heat from the object being cooled. As the gas passes though the regenerator matrix its temperature increases as the regenerator gives up the thermal energy that it had accepted earlier in the cycle. Note that due to the net gas flow, the compliant gas piston within the pulse-tube component moves towards the cold end heat exchanger.

(5-1) During the final phase of the cycle, the pressure inside the system again equilibrates with the reservoir pressure and the net flow in the system ceases. At this time, the cycle is repeated.

These processes are illustrated schematically in Figure 1.2 for the idealized PTC cycle.

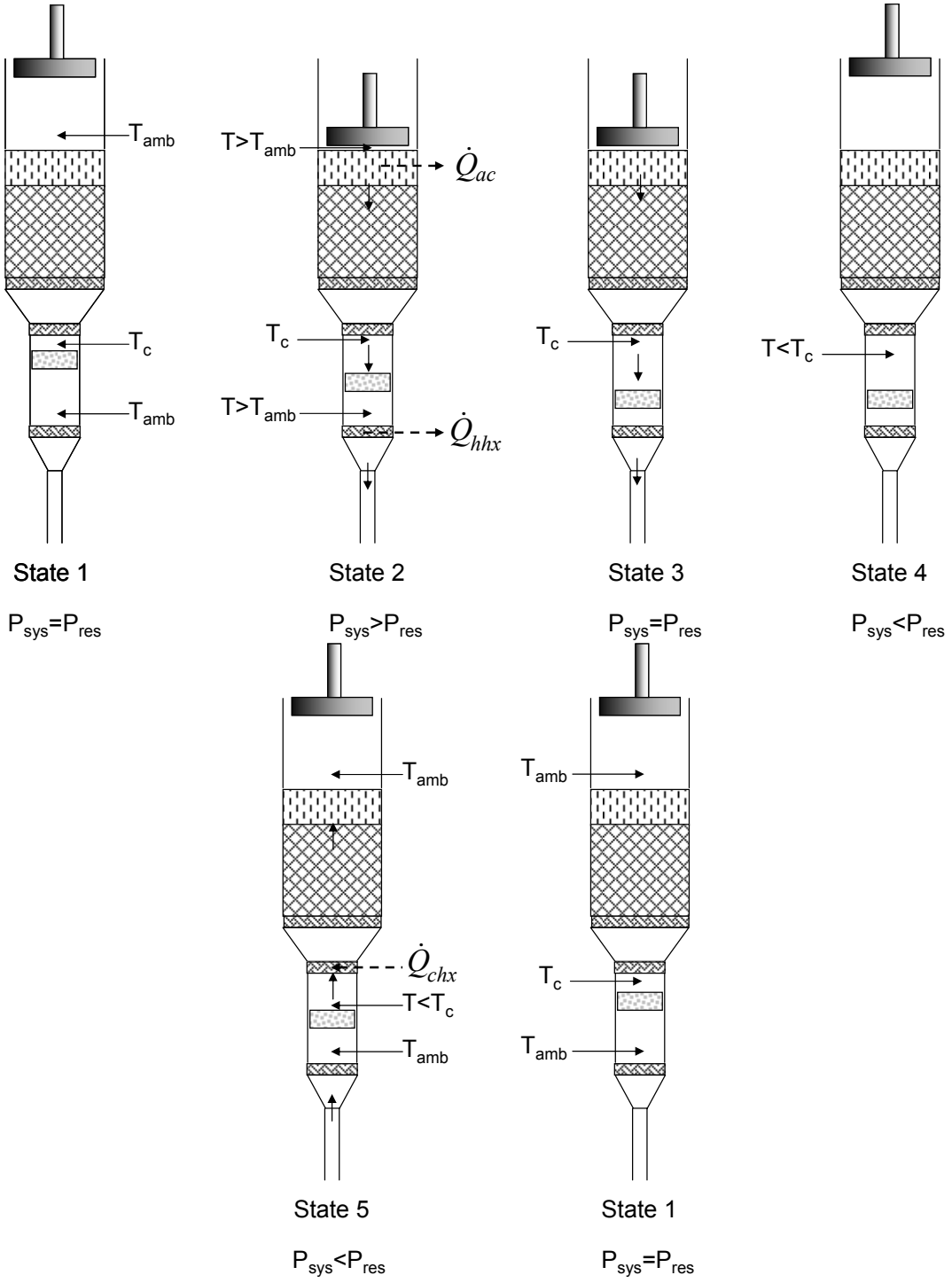

Figure 1.2: Schematic illustrating an idealized version of the processes that occur during a single PTC cycle.

1.2 Importance of the Pulse-Tube Component

The specific role and importance of the pulse-tube component in a PTC can be illustrated by defining a control volume around the cold end heat exchanger and carrying out an energy balance on this control volume for a single cycle under cyclic steady-state operation. This control volume is illustrated in Figure 1.3.

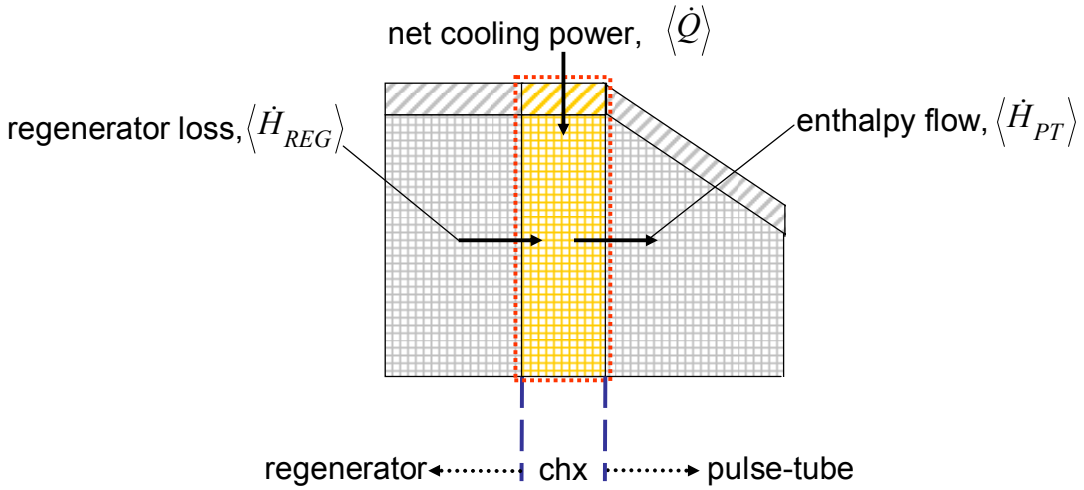

Figure 1.3: Control volume applied to the cold end of a PTC with delineated energy flows.

According to the energy balance shown in Figure 1.3, the cooling power available for refrigeration can be expressed as,

$$\langle \dot{Q} \rangle = \langle \dot{H}_{PT} \rangle - \langle \dot{H}_{REG} \rangle \tag{1.1}$$

where $\langle \dot{Q} \rangle$ is the useful cooling provided by the pulse tube, $\langle \dot{H}_{PT} \rangle$ is the cyclic average rate of enthalpy flow in the pulse tube, and $\langle \dot{H}_{REG} \rangle$ is the loss of cooling power associated with the ineffectiveness of the regenerator; note that $\langle\ \rangle$ indicates the quantity has been time-averaged over a single cycle. For this analysis, an ideal regenerator is considered and

therefore $\langle \dot{H}_{REG} \rangle$=0. Using the analysis presented by Storch and Radebaugh (1988), the combination of the 1st and 2nd laws allows the cyclic average enthalpy flow to be written as,

$$\langle \dot{H}_{PT} \rangle = \langle P\dot{V} \rangle + T_0 \langle \dot{S} \rangle \tag{1.2}$$

where P is the dynamic pressure, $\dot{V}$ is the volumetric flow rate, T_o is the ambient temperature, and $\langle S \rangle$ is the cyclic averaged entropy flow. The quantity $\langle P\dot{V} \rangle$ is commonly referred to as the acoustic power flow or, the ability to do work on a piston if the gas were expanded reversibly. In the case of an ideal system with no losses ($\langle S \rangle$=0), the enthalpy flow $\langle \dot{H}_{PT} \rangle$ (which is the maximum possible cooling power) is equivalent to the acoustic power. From this analysis it is clear that the pulse-tube in the PTC is directly responsible for transforming the acoustic power that is delivered to the cold end via the oscillating pressure and mass flow into useful cooling. Each of the other components within the system is responsible for either the production of acoustic power (e.g., the compressor and inertance tube) or the transmission of the acoustic power with minimal attenuation to the cold end (e.g., the regenerator and aftercooler). The success of the PTC cycle is directly related to the ability of the pulse-tube component to efficiently accomplish this acoustic-to-thermal energy conversion process. Quite simply, if the pulse-tube component is unable to convert the acoustic power flow into useful cooling then the cycle does not work.

In practice, many of the processes occurring during the PTC cycle are not ideal and, as a result, the enthalpy flow in the pulse-tube is less than the acoustic power. A qualitative indication of the relative magnitude of the losses specific to the pulse-tube component in a PTC for two common operational cold end temperatures is illustrated in Figure 1.1(b).

Figure 1.1(b) shows that the dominant loss of cooling power is related to losses that occur within the regenerator. However, losses within the pulse-tube (i.e., losses associated with the acoustic to thermal energy conversion process) do represent a substantial reduction in the available cooling power. If the pulse-tube is designed properly for a given set of operating conditions then the majority of these pulse-tube related losses can be minimized, resulting in a significant increase in system efficiency. The loss mechanisms in the pulse-tube component of a PTC, described subsequently, have been investigated previously by various researchers. However, unlike other components within a PTC (such as the regenerator and inertance network), no design software currently exists that is capable of providing a detailed assessment of the efficiency of the pulse-tube component based upon the fluid dynamics in the pulse-tube and its flow transitions by explicitly considering the geometry and operating conditions for a given application. Rather, the design of this component is typically performed using "rules of thumb" that have been developed based on experience.

1.3 Pulse-Tube Losses

In the ideal case, the gas in the pulse-tube acts as a compliant piston, transmitting pressure and displacement from the cold end to the hot end and therefore converting acoustic power into useful cooling. This compliant piston serves the same purpose that a mechanical piston does in a Stirling cycle; it transmits energy as a work transfer from the cold end to the warm end. In practice, there are several loss mechanisms that can affect this component and therefore degrade the system performance; these losses are discussed briefly below.

1.3.1 Surface Heat Pumping and Shuttle Heat Transfer Loss

In the PTC there are two heat transfer processes that can either serve to aid or degrade the refrigeration power and are directly related to the thermal interaction between the wall of the pulse tube and the oscillating gas flow. The first heat transfer process is referred to as the surface heat pumping effect and is described by Wheatley et al. (1985). This effect is best described in the context of the gas flow during a single cycle. During the compression portion of the cycle, the gas in the pulse-tube component will move towards the hot end of the pulse tube as the pressure and temperature are increasing. Likewise, during the expansion process, the gas will move towards the cold end with decreasing pressure and temperature. If one imagines a small fluid particle in the presence of a small temperature gradient in the pulse-tube component, the hot gas will transfer heat to the wall of the pulse-tube during the compression half of the cycle, and absorb heat during the expansion half. The result of this energy exchange is the surface heat pumping effect; each of the gas particles will move energy from cold to hot during each cycle, thus providing a small, but measurable amount of cooling. This effect is illustrated in Figure 1.4(a). Note that the surface heat pumping effect was the only cooling effect that energized early PTC's (which were not able to reach very cold temperatures, thus explaining the presence of a small temperature gradient in the pulse-tube).

In practical applications of PTC's there must be a steep temperature gradient in the pulse-tube, causing the effect to reverse direction and become shuttle heat transfer loss. Because of the steep temperature gradient, the hot gas remains at a temperature that is below the wall during the compression process and therefore receives energy during the compression

process. However, the cold gas during the expansion process is at a temperature greater than the wall and therefore rejects heat. Energy is moved from the hot end to the cold end of the pulse-tube in this fashion, manifesting itself as the shuttle heat loss. This effect is illustrated in Figure 1.4(b).

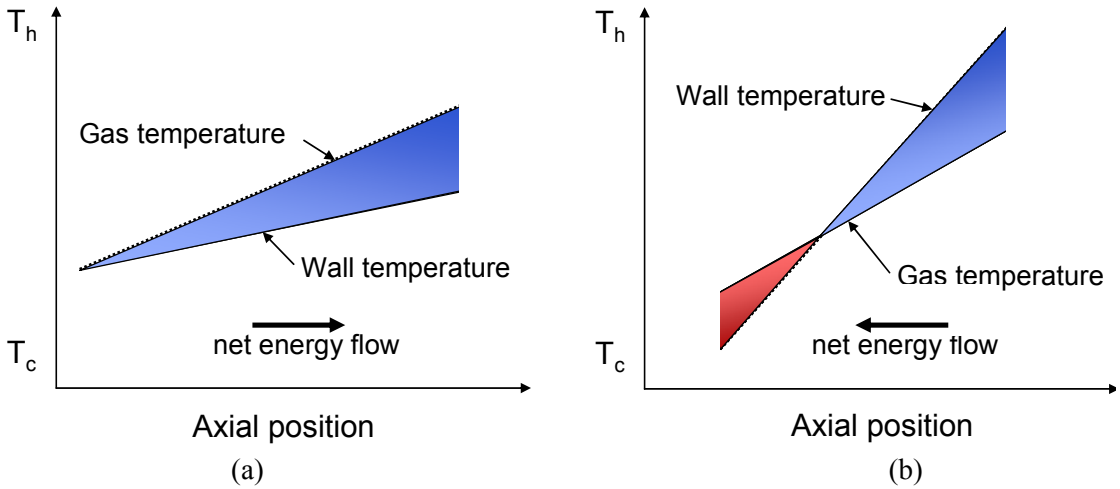

Figure 1.4: (a) Plot showing relative temperatures and net energy flow for the surface heat pumping effect, and (b) Plot showing relative temperatures and net energy flow for the shuttle heat transfer effect

1.3.2 Acoustic Streaming Loss

Acoustic streaming is a DC mass flow from the cold end of the pulse-tube to the warm end that is driven by oscillatory flow phenomena in the boundary layer. Under oscillatory flow conditions, the fluid in the near wall region of an internal pipe flow will tend to lag and be out of phase with the predominant core flow due to the viscosity of the working fluid as well as the imperfect heat transfer during the compression and expansion portions of the cycle. As a result, a DC mass flow will forms in the boundary layer region of the flow field (from cold to warm) and an equal and opposite DC mass flow forms in the core region (from warm

to cold) due to mass conservation. This effect is illustrated in Figure 1.5; the path of a helium particle in the boundary layer is shown qualitatively during different phases of a cycle.

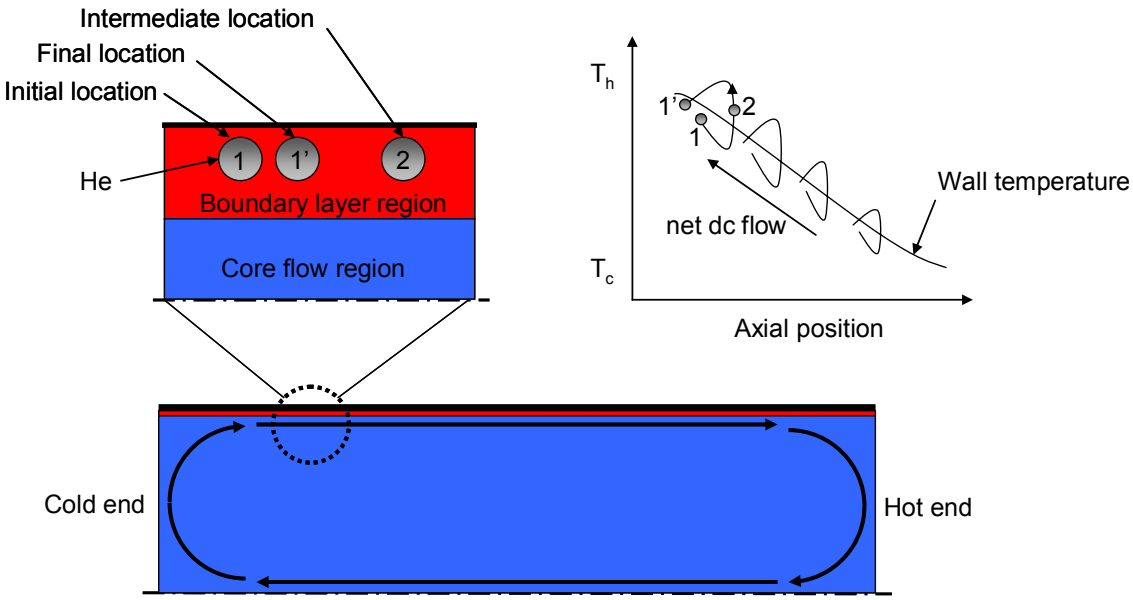

Figure 1.5: Illustration showing the DC flows that form in the pulse tube component due to acoustic streaming effects.

In the context of the pulse-tube component of a PTC, this DC mass flow can result in a large, convective transport of energy from the hot to the cold end of the pulse tube, thus significantly reducing the PTC performance. The acoustic streaming effect was been theorized by many researchers such as Richardson (1986) and Jeong and Smith (1992), and has been visually observed in experiments by Lee et al. (1993). Work by Olson and Swift (1997, 1999) demonstrated that these secondary flows could be reduced or eliminated by tapering the pulse tube from its cold to hot end, as initially suggested by Lee et al. (1993).

1.3.3 Flow Mal-distribution Losses

The flow distribution within the pulse tube plays an important role in its ability to transform acoustic power into useful cooling power. The buffer gas (i.e., the gas that remains in the pulse tube at all times) must act like a compliant piston. In order for this to occur, the flow distribution must be highly ordered and stratified. If the flow transitions between the regenerator and the pulse tube or the pulse-tube and the inertance network are not properly designed in order to allow the flow to radially equilibrate between components with different diameters then the flow entering the pulse tube will not be uniform and "jetting". Flow mal-distribution inevitably leads to regions of high velocity flow that destroy the compliant gas piston and transfer energy between the hot and cold ends of the pulse tube.

The flow mal-distribution effect has been recently documented for a high capacity 50K single stage PTC that exhibited severe jetting problems, as described by Lewis et al. (2008). The PTC considered by Lewis had numerous flow transitioning problems that were attributed to a radially non-uniform hydrodynamic flow resistance in the cold and warm heat exchangers that resulted in severe jetting and therefore limited system performance. Lewis et al. (2008) describe many diagnostic tests that were performed in order to understand and mitigate these flow mal-distribution effects. Eventually, the performance of the PTC was increased via the insertion of a diffusion bonded screen pack backed with copper mesh screens directly upstream of the warm heat exchanger in order to uniformly distribute the flow entering the pulse tube at the warm end. Subsequent testing showed drastic improvements in temperature and cooling power. This effect was also confirmed by Garaway et al. (2008) via thermographic (i.e., infrared) imaging of the system under normal

operating conditions. Garaway imaged both the original design that had poor flow transitioning at the warm end of the pulse tube as well as the subsequent design in which the flow transitioning was improved via the addition of the diffusion bonded screen and copper disks. Figure 1.6 illustrates the thermographic images that show the flow profile in the pulse tube component with jetting and with jetting effects suppressed.

One interesting outcome of this work is the demonstration that a relatively simple modification in the flow transition for two otherwise identical systems can have a drastic impact on overall performance. In many advanced pulse-tube systems there are multiple stages and the components that span large temperature ranges must be of different diameters. Therefore, efficient system operation requires that flow transitions be properly designed in order to help mitigate flow mal-distribution losses.

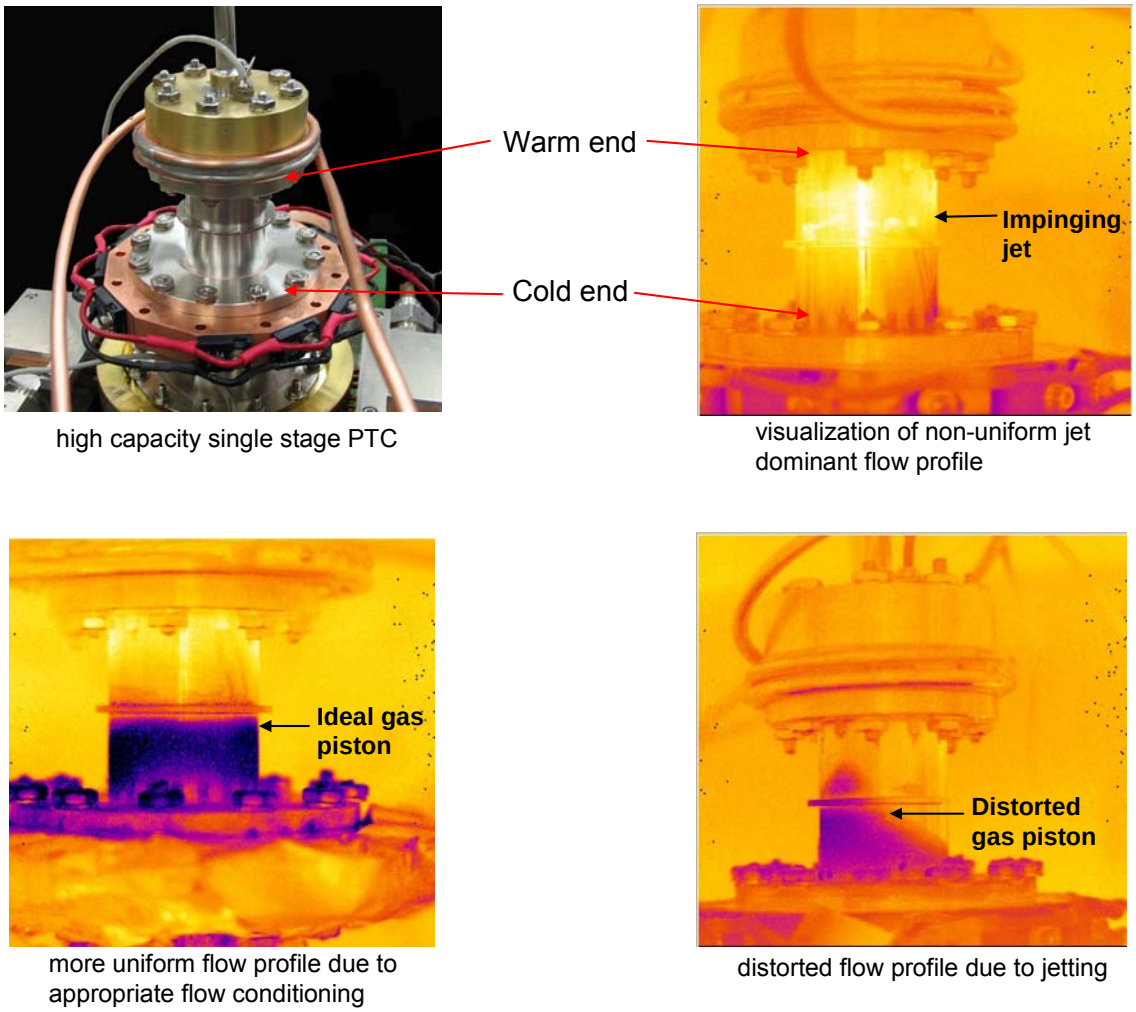

Figure 1.6: (*upper left)* Photo of a high capacity single stage PTC for 50K operation, *(upper right)* thermographic image of wall temperature profile showing the hot sport created by jetting effects in the flow field, *(lower right)* corresponding thermographic image to upper left photo that shows the effect of the jetting on the shape of the gas piston in the pulse tube, and (lower left) thermographic image of corrected thermal gas piston shape via use of flow conditioners; from Garaway et al. (2008). Note that the temperatures depicted are qualitative and the temperature scale runs from WHITE (hot) to BLACK (cold).

1.4 Research Objectives

The overall objective of this research is to carry out fundamental work that will enable the deployment of high efficiency PTC's by developing a powerful and experimentally verified computational fluid dynamic (CFD) model of the pulse tube and its transitioning

components. The CFD model can be used to optimize the design of these components for a specific application. A design model has been developed that is capable of predicting the performance and delineating the loss mechanisms associated with the pulse-tube and flow transitioning components. The model is implemented using the FLUENT software.

Development of a CFD model for the pulse-tube and flow transitioning components

The first goal of this research is the development of a 2-D axisymmetric computational fluid dynamic model of the pulse-tube and flow transitioning components within a PTC. The specific objectives in developing this model are:

1. generalize the geometric model such that it is user modifiable for the simulation of any reasonable pulse-tube or pulse-tube coupled to flow transitions,
2. integrate temperature-dependent material properties in the computational model,
3. accurately model the porous media (e.g., screens) that are typically utilized for flow straightening in actual PTC's.
4. account for the thermal interaction between the gas within in the system and solid materials such as the wall and the porous media, and
5. develop a criteria based upon the flow conditions such that a determination can be made regarding the need for inclusion of a turbulence model.

Development of a Post-Processing Methodology

The second goal of this research is the development of a post-processing routine that can be coupled to the computational model. This post-processing routine is implemented in the mathematical software package MATLAB as this software allows easy input and output of

large data files and can efficiently perform the complex calculations that are needed for data reduction. This post-processing routine is required to:

1. reduce the large quantity of data generated by the CFD solver into meaningful results for a PTC designer,
2. determine the convergence of a simulated model to a cyclic steady-state condition, and
3. report to the user the energy imbalance in the model, the cycle pressure, the mass flow rates, enthalpy flow, conductive energy flows, acoustic power, and a figure of merit that quantifies system performance.

Model Validation and Convergence

The third objective of the research is to validate and verify the convergence of the computational model. The convergence of the mesh and the suitability of the numerical discretization scheme were evaluated by parametric study and progressive mesh refinement. To judge the when the model has attained a sufficient grid resolution such that the solutions become independent of the grid size, various specifically incremented mesh sizes have been created around a nominal value and each of these meshes were simulated. The predicted energy flows were compared in order to judge when the model attained grid independence. Coupled with this mesh analysis was a study of the convective term discretization scheme used by the model.

One of the critical aspects of an unsteady numerical model is the judge of convergence to an accurate solution while minimizing computation time. The convergence of the model to a

cyclic steady state condition was evaluated using a 1st law energy balance implemented using the post-processing routine.

Finally, the model was compared in some limits to analytical solutions. The primary purpose of this exercise was to ensure that the CFD solver is capable of accurately predicting the two flow regimes that are typically encountered in internal viscous oscillatory flow; a viscous dominated region near the wall which can reverse the flow velocity, and a center core flow region.

Design and Construction of an Experimental Test Facility

The fourth objective of the work is the design and construction of an experimental test facility that enables the experimental verification of the CFD model. This test facility has been built in collaboration with the Cryogenic Technologies Group at NIST. The test facility allows precise measurements of the relevant energy flows within a PTC as well as the boundary conditions required for the model. Therefore, the test facility allows a complete and unambiguous verification of the CFD model. The test facility has been designed such that it is modular in nature, allowing different geometric designs to be experimentally characterized over a wide range of system parameters.

Experimentally Verify the Developed Model

The fifth and most important objective of this research is the experimental verification of the developed model. The specific objectives of these experimental measurements are to:

1. experimentally calibrate a custom-designed thermal pathway that allows the measurement of heat flow from the system to an external source of cooling or heating,
2. measure the regenerator energy flow (losses) for a test PTC using the calibrated thermal pathway,
3. experimentally calibrate a custom-designed mass flow meter for use under oscillatory flow conditions at cryogenic temperatures,
4. measure the net cooling power for a test PTC via the use of the calibrated thermal pathway,
5. measure the acoustic power flow using the measured mass flow rate, measured pressures, and phase angles, and
6. compare the results of the experimental measurements for the total energy flow in the pulse-tube to the predicted total energy flow from the model.

It should be noted that the precise, direct, and separate measurements of the pulse tube and regenerator loss has not previously been accomplished. The test facility developed for this project is unique in this respect.

Extend Model to Lower Temperatures

The sixth objective of this research is to integrate a real gas material property routine for ^{4}He with the FLUENT solver. This is required because at low temperatures (i.e., 4.2 K to 40 K) the thermophysical properties of helium deviate from an ideal gas significantly; therefore, a more sophisticated equation of state is required for accurate simulations.

1.5 Dissertation Document Outline

This document presents the methodology associated with the development and experimental verification of a CFD model of the pulse tube and flow transitioning components in a PTC. Chapter 2 explores the recent work related to CFD modeling of pulse-tube cryocooler as well as the experimental methods utilized by previous researchers in order to measure the performance of PTC's. Chapter 3 provides the specific details of the CFD model for the pulse tube and associated flow transitions. Chapter 4 describes the methodology for reduction of the numerical results from the developed model to a useful form. Chapter 5 describes the specific quantities that must be measured in order to experimentally verify the model, the design and construction of an experimental test facility for this purpose, and an analysis of the expected accuracy of the experimental measurements. In Chapter 6, the uncertainty related to the experimental measurements is discussed. Chapter 7 presents a comparison of the modeling results to the experimentally measured quantities and discusses these results. The extension of the developed model for 4K PTC operation is discussed in Chapter 8. Concluding remarks and discussion of future work related to high-order modeling of the PTC is addressed in Chapter 9.

2. Literature Review

Since the introduction of the modern PTC configuration by Mikulin et al. (1984), a substantial amount research has been directed at modeling and measuring PTC behavior. This chapter provides an overview of these previous modeling efforts, which range from simple analytical thermodynamic models to full 2-D or 3-D CFD models of the PTC flows. Additionally, the experimental methods that have been utilized for the characterization of PTC performance are discussed.

2.1 Pulse-Tube Cryocooler Modeling

The models developed to predict the performance of PTC's vary widely in complexity and accuracy. This section discusses these modeling efforts and delineates between low-order and high-order (CFD) modeling techniques.

2.1.1 Analytical 1-D and Quasi 2-D Models

Since the introduction of the orifice PTC in the early eighties, many researchers have either developed their own models or extended the models developed by other researchers' in an effort to accurately predict the performance of the PTC. Zhu and Chen (1994) and Liang et al. (1996a) developed PTC models that consider only the resistance and compliance of each component in the PTC. The modeled components are assumed to be isothermal (or, for the pulse tube, adiabatic) and linear in order to arrive at solutions for the pressure and flow rates that are finally used to predict the gross refrigeration power. Huang and Chuang (1996), Wang et al. (1992), de Boer (1995), Kittel et al. (1996), Wang (1997), Smith (2001), and Zhu and Matsubara (2004) have all developed PTC models in which the flow though the

regenerator and its thermal behavior are considered explicitly but only approximately. Yuan and Radebaugh (1996) developed a numerical model of a PTC that was later experimentally verified by Yuan (1996). Note that each of the above-mentioned models treats the flow as 1-D and all 2-D effects are ignored. Lee et al. (1997) attempt to model higher-order effects by solving the 2-D governing differential equations for the flow within the pulse tube based on an asymptotic expansion of the mass, momentum, and energy balances. Kuehl and Shultz (1996) present expressions for various regenerator loss mechanisms (e.g., micro- or macro-scale flow nonuniformities) that can be integrated with a 1-D regenerator code to approximately account for these higher-order effects. Lee et al. (1997) provide a qualitative comparison of several different modeling approaches that are appropriate for PTCs and conclude that a complete solution to the 2-D differential equations that govern the flow is the most appropriate modeling methodology. Kuriyama and Radebaugh (1999) discuss a harmonic analysis of the energy flows in the orifice pulse tube; the analysis is based upon the contribution of higher-order harmonic terms (that are typically neglected).

In addition to the models discussed above that have been developed and published by various research groups, there are three well-documented commercial codes/models that exist and have successfully predicted various aspects of the PTC performance. The REGEN program developed at NIST has evolved over the past three decades (Gary et al. 1985 and Gary et al. 2001) and provides a useful and publically accessible tool that is widely used by researchers in order to understand and design regenerators for PTC's. Other commercial models developed for PTC performance predictions include the Delta-E software that is available from Los Alamos National Laboratory (Ward and Swift 1996) and the SAGE software that

can be purchased from Gedeon Associates (Gedeon 1995). Both of the Delta-E and SAGE programs integrate the equivalent thermo-acoustic behavior of each component within the PTC in order to predict the overall system performance. Note that all three of these models are one-dimensional.

Various researchers have developed specific models that are meant to predict one or more of the higher-order loss mechanisms associated with the pulse tube component in a PTC. Jeong (1996) developed an analytical solution for the interaction of the boundary layer with the core in the pulse-tube component in order to study the phenomena of acoustic streaming. Acoustic streaming was studied further by Olson and Swift (1997), who extended the analysis presented by Rott (1974). Olson and Swift (1999) subsequently predict and then demonstrate a method to reduce or eliminate this acoustic streaming using a tapered pulse-tube. Baek et al. (2000a) and (2000b) further extend the model by Olson and Swift (1997) via the development of a 2-D model of the pulse tube that relaxes the assumption of a small boundary layer thickness; also, the temperature distribution in the pulse tube wall is not assumed but rather calculated in their model. Work by Liang et al. (1996b) expands upon 1-D PTC models by proposing that the flow in the pulse tube may be broken into a core region and a region near the wall in order to approximately predict the shuttle heat loss within a pulse tube. Koshimizu et al. (2005) present a numerical model of a basic pulse tube cryocooler in which surface heat pumping and shuttle heat loss effects are studied; clear visual delineation between the two effects are illustrated in this work. Liang and de Waele (2007) develop a numerical model that predicts a new type of streaming (i.e., DC flow) that

is different than the acoustic streaming discussed by Olson and Swift (1999) and is driven by the asymmetric entrance and exit of the gas flow in the pulse tube.

2.1.2 CFD Models

There has been relatively little work in which CFD codes are applied to the complex hydrodynamic flow processes that occur within a PTC. One reason for this may that the large amount of computational resources necessary to accurately model even one component within the PTC have not been available to most researchers until the past decade. However, the recent growth in the computational power associated with desktop computer has changed this situation and CFD codes are now being applied to the development of the PTC. This work is summarized below.

Hozumi (1999) describes a CFD model of a pulse tube and illustrates that the velocity profile uniformity at the inlet is often the most critical parameter that governs the ability of the pulse tube to convert acoustic power to cooling. Hozumi et al. (2001) expand on their previous CFD model in order to include the flow within the regenerator and the aftercooler; their results are in good agreement with the experimental results presented by Nakamura et al. (1998). Willems and Dam (2002) present a 3-D model of a pulse tube in which perfect flow transitions are assumed (i.e., all of the components in the PTC have the same diameter); the acoustic streaming predicted is shown to agree well with the analytical predictions of de Waele et al. (1998) as well as work by Olson and Swift (1997).

Ibrahim et al. (2002) present a 2-D axisymmetric CFD model that is developed using the CFD-ACE+ software. This model showed good comparison of frequency dependent flow features with experimental results from a developed experimental test facility. Flake and Razani (2004) present an axisymmetric, 2D model of an entire OPTR; this model explicitly includes the compressor (simulated using a sinusoidally moving surface and a deforming grid), the aftercooler, regenerator, cold heat exchanger, pulse tube, hot heat exchanger, and orifice. The heat exchangers consist of wire mesh screens that are modeled as porous regions characterized by inertial and viscous coefficients; these coefficients are derived based on the micro-scale behavior of the wire mesh. The reservoir was not explicitly modeled but rather a separate user-defined subroutine was integrated with the model in order to relate pressure to mass flow rate at the exit boundary based on the equations that govern an isothermal, fixed volume. Cha et al. (2005) perform a study that is similar to the one presented by Flake and Razani (2004), except that the inertance tube and reservoir volume are explicitly modeled. The results presented by Cha et al. (2005) clearly demonstrate the existence of significant 2-D flow mal-distribution effects generated at transitions between components of varying diameter. Work by Potratz (2005) utilized the CFD model developed by Flake and Razani (2004) in order to qualitatively examine the flow field in the pulse-tube component within a large capacity PTC. The results of this analysis indicated that poor design of the flow transition elements at the warm end heat exchanger result in the destruction of the thermal stratification in the pulse-tube component. A redesign of the flow transitions based on the qualitative characteristics of the CFD simulation was carried out in order to achieve much higher system performance, verified experimentally. Gan et al. (2007) perform a study of an orifice pulse tube cryocooler with an emphasis on the boundary layer development and

destruction at the inlet to the warm heat exchanger and the resultant flow circulation that is developed. Cha (2007) provide an extension of their previous CFD system level model for an orifice pulse tube cryocooler in which the experimentally measured loss coefficients are used to characterize common screen configurations.

2.2 Pulse-Tube Cryocooler Experimental Methods

Most experimental measurements for PTC's are limited to the net refrigeration power as a function of temperature; researchers are then left to estimate the gross power and the distribution of the associated losses that can be attributed to the various components and physical phenomena. The loss attributed to the pulse-tube component is often taken to be whatever is left over after other, more readily calculated losses (e.g., the loss associated with the regenerator ineffectiveness) have been estimated and removed. Unfortunately, little work has been directed at separately measuring the behavior of the pulse-tube or the loss that can be directly attributed to it. Note that since the measurement of the cooling power and cold end temperature for a PTC is straightforward and these measurements are ubiquitous in the literature, this section discusses specific measurements that are related to the pulse-tube component only.

2.2.1 Flow Field Measurements

In practice, the measurement of the flow field within a PTC is extremely difficult due to the complex hydrodynamic and thermal processes that occur within the pulse-tube component. The addition of point probes in the flow will affect the measurement due to disturbance of the local flow and temperature fields. David et al. (1992) present a technique for measuring the

local gas velocity within a pulse tube using hot wire anemometry. The results from this study indicate that the presence of the probe itself had a significant impact on the performance of the pulse-tube. Rawlins et al. (1993a) describe a technique for measuring the time-resolved instantaneous mass flow rates and temperatures in an orifice PTR using constant-temperature anemometers and small resistance temperature detectors (RTDs). This measurement was later extended in order to measure the enthalpy flux in a pulse-tube (1993b). Tanaka et al. (1992) describe measurements of the instantaneous temperature at three locations within the pulse tube using very small platinum wires; the delicate wires are required in order to achieve the necessary response time for time-resolved flow measurements. Seo et al. (1997) also measured the instantaneous temperature and velocity at a few points along pulse tube using a small hot wire and thermocouple. Jeong et al. (2001) performed a study of the oscillating heat transfer processes within a PTC via the use of a heat flux sensor and fast response temperature sensor.

2.2.2 Optical Based Measurements

Flow visualization experiments using smoke wires and a high-speed camera have been reported by Shiraishi and Masao (1997) and (1999). Shiraishi et al. (2001) used a smoke wire to visualize the DC flow that is often present in a DIPTC. Shiraishi et al. (2004) also used smoke wires to study the flow patterns within a pulse tube that is inclined with respect to gravity; the development of secondary flows driven by acoustic streaming and by buoyancy effects were clearly identified. The data in all of these studies are limited to velocity or temperatures at a few specific locations or along a line. While particle tracking does provide insight into the complex flow features in a pulse-tube, these data are not

sufficient to allow a thorough understanding of the interactions between the oscillating flows and temperatures in the boundary layer and core regions of the flow.

More promising laser-based measurement techniques that employ Rayleigh scattering techniques have been described by Nara et al. (1999) and Hagiwara et al. (1999). These measurements hold promise and could eventually be utilized in order to obtain cross-sectional temperature measurements rather than point measurements. Additionally, while yet to be demonstrated in the open literature, precise flow field measurements for velocity and across an entire 2-D cross section of a pulse tube seems to be achievable using a combination of Particle Image Velocimetry (PIV) and Planer Laser Induced Fluorescence (PLIF). The coupled measurement of velocity and temperature at identical spatial locations for an entire cross-section of a pulse tube in operation would be extremely valuable in understanding the underlying physical processes that are occurring and would also provide a comprehensive and detailed validation for high-order CFD models. One limitation of this technique currently is the lack of a suitable tracer for the PIV measurement coupled with a secondary tracer for the PLIF measurement. Additionally, currently available systems are limited for fast response PLIF systems due to the lack of high repetition rate lasers that have the power required to illuminate large cross-sections, as discussed in TSI (2008).

3. Computational Fluid Dynamic Model Development

The primary focus of this work is to develop a CFD design model for the design and optimization of pulse tube cryocoolers. A commercial CFD code, FLUENT, was utilized as the basis for the pulse tube model. This chapter discusses the set of solver parameters, boundary conditions, and sub-models that were utilized in the model development..

3.1 Computational Model Background

A commercial CFD package was chosen to perform the necessary numerical calculations for the CFD model of the pulse tube and associated flow transitions. The software package chosen to perform the numerical analysis was FLUENT as it is one of the most widely used CFD codes available. The remainder of this section describes the specific details of this software package in more detail.

3.1.1 GAMBIT

GAMBIT is the native pre-processor for FLUENT. The pre-processor is essentially a solid modeling program that allows any 2-D or 3-D geometry to be created (or imported from other CAD packages), definition of the mesh, and specification of the continuum types and boundary conditions. The creation of geometric models using this software is similar to programs such as SolidWorks and Pro-Engineer. Meshing of the geometric model is required in order to define the computational domain for the CFD solver. This involves (for 2-D models) sectioning the computational domain into rectangular (quadrilateral) or triangular (tetrahedral) elements as illustrated in Figures 3.1(a) and (b), to which the continuity, Navier-Stokes, energy, and other scalar equations are applied and solved. The

continuum types and boundary conditions must be specified. The regions of the mesh that should be a fluid are specified as a "fluid" continuum and those regions that are solid are specified as a "solid" continuum. The boundaries of the computational domain are specified as flow inlets, outlets, walls, etc. Once the model is completely defined in GAMBIT, the results are exported to FLUENT for use in a CFD simulation. In the development of this computational design tool, all geometric models of the pulse tube and associated flow transitions, spatial discretization of the geometric domains, and continuum/boundary types are created exclusively using GAMBIT.

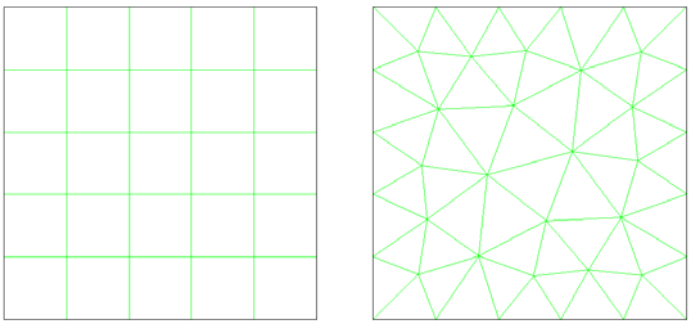

(a) (b)

Figure 3.1: Illustrations showing (a) a structured quadrilateral mesh, (b) an unstructured tetrahedral mesh, for an arbitrary geometric shape.

3.1.2 FLUENT

FLUENT is the solver component of the CFD package; this software solves the governing mass, momentum, energy, and other scalar equations using the Finite Volume numerical method. The FLUENT solver is one of the most advanced simulation tools currently available for modeling fluid and energy flows in a user-defined computational domain. This section discusses the governing equations as well as the solver settings that were employed for these simulations.

3.1.2.1 Governing Equations

In a pulse tube cryocooler, there are a variety of complex hydrodynamic and thermal processes that occur that are described by the continuum continuity, Navier-Stokes, and energy equations. Solving the Navier-Stokes equations is not a trivial matter due to the high level of non-linearity present in the equations. To date there have only been approximately 21 analytical solutions of the Navier-Stokes equations for fluid flow problems; all of these solutions employ a wide range of limiting assumptions or conditions. In the development of this model, there has been a conscious effort to minimize any limiting assumptions so that the results accurately represent an actual pulse tube.

The time-dependent compressible forms of the continuity equation and the Navier-Stokes equations in Eqns (3.1) and (3.2), respectively are solved in order to predict the flow field at a given time during the course of a cycle,

$$\frac{\partial \rho_f}{\partial t} + \left(\nabla \bullet \rho_f v\right) = 0 \tag{3.1}$$

$$\rho_f \left(\frac{\partial v}{\partial t} + v \bullet \nabla v\right) = -\nabla P - \frac{2}{3}\nabla\left(\mu \nabla \bullet v\right) + 2\nabla \bullet \left(\mu S\right) + \rho_f g \tag{3.2}$$

where, v is the velocity of the fluid in a specific vector direction, P is the fluid pressure, S is the fluid strain tensor, μ is the dynamic viscosity of the fluid, g is the gravitational acceleration, and ρ_f is the fluid density. For simulations at relatively high temperature, the fluid density is calculated from the ideal gas law,

$$\rho_f = \frac{P}{RT} \tag{3.3}$$

For low temperature operation, the fluid density is obtained from a real gas equation of state as described in the specific fluid property routine for ^{4}He in the REFPROP software (REFPROP, 2007).

There are large temperature gradients present in the pulse tube, corresponding to the large temperature difference between its cold and hot ends; therefore, the energy equation in Eqn. (3.4) is coupled to the fluid flow equations,

$$\frac{\partial}{\partial t}\left(\rho_f E_f\right)+\nabla\bullet\left(\vec{v}\left(\rho_f E_f+P\right)\right)=\nabla\bullet\left[k_f\nabla T+\left(\overline{\overline{\tau}}\bullet\vec{v}\right)\right] \tag{3.4}$$

where T is the temperature, k_f is the thermal conductivity of the working fluid, τ is the shear stress tensor, and E_f is the total energy of the fluid given by Eqn. (3.5),

$$E=h_f-\frac{P}{\rho_f}+\frac{v^2}{2} \tag{3.5}$$

where h_f is the enthalpy of the working fluid.

For the solid continuums that are present in the models (e.g., the wall of the pulse tube and flow transitions) a simpler form of the energy equation, given by Eqn. (3.6), is solved to yield the temperature distribution and energy flows,

$$\frac{\partial}{\partial t}\left(\rho_s h_s\right)=\nabla\bullet k_s\nabla T \tag{3.6}$$

where ρ_s is the density of the material in the solid continuum, h_s is the enthalpy of the material in the solid continuum, and k_s is the thermal conductivity of the material in the solid continuum.

3.1.2.2 Solver Type and Algorithm

The FLUENT solver allows the user to select from two distinctly different solver schemes (solution algorithms): a pressure based solver (segregated) and a density based solver (coupled). Due to the high level of non-linearity in the governing equations and the coupling between the temperature and flow field, multiple iterations must be performed using either of these solution algorithms in order to reach a user-defined convergence criteria that is necessary for the solver to update the solution field and move to the next time step (in the case of an unsteady system) (Fluent, 2005). In the development of the pulse tube design model, the segregated solver was selected because the Mach numbers that are present in a pulse tube cryocooler are typically much less than 1 (on the order of 0.1 and lower); the segregated solver is ideally suited for low Mach number flows.

3.1.2.3 Spatial and Numerical Discretization

The flow field governing equations, the energy equation, and other scalar partial differential equations (such as the equations that govern the turbulence intensity) are spatially discretized using the Finite Volume method and converted to a system of linear algebraic equations that are integrated over a control volume in order to enforce conservation of some quantity (e.g., mass or energy) for the control volume (Fluent, 2005). There are multiple discretization schemes for the convective terms in the governing equations; these are summarized below:

- a 1st order upwind scheme that assumes that cell-centered values represent the cell-averaged value and are used as the cell face values for computations,

- a 2nd order upwind scheme that gives second-order accuracy for the cell face value through the use of a Taylor series expansion about the cell-centered value,
- a Power Law scheme that uses interpolation in order to obtain the face value for a given quantity using a 1-D convection diffusion equation,
- a QUICK scheme that uses a weighted average of second-order and centrally interpolated values for face values, and
- a 3rd order MUSCL scheme that is specifically designed for use with structured meshes (flow being aligned with the numerical grid) and uses a combination of central-differencing and second-order upwind schemes to compute cell face values (Fluent, 2005).

In the development of the computational model, the 2nd order upwind discretization scheme was chosen as the default discretization scheme for the convective terms. The primary reasons for choosing this scheme was the need for high accuracy solutions (2nd order vs. 1st order) and the ability to utilize both structured and unstructured grids (quadrilateral and tetrahedral meshes) which is not supported by the higher order discretization schemes in FLUENT.

3.1.2.4 Temporal Discretization

In normal pulse tube operation, the system operates on a cyclic steady-state basis. During the course of a single cycle, there are many unsteady phenomena taking place. However, when the system reaches cyclic steady-state these unsteady phenomena are repeated from cycle-to-cycle. As a result of the characteristic unsteadiness that is present in a single cycle, it is

necessary to model the system as unsteady. Due to the selection of the segregated solution algorithm, the temporal discretization scheme provided by FLUENT is implicit time marching with the option of either 1st or 2nd-order accuracy. The 2nd-order implicit time marching scheme was selected as the default temporal discretization scheme in order to provide high accuracy.

Since a single pulse tube cycle is unsteady, one of the important parameters that define the computational model is the duration of the time step that is used to march the solution forward in time. If the time step size is too large relative to the temporal scales that are present in the problem then significant computation errors can be introduced that will lead to unsatisfactory solutions and/or solutions which fail to capture the desired physics of the problem. However, if the time step is too small then computation times are drastically increased without a significant improvement in solution accuracy. In the development of the computational model the temporal scale of the problem was estimated using Eqn. (3.7),

$$\Delta t = \frac{\Delta x_{min}}{u_{max}} \tag{3.7}$$

where Δx_{min} is the minimum distance across any element in the domain and u_{max} is the maximum fluid velocity in the domain. This relationship between the minimum grid size and the maximum velocity is commonly referred to as the residence time for the fluid in the smallest cell (volume). This method for selection of the time step is a more rigorous approach than methods selected in most applications of CFD models to pulse tube systems where the cycle time is typically divided by a fixed number of steps (e.g., Lyulina (2004)).

3.1.2.5 Material Properties

It is necessary to specify the thermophysical properties of the fluid continuum (helium) as well as the solid continuums (the porous media and walls). The temperature range of all required material property data is 4.2 K to 400 K; these upper and lower temperatures are the practical limits which can be expected in an actual pulse tube cryocooler.

The property data required for the fluid continuum (helium) include the density, dynamic viscosity, specific heat capacity at constant pressure, and the thermal conductivity. For simulations that have a cold temperature that is greater than 60 K, the density is computed using the ideal gas law and the other properties are defined using multi-temperature range piece-wise polynomial fits to property information obtained from the Engineering Equation Solver software (EES, 2007). The validity of the ideal gas assumption for temperatures above 60 K can be justified based upon the compressibility factor for helium gas. For typical values of the operating pressure, the compressibility factor is within 1-2% percent of unity for temperatures in the range of 60 K to 400 K. Models of pulse tubes with cold end temperatures below 60 K cannot use the ideal gas assumption. A more accurate equation of state is required for these simulations. The NIST REFPROP 8 real gas routine has been integrated with the FLUENT solver for these low temperature simulations. This is not a normal option available in the FLUENT software but subroutines have been written and integrated with the code in order to allow FLUENT to call the external REFPROP code and compute the real gas thermophysical property data. When the real gas model is employed, all of the required fluid properties are determined via calls to this routine. Therefore, both

the pressure and temperature dependence of the viscosity, conductivity, and specific heat capacity are included in the model.

For the solid continuums in the model (wall and porous media) the property data required include the specific heat capacity and the thermal conductivity. The material property data are represented by multi-temperature range piece-wise polynomials that are fit to property information obtained from the Engineering Equation Solver software (EES, 2007).

3.2 Model Geometry and Boundary Conditions

3.2.1 Geometry

An axisymmetric representation of the pulse tube has been used in an effort to ensure that the total computational time between problem definition and solution is reasonable and comparable to other current PTC design tools such as REGEN 3.3. The 2-D axisymmetric representation of a pulse tube is illustrated in Figure 3.2. The primary assumptions and limitations of the 2-D axisymmetric model are that there are no circumferential non-uniformities in the flow and temperature fields. Gravitational or body forces are neglected and therefore it is only possible to simulate a horizontal pulse-tube.

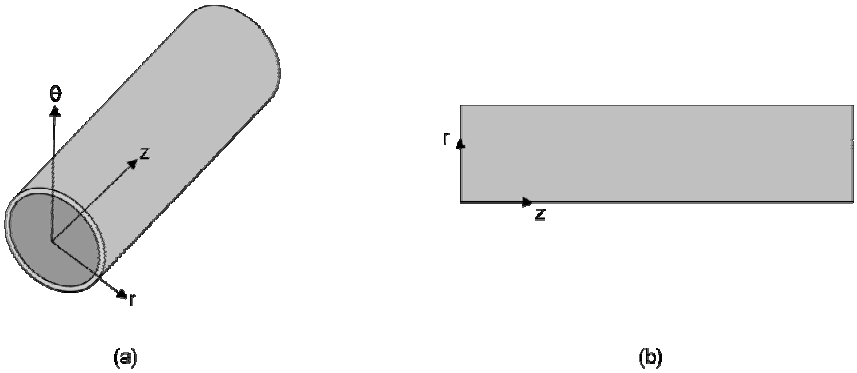

Figure 3.2: Illustrations of (a) a 3-D model of a pulse-tube in cylindrical coordinates and (b) a simplified 2-D axisymmetric model of the 3-D pulse-tube.

The generalized geometric model for the pulse tube and flow transitions is illustrated in Fig. 3.3. The parameters that define this geometric model are easily modified so that a wide range of configuration options can be simulated. Note that in Figure 3.3, the cold and hot flow transitions can be specified as being either fully open or completely/partially filled with a porous medium.

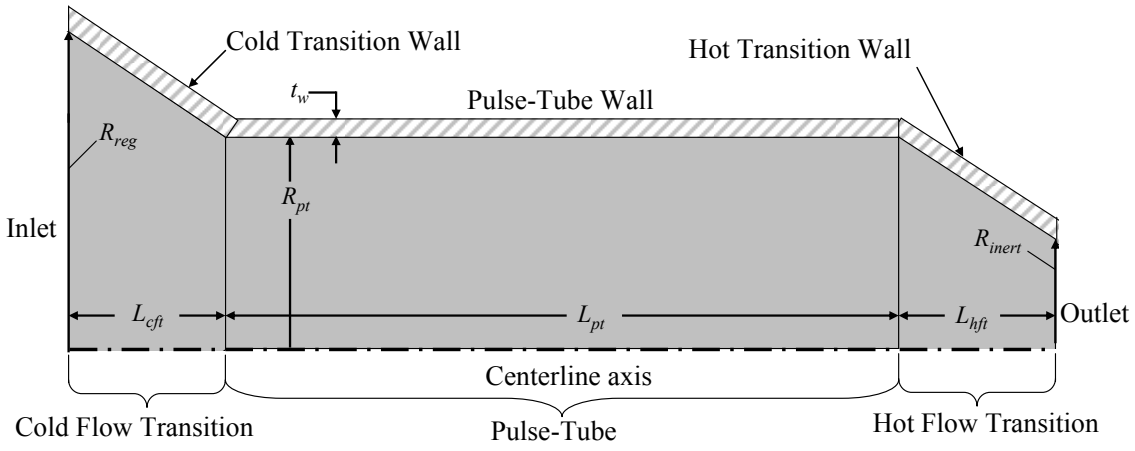

Figure 3.3: Schematic of the geometric model used for simulating an ideal pulse tube including wall heat transfer effects; note the solid grey region represents the area occupied by the helium while the grey slanted region represents the solid wall of the pulse tube.

3.2.2 Boundary Conditions

The pulse tube model requires the specification of four boundary conditions; the flow inlet, the flow outlet, the flow bounding wall(s), and the centerline of the model (requirement for axisymmetric simulations).

The flow inlet of the model is specified as a mass flow inlet according to the mass flow rate (or mass flux), the unit direction of the flow, and the temperature of the entering fluid. The mass flow rate is an input quantity to the pulse tube model; the mass flow rate may be separately determined from a system-level model of the pulse-tube and then specified in this component-level model. Because the mass flow rate is a sinusoidal function of time, it is necessary to use a routine written in the C programming language to provide the inlet mass flux; this routine is interfaced with FLUENT in order to enforce a time varying boundary condition. The general form of the mass flux function imposed at the inlet of the domain is given by Eqn. (3.8) and illustrated by the solid line in Fig. 3.4:

$$\dot{m}'' = \frac{4\,\dot{m}_{amp}\sin\left(2\,\pi f\,t\right)}{\pi\,D^2} \tag{3.8}$$

where $\dot{m}_{amp}$ is the amplitude of the mass flow rate, f is the pulse tube frequency, t is time (defined relative to the beginning of the cycle), and D is the diameter of the pulse tube or the cold flow transition.

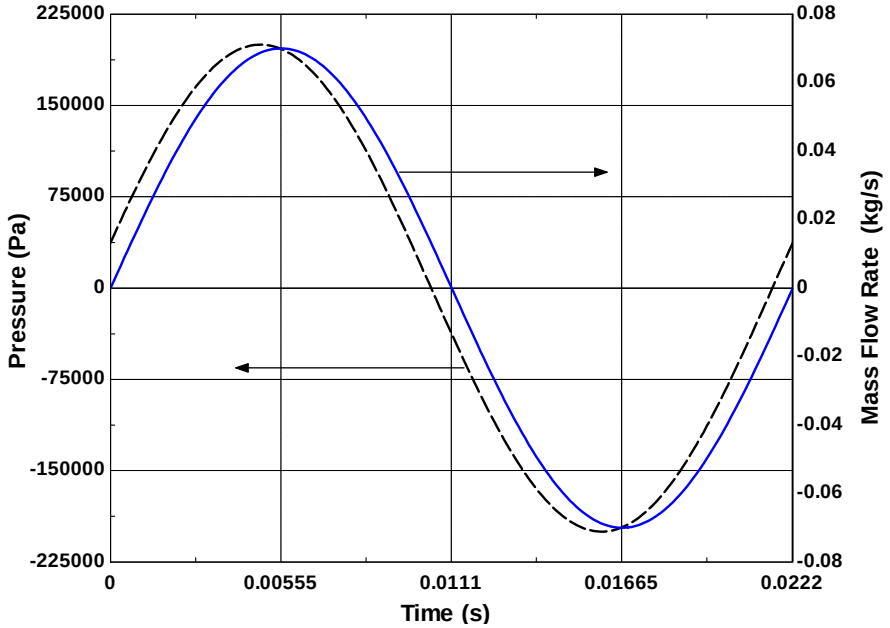

Figure 3.4: Plot illustrating the form of the functions that are used to specify the applied mass flux at the inlet to the model and the applied pressure at the outlet of the model as a function of time for one cycle.

The flow outlet boundary condition is defined as a pressure outlet. The parameters required to completely specify the outlet boundary condition include the static pressure and the temperature of the fluid that enters the domain when flow reversal occurs. In order to simulate the oscillating pressure at the outlet of the pulse tube with a specified phase shift, it was necessary to write a routine in the C programming language that is compiled and interfaced with FLUENT in order to provide the time varying pressure boundary condition; see Appendix A. The general form of the pressure function imposed at the outlet of the model is given by Eqn. (3.9) and illustrated by the dashed line in Fig. 3.4:

$$P = \bar{P} + \tilde{P}\sin\left(2\,\pi f\,t + 2\,\pi\,\frac{\phi}{360^{\circ}}\right) \tag{3.9}$$

where $\bar{P}$ is the mean charge pressure, $\tilde{P}$ is the amplitude of the pressure variation and ϕ is the phase angle between the pressure (at the warm end) and the mass flow rate (at the cold end).

The walls of the pulse tube and the flow transitions are specified as wall boundaries. The input conditions required to specify the wall include the thermal boundary condition at the exterior of the wall surface (i.e., convection, radiation, temperature, heat flux, etc.), the velocity of the wall, and the velocity boundary condition associated with the fluid at the wall. Either the external surface temperature of the wall or the heat flux imposed on the exterior wall is specified; note these two conditions cannot be used simultaneously; the value of this parameter depends on the model. The velocity of the wall is set to zero with a no-slip condition.

3.3 Specialized Sub-Models

Additional non-standard models are required to accurately simulate the flow processes occurring in certain regions of the CFD model. Sub-models are required to represent the porous media that is often utilized in the flow transitions and heat exchanger, the thermal interaction between the gas and solid wall material, and turbulent effects present in the pulse tube. These models are discussed in more detail in the following sections.

3.3.1 Porous Media Modeling

One of the most critical aspects associated with pulse tube cryocooler operation is the use of flow straighteners at the cold and hot ends of the pulse tube. Typically the pulse tube is at a

different diameter than either the regenerator or the inertance tube and therefore the flow must contract/expand as it transitions between these components. Flow straightening is utilized at these interfaces in an effort to ensure that there is a radially uniform distribution of the gas velocity as it enters the pulse tube; this uniformity prevents fluid jetting, excessive turbulence, and recirculation zones within the pulse tube that destroy the thermal isolation associated with the gas that is trapped within the pulse tube and acts as a compliant displacer. Typically, the flow straighteners are fabricated from packed metallic screens, much like the regenerator packing, due to the ready availability of these screens.

Because the flow straighteners result in a substantial loss of cooling power, it is necessary that they be explicitly included in the pulse tube models. The FLUENT porous media model is utilized for this purpose. The porous media model requires the specification of viscous and inertial loss coefficients in the axial and radial flow directions; the methods by which these coefficients are determined are presented in the following sections.

3.3.1.1 FLUENT Porous Media Model

FLUENT simulates a porous media by adding a "source" term (that is negative and therefore actually represents a sink) to the right side of the standard momentum equation(s); the source term is defined by:

$$S_i = -\left(\sum_{j=1}^{3} D_{ij}\, \mu u_j + \sum_{j=1}^{3} C_{ij}\, \rho u_{mag}\, u_j \right) \tag{3.10}$$

where S_i is the momentum source term for the i^{th} momentum equation, j is an index which indicates the components of a vector in a specific direction (e.g., *x, y,* and *z*); D_{ij} and C_{ij}

represent user defined matrices for the porous media being modeled, μ is the dynamic viscosity of the fluid, u is the velocity in the direction of the momentum equation being considered, u_{mag} is the magnitude of the velocity, and ρ is the density of the fluid.

For the case of a homogeneous porous medium, Eqn. (3.10) can be simplified to,

$$S_i = -\left(\frac{\mu u_i}{\alpha_i} + C_{2,i} \frac{1}{2} \rho u_{mag} u_i \right) \tag{3.11}$$

where α is defined as the permeability of the porous media, and C_2 is defined as the inertial resistance coefficient. There is a clear link between Eqn. (3.11) and Eqn. (3.10); if the permeability and inertial loss coefficients are known for the porous medium, the coefficient matrices, C and D in Eqn. (3.10), can be determined.

In practice, the permeability and inertial loss coefficients are derived for a specific porous media type and are typically inferred from published empirical correlations to steady flow data. Before applying these correlations in their typical form, Eqn. (3.11) must be cast in the form of pressure drop per unit length. This transformation can be performed by examining the two components of Eqn. (3.11) in more detail. The first term is exactly Darcy's Law for viscous pressure drop associated with laminar flow through porous media, Fluent (2005):

$$\left(\frac{\partial p}{\partial s} \right)_{v,i} = -\frac{\mu u_i}{\alpha_i} \tag{3.12}$$

where p is pressure and s is distance along the i^{th} coordinate axis; the v subscript indicates viscous effects. The second term of Eqn. (3.12) represents inertial pressure loss:

$$\left(\frac{\partial p}{\partial s}\right)_{in,i} = -C_{2,i}\frac{1}{2}\rho u_{mag} u_i \tag{3.13}$$

The total pressure drop per unit length in a specific coordinate direction is the sum of the inertial and viscous pressure losses and can be obtained by adding Eqns. (3.12) and (3.13):

$$\left(\frac{\partial p}{\partial s}\right)_i = -\left(\frac{\mu u_i}{\alpha_i} + C_{2,i}\frac{1}{2}\rho u_{mag} u_i\right) \tag{3.14}$$

In cylindrical coordinates, assuming axisymmetric flow, Eq. (3.14) becomes:

$$\frac{\partial p}{\partial r} = -\left(\frac{\mu u_r}{\alpha_r} + C_{2,r}\frac{1}{2}\rho u_{mag} u_r\right) \tag{3.15}$$

$$\frac{\partial p}{\partial z} = -\left(\frac{\mu u_z}{\alpha_z} + C_{2,z}\frac{1}{2}\rho u_{mag} u_z\right) \tag{3.16}$$

3.3.1.2 Loss Coefficient Evaluation

FLUENT requires that the user enter two loss coefficients (the viscous and inertial loss factors, α and C_2) as well as the porosity of the medium (ϕ) being modeled. Packed screens are not homogeneous (the resistance to flow in the radial direction is typically much higher than the resistance in the axial direction) and therefore the loss coefficients are different in the axial and radial flow directions.

In order to accurately model the anisotropy of packed screens, it is necessary to integrate published, steady-flow correlations, for flow through packed metallic screens into the porous media model in FLUENT. Typical correlations for the steady flow pressure drop are

presented in the form of a friction factor (f) as a function of Reynolds number (Re). The correlations typically have the form shown in Eqn. (3.17),

$$f = \frac{\lambda_1}{Re} + \lambda_2 \tag{3.17}$$

where λ_1 and λ_2 are empirical fitting constants. Steady flow correlations are used here as opposed to oscillating flow correlations because there are only a limited number of papers that deal with oscillating flow pressure drop and these correlations require a third term that is related to the frequency of the flow; e.g., the Valensi number or an oscillating Reynolds number. In the development of this model, the effects of the oscillating flow on the thermal fluid behavior of the porous media are neglected; the FLUENT porous medium model does not handle a third, frequency-dependent term cleanly and it is unclear how important this term is in general.

Axial Flow Loss Coefficients

The pressure drop associated with internal flow through a duct (Δp) can be expressed in terms of the friction factor,

$$\Delta p = \frac{1}{2}\left(\frac{L}{D}\right) f \rho u^2 \tag{3.18}$$

where L is the length of the tube, D is the diameter of the tube, and u is the mean velocity in the direction of flow. The results associated with a packed screen bed are correlated in a similar manner; the diameter of the tube is replaced with the hydraulic diameter of the passages or another characteristic length that is relevant to woven metallic screens, for

example the screen diameter (d_{wire}). Based on Miyabe et al. (1982), Eqn. (3.18) can be re-written as,

$$\Delta p = \frac{1}{2}\left(\frac{L}{2\,d_{wire}}\right) f \rho u_s^{\,2} \tag{3.19}$$

where u_s is the superficial velocity in the porous matrix defined as,

$$u_s = \frac{u}{\phi} \tag{3.20}$$

where u is the frontal flow velocity (i.e., the velocity upstream of the matrix or the velocity that would exist in the absence of any matrix material) and ϕ is the porosity of the matrix. Miyabe et al. (1982) presents an empirically-determined correlation for steady-flow through screens,

$$f = \frac{33.6}{Re_l} + 0.337 \tag{3.21}$$

where Re_l is the Reynolds number based upon a screen characteristic length (ℓ), defined as the distance between meshes for one screen, as illustrated in Fig. 3.5),

$$Re_l = \frac{\rho u_s \ell}{\mu} \tag{3.22}$$

where,

$$\ell = P - d_{wire} \tag{3.23}$$

where P is the pitch of the screen. Combining Eqns. (3.19) through (3.23) leads to an equation for the axial pressure drop per unit length in the porous medium:

$$\frac{\partial p}{\partial z} = \left(\frac{33.6}{4\,d_{wire}\,\phi\,\ell}\right)\mu u + \frac{1}{2}\rho u^2\left(\frac{0.337}{2\,d_{wire}\,\phi^2}\right) \tag{3.24}$$

Note that in Eqn. (3.16), the magnitude of the velocity was used for the inertial loss term. Here, this magnitude has been replaced with the velocity that is present in the axial direction as it is expected that it that the axial velocity will be much larger than the radial velocity term. Comparing Eqn. (3.24) to Eqn. (3.16), the analytical expressions representing the viscous and inertial pressure loss terms are,

$$D_z = \frac{1}{\alpha_z} = \left(\frac{33.6}{4 d_{wire} \phi \ell} \right) \tag{3.25}$$

$$C_{2,z} = \left(\frac{0.337}{2 d_{wire} \phi^2} \right) \tag{3.26}$$

Using the relations defined by Eqns. (3.25) and (3.26) allows the inputs required by the porous media model to be specified based only the geometric parameters associated with a screen bed, as illustrated in Figure 3.5.

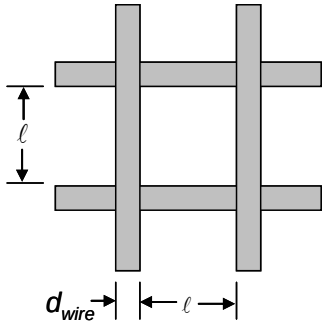

Figure 3.5: Illustration showing the pertinent geometrical parameters for axial flow through a woven mesh screen.

Radial Flow Loss Coefficients

Due to the inherent anisotropy associated with packed screens, it is also necessary to estimate the inertial and viscous loss coefficients for the radial flow. By intuition, one can determine that the resistance to flow should be higher in the radial direction due to the much more

tortuous path for gas flow in this direction, as shown in Figure 3.6. However, unlike flow through screens in the axial direction (i.e., perpendicular to the screen), there are very little data available in the open literature that can be used to infer the inertial and viscous flow coefficients in the radial direction. However, Tian et. al. (2004) measure the friction factor for radial flow through packed metallic screens. Unfortunately, there is no empirical fit to the data from Tian et al.; instead, the friction factor for radial flow is compared graphically to the friction factor for axial flow. Using these data, it appears that the friction factor for radial flow through screens is approximately 3-5 times larger than it is for axial flow. Therefore, the axial loss coefficient values are determined using the methodology described in the previous section and are multiplied by a factor of 4 in order to arrive at approximate values for the radial loss terms. When experimental measurements for radial flow through packed screens are eventually published in the literature, then the procedure described in the previous section can be applied to these data in order to arrive at analytical expressions for the radial porous media loss coefficients.

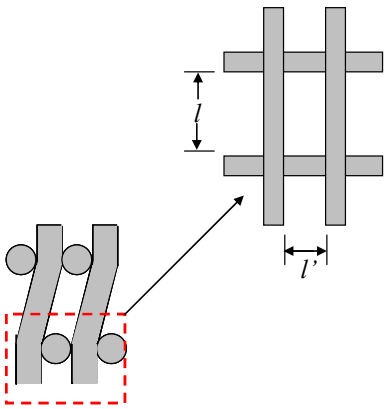

Figure 3.6: Illustration showing the pertinent geometrical parameters for radial flow through a woven mesh screen.

3.3.1.3 Porous Media Model Validation

The loss coefficients used in the porous media model were validated by developing a simple computational model that simulated the pressure drop through a packed bed of screens (represented using the porous media model). The predicted pressure drop from FLUENT was subsequently compared to the value predicted using the friction factor correlation presented by Miyabe et al. (1982). This verification was performed only for the axial flow case. The nominal parameters summarized in Table 3-1 were used to develop the CFD model; note the computational domain is a simple cylindrical tube. The analysis was carried out for a Reynolds number range of 1-1000, which bounds most flows encountered in either the cold or warm flow transitions.

Table 3.1: Nominal Porous Media Test Parameters

Input Parameter	**Symbol**	**Nominal Value**
Tube radius	R	0.02985 m
Tube length	L	0.0762 m
Mean system pressure	$\overline{P}$	0 Pa
Frontal flow velocity	u	$f(Re)$
Screen mesh size	-	#200 mesh
Wire diameter	d_{wire}	0.05e-3 m
Pitch	p	0.127e-3 m
Mesh distance	ℓ	0.077e-3 m
Porosity	ϕ	0.668

Figure 3.7 illustrates the friction factor results obtained from the CFD model overlaid on the published correlation from Miyabe et al. (1982). The results agree essentially exactly, as they should given that this correlation was used to derive the coefficients of the porous media model, and confirm that there is no error in algebra or implementation.

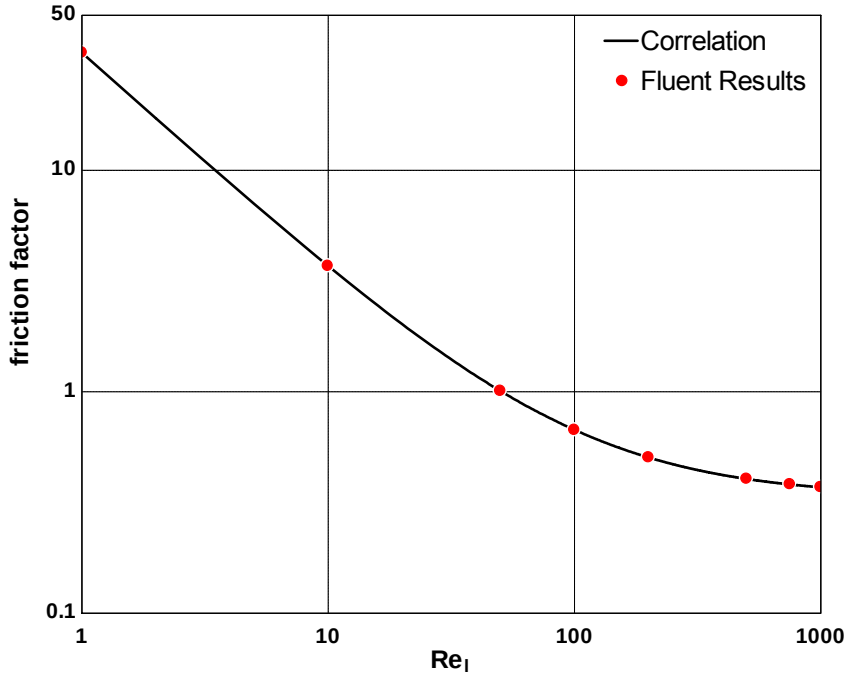

Figure 3.7: Plot showing the FLUENT results for axial flow friction factor as a function of Reynolds number overlaid on the empirical correlation presented by Miyabe et al. (1982).

3.3.2 Thermal Solid Modeling

Another critical aspect of pulse tube operation is the heat transfer interaction between the gas and the wall of the pulse tube. This phenomenon is referred to as a shuttle heat transfer loss and is discussed in detail in Chapter 2. In order to model this effect in the computational model, it was necessary to implement a thermal model for the wall that allows the wall temperature distribution to be computed and coupled to the gas temperature distribution.

In practice, modeling the thermal behavior of the wall is not trivial due to the large difference in the time constant of the wall compared to the time constant of the bulk gas flow. For the typical materials used in PTC's (such as stainless steel) at normal operating temperatures, the thermal capacity of the metal may be more than 2 orders of magnitude larger than that of the

helium gas. This difference means that (1) the wall temperature will not change (to within any reasonable tolerance) during any single cycle and (2) the computational time required to attain a cyclic steady-state solution for the wall temperature will be extremely large compared to the time required to attain a cyclic steady state for the gas.

In order to address these problems, the heat capacity of the pulse tube wall is artificially reduced and adjusted so that the thermal time constant of the wall (τ_w) is substantially larger than the period of one cycle (therefore the wall temperature will not change during any given cycle) but not more than 10x the period of one cycle (so that a steady state solution can be obtained in a reasonable amount of computational time). The wall time constant is estimated according to Eqn. (3.27),

$$\tau_w = \frac{c_{w,eff}\,\rho_w V_w}{h_g\,A_{s,w}} \tag{3.27}$$

where V_w is the volume of the wall, $A_{s,w}$ is the surface area of the wall exposed to gas, and $c_{w,eff}$ is the artificially adjusted wall specific heat capacity. The convective heat transfer coefficient between the gas and the wall, h_g, is estimated using relations for fully developed laminar flow (Incropera, 2002). Initial calculations indicated that the specific heat capacity of the wall should be approximately 0.05 J/kg-K in order for the wall time constant to be several times the cycle time. Using this value as a constant for the wall heat capacity input in FLUENT, a simple model was run for 20 cycles and the results of this analysis are presented in Fig. 3.8(a). Notice that $c_{w,eff}$ = 0.05 J/kg-K is clearly too small as there are substantial temperature oscillations within the wall during a cycle; this is not surprising as the laminar

flow correlation underestimates the heat transfer coefficient and therefore the actual wall time constant is less than the target.

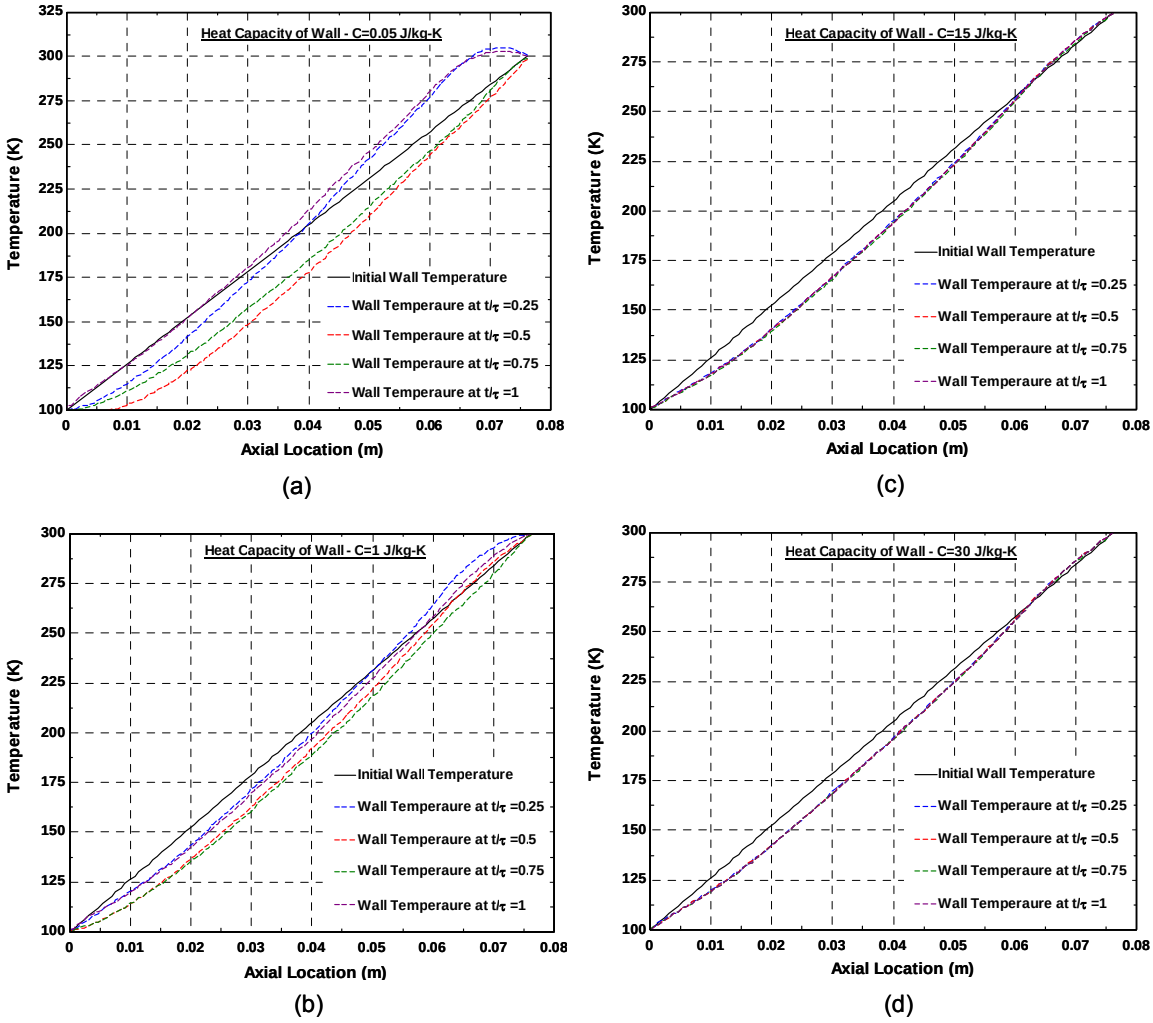

Figure 3.8: Plot showing the temperature of the wall (dashed lines) overlaid on the analytical solution (solid black line) for non-dimensional cycle times of (a) $t/\tau=0.25$, (b) $t/\tau=0.5$, (c) $t/\tau=0.75$, and (d) $t/\tau=1$.

The heat capacity was subsequently increased to 1 J/kg-K and the results are shown in Fig. 3.8(b); notice that the wall temperature oscillates substantially less over one cycle, but the variation is still more than desired. The heat capacity value was increased again to 15 J/kg-K

leading to the results shown in Fig. 3.8(c). The wall temperature changes only by a small amount over the course of one cycle; one final increase in the wall heat capacity to 30 J/kg-K was used to eliminate any observable oscillation, as shown in Fig. 3.8(d).

To practically implement this methodology, the wall material in the model is defined with an effective specific heat capacity of 30 J/kg-K and simulated for approximately 25 cycles in order to obtain the cyclic wall temperature profile. Subsequently, the effective heat capacity is defined as the actual specific heat of the wall and the model is solved again until a cyclic steady-state condition is reached. This approach allows the modeled system to reach cyclic steady state in a reasonable number of cycles and reduces the computational time by nearly an order of magnitude.

3.3.3 Turbulence Modeling

Typically in pulse tube design, there are "rules of thumb" design constraints that are applied in order to guarantee that the fluid velocity in the pulse tube remains less than a critical Reynolds number in order to minimize the effect of turbulence. Unfortunately, these design constraints often interfere with other pulse tube design constraints and limit the geometries that can be considered for various components of the PTC such as the regenerator and the inertance network. As a result, turbulence can play a key role in the development and sustainability of the thermal gas piston in the pulse tube and subsequently the performance of the system.

3.3.3.1 Oscillatory Turbulence

The addition of turbulence modeling in FLUENT can add considerable computational time to the simulation. Therefore, it is worthwhile to predict whether turbulence will exist for a specific simulation in order to determine whether the turbulent equations must be included in the model. There are several papers in the literature that address turbulent internal oscillatory flows. For this analysis, the work presented by Brereton et. al. (1995) is utilized. Brereton et. al. (1995) presents a flow map in terms of two non-dimensional parameters that can be used to determine whether the flow will become turbulent during the course of cycle. These non-dimensional parameters are a Reynolds number based upon the Stokes layer thickness, given by Eqn. (3.28),

$$\mathrm{Re}_{st} = \tilde{U}_o \sqrt{\frac{2}{\omega \nu}} \tag{3.28}$$

where $\tilde{U}_o$ is the maximum periodic free stream velocity, ω is the angular velocity, and υ is the kinematic viscosity of the fluid, and a non-dimensional length scale based upon the Stokes layer thickness given by Eqn. (3.29),

$$l_t = \frac{D}{\sqrt{\frac{2\nu}{\omega}}} \tag{3.29}$$

where D is the diameter of the tube.

The flow map is illustrated in Fig. 3.9. The flow regimes for internal oscillatory flow include: I – laminar flow, II – perturbed laminar flow, III – intermittently turbulent flow, and IV – fully turbulent flow (Brereton et. al. (1995)).

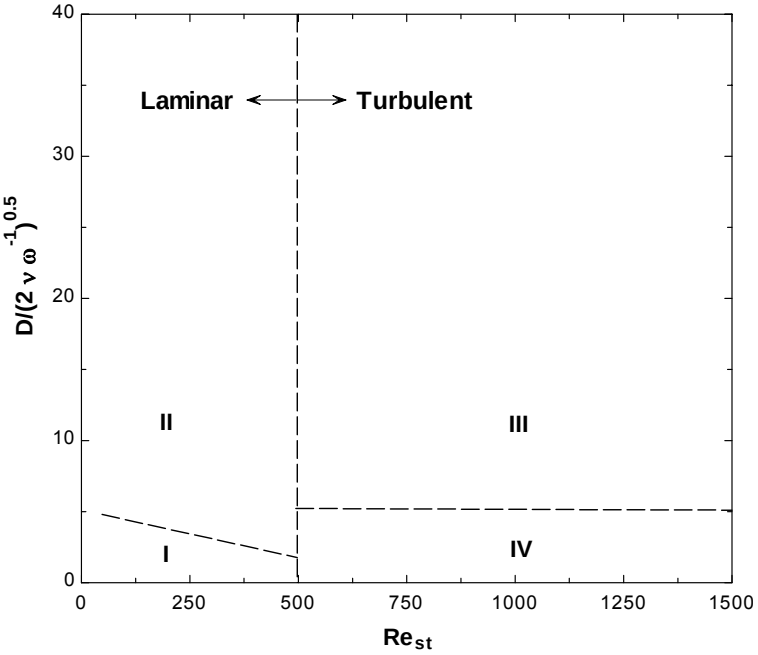

Figure 3.9: Plot illustrating the four flow regimes which occur during oscillatory internal flow; adapted from Brereton et. al. (1995).

Figure 3.9 shows that the critical Reynolds number for transition to turbulence in internal oscillating flow is at a Reynolds number of 500. For an ideal pulse tube (i.e., one with no change in diameter) the flow occupies the perturbed laminar range (region II in Figure 3.9) and therefore turbulence modeling is not required. However, for the pulse tube model developed here that includes the flow transitions from the regenerator and the inertance network, the flow begins in the perturbed laminar range (at the beginning of a cycle) and moves into the intermittently turbulent flow range before finally ending in the perturbed laminar range. Due to the cross over of the flow into a turbulent regime, the addition of an appropriate turbulence model in the computational model is required.

3.3.3.2 FLUENT Turbulence Models

In FLUENT there are six turbulence models that are available for use:

1) Spalart-Allmaras Model,
2) k-ε Models (Standard, RNG, and Realizable),
3) k-ω Models (Standard and SST),
4) The Reynolds Stress Model (RSM),
5) Large Eddy Simulation (LES) Model,
6) Detached Eddy Simulation (DES) Model

In selecting an appropriate turbulence model care must be taken to balance the complexity of the model with the computational efficiency so that the design tool can be used for parametric studies and optimization in a reasonable amount of time. Therefore, the RSM, LES, and DES models are not considered viable turbulence model options as these three models are all very sophisticated and are primarily utilized for flows in which resolution of all pertinent time/length scales is desired; this level of detail is beyond the scope of this project and the requirements of the pulse tube model. The remaining turbulence models are summarized briefly in the following sections; the information was taken primarily from Fluent (2005).

Spalart-Allmaras Turbulence Model

The Spalart-Allmaras model is a relatively simple, single equation, turbulence model that utilizes a "turbulent viscosity" that is a characteristic of the flow. In its general form, this model is appropriate for low-Reynolds-number flows (which are characteristic of pulse

tubes) in which the viscous sub-layer must be resolved all the way to the wall. However, the model that is accessible in FLUENT has been modified to allow for the use of built-in wall-functions that do not require resolution throughout the viscous sub-layer and therefore allow a coarse mesh to be used even near the wall; this approach leads to significantly reduced computational times. The main drawbacks of this turbulence model are that it is not able to accurately resolve certain flow situations (e.g., isotropic turbulence decay and flows which have rapidly changing length scales), and that it was developed for primary use in very high mach number external flows.

k-ε Turbulence Models

The *k-ε* turbulence model is the industry standard "complete" turbulence model and has been used to model a wide-range of flow problems. The model is based on two scalar equations that govern the turbulent kinetic energy (*k)* and the dissipation rate (*ε*); these two equations are solved simultaneously in order to provide closure to the turbulent momentum equations. This model has been used for many years and therefore it has been verified and refined. The standard model is derived using the assumption of fully turbulent flow. However, two variations of this model that yield higher accuracy for wider range of flow are available in FLUENT and are briefly summarized below.

The first variant of the standard *k-ε* model is the RNG *k-ε* model. This model was developed using a statistical process called Renormalization Group Theory. The most important refinement of the RNG model is the use of an analytical formula for the turbulent Prandtl number. The analytical formula allows the Prandtl number to be computed directly based on

flow conditions (rather than specified as a user input). Additionally, the RNG model uses an analytically derived differential equation for the effective viscosity that accounts for low-Reynolds-number viscous effects much better than the standard model.

The second variant of the standard k-ε model is the Realizable k-ε model; the term "realizable" refers to the fact that the equations satisfy specific mathematical constraints related to the Reynolds stresses. The Realizable k-ε model improves on the standard model and yields higher accuracy in some situations. The model employs an alternative method for calculating the turbulent viscosity and a new equation for dissipation, derived from an exact solution of the mean-square vorticity perturbation, is used.

k-ω Turbulence Models

The k-ω turbulence model in FLUENT is empirically based and computes the turbulent kinetic energy *(k*) as well as the specific dissipation rate (ω) in order to provide closure to the turbulent momentum equations. The benefit of the k-ω turbulence model is that it accounts for low-Reynolds-number viscous effects, compressibility, and spreading in shear flows (which are present in a pulse tube refrigerator).

One variant of the standard k-ω model is the Shear Stress Transport (SST) k-ω model that accounts for principal turbulent shear stress using a modified definition for the turbulent viscosity. This modification provides a performance advantage over the standard k-ε and k-ω models. This model can be thought of as hybrid model because it uses a blending function to

incorporate a modified/transformed standard *k-ε* model in the core flow region while using the more accurate *k-ω* model in the near wall (viscous) region.

3.3.3.3 Turbulence Model Selection

The selection of the turbulence model was a difficult task. Discussions with Professor Rutland of the UW-Madison Engine Research Center (UW-ERC) regarding appropriate turbulence models for oscillatory flows in a pulse tube (which are consistent with those encountered in internal combustion engines) suggest that the RNG *k-ε* turbulence model is most suitable. Researchers in the UW-ERC have found that the RNG *k-ε* turbulence model is the most accurate choice for a wide range of flows when compared to the standard and Realizable *k-ε* turbulence models (Rutland, 2007). Based upon these discussions, the RNG *k-ε* turbulence model was chosen as the turbulence model to be utilized for all simulations.

The addition of turbulence effects in the FLUENT simulations using the RNG turbulence model requires that the continuity and Navier-Stokes equations be averaged using the Reynolds decomposition in order to yield the Reynolds Averaged Navier-Stokes (RANS) equations. Additionally, to provide closure to these turbulent momentum equations, two scalar equations for *k* (turbulent kinetic energy) and *ε* (turbulent dissipation rate) must be solved. The partial differential equations for *k* and *ε* according to the RNG theory are given by Eqns. (3.30) and (3.31) respectively,

$$\frac{\partial}{\partial t}\left(\rho_f\, k\right)+\frac{\partial}{\partial x_i}\left(\rho_f\, k\, u_i\right) = \frac{\partial}{\partial x_j}\left(\alpha_k\, \mu_{eff}\, \frac{\partial k}{\partial x_j}\right)+G_k+G_b-\rho_f\, \varepsilon-Y_M \tag{3.30}$$

$$\frac{\partial}{\partial t}(\rho\,\varepsilon)+\frac{\partial}{\partial x_i}(\rho_f\,\varepsilon\,u_i)=\frac{\partial}{\partial x_j}\left(\alpha_k\,\mu_{eff}\,\frac{\partial \varepsilon}{\partial x_j}\right)+C_{1\varepsilon}\,\frac{\varepsilon}{k}(G_k+C_3\,G_b)-C_{2\varepsilon}\,\rho_f\,\frac{\varepsilon^2}{k}-R_\varepsilon \qquad (3.31)$$

where G_k is the generation of turbulent energy due to mean velocity gradients, G_b is the generation of turbulent energy due to buoyant effects, Y_m is the component of compressible flow dilatation, α is the inverse Prandtl number, and μ_{eff} is the effective viscosity which includes the turbulent viscosity contribution.

4. Post-Processing Methodology

A large quantity of "raw" information is generated by the CFD solver and saved as text files. In its raw form, the information does not help the user as it does not present the energy flows of interest. Therefore, the numerical output must be post-processed externally in order to generate meaningful results. This chapter discusses the basis for specifying the convergence of the model to a cyclic steady-state condition as well as the mathematical operations that are employed in order to reduce the numerical information to meaningful information.

4.1 Pulse-Tube Energy Balance

In order to determine when a given computational model has reached a cyclic steady state condition, as well as to determine the various quantities of interest to a pulse-tube designer, a 1st law energy balance is utilized. A control volume is specified that includes the modeled system, as illustrated in Fig. 4.1.

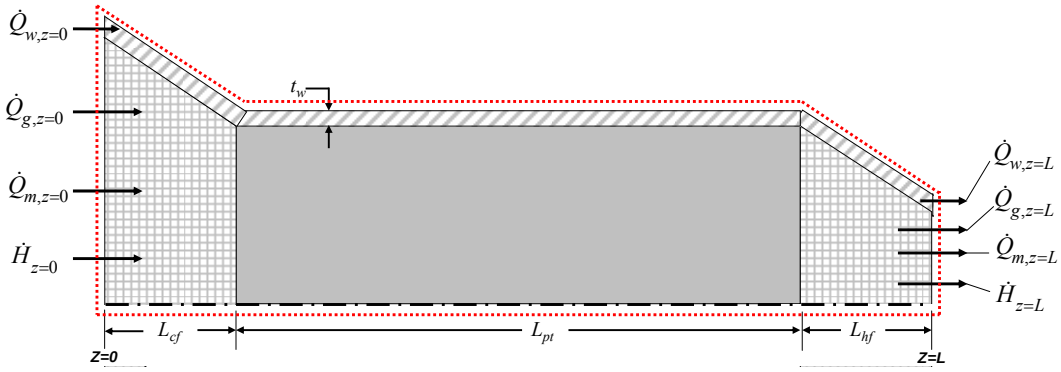

Figure 4.1: Control volume (dashed line) used for the energy balance on the pulse-tube and flow transitioning components.

The 1st law balances the energy flows into and out of the pulse-tube against the storage of energy in the pulse tube.

$$\frac{dU}{dt} = \dot{H}_{z=0} - \dot{H}_{z=L} + \dot{Q}_{g,z=0} - \dot{Q}_{g,z=L} + \dot{Q}_{w,z=0} - \dot{Q}_{w,z=L} + \dot{Q}_{m,z=0} - \dot{Q}_{m,z=L} \tag{4.1}$$

where $\dot{H}_{z=0}$ is the rate of enthalpy flow into the pulse-tube from the cold heat exchanger, computed using a cross-sectional area weighted average of the energy carried by the fluid at the cold end of the pulse-tube,

$$\dot{H}_{z=0} = \int_0^{R_i} \left(\phi \rho_g u c_{p,g} T_g \right)_{z=0} 2\pi r \, dr \tag{4.2}$$

where ρ_g is the gas density, u is the axial velocity, $c_{p,g}$ is the constant pressure specific heat of the gas, ϕ is the porosity of the pulse tube at the cold end, T_g is the temperature of the gas all evaluated at $z = 0$ (the cold end), and R is the outer radius of the computational domain at $z = 0$. The rate of enthalpy flow out of the hot end, $\dot{H}_{z=L}$, is computed according to,

$$\dot{H}_{z=L} = \int_0^{R_i} \left(\phi \rho_g u c_{p,g} T_g \right)_{z=L} 2\pi r \, dr \tag{4.3}$$

The rate of axial conduction through the gas at the cold end of the pulse-tube, $\dot{Q}_{g,z=0}$, is computed using a cross-sectional area weighted average of the conduction heat transfer rate,

$$\dot{Q}_{g,z=0} = \int_0^{R} -\left(\phi k_g \frac{dT_g}{dz} \right)_{z=0} 2\pi r \, dr \tag{4.4}$$

where k_g is the thermal conductivity of the gas which is a function of temperature. The rate of axial conduction through the gas at the hot end of the pulse-tube, $\dot{Q}_{g,z=L}$, is computed according to,

$$\dot{Q}_{g,z=L} = \int_0^R -\left(\phi k_g \frac{dT_g}{dz}\right)_{z=L} 2\pi r\, dr \tag{4.5}$$

The rate of axial conduction through the wall at the cold end of the pulse-tube, $\dot{Q}_{w,z=0}$, is computed according to,

$$\dot{Q}_{w,z=0} = \int_R^{R+t_w} -\left(k_w \frac{dT_w}{dz}\right)_{z=0} 2\pi r\, dr \tag{4.6}$$

where T_w is the wall temperature, t_w is the thickness of the pulse-tube wall and k_w is the thermal conductivity of the pulse tube material which is a function of temperature. The rate of axial conduction through the wall at the hot end of the pulse-tube, $\dot{Q}_{w,z=L}$, is computed according to:

$$\dot{Q}_{w,z=L} = \int_R^{R+t_w} -\left(k_w \frac{dT_w}{dz}\right)_{z=L} 2\pi r\, dr \tag{4.7}$$

The rate of axial conduction through the filler material (e.g., a porous stack of flow straightening screens, if these are present) at the cold end of the pulse-tube, $\dot{Q}_{m,z=0}$, is computed using a cross-sectional area weighted average of the conduction heat transfer rate,

$$\dot{Q}_{m,z=0} = \int_0^R -\left((1-\phi) k_{m,eff} \frac{dT_m}{dz}\right)_{z=0} 2\pi r\, dr \tag{4.8}$$

where T_m is the matrix temperature and $k_{m,eff}$ is the effective thermal conductivity of the packed screens in the transition region. The effective thermal conductivity is a fraction of the thermal conductivity of the screen material itself; the value of the effective thermal conductivity is based upon experimental results from Lewis et al. (2003).

The axial heat transfer in the screen matrix at the hot end of the pulse-tube, $\dot{Q}_{m,z=L}$, is computed according to:

$$\dot{Q}_{m,z=L} = \int_0^R -\left((1-\phi) k_{m,eff} \frac{dT_m}{dz} \right)_{z=L} 2\pi r \, dr \tag{4.9}$$

The term U in Eq. (4.1) is the energy stored in the gas, wall, and porous matrix of the pulse-tube. The total energy computed according to,

$$\begin{aligned} U = & \int_0^{L_{cf}} \int_0^R \phi \rho_g c_{v,g} T_g \, 2\pi r \, dr \, dz + \int_{L_{pt}}^{L_{hf}} \int_0^R \phi \rho_g c_{v,g} T_g \, 2\pi r \, dr \, dz \\ & + \int_0^{L_{cf}} \int_0^R (1-\phi) \rho_m c_m T_m \, 2\pi r \, dr \, dz + \int_{L_{pt}}^{L_{hf}} \int_0^R (1-\phi) \rho_m c_m T_m \, 2\pi r \, dr \, dz \\ & + \int_0^{L_{hf}} \int_0^{R+t} \rho_w c_w T_w \, 2\pi r \, dr \, dz + \int_{L_{cf}}^{L_{pt}} \int_0^R \rho_g c_{v,g} T_g \, 2\pi r \, dr \, dz \end{aligned} \tag{4.10}$$

where ρ_w is the wall density, ρ_m is the matrix density, $c_{v,g}$ is the specific heat of the gas at constant volume, c_w is the specific heat of the wall, c_m is the specific heat of the matrix, L_{cf} is the length of the cold end flow transition, L_{pt} is the length of the pulse-tube, and L_{hf} is the length of the hot flow transition.

The energy balance associated with Eqn. (4.1) is integrated over one cycle (i.e., from time, t = 0 to $t = \tau$),

$$\frac{\left(U_{t=\tau} - U_{t=0}\right)}{\tau} = \left\langle \dot{H}_{z=0} \right\rangle - \left\langle \dot{H}_{z=L} \right\rangle + \left\langle \dot{Q}_{g,z=0} \right\rangle - \left\langle \dot{Q}_{g,z=L} \right\rangle + \left\langle \dot{Q}_{w,z=0} \right\rangle - \left\langle \dot{Q}_{w,z=L} \right\rangle + \left\langle \dot{Q}_{m,z=0} \right\rangle - \left\langle \dot{Q}_{m,z=L} \right\rangle \tag{4.11}$$

where $U_{t=\tau}$ is the energy in the pulse-tube and the wall at the end of a cycle and $U_{t=0}$ is the energy in the pulse-tube and the wall at the beginning of a cycle. The notation $\langle\ \rangle$ indicates that the quantity contained within the brackets has been time averaged over a single cycle and divided by the cycle time so that it represents the average over a cycle. Therefore, for example, $\left\langle \dot{H}_{z=0} \right\rangle$ is the average enthalpy flow at z = 0 during the cycle, $\dot{H}_{z=0}$, computed according to,

$$\left\langle \dot{H}_{z=0} \right\rangle = \frac{1}{\tau} \int_0^{\tau} \dot{H}_{z=0}\, dt \tag{4.12}$$

This time averaging is performed for all the energy flows entering and exiting the system. For a cyclic steady-state condition, the internal energy associated with the gas, matrix, and wall at the end of the cycle must equal the internal energy at the beginning of the cycle. Therefore, the left side of Eqn. (4.11) will approach zero as the system approaches a cyclic steady state. The refrigeration provided by the pulse-tube is directly related to (and at most equal to) the sum of the energy terms evaluated at z = 0; the sum of the energy flows at the cold end of the pulse tube, $\left\langle \dot{E}_{z=0} \right\rangle$, is computed according to ,

$$\left\langle \dot{E}_{z=0} \right\rangle = \left\langle \dot{H}_{z=0} \right\rangle + \left\langle \dot{Q}_{g,z=0} \right\rangle + \left\langle \dot{Q}_{w,z=0} \right\rangle + \left\langle \dot{Q}_{m,z=0} \right\rangle \tag{4.13}$$

Note that the refrigeration provided once the device has reached cyclic steady state can also be determined from the cycle average energy flow evaluated at any axial location; for example, at the outlet of the pulse-tube. The net energy flow through the outlet plane of the pulse tube, $\left\langle \dot{E}_{z=L} \right\rangle$, is calculated according to,

$$\left\langle \dot{E}_{z=L} \right\rangle = \left\langle \dot{H}_{z=L} \right\rangle + \left\langle \dot{Q}_{g,z=L} \right\rangle + \left\langle \dot{Q}_{w,z=L} \right\rangle + \left\langle \dot{Q}_{m,z=L} \right\rangle \tag{4.14}$$

Substituting Eqns. (4.13) and (4.14) into Eqn. (4.11) for a cyclic steady state leads to,

$$\left\langle \dot{E}_{z=0} \right\rangle = \left\langle \dot{E}_{z=L} \right\rangle = \left\langle \dot{E} \right\rangle \tag{4.15}$$

The average net energy flow rate should be constant with position along the pulse-tube for cyclic steady-state operation; the degree to which the average energy flow is constant with position is an indication of the convergence of the model as well as the numerical accuracy.

In order to compare different designs using a single quantity that characterizes the performance, a figure of merit (*FOM*) for the operation of the pulse-tube can be defined as,

$$FOM = \frac{\left\langle \dot{E} \right\rangle}{\left\langle P\dot{V}_c \right\rangle} \tag{4.16}$$

where $\left\langle P\dot{V}_c \right\rangle$ is the theoretical potential of the flow to provide refrigeration (theoretical maximum cooling power referred to as the acoustic power) discussed in Chapter 1 and expressed as,

$$\left\langle P\dot{V}_c \right\rangle = \frac{1}{\tau}\int_0^{\tau}\int_0^{R} \left(\tilde{P}u \right)_{z=0} 2\pi r \, dr \, dt \tag{4.17}$$

where $\tilde{P}$ is the dynamic pressure at the cold end and *u* is the velocity at the cold end.

4.2 Post-Processing

The manipulations required to carry out the pulse-tube energy analysis discussed in Section 4.1 are implemented via a custom-written MATLAB routine. To facilitate this analysis, the FLUENT solver is setup so that the temperature, temperature gradient, pressure, axial velocity, and radial velocity are exported to text files at each time step. The exported data contains the selected variables at every radial node over a defined set of axial grid locations (corresponding to planes in the computational domain located at various axial locations) for each time step during the simulation.

4.2.1 Data Reduction

The reduction process for the exported data from the FLUENT solver begins by reading in the data files (the data files are sequential and numbered by time step). From this input data, the cross-sectional area weighted average temperature, velocity, pressure, density, mass flow rate, enthalpy, conductive energy flows, and acoustic power are computed using a trapezoidal numerical integration scheme. The results are written to an intermediate file. Once the area weighted averaging has been performed for all data files and quantities, these results are time averaged using a trapezoidal numerical integration scheme. The results that are reported to the user include: the energy imbalance in the computational domain, the time averaged mass flow rate, the time averaged conductive heat flows, the time averaged enthalpy flows, the time averaged acoustic power flows, and the figure of merit for the modeled system.

4.2.2 Convergence

In transient numerical simulations, two types of convergence can be defined: (1) local model convergence, and (2) global convergence. Local convergence refers to the numerical solvers' iterative minimization of the error in the governing equations at a given point in the time marched solution. The required minimum error is defined as the convergence criteria and is defined by the user for each of the equations being solved (e.g., the continuity equation, the momentum equations in each direction, the energy equation, as well as other scalar equations that might be related to the turbulence model). For the results presented in this thesis, the tolerances set for these equations are: continuity: $1x10^{-6}$, x and y momentum equations: $1x10^{-5}$, energy equation: $1x10^{-7}$, and k and ε equations: $1x10^{-4}$. An example of the local model convergence behavior that is typical for the simulations carried out in this thesis is illustrated in Figure 4.2; note that the multiple vertical lines represent the local convergence at each time step.

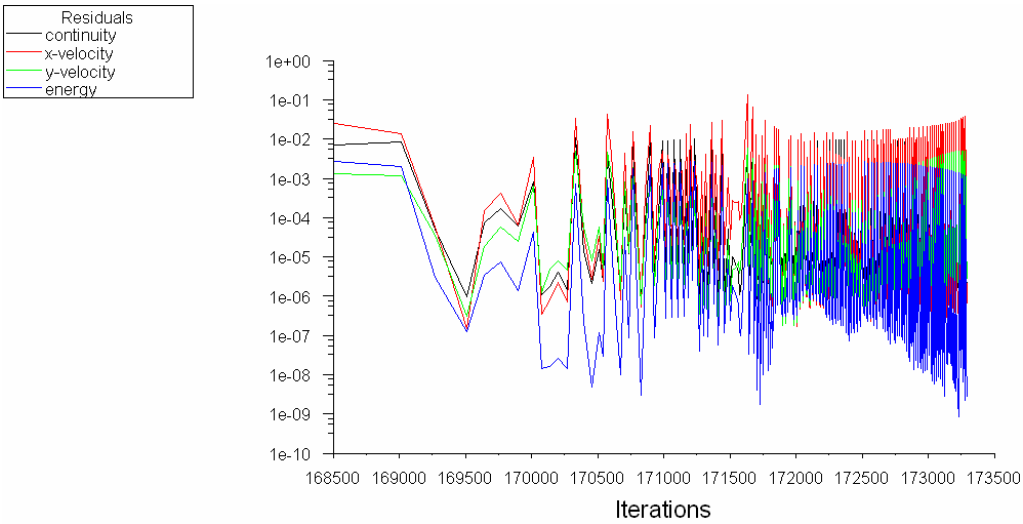

Figure 4.2: Plot showing local convergence behavior for a simulated model where the absolute residual error magnitude is plotted on the dependent axis as a function of the iteration number on the independent axis.

Often with transient numerical models, the criteria on the local grid convergence assures that the model is converging at each timestep in the solution but does not explicitly define the convergence for the overall model. The global convergence criteria must be defined by the user based upon the physics present in the model as well as the qualities of interest. For the pulse tube model, a logical choice for a global convergence parameter is the minimization of the error in the 1st law balance that is discussed in section 4.1. More specifically, Eqn. (4.15) shows that at a cyclic steady state condition, the energy flowing into the domain must equal that flowing out. Using this result, a convergence parameter can be defined as the normalized difference between these energy flows.

$$\dot{E}_{imb} = \frac{\left\langle \dot{E}_{z=0} \right\rangle - \left\langle \dot{E}_{z=L} \right\rangle}{\left\langle \dot{E}_{z=0} \right\rangle} \tag{4.18}$$

The normalized energy imbalance is utilized to judge the global convergence of the pulse tube model to a satisfactory cyclic steady state solution. The behavior of the normalized energy imbalance (the global convergence parameter) is illustrated in Figure 4.3 as a function of the cycle number. Note that the initial the imbalance is extremely large but after a sufficient number of cycles have been simulated, the imbalance approaches zero.

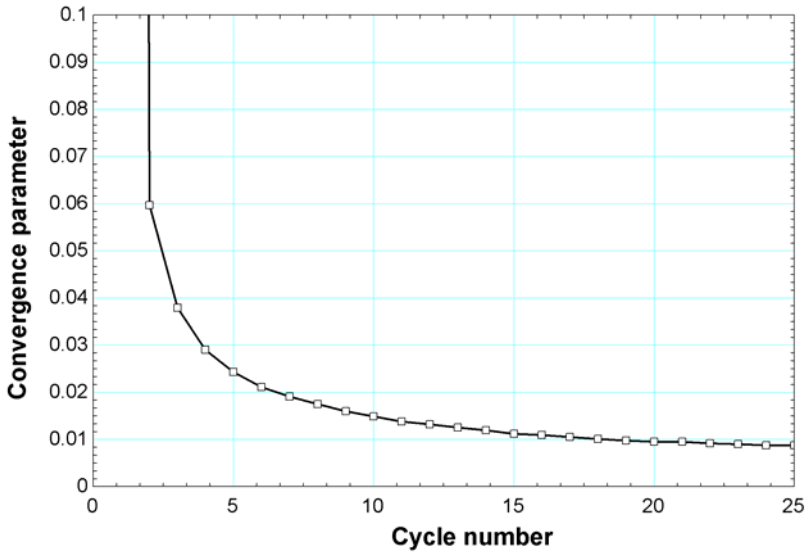

Figure 4.3: Plot illustrating behavior of the convergence parameter as a function of the number of simulated cycles.

4.3 Grid/Numerical Convergence

Two critical aspects associated with the development of any computational fluid dynamic model are the selection of an appropriate grid size (resolution) and the discretization scheme for the convective terms in the governing equations. The methodology employed here to establish grid independence is to vary the grid size relative to a nominal value. This variation maintained consistent scaling of the grid in the axial and radial directions for consistency. An appropriate nominal grid size was estimated using work by Lyulina (2004) and Cha (2004) and determined to be 5000 elements. The residence time for a fluid element using the maximum fluid velocity was used to determine a reasonable value for the time step size. The numerical discretization scheme used for the convective terms in the momentum equations was parametrically varied for each grid size. The quantity used to compare these various configurations was the predicted total energy flow $\left\langle \dot{E}_{z=0} \right\rangle$. The results are presented in Table 4.1.

Table 4.1 – Cyclic energy flow for various grid size and discretization schemes.[1]

Grid Size	1st Order Upwind	2nd Order Upwind	3rd Order MUSCLE
1000	411.2 W	516.4 W	513.8 W
2500	497.7 W	608.6 W	603.5 W
5000[2]	557.6 W	684.3 W	683.1 W
7500	558.0 W	684.8 W	683.8 W
10000	558.3 W	685.4 W	684.3 W

[1] FLUENT allows the selection of four convective discretization schemes, only three were modeled. The QUICK scheme is not valid with the meshing scheme chosen for the model (tetrahedral and quadrilateral elements).
[2] Nominal mesh value.

Based upon the results presented in Table 4.1, it is clear that low grid resolution (for all discretization schemes) leads to a rather large under-prediction in the energy flow. However, as the grid size approaches and exceeds the nominal value, the predicted energy flow becomes insensitive to the grid size. Additionally, the results show that the higher-order discretization schemes are more accurate than the 1st order scheme for a given grid size; the higher order schemes are in agreement with each other while the 1st order scheme severely under predicts the energy flow even when a relatively fine grid is used. From this analysis, the nominal mesh size selected for the model was in the range of 7500-10000 elements (depending somewhat on the complexity of the flow transitions being studied) and the selected discretization scheme was 2nd order upwinding as this approach requires less solution time than the 3rd order MUSCLE discretization scheme while providing essentially identical results.

4.4 Analytical Verification

There are relatively few analytical solutions that are particularly relevant to the complex hydrodynamic and thermal processes that occur during a pulse-tube cryocooler cycle.

However, the model was verified against the analytical solution for fully developed laminar flow in a round tube that is subjected to a spatially uniform but oscillating pressure gradient.

4.4.1 Analytical Solution for Oscillating Pipe Flow

One of the classic solutions to the Navier-Stokes equations is for fully developed laminar flow in a round duct that is subjected to a spatially uniform but oscillating pressure gradient. There is an obvious similarity between the flow within a pulse-tube and this solution and therefore the solution was used as a point of verification for the numerical model.

The primary limiting assumptions of the analytical solution are:

1) incompressible fluid
2) velocity in the axial direction is a function of radius and time only; i.e., $v_z=v_z(r,t)$
3) the radial and angular velocity components are zero; i.e. $v_r=0$ and $v_\theta=0$
4) fully developed laminar flow
5) constant fluid properties
6) spatially uniform harmonic pressure gradient
7) zero body forces

The first step in deriving the analytical solution involves evaluating the general continuity equation in cylindrical coordinates,

$$\frac{d\rho}{dt}+\frac{1}{r}\frac{d\left(\rho r v_r\right)}{dr}+\frac{1}{r}\frac{d\left(\rho v_\theta\right)}{d\theta}+\frac{d\left(\rho v_z\right)}{dz}=0 \tag{4.19}$$

where ρ is the density of the fluid, t is time, r is the radius of the tube, v_r is the r component of the velocity, v_θ is the velocity in the θ direction, v_z is the velocity in the z direction. Based upon the assumptions listed above for the velocity components, the continuity equation is exactly satisfied as each term must be identically zero. The incompressible form of the Navier-Stokes (momentum) equations in cylindrical coordinates are (Panton, 2005):

r-momentum

$$\rho\left(\frac{dv_r}{dt}+v_r\frac{dv_r}{dr}+\frac{v_\theta}{r}\frac{dv_r}{d\theta}-\frac{v_\theta^{\,2}}{r}+v_z\frac{dv_r}{dz}\right) = -\frac{dP}{dr}+\mu\left[\frac{1}{r}\frac{d\left(r\tau_{rr}\right)}{dr}+\frac{1}{r}\frac{d\tau_{\theta r}}{d\theta}+\frac{d\tau_{zr}}{dz}+\frac{\tau_{\theta\theta}}{r}\right]+F_r \tag{4.20}$$

θ-momentum

$$\rho\left(\frac{dv_\theta}{dt}+v_r\frac{dv_\theta}{dr}+\frac{v_\theta}{r}\frac{dv_\theta}{d\theta}+\frac{v_r v_\theta}{r}+v_z\frac{dv_\theta}{dz}\right) = -\frac{1}{r}\frac{dP}{d\theta}+\mu\left[\frac{1}{r^2}\frac{d\left(r^2\tau_{r\theta}\right)}{dr}+\frac{1}{r}\frac{d\tau_{\theta\theta}}{d\theta}+\frac{d\tau_{z\theta}}{dz}+\frac{\tau_{\theta r}-\tau_{r\theta}}{r}\right]+F_\theta \tag{4.21}$$

z-momentum

$$\rho\left(\frac{dv_z}{dt}+v_r\frac{dv_z}{dr}+\frac{v_\theta}{r}\frac{dv_z}{d\theta}+v_z\frac{dv_z}{dz}\right) = -\frac{dP}{dz}+\mu\left[\frac{1}{r}\frac{d\left(r\tau_{rz}\right)}{dr}+\frac{1}{r}\frac{d\tau_{\theta z}}{d\theta}+\frac{d\tau_{zz}}{dz}\right]+F_z \tag{4.22}$$

where P is the pressure, μ is the viscosity of the fluid, $F_{r,\theta,z}$ represent the body forces on the fluid in cylindrical coordinates, and τ represents the momentum flux (shear stress) (i.e. τ_{rz} would be the flux of z momentum transferred across a plane perpendicular to the r direction on a fluid element).

Using assumptions 1, 2, 3, 4, 5, and 7, the Navier-Stokes equations reduce to:

$$\frac{dP}{dr} = 0 \tag{4.23}$$

$$\frac{dP}{d\theta} = 0 \tag{4.24}$$

$$\rho \frac{dv_z}{dt} = -\frac{dP}{dz} + \frac{1}{r}\frac{d\left(r\,\tau_{rz}\right)}{dr} \tag{4.25}$$

The shear stress term, τ_{rz}, in Eqn. (4.25) can be expanded and simplified using assumption 3:

$$\tau_{rz} = \mu\left(\frac{dv_z}{dr} + \frac{\cancel{dv_r}}{\cancel{dz}}\right) = \mu\frac{dv_z}{dr} \tag{4.26}$$

Using this simplification and realizing that the shear stress is a function of *r* only, the second term of Eqn. (4.25) can be simplified using the chain rule:

$$\frac{1}{r}\frac{d\left(r\,\tau_{rz}\right)}{dr} = \mu\frac{1}{r}\frac{d}{dr}\left(r\frac{dv_z}{dr}\right) = \mu\left(\frac{1}{r}\frac{dv_z}{dr} + \frac{d^2v_z}{dr^2}\right) \tag{4.27}$$

Using this result and bringing the density in Eqn. (4.25) to the right side of the equation, the governing equation for the analytical solution is given by:

$$\frac{dv_z}{dt} = -\frac{1}{\rho}\frac{dP}{dz} + \upsilon\left(\frac{1}{r}\frac{dv_z}{dr} + \frac{d^2v_z}{dr^2}\right) \tag{4.28}$$

where υ is the kinematic viscosity of the fluid. The pressure gradient is assumed to vary sinusoidally; therefore, the first term on the right side of Eqn. (4.28) can be expressed as:

$$-\frac{1}{\rho}\frac{dP}{dz} = K\sin\left(\omega t\right) \tag{4.29}$$

where K is the magnitude of the pressure gradient normalized with respect to density, and ω is the angular frequency of the variation. Equation (4.29) can be re-written as:

$$-\frac{1}{\rho}\frac{dP}{dz} = -i\,Ke^{i\omega t} \tag{4.30}$$

and inserted into Eqn.(4.28) to obtain:

$$\frac{dv_z}{dt} = i\,Ke^{i\omega t} + \upsilon\left(\frac{1}{r}\frac{dv_z}{dr} + \frac{d^2v_z}{dr^2}\right) \tag{4.31}$$

Because the governing equation is linear, the functional form of the solution can be expressed as:

$$v_z(r,t) = f(r)e^{i\omega t} \tag{4.32}$$

Based upon the analysis presented by Uchida (1956) and Grace (1928), the solution to this equation is:

$$v_z(r,t) = -\frac{K}{\omega}e^{i\omega t}\left\{1 - \frac{J_o\left(r\sqrt{\frac{i\omega}{\upsilon}}\right)}{J_o\left(R\sqrt{\frac{i\omega}{\upsilon}}\right)}\right\} \tag{4.33}$$

where R is the outer radius of the tube, J_o is the Bessel function of the 1st kind, and i is notation used to signify complex components (i.e. the solution has real and imaginary components). This result can be further reduced in the limit of very low and high angular frequencies using asymptotic expansions. Since it is envisioned that the pulse-tube design tool will be used for PTR systems that are operated at high angular frequencies, the most

relevant solution is in the limit of high angular frequency which has been provided by Uchida (1956), Grace (1928), and Schlichting (2003):

$$v_z(r,t) = \frac{K}{\omega}\left[\cos(\omega t) - \sqrt{\frac{R}{r}}\, e^{-\sqrt{\frac{\omega}{2\upsilon}}(R-r)} \cos\left(\omega t - \sqrt{\frac{\omega}{2\upsilon}}(R-r)\right)\right] \tag{4.34}$$

4.4.2 CFD Validation Model

A simple CFD model of a round tube subjected to a sinusoidally varying pressure gradient was developed using the solution parameters and techniques discussed in this and the previous chapter. The parameters used for the development of the CFD validation model are summarized in Table 4.2.

Table 4.2: Nominal Model Parameters

Input Parameter	**Symbol**	**Nominal Value**
Radius	R	0.1 m
Length	L	3 m
Mean system pressure	$\bar{P}$	0 Pa
Pressure amplitude	$\tilde{P}$	100 Pa
Angular frequency	ω	100 rad/s

The model conditions were defined according to the assumptions associated with the analytical solution. The constant property data for helium that is provided by FLUENT was utilized. It should be noted that the viscosity was artificially set to a high value (0.002 Pa-s) in order to allow for a simulation where which the viscous effects could be easily observed. The actual viscosity value for helium causes the viscous effects to be small and therefore confined to a small region at the wall. Also, because the analytical solution assumes no body forces, gravitational acceleration in the model was disabled.

The boundary conditions utilized for the model were an oscillating pressure at the inlet of the model, a constant pressure at the outlet of the model, a fixed wall boundary condition, and a centerline axis. The oscillating pressure gradient given in Eqn. (4.29) was integrated with respect to length in order to provide the inlet pressure boundary condition:

$$P = \int_0^L -\frac{1}{\rho}\frac{dP}{dz}dz = \int_0^L -\rho K \sin(\omega t)\,dz = -\rho L K \sin(\omega t) \tag{4.35}$$

The product $\rho L K$ is equal to the amplitude of the pressure oscillation at the inlet:

$$\tilde{P} = \rho L K \tag{4.36}$$

The harmonic pressure boundary condition imposed at the inlet of the tube given by Eqn. (4.37) was implemented using an external C program:

$$P = -\tilde{P}\sin(\omega t) \tag{4.37}$$

The pressure outlet boundary was specified to be a constant gage pressure of 0 Pa. The wall boundary condition was set to be stationary with a no-slip condition and the centerline axis of the model was defined as an axis.

4.4.3 CFD Validation Results

The computational model was solved for 20 cycles in order to ensure that the flow in the tube had reached a cyclic steady state; this assumption was verified by comparing the percent difference between the velocity profiles for consecutive cycles until the change was less than one percent. For the 20th cycle, the velocity at each radial node was exported for

dimensionless cycle times (i.e., time normalized by the period of the cycle and multiplied by 2π) of $\pi/2\omega$, π, $3\pi/2$, and 2π at five equally spaced radial planes along the tube. The velocity profiles at each these radial planes are presented in Figs. 4.4(a) through (d) at each of the times, respectively, and these results are compared with the analytical solution evaluated at the same times.

Figure 4.4(a) illustrates the radial velocity profiles computed in FLUENT overlaid on the analytical solution for a dimensionless cycle time of $\pi/2$. The results from the numerical solution compare extremely well with the analytical solution. The only deviation from the analytic solution is seen by the dashed blue line, which represents the velocity at the inlet of the tube. The reason for the lack of agreement associated with the velocity at the inlet is related to the fact that the flow at the entrance of the tube is not fully developed. Figure 4.4(b) illustrates the radial velocity profiles computed in FLUENT overlaid on the analytical solution for a dimensionless cycle time of π. Again, there is excellent agreement between the numerical solution and the analytical solution. The only deviation is associated with the dashed dark green line, which represents the velocity at the outlet of the tube. This deviation is also due to the developing flow region, which is now located at the outlet of the tube due to the flow reversal. Figures 4.4(c) and 4.4(d) present results that are equal and opposite to those seen in Figs. 4.4(a) and 4.4(b); excellent agreement is observed between the numerical results and the analytical solution with the only deviation occurring at the entrance and exit of the tube.

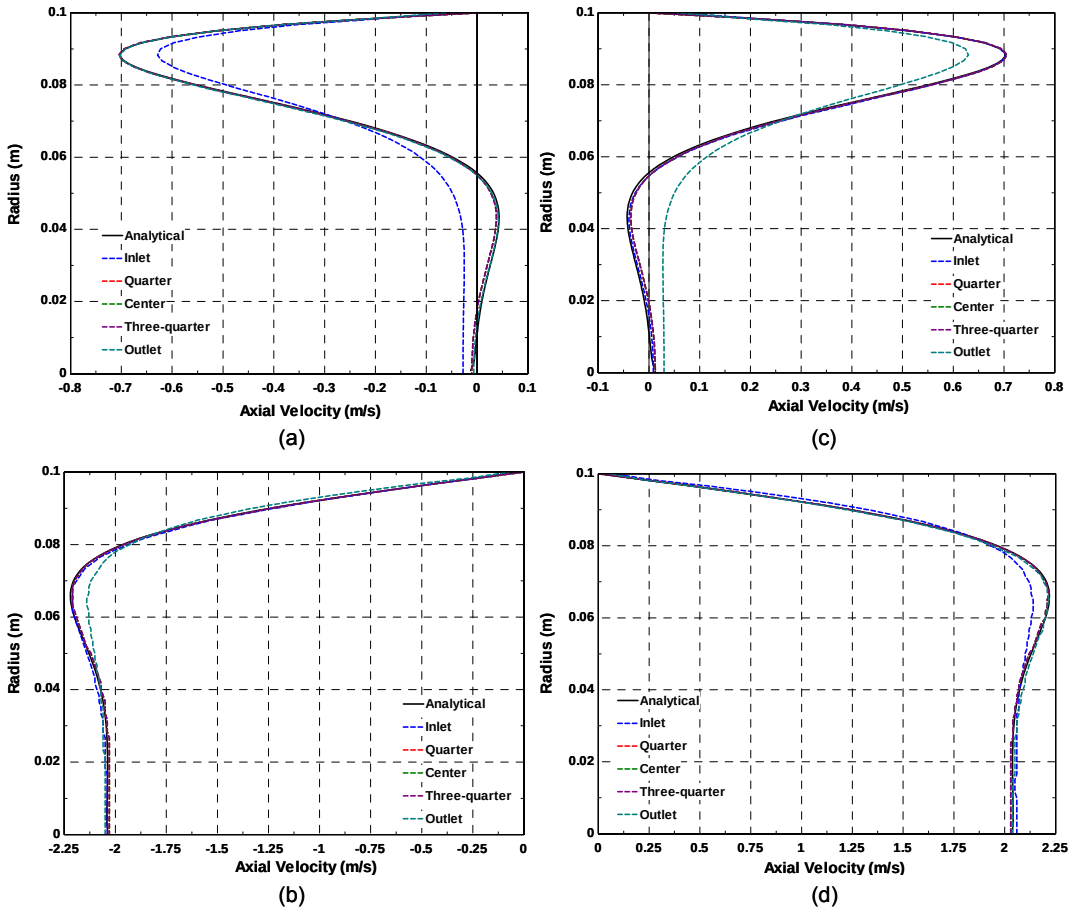

Figure 4.4: Velocity as a function of radial position (dashed lines) predicted by the numerical solution at five equally axial spaced planes overlaid on the analytical solution (solid black line) for dimensionless cycle times of (a) $\omega t=\pi/2$, (b) $\omega t=\pi$, (c) $\omega t=3\pi/2$, and (d) $\omega t=2\pi$.

The results of this analysis validates that, (1) FLUENT is able to capture the effects of oscillating pipe-flow, and (2) the modeling methodology, solver settings, and grid size are sufficient to resolve the complex flow features that are inherent in the more complex pulse tube flow. Notably, the results show that the FLUENT code is able to accurately capture the two-layered viscous effects at all times during the cycle as predicted by the analytical solution; there is a layer near the wall where viscous effects dominate and cause the flow to lag the center core flow.

4.5 Parametric Design Study and Results

The developed CFD model (discussed in Chapter 3) in conjunction with the developed post-processing methodology was utilized to perform a parametric design analysis for the anticipated experimental cooler to be utilized for experimental validation of the developed model. This parametric study focused on the geometric design of the pulse-tube and flow transitions at defined operating conditions. The specific goal of this study was to investigate how the efficiency of the pulse-tube (*FOM*) was affected by varying the pulse tube diameter (from short and fat to long and skinny) and the specific configuration of the flow transitions. The dimensionless pulse-tube diameter ($\tilde{D}$) is defined as:

$$\tilde{D} = \frac{D_{pt} - D_{in}}{D_{reg} - D_{in}} \tag{4.38}$$

where D_{pt} is the diameter of the pulse-tube, D_{reg} is the diameter of the regenerator, and D_{in} is the diameter of the inertance tube. In the limit that $\tilde{D}$ is 0, the pulse-tube has the same diameter as the inertance tube and if $\tilde{D}$ is 1 then the pulse-tube has the same diameter as the regenerator. For any run, the volume of the pulse tube and the flow transitions were held constant and equal to 3x and 0.2x, respectively, the volume of the gas entering the cold end during one cycle. The system parameters utilized for the parametric study were: a frequency of 50 Hz, a cold end acoustic power of 40 W, a mass flow amplitude of 5 g/s, mean pressure of 2.5 MPa, cold end pressure ratio of 1.22, a cold end temperature of 80 K, hot end temperature of 300 K, cold end phase angle of -12 deg, a regenerator diameter of 25.4 mm, and an inertance tube diameter of 6.4 mm; the parameters are consistent with a experimental facility at NIST used to validate the model.

The parametric study was performed for two flow transition configurations: (1) the flow transitions are empty but include regions at either end that are filled with 10, #100 mesh wire screens and (2) the flow transitions are completely filled with #100 mesh wire screens. For all following results the developed post-processing algorithm was utilized for all numeric results while the program Ensight was utilized for visualizing the flow field (CEI, 2008). For all simulations the cyclic averaged mass conservation was computed at each end of the system for all simulated models with values not exceeding 1e-7 g/s. Figure 4.5 illustrates the pulse tube efficiency (*FOM*) as a function of the dimensionless pulse-tube diameter for both flow transition configurations.

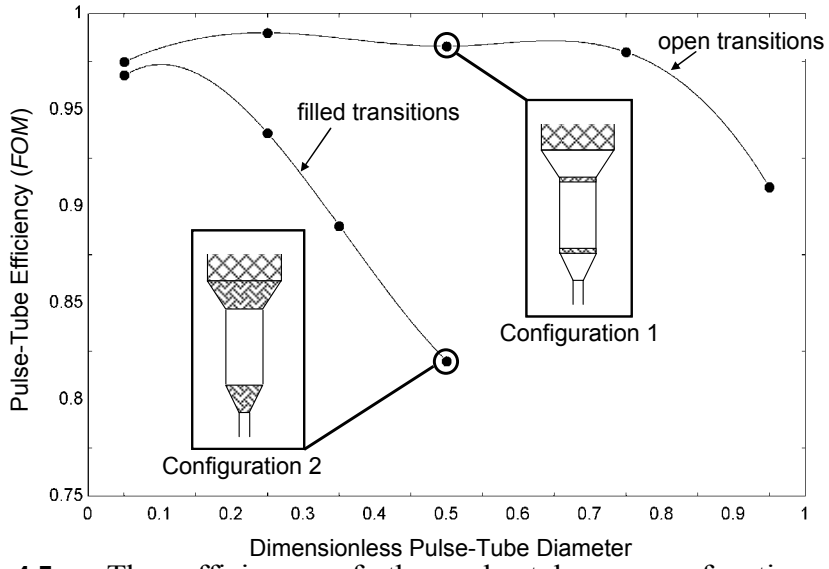

Figure 4.5: The efficiency of the pulse-tube as a function of the dimensionless pulse-tube diameter for the two flow transition configurations.

The results presented in Figure 4.5 are interesting; a relatively small modification to the location and number of the screens in the flow transitions can lead to a substantial improvement in the predicted pulse-tube efficiency. For the case of filled flow transitions, an optimum peak at low dimensionless pulse-tube diameters is observed followed by a dramatic

decrease in efficiency. This decrease in efficiency is directly influenced by the packed screen flow transitions; the anisotropy of the screens causes the fluid to jet into the pulse-tube from the inertance network, destroying the thermal stratification of the gas piston. This effect is illustrated qualitatively in Figure 4.6(b), which shows the temperature contours overlaid onto the velocity vectors at one instant of time for this configuration. However, when the flow transitions are left open except for the small packs of wire mesh screen at either end of the pulse-tube, the efficiency remains relatively constant over a large range of the dimensionless pulse-tube diameter. In this case, the jetting effects have been alleviated because the empty spaces allow the flow to equalize before entering the pulse-tube. The characteristic temperature contours and velocity vectors for this configuration at one instant in time are illustrated in Figure 4.6(a). From this parametric analysis it is clear that the open transitions provide a superior flow transition design.

The results of the parametric study indicate that the model is correctly predicting the flow features expected, the CFD model can provide valuable guidance relative to the optimal design of the pulse tube and flow transitions, and the post-processing routine works as designed.

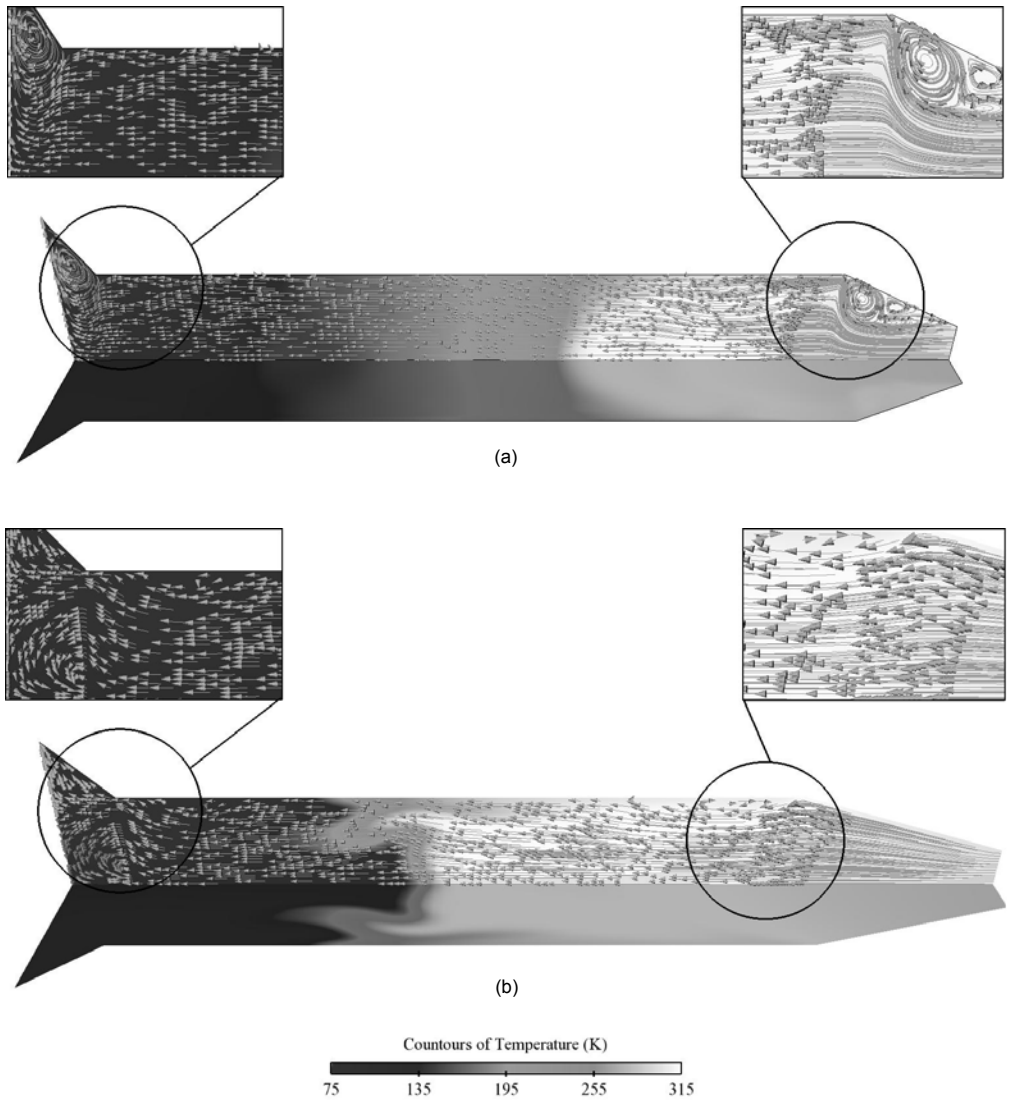

Figure 4.6: The temperature contours and velocity vectors at one instant in time for (a) configuration (1) in Figure 4.5 and (b) configuration (2) in Figure 4.5.

5. Experimental Validation Methodology

In order for any computational model to be accepted, it must be verified; this verification may be based on limiting analytical solutions (if they are available), or by direct comparison to experimental data. Due to the complex hydrodynamic and thermal aspects of the oscillating cryogenic gas flow that is present in Pulse Tube Cryocoolers (PTC's), analytical solutions that can be used to validate the CFD model do not exist. As a result, it is necessary to rely on experimental measurements for validation. Experimental validation for a model of a complex, thermal-fluid system is difficult and requires careful design and fabrication of precise experiments. This is particularly true for PTC's because the experimental measurements must be performed at cryogenic temperatures. This chapter discusses the specific quantities that must be measured for verification, the experimental measurement methodology, and the design and setup of the experimental test facility.

5.1 Experimental Validation Methodology

This section discusses the specific quantities of interest and the associated measured quantities. Illustrated in Figure 5.1 is an energy balance applied to the cold end of a PTC. This energy balance is,

$$\dot{E}_{REG,c} + \dot{Q}_{net} = \dot{E}_{PT,c} \tag{5.1}$$

where $\dot{E}_{REG,c}$ is the regenerator energy flow term (also called the regenerator loss), $\dot{Q}_{net}$ is the net cooling power, and $\dot{E}_{PT,c}$ is the net enthalpy flow through the pulse-tube and flow transitioning components.

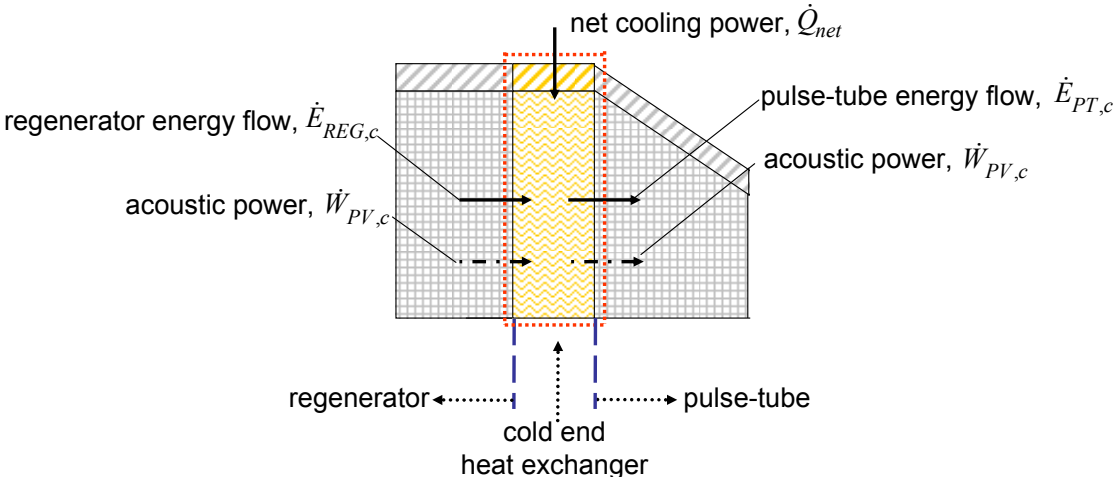

Figure 5.1: Illustration showing an energy balance applied to the cold end heat exchanger in a PTC with delineation of the energy and power flows.

Also illustrated in Figure 5.1 (but not part of the energy balance) is a fourth term, $\dot{W}_{PV,c}$, which is the acoustic power flow at the cold end of the system. The acoustic power is not a thermodynamic energy flow. Rather, the acoustic power represents the theoretical maximum refrigeration that could be provided if the gas at the cold end of the pulse-tube were expanded reversibly against a piston. The acoustic power term is computed based on the pressure and mass flow rate present at the cold end and is therefore often used by designers in order to predict the performance of the pulse-tube component. A typical approach is to estimate the performance as being some fraction (the value of the fraction is based on the designer's experience and intuition) of the available acoustic power. The most relevant figure of merit (*FOM*) that characterizes a pulse tube is therefore the ratio of pulse-tube enthalpy flow ($\dot{E}_{PT,c}$) to the acoustic power flow ($\dot{W}_{PV,c}$).

The pulse tube enthalpy flow and the acoustic power flow are the primary quantities predicted by the CFD model; therefore, these are the two quantities that must be measured in

order to verify the CFD model. However, the quantity that is most directly measurable in a pulse-tube is the net cooling power. According to Eqn. (5.1), the net cooling power is equal to the pulse-tube enthalpy flow less the regenerator energy flow (i.e., the "regenerator loss"), as illustrated in Figure 5.1. As a result, the regenerator energy flow at the cold end of an actual PTC system must be separately measured in order to infer the pulse tube enthalpy flow from the net cooling power. The acoustic power must also be measured in order to determine the figure of merit from the pulse tube enthalpy flow.

Based on this discussion, the primary quantities that must be measured are the regenerator loss, the net cooling power, and the acoustic power flow; from these quantities, the pulse-tube enthalpy flow and pulse tube figure of merit can be determined. Since none of these energy flows are directly measurable, it is necessary to develop experimental methods that allow these terms of interest to be computed based on directly measurable quantities.

5.2 Experimental Measurement Methodology

The experimental methodology is summarized below and discussed in the subsequent sections. The details of the experimental apparatus are discussed in Section 5.3.

1. Calibration of a thermal bus that allows the rate of heat transfer from/to the cold end to be measured.
2. Calibration of a custom mass flow meter for use under oscillatory flow conditions at cryogenic temperatures.
3. Measurements of the regenerator loss, independent of the pulse tube component.
4. Measurement of the net cooling power with a pulse tube component.
5. Measurement of the acoustic power flow at the cold end of the system.

5.2.1 Thermal Bus Calibration

It is necessary to precisely measure heat flows entering and exiting the cold end of the system; during operation; these heat flows correspond to either the cooling power or regenerator losses depending on the configuration. The measurements of the heat flow at the cold end of the system involve the use of a conductive path (referred to as a thermal bus bar) installed between the experiment and an auxiliary source of cooling or heating, which is a commercial GM cryocooler outfitted with a heater system. The bus bar must be calibrated in-situ in order to be useful; a schematic of this calibration set-up is illustrated in Figure 5.2.

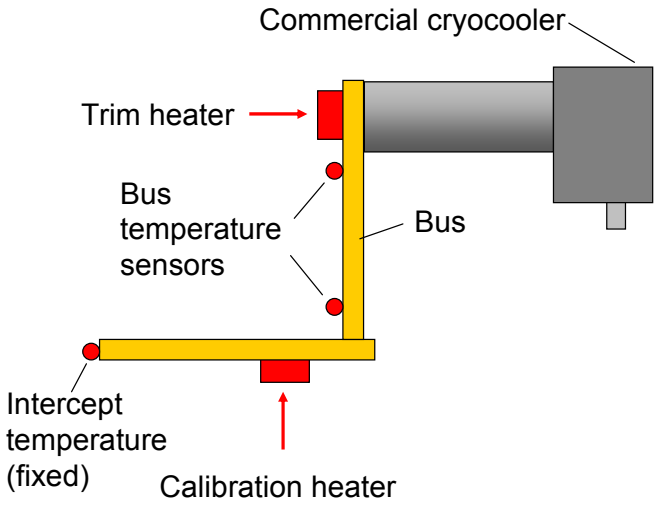

Figure 5.2: Illustration showing a schematic of the test set-up utilized for calibration of thermal bus bar for measurement of energy flows entering and exiting the cold end of the experimental test system.

The heat transfer rate through the bus bar is calibrated by installing temperature sensors along the length of the bar. The warm end of the bus bar (the intercept temperature in Figure 5.2, which is the end that is to be interfaced with the cold end of the experimental system) is set to a desired operating temperature using the trim heaters on the cold stage of the cryocooler. A second set of heaters (the calibration heaters) are placed at the warm end of

the bar and a precisely measured amount of electrical heating is applied, generating a finite temperature difference across the bus bar. The relationship between the temperature difference across the bus bar and the calibration heater power that is being conducted through it results in a calibration curve.

5.2.2 Mass Flow Sensor Calibration

In an operational PTC, it is difficult to measure the instantaneous mass flow rate because the instruments that are typically used (e.g., hot-wire anemometers) tend to disturb the flow field as well as introduce un-wanted dead-volume in the system. Rawlins et al. (1993) have shown that the instantaneous mass flow rate inside a PTC can be measured using specially designed hot-wire anemometers. However, discussions with the Cryogenics Group at NIST (who pioneered this measurement technique) indicate that hot -wire based mass flow rate measurements are still very difficult to make in the pulse-tube environment because the hot wire instrumentation often fails due to the oscillating flow field and the instruments themselves do not work well below about 77 K. The researchers at NIST also found that any small particles in the system (for example, debris from the regenerator) will cause the thin wires used for the hot-wire probe to break. The probes protrude into the flow stream which disturbs the flow and subsequently effects the results of the mass flow measurements. Additionally, once the probes are cooled below 77 K the resistance of conventional hot-wire materials drops substantially and therefore extremely large input powers are required in order to generate a meaningful signals. The large power leads to a substantial amount of power dissipated into the flow field that further biases the measurement.

An alternative method for measuring the mass flow rate at the cold end of the system correlates the amplitude of the pressure drop measured across a flow resistance to the mass flow rate. The calibration of the flow measurement device is accomplished by comparing the measured pressure difference amplitude under oscillating conditions across a flow resistance to the actual mass flow rate amplitude into/out of a known volume. The flow resistance used in the experiment consists of a stack of copper mesh screens that serves the dual role of a thermal intercept (i.e., the screens are thermally connected to the heat path leading to the cryocooler) as well as a flow measurement sensor. The calibration of the differential pressure amplitude across the screens to the mass flow rate amplitude is performed by installing the measuring device on the cold end of the regenerator component and connecting it via a short transfer line to a reservoir of known volume, as shown in Figure 5.3.

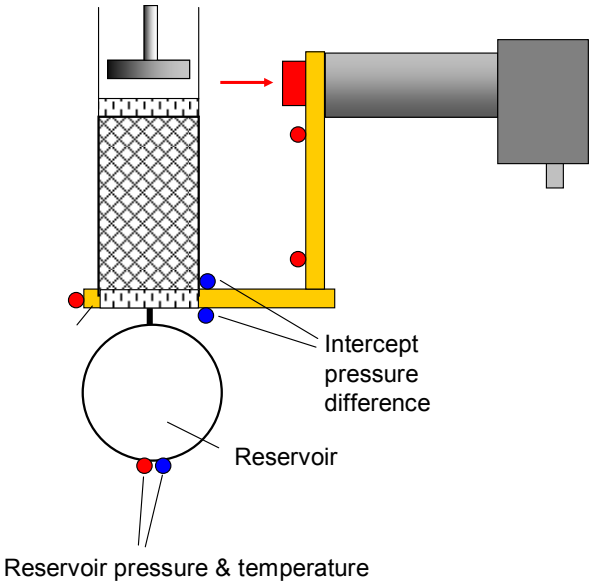

Figure 5.3: Illustration showing a schematic of the mass flow and phase angle measurement apparatus.

To generate the required calibration curve (mass flow amplitude as a function of the pressure drop calibration curve), the GM cryocooler is used to cool the thermal sink, the connecting

line, and the reservoir volume to the desired calibration temperature. The differential pressure amplitude across the sink is measured. The average gas temperature (i.e., reservoir wall temperature) and pressure amplitude are also measured. These quantities, together with the known volume of the reservoir, are used to determine the magnitude of the mass flow rate entering and exiting the reservoir volume, $\left|\dot{m}_{res}\right|$, according to Eqn. (5.2) (this equation is derived assuming that the gas in the reservoir behaves adiabatically and according to the ideal gas law),

$$\left|\dot{m}_{res}\right| = \frac{\left|\tilde{P}\right| V_{res}}{\gamma T_{res} R} \tag{5.2}$$

where V_{res} is the volume of the reservoir, $\left|\tilde{P}\right|$ is the amplitude of the dynamic pressure, T_{res} is the temperature of the reservoir gas, and γ is the ratio of specific heats for the working fluid. The dead volume and flow resistance between the flow sensor and the reservoir volume is made as small as possible and therefore the mass flow rate entering the reservoir is very nearly equal to the mass flow passing through the flow sensor. The assumption of adiabatic conditions within the reservoir is justified by the fact that the size of the reservoir volume is orders of magnitude larger than the thermal penetration depth of the gas and that the period of time associated with each cycle is small relative to the time required to transfer any substantial heat to/from the wall. This implies that while there is some small heat transfer with the reservoir wall, the bulk of the gas in the reservoir experiences nearly an adiabatic process.

5.2.3 Regenerator Loss Measurement

The total energy flow towards the cold end of the regenerator, also called the regenerator loss, is a combination of two terms:

$$\dot{E}_{REG,c} = \dot{H}_{REG} + \dot{Q}_{cond,REG} \tag{5.3}$$

where $\dot{H}_{REG}$ is the regenerator enthalpy flow rate, which is directly proportional to the amplitude of the mass flow rate in the regenerator, and $\dot{Q}_{cond,REG}$ which is the sum of the conduction losses in the regenerator (matrix, gas, and wall). Since $\dot{Q}_{cond,REG}$ is always from the warm end to the cold end of a passive regenerator, the resulting effect of these two terms is an undesired heat load at the cold end (i.e., a loss of available cooling power). The regenerator is isolated from the pulse-tube component so that there is no possibility of generating an enthalpy flow and cooled instead using an external source. In this configuration, the regenerator loss can be determined using the calibrated thermal bus bar installed between the cold end of the regenerator and the source of external cooling, a commercial GM cryocooler. This experiment is shown schematically in Figure 5.4. Convection and radiation from the exterior of the regenerator are minimized by placing the system in a high vacuum environment and using multiple radiation shields.

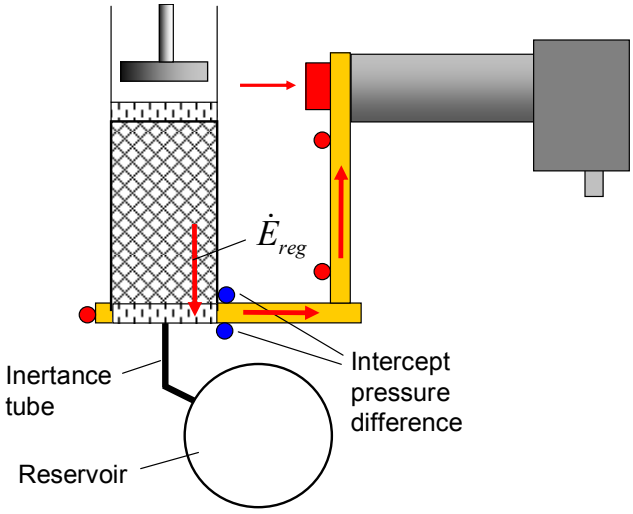

Figure 5.4: Illustration showing the schematic of the system configuration for measurement of the regenerator energy flow (loss).

At a given set of test conditions (i.e., pressure ratio at the cold end, cold end temperature, and mean pressure) the loss associated with the regenerator must be conducted through the bus bar and intercepted at the cryocooler cold stage. The heat flow is measured using the previously measured calibration curves for the thermal bus.

The phase angle between the pressure and the mass flow rate at the cold end of the regenerator must be measured simultaneously in order to define the regenerator operating condition. This phase angle is determined via the measurement of the phase associated with the pressure amplitude signals installed upstream and downstream of the thermal intercept using DSP (Digital Signal Processing) lock-in amplifiers. The phase associated with this differential signal is not the same as the phase that one would compute if the phases for the individual pressure signals were measured and mathematically subtracted but rather the phase associated with the actual differential voltage between the two pressure signals (i.e.,

the pressure difference). This difference is illustrated in Figure 5.5 via a vector analysis of the pressure signals directly upstream and downstream of the thermal intercept.

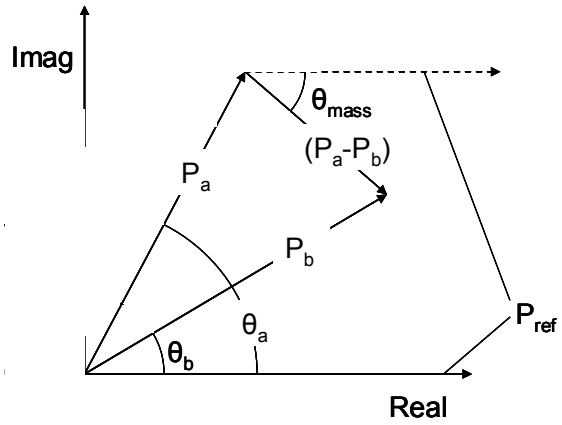

Figure 5.5: Plot illustrating the vector analysis of the pressure signals measured across the thermal sink from which the mass flow phase angle is determined; Note that P_a is the upstream pressure and P_b is the downstream pressure.

5.2.4 Pulse-Tube Net Cooling Power Measurement

The pulse tube energy flow is inferred from the measurement of the regenerator loss (discussed in the previous section) and the net cooling power. Measuring the net cooling power is relatively simple. The electrical power provided to a heater that is attached to the cold end thermal intercept is measured. An illustration of this measurement set-up is illustrated in Figure 5.6.

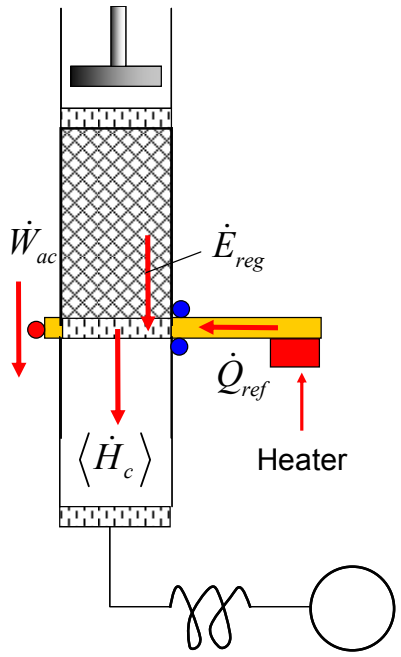

Figure 5.6: Illustration showing a schematic of the experimental test set-up for measurement of the net cooling power.

The complete PTC system is operated at a desired set of operating conditions. A precise amount of heat is applied to the thermal intercept and the corresponding steady state temperature is recorded.. As with the regenerator tests, convection and radiation are minimized using a high vacuum environment and multiple radiation shields. Using this relatively simple system set-up, the net cooling power of a PTC can be measured at any desired temperature, operational frequency, and cold end pressure ratio; by subtracting the regenerator loss measured at the same temperature and operating condition it becomes possible to infer the pulse-tube energy flow.

5.2.5 Acoustic Power Measurement

The previous sections indicated the methodology used to measure the pulse tube energy flow. The pulse tube energy flow must be normalized against the acoustic power in order to determine the pulse tube figure of merit. The difference between the acoustic power and the

pulse tube energy flow is the loss of cooling power that can be attributed to the pulse tube. The acoustic power is one of the more complex experimental measurements that is required because it requires the measurement of the actual, time-resolved flow conditions at the cold end of the pulse tube (i.e., the amplitude of the mass flow rate, the pressure variation and the phase angle between these quantities).

The expression for the acoustic power flow (assuming a sinusoidally varying pressure and mass flow) is given by,

$$W_{pv} = \frac{1}{2}\left|\dot{V}\right|\left|\tilde{P}\right|\cos\theta \tag{5.4}$$

where θ is the phase angle between mass flow and pressure, $\left|\tilde{P}\right|$ is the amplitude of the dynamic pressure, and $\left|\dot{V}\right|$ is the amplitude of the volumetric flow rate, which can be expressed approximately for an ideal gas according to,

$$\left|\dot{V}\right| = \frac{RT\left|\dot{m}\right|}{\bar{P}} \tag{5.5}$$

where $\left|\dot{m}\right|$ is the amplitude of the mass flow rate, R is the working fluid gas constant, T is the temperature of the gas flow, and $\bar{P}$ is the mean (static) system pressure. The acoustic power measurement is performed simultaneously with the cooling power measurement.

5.3 Experimental Test Facility

The test facility design and fabrication was performed in collaboration with the Cryogenics Group at the National Institute of Standards and Technology. The remainder of this section discusses the fundamental components of the test facility, the experimental test configurations that were used (based on the methodology discussed in Section 5.2), and the selection of instrumentation.

5.3.1 Test Facility Components

This section is sub-divided according to the components of the test facility.

5.3.1.1 Pressure Wave Generator

The pressure wave generator (i.e. a linear compressor) that was utilized for all experimental measurements in the test facility was designed specifically for this facility by CFIC Incorporated. The specifications for the pressure wave generator include a maximum acoustic power delivery of 2000 W, a maximum mean pressure of 2.5 MPa, and an efficiency (electrical to acoustic power) of 75%, provided the system is impedance matched to the compressor. The pressure wave generator is illustrated in Figure 5.7.

Figure 5.7: Photos illustrating the pressure wave generator utilized in the experimental test facility.

5.3.1.2 Aftercooler

A specially designed aftercooler was utilized to reject the heat of compression before the working fluid enters into the regenerator matrix. The basic structure of the aftercooler was a packed screen design utilizing a single row of cooling tubes thermally interfaced with the packed copper screen material. During testing, chilled water is circulated through the tubes, accepting the heat of compression from the working fluid and rejecting it outside the system. The aftercooler is illustrated in Figure 5.8.

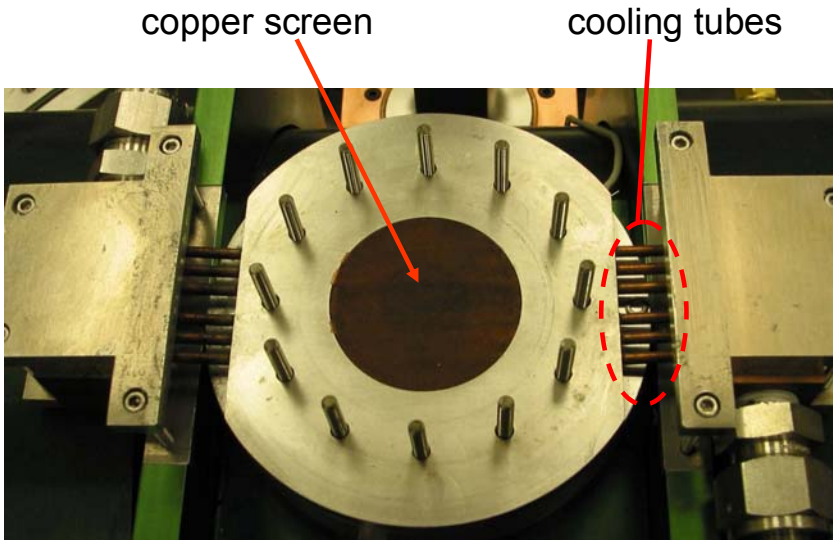

Figure 5.8: Photo illustrating the aftercooler utilized in the experimental system.

5.3.1.3 Regenerator

The regenerator utilized for all experimental measurements was designed based upon optimization of the COP using the desired system operating conditions. These conditions are summarized in Table 5.1.

Table 5.1: Nominal Regenerator Design Parameters

Parameter	**Symbol**	**Nominal Value**
Matrix material	-	400 mesh SS304
Mean system pressure	$\overline{P}$	2.5 MPa
Pressure ratio (cold end)	PR	1.3
Frequency	f	60 Hz
Cold end temperature	T_c	80 K
Warm end temperature	T_h	300 K
Mass flow rate	$\dot{m}$	16 g/s
Cold end phase angle	θ	-25 deg

The geometric design of the regenerator (diameter and length) was accomplished via parametric analysis using the REGEN3.3 program. In this analysis, the COP was studied as a function of a specialized parameter which is the ratio of the cross sectional area to the mass flow rate for various values of regenerator length. From the analysis, the data showed a clear optimum COP based upon the ratio of the cross sectional area to mass flow as well as the regenerator length. The results of this analysis are presented in Figure 5.9. Based upon these results, a length of 0.5 m was chosen for the regenerator with a ratio of area to mass flow of 0.05.

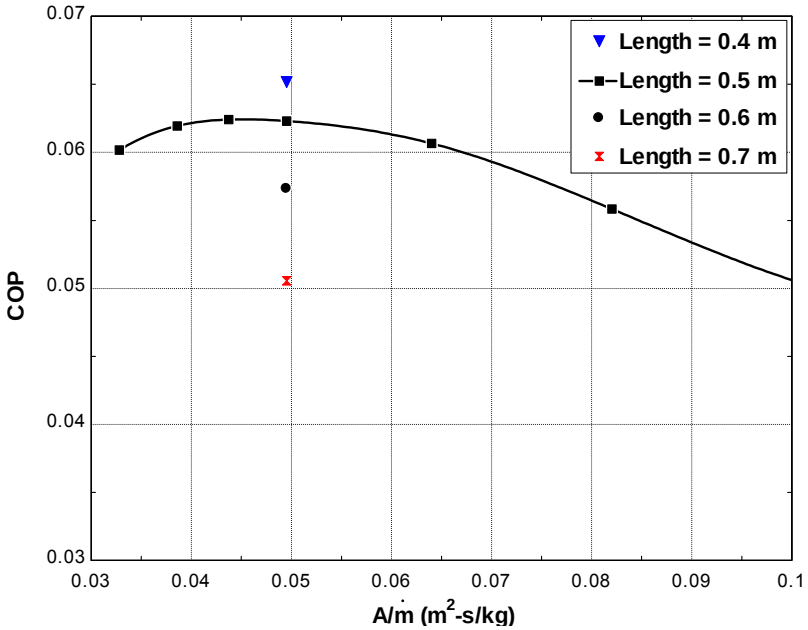

Figure 5.9: Plot illustrating the results from the optimization analysis of the regenerator utilized for experimental testing using the program REGEN3.3. Plotted is the COP as a function of the cross sectional area mass flow. Various lengths are plotted to indicate the behavior of the COP as a function of the regenerator length.

When designing and constructing cryogenic regenerators, care must be taken to mitigate two common problems: bypass flow in the regenerator matrix and non-uniform radial temperature profiles in the matrix. To mitigate bypass flow, special attention was paid to the concentricity of the regenerator tube and the screens that make up the matrix. The regenerator tube was precision machined from a solid piece of stainless steel bar stock, rather than using standard SS304 tubing. To ensure that the tube was concentric, the inside diameter was machined using Wire EDM (Electro-Discharge Machining). The regenerator matrix itself consisted of hundreds of layers of diffusion bonded 304 stainless steel screen. Diffusion bonding requires that the screens be stacked and placed into a furnace under high mechanical pressure at a temperature that is within 90% of the absolute melting temperature and held at this temperature for several hours. During this process, the molecules between

the screens form strong molecular bonds which results in a single monolith porous stack of screen. To ensure that the screens are concentric, 7 individual screen pucks were cut from a solid plate of the diffusion bonded screen material using Wire EDM. Each puck is 0.001 inch oversize relative to the inside diameter of the regenerator tube. The regenerator tube and associated screen pucks are illustrated in Figure 5.10.

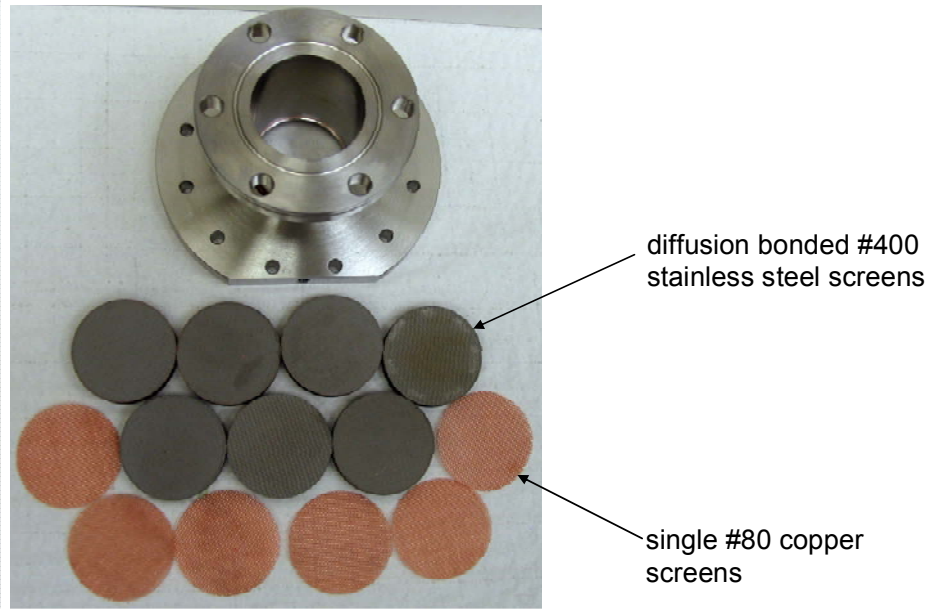

Figure 5.10: Photo illustrating the stainless screen pucks which were diffusion bonded and wire EDM cut to match the ID of the regenerator tube. Between each layer of stainless steel screens, a single layer of 80 mesh copper screen was placed to aid in radial thermal uniformity.

To assemble the regenerator, the screen pucks were cooled using liquid nitrogen and then press fit into the regenerator tube. To ensure radial thermal uniformity, an 80 mesh copper screen was placed between each of the SS304 pucks. The copper screen has a substantially lower hydraulic resistance than the SS304 pucks and a very high radial thermal conductivity. These characteristics allow the flow to achieve a uniform temperature and velocity before entering the next puck in the regenerator. The regenerator tube is shrink fit to the matrix

screens, locking them in place and eliminating any radial gaps through which by-pass gas could flow. The assembled regenerator is shown in Figure 5.11.

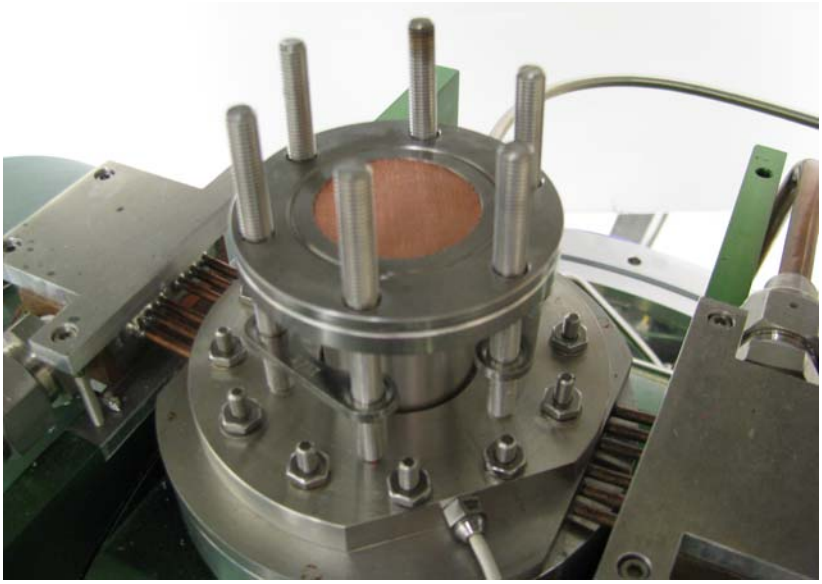

Figure 5.11: Photo illustrating the assembled regenerator.

5.3.1.4 Thermal Intercept

One of the critical components is the thermal intercept. The thermal intercept serves the dual role of heat exchanger and mass flow meter. The design of this component was performed using the heat exchanger design code ISOHX; this software was developed at NIST by Ray Radebaugh and Vince Arp (ISOHX, 2008). The results from this analysis were compared to experimental measurements for pressure drop as a function of the mass flow amplitude from an initial prototype of the thermal intercept.

The basic structure of the thermal intercept is a 101 OFHC copper flange filled with packed copper screens that serve as the heat transfer surface. Packed screens are used as they have a high surface area to volume ratio that is ideal for a compact heat exchanger design. The

screen material chosen was OFHC copper due to its high thermal conductivity, particularly at cryogenic temperatures. Typically this type of heat exchanger is fabricated from multiple individual discs of the copper material that are then sandwiched manually inside the heat exchanger flange. In this case, the screens were diffusion bonded, as discussed previously.

The thermal intercept was also utilized as a mass flow meter. Therefore, pressure measurements ports were installed on either side of the thermal intercept flange. These ports allow direct measurement of the pressure directly up and downstream of the hydraulically resistive screens. The pressure ports were designed to have minimal dead volume and resistance so as not to attenuate the pressure signal. The pressure transducers were installed in the flange using a standard machine thread with an indium wire ring seal. The thermal intercept is illustrated in Figure 5.12 and mechanical drawings are provided in Appendix D.

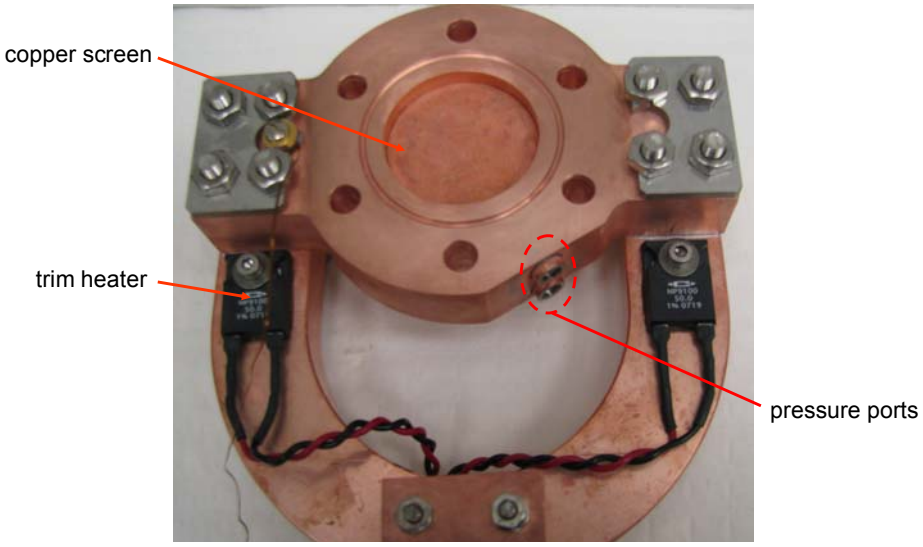

Figure 5.12: Photo illustrating the assembled thermal intercept.

5.3.1.5 Thermal Bus Apparatus

The bus system links the thermal intercept to the commercial cryocooler in the experimental system in order to allow measurement of heat flows and regulation of intercept temperature. The bus system was designed such that the thermal resistance from the cryocooler stage to the intercept was small enough that it did not interfere with the operating conditions that could be achieved for testing but still large enough that a measurable temperature difference was created. The only parameter that could easily be modified was the cross sectional area of the bus bar. The length of the bus bar was fixed by the spatial distance between the thermal intercept and the cryocooler cold stage.

The design of the correct cross sectional area (and therefore the thermal resistance) of the bus bar was accomplished via analysis of the bus bar temperature difference as a function of the cross sectional area for a maximum heat flow of 40 W; 40 W was chosen as it represented the largest regenerator loss predicted by REGEN3.3. Since the intercept temperature is fixed and a temperature difference is generated across the bus bar, the cold stage temperature must be lower than the intercept temperature by an amount that is equal to the temperature difference across the bus bar to accept the heat load. Using the manufacturers' load curve for the cryocooler, the cold stage temperature that corresponded to a 40 W heat load is 40 K. The intercept temperature was fixed at 80 K, therefore the maximum allowable temperature difference between the intercept temperature and cold stage was 40 K. Using the results in Figure 5.13, which illustrate the relationship between the bus bar temperature difference and the cross sectional area, the required cross sectional area of the bus bar was identified. The

thermal bus apparatus and the commercial cryocooler (a Sumitomo 415D 2-stage GM cooler) are illustrated in Figure 5.14.

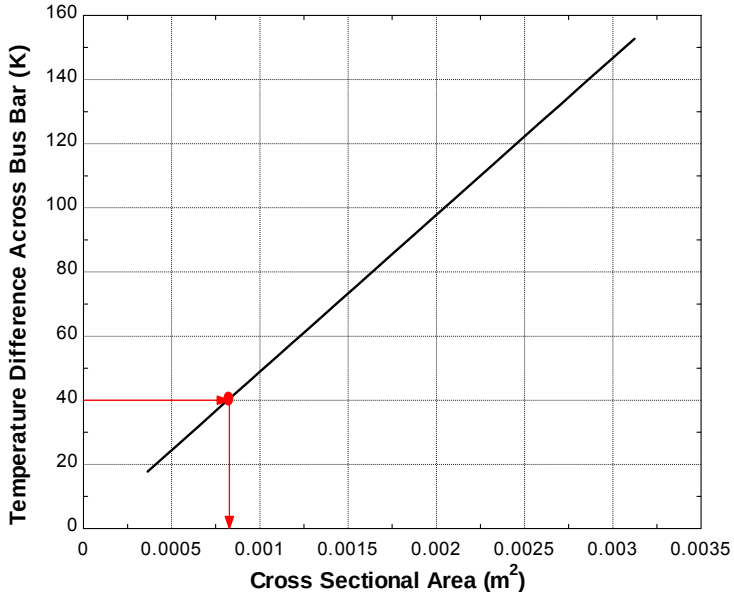

Figure 5.13: Plot illustrating the required cross sectional area of the bus bar dictated by the temperature difference across the bar with a warm temperature of 80K. The red dot indicates the maximum load which can be accepted by the commercial cryocooler at a temperature corresponding to the difference between the temperature difference across the bus bar and the warm temperature.

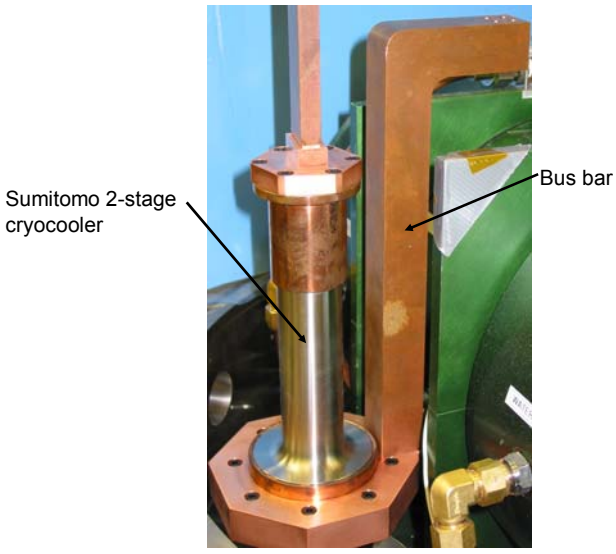

Figure 5.14: Plot illustrating the thermal bus apparatus in which the bus bar is attached to the Sumitomo 2-stage cryocooler.

5.3.1.6 Pulse Tube Designs

The design of the pulse tubes used for experimental testing was guided by the CFD model. The goal when designing the pulse tubes was to be able to experimentally measure a difference in performance based upon geometric differences in the pulse tube designs. Using results generated from an initial parametric modeling study discussed in Chapter 4, two pulse tube designs were selected. Each design had a different non-dimensional pulse tube diameter, defined as:

$$D_{ND} = \frac{D_{pt} - D_{inert}}{D_{reg} - D_{inert}} \tag{5.6}$$

where D_{pt} is the diameter of the pulse tube, D_{inert} is the diameter of the inertance tube, and D_{reg} is the diameter of the regenerator. The pulse tube diameter was specified in order to achieve values of $D_{ND} = 0.25$ and $D_{ND} = 0.4$, given the diameter of the regenerator and the diameter of the inertance tube that was utilized to generate the desired phase shift at the cold end of the regenerator. The length for each pulse tube was specified in order to achieve a pulse tube volume that is 3x the swept volume of gas at the cold end of the regenerator for one half of the cycle. The results of this analysis are summarized in Table 5.2. The two experimental pulse tube designs are shown in Figure 5.15.

Table 5.2: Nominal Pulse Tube Designs

Parameter	**Symbol**	**Design 1**	**Design 2**
Gas Volume	V	50 cc	50 cc
Non-dimensional diameter	D_{ND}	0.25	0.4
Aspect Ratio	PR	10	4.5
Length	L	5.5 in	3.1 in
Diameter	D	0.543 in	0.71 in

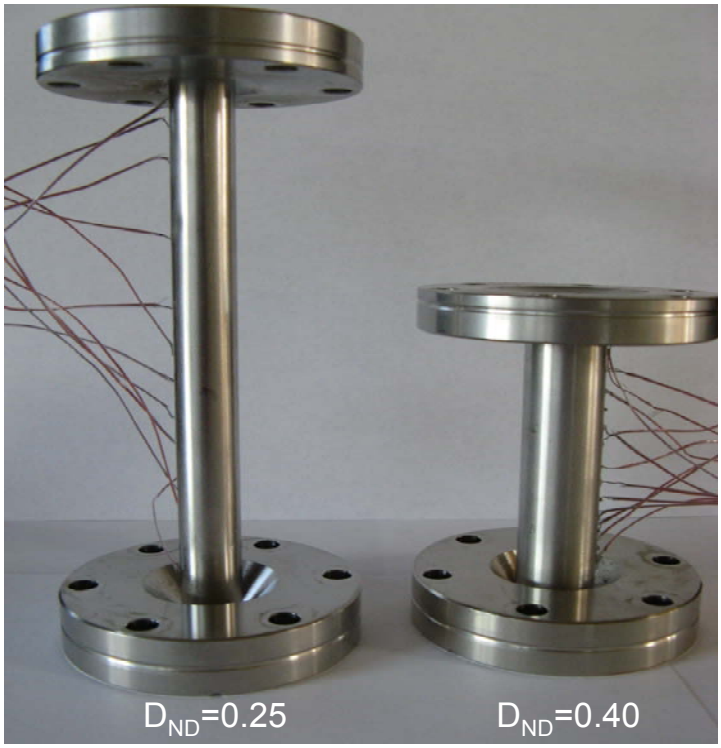

Figure 5.15: Photo showing the two experimental pulse tube designs.

5.3.1.7 Hot Heat Exchanger

The design of the hot heat exchanger, used to reject the enthalpy flow in the pulse tube component, was performed in a similar manner as the thermal intercept. The heat transfer surface was fashioned from diffusion bonded OFHC copper screens that were press fit into the heat exchanger flange. To reject heat during operation, a cooling water jacket was utilized. The water jacket consisted of copper tubing mechanically attached to the wall of the heat exchanger using solder. Note that this soldered connection also offers excellent thermal communication between the heat exchanger and the cooling water facilitating heat rejection from the copper screens. The assembled hot heat exchanger is show in Figure 5.16.

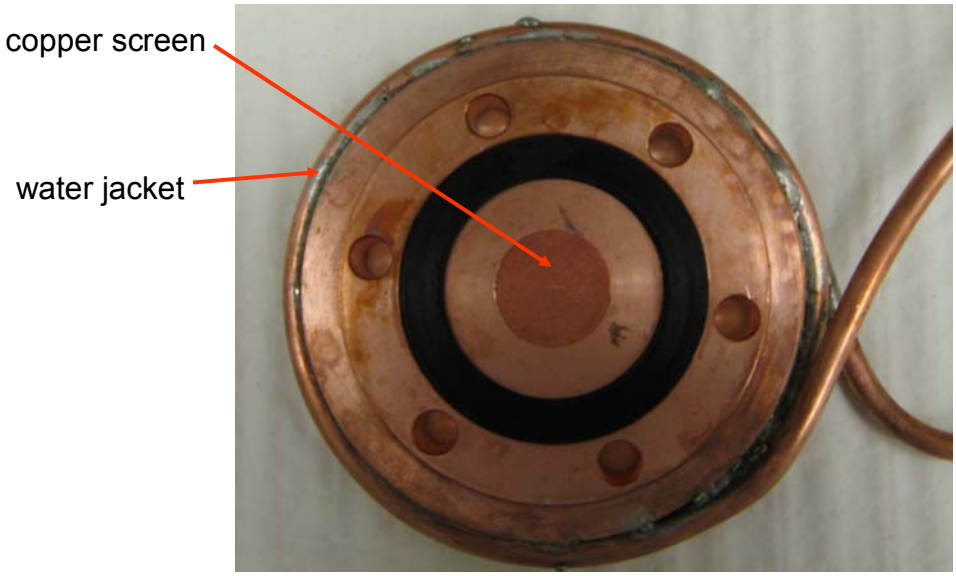

Figure 5.16: Photo illustrating the warm heat exchanger.

5.3.1.8 Flow Transitions

One of the critical aspects of pulse tube operation is the manner in which flow is transitioned from the high velocity region at the inertance tube exit to the lower velocity region in the larger diameter pulse tube. Previous modeling efforts discussed in Chapter 4 identified that an empty conical flow transition with a screen pack placed at the pulse-tube to flow transition boundary was ideal for allowing the high velocity flow to decelerate and equilibrate radially before entering the pulse tube component. As a result, the flow transition design used for the experimental measurements was of this design.

In order to investigate the effect of the volume of the conical flow transition component on the pulse tube performance, three hot end flow transitions were manufactured for each pulse tube design. The gas volumes of the transitions were set at 5%, 15%, and 25% of the pulse tube gas volume. The experimental flow transitions are illustrated in Figure 5.17.

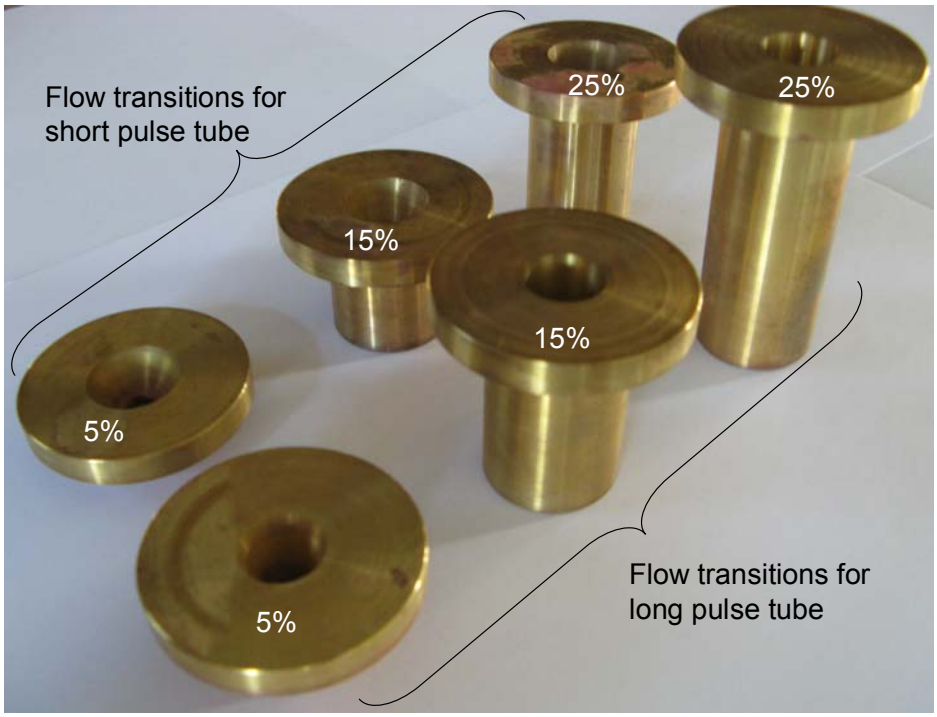

Figure 5.17: Photo illustrating the two sets of flow transitions for the experimental pulse tube designs with the transition having volumes of 5, 15, and 25 % of the pulse tube gas volume.

5.3.2 Experimental Test Set-ups

To perform the experimental measurements discussed in section 5.2, various experimental test set-ups were required. These test set-ups are summarized briefly in the following sections.

5.3.2.1 Bus Bar Calibration

Calibration of the bus bar (the thermal linkage) is required in order to allow precise measurement of the experimental energy flows. This calibration required an assembly that consisted of the thermal intercept, bus bar, and the commercial GM cryocooler. The solid copper bus bar was attached to the thermal intercept via three compliant copper straps. These mechanical and thermal connections were fashioned by placing indium filler material

between each contact layer and secured using torqued stainless steel studs. Indium foil was utilized to enhance the thermal interaction between the mechanical connections (i.e., decrease the contact resistance for heat transfer). To minimize radiative and convective heat transfer, the test set-up was wrapped in multi-layer insulation and enclosed in a high vacuum chamber. An illustration of the assembled test set-up is illustrated in Figure 5.18.

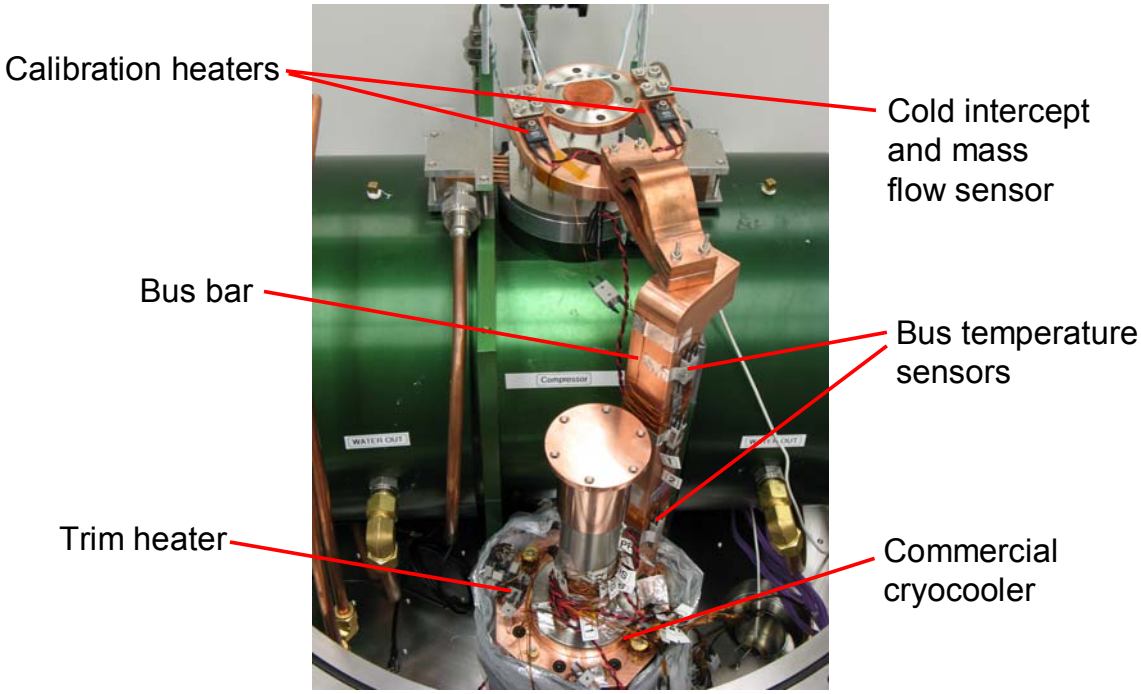

Figure 5.18: Photo illustrating the test facility set-up for calibrating the thermal bus bar.

5.3.2.2 Mass Flow Calibration

Calibration of the mass flow meter required an assembly consisting of the regenerator, the connection to the thermal bus system, and a reservoir volume installed immediately downstream of the thermal intercept. The thermal intercept was connected to the cold end of the regenerator and a flanged reservoir volume was connected to the thermal intercept. To maintain a hermetic pressure seal at cryogenic temperatures, the sealing surfaces of the

regenerator and thermal intercept were machined with grooves to allow for indium seals to be used. To minimize radiative and convective heat transfer, the cold end of the test set-up was wrapped in multi-layer insulation and enclosed in a high vacuum chamber. An illustration of the assembled test set-up is illustrated in Figure 5.19.

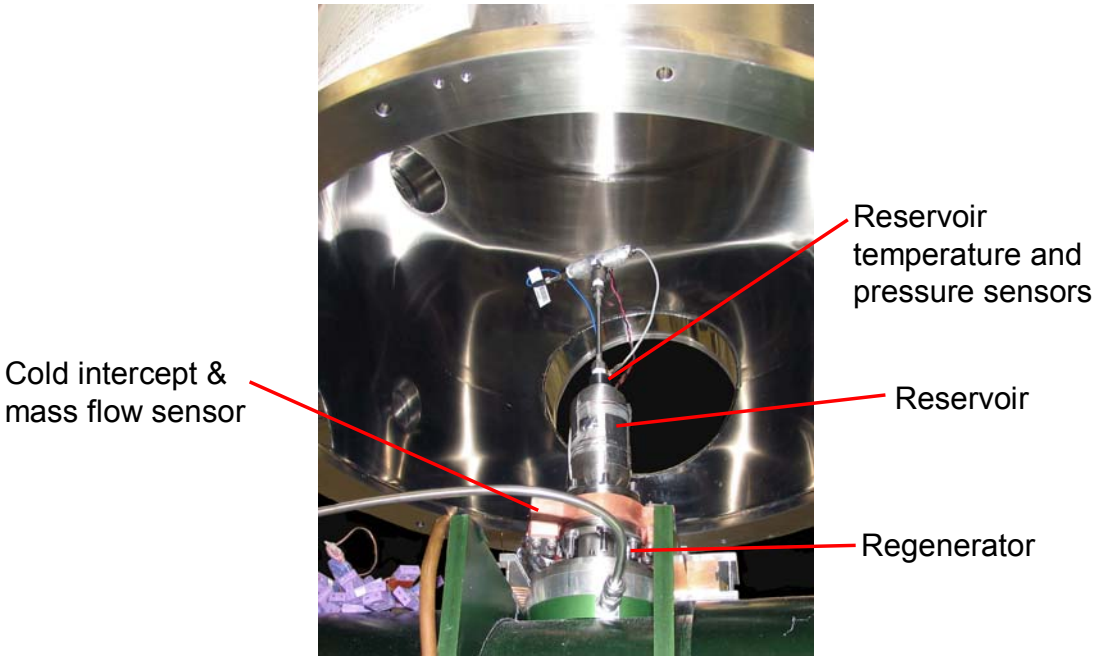

Figure 5.19: Photo illustrating the test facility set-up for calibrating the mass flow sensor.

5.3.2.3 Regenerator Loss Test Set-up

Measurement of the regenerator loss required essentially the same experimental test set-up used for calibration of the mass flow meter. The main modification to the assembly was the removal of the reservoir volume that was directly connected to the thermal intercept. In its place, an inertance tube was attached to the thermal intercept. The other end of the inertance tube was then connected to a much larger reservoir volume (specified when designing the inertance tube). This larger reservoir volume (500 cc) had a sizable thermal mass and was connected to the cold stage via a long thin walled stainless steel tube. Therefore, its thermal

communication with the cold end had to be enhanced in order to allow it to cool in reasonable time and attain a temperature consistent with the cold end temperature. The reservoir volume was mechanically attached to a solid plate of copper using a solder joint. The copper plate was bolted directly to the thermal intercept. This enhanced thermal communication allowed the reservoir volume to cool to the cold end temperature quickly during experimental testing. To minimize radiative and convective heat transfer, the test set-up was wrapped in multi-layer insulation and enclosed in a high vacuum chamber. An illustration of the assembled test set-up is illustrated in Figure 5.20.

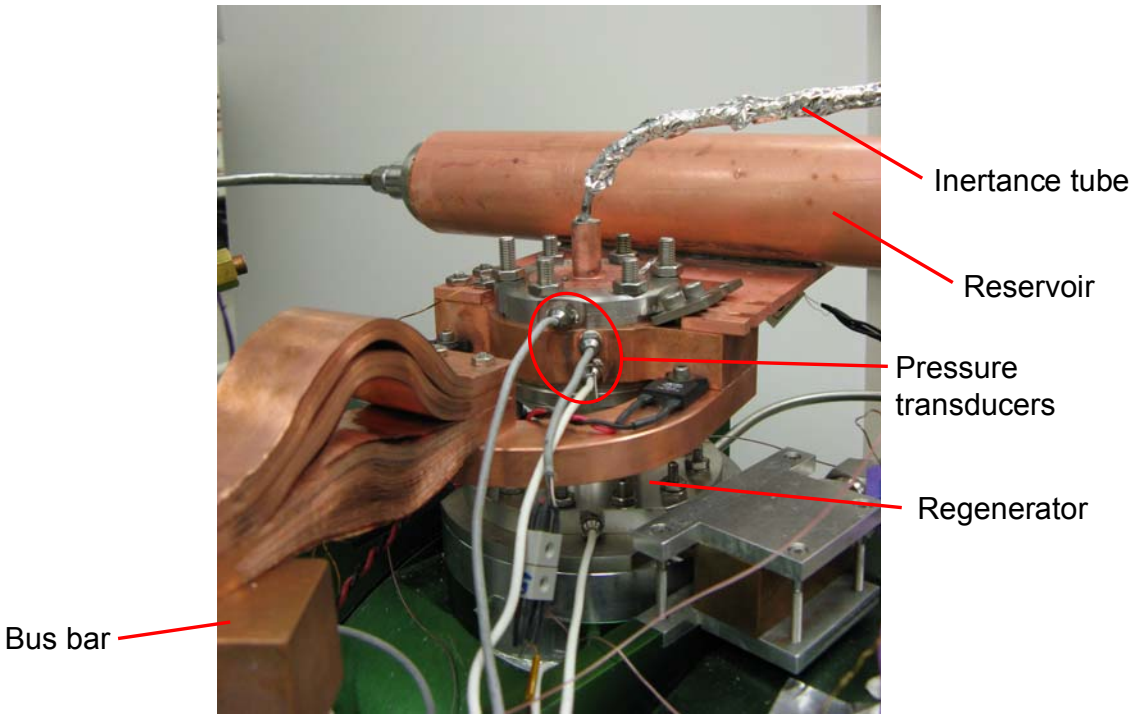

Figure 5.20: Photo illustrating the test facility set-up for performing regenerator energy flow measurements.

5.3.2.4 Cooling Power and Acoustic Power Measurement Test Set-up

Measurement of the cooling power and acoustic power required removal of the thermal bus apparatus from the thermal intercept as well as removal of the inertance tube and reservoir volume used to measure the regenerator loss. The complete, experimental pulse tube system was installed in the facility. This included the installation of one of the two experimental pulse tube designs to the thermal intercept, the hot heat exchanger to the warm end of the pulse tube, one of the three warm flow transition test pieces to the warm heat exchanger, and finally the specific inertance tube to be used for that set of experimental components. In the case of the thermal intercept to pulse tube connections, a hermetic gas seal was formed using indium wire seals. The warm end seals were accomplished using standard o-rings seals. Note that for this test set-up, the reservoir volume was connected to the inertance tube but thermal communication with the cold end was not desired. As a result, the reservoir volume was placed outside of the vacuum chamber. To minimize radiative and convective heat transfer, the cold end of the system was wrapped in multi-layer insulation and enclosed in a high vacuum chamber. An illustration of the assembled test set-up is illustrated in Figure 5.21.

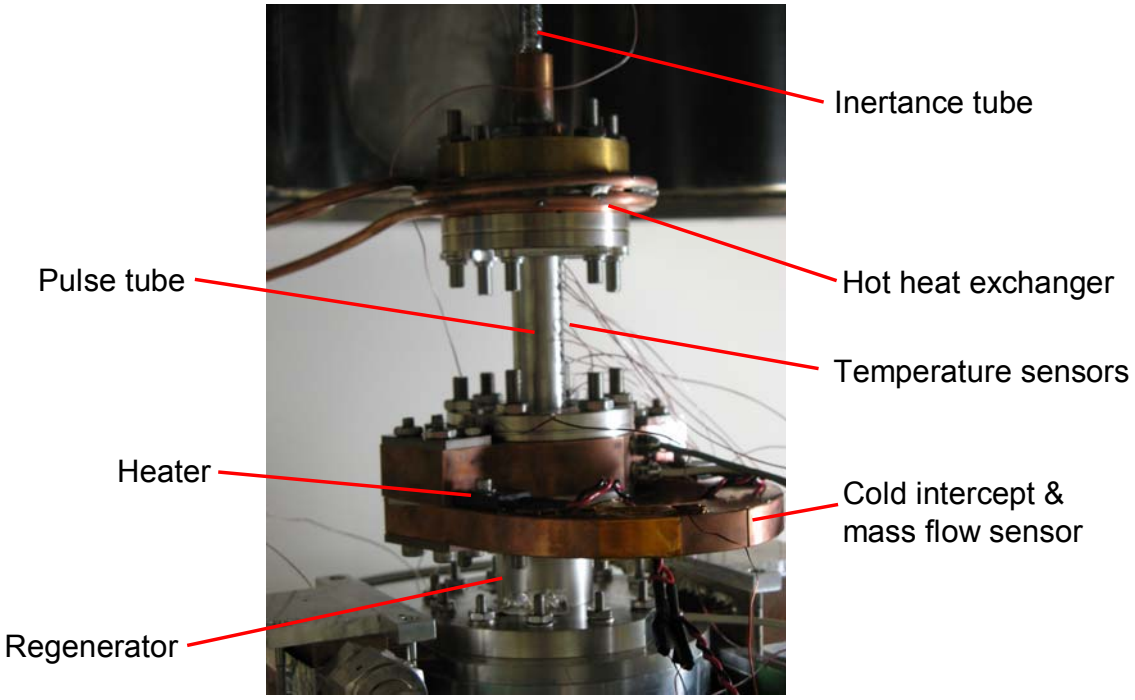

Figure 5.21: Photo illustrating the test facility set-up for measuring the net cooling power and acoustic power flow.

5.3.3 Instrumentation

In order to accurately measure the experimental quantities of interest for validation of the model, selection of the proper instrumentation was one of the more important tasks. The remainder of this section provides an overview of the selected instrumentation and the reasons for selection. A complete analysis of the measurement uncertainty associated with the instrumentation is discussed in detail in Chapter 6.

5.3.3.1 Pressure Measurement

For the measurement of the pressures in the experimental test facility, two types of pressure transducers are utilized. For measurement of static (DC) and large amplitude dynamic (AC) pressure signals, Model 8510B Endevco piezoresistive pressure transducers were selected.

The selection of these transducers was based on several requirements including minimal dead volume, the ability to configure these sensors for differential pressure readings (if required), as well as the ability to withstand and function at cryogenic temperatures. To measure small amplitude dynamic pressure signals, Model 122433 PCB piezoelectric pressure transducers were selected. These transducers were selected as they are specifically designed to accurately measure small amplitude dynamic pressure signals that are present in the reservoir volume during calibration of the mass flow sensor. The signals generated by both of these transducers were conditioned and amplified; the output and phase were measured using 7 Stanford Research System DSP lock-in amplifiers. In both sets of pressure measurement, the lock-in amplifiers were interfaced with a main Labview data acquisition program for direct measurement and logging of the readings. The specific location of the various pressure measurements are illustrated in Figure 5.22.

5.3.3.2 Temperature Measurement

For the measurement of the various temperatures in the experimental test facility, a wide range of thermometry was utilized. For the measurement of non-critical temperatures, such as the cryocooler cold stage temperature, backup temperature measurement on the thermal intercept, as well as the temperature of both the hot end heat exchanger and the buffer volume, a combination of Lakeshore Model CX-1050-4.2 calibrated Cernox RTD's and Lakeshore SD-670 silicon diodes were utilized. The silicon diodes are chosen for temperature measurement of the buffer volume and hot heat exchanger as these sensors have a high sensitivity near room temperature. The measurement of the cryocooler cold stage temperature is also measured using a silicon diode; the required accuracy of this

measurement is not as high as other temperature measurements because this measurement is used only for diagnostic purposes. The backup measurement of the thermal intercept temperature is performed via the use of a calibrated Cernox RTD. For the measurement of more critical temperatures, such as those in the bus bar for heat flow measurements, Lakeshore Model PT-102-14L calibrated platinum resistance thermometers with a calibration range of 14-325 K were used. All temperature measurements were excited and read using two Lakeshore 218S temperature monitors. For other non-critical temperature measurements, such as the relative temperature of the pulse tube component wall and the inertance tube, 20 Type-E thermocouples were utilized. These thermocouples were read via a HP3458A mainframe data acquisition system. For all temperature measurements, the instruments utilized for excitation and reading of the various thermometers employed were interfaced with a main Labview data acquisition program for direct measurement and logging of the readings. The specific location of the various temperature measurements are illustrated in Figure 5.22.

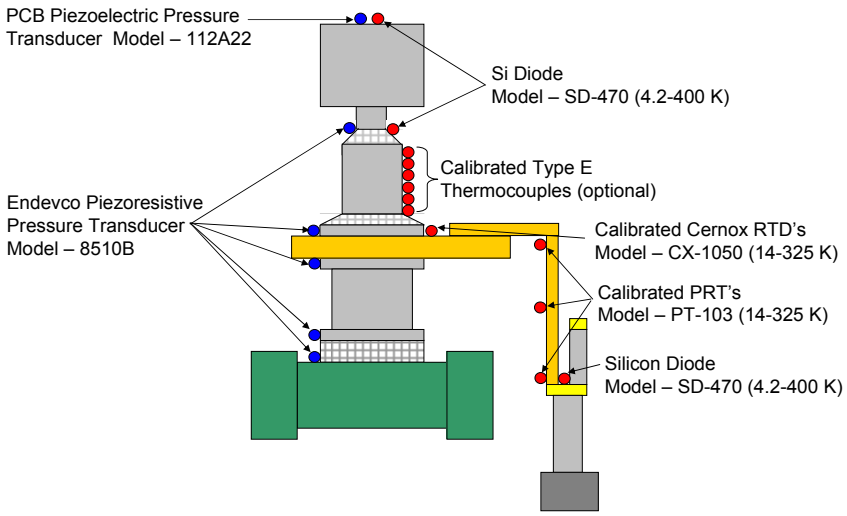

Figure 5.22: Schematic illustrating the location of the pressure and temperature measurements in the fully assembled experimental test facility.

6. Experimental Uncertainty

High accuracy data are required for validation of the CFD model discussed in Chapter 3. Therefore, a complete uncertainty analysis of the fundamental measurements obtained from the experimental test facility discussed in Chapter 5 is presented in this chapter. The propagation of the uncertainty from the fundamental measurements through to the calculated experimental measurements that are required for validation of the model is also discussed.

6.1 Instrumentation Uncertainty

6.1.1 Temperature Measurement Uncertainty

In the experimental test facility there are three calibrated platinum resistance thermometers (PRTs) that are utilized for measurement of the cold end temperature as well as temperatures along the length of the bus bar that connects the cold end to the cryocooler; these temperature sensors are used to determine the heat flow through the bus bar. The temperature sensors are Model PT-103 PRTs manufactured by Lakeshore Cryotronics and they have a calibration range that extends from 14 K to 325 K. The PRTs are wired with a 4-wire configuration to a Lakeshore Cryotronics Model 218S temperature monitor; the temperature monitor provides a known current to the each sensor and measures the resulting voltage in order to determine the resistance and, based on the calibration curve, the temperature. The specifications of the temperature measurement system are summarized in Table 6.1 at two representative temperatures.

Table 6.1 – Temperature Measurement System Specifications

Measurement Specifications	Symbol	Temperature	
		20 K	**77 K**
Excitation Current[1] (mA)	I	1±0.3%	1±0.3%
Sensor Resistance[2], (ohm)	R_{sensor}	1.9651	20.2203
Sensor Sensitivity[2], (ohm/K)	$\frac{\partial R_{sensor}}{\partial T}$	0.0867	0.4251
Measurement Resolution[3], (ohm)	u_{meas}	0.002	0.002
Electronic Accuracy[3], (ohm)	u_{elec}	0.004±0.02% RDG	0.004±0.02% RDG

[1] Nominal value reported in the sensor literature [Lakeshore].
[2] Average value of the three computed values for the three PRT sensors [PRT].
[3] Nominal value reported by the manufacturer in the calibration reports for each of the PRT sensors [PRT].

The PRTs and the temperature monitor were selected for their superior performance and accuracy at cryogenic temperatures; however, there are a number of factors that adversely influence the temperature measurements. The uncertainty in the temperature measurement can be broken into three categories: inherent sensor uncertainty, instrumentation uncertainty, and overall system uncertainty.

The uncertainty in the temperature measurement that is inherent to the PRT temperature sensor can be further sub-divided into an uncertainty that is related to (1) the accuracy of the sensor calibration compared to an international temperature scale such as ITS-90, (2) the uncertainty related to the fitting function used to implement the calibration data (interpolation uncertainty), and (3) an uncertainty that is related to the reproducibility of the temperature measurement. For the three calibrated PRT sensors, the uncertainty in the temperature calibration (U_{cal}) relative to ITS-90 is [PRT],

$$U_{cal} = \begin{matrix} \pm 8\,mK\ at\ T = 20K \\ \pm 10\,mK\ at\ T = 77K \end{matrix} \tag{6.1}$$

During the reduction of the experimental calibration data and the subsequent data processing for each sensor, an interpolation uncertainty arises due to imperfect curve fitting of the experimental calibration data. This interpolation error (U_{int}) can be expressed as [PRT],

$$U_{int} = \pm\sqrt{\frac{N}{N-n}\left(\Delta T_{rms}\right)^2} \tag{6.2}$$

where N is the number of points in the specific fitting range, n is the number of fitting coefficients, and ΔT_{rms} is the root mean square temperature difference associated with the fitting function [PRT]**.** The final source of sensor uncertainty is related to the ability of the sensor to repeat a temperature measurement under identical conditions and achieve the same result. Per the manufacturers' specification, this reproducibility uncertainty (U_{rep}) is specified as [Lakeshore],

$$U_{rep} = \pm 5\,mK \; at \; T = 77K \tag{6.3}$$

The uncertainty due to the instrumentation equipment that is used to actually read the temperature can be sub-divided into an uncertainty related to the electronic accuracy of the temperature monitor and an uncertainty due to the measurement resolution of the temperature monitor. The Lakeshore Model 218S temperature monitor has an electronic measurement uncertainty, (u_{elec}), for resistance thermometers that is given by [Lakeshore],

$$u_{elec} = 0.004\Omega \pm 0.02\%\, RDG\,\Omega \tag{6.4}$$

where RDG is the sensor resistance at a given temperature. Note that the value of u_{elec} is in units of ohms and not temperature. The uncertainty in the resistance measurement is converted into an uncertainty in the temperature measurement, (U_{elec}), using the sensor sensitivity,

$$U_{elec} = \pm \left(\frac{0.004\Omega \pm 0.02\% \, RDG\,\Omega}{\frac{\partial R_{sensor}}{\partial T}} \right) \tag{6.5}$$

where $\frac{\partial R_{sensor}}{\partial T}$ is the sensitivity of the sensor at a given measurement temperature. The uncertainty related to the measurement resolution of the temperature monitor, (U_{meas}), is given by the manufacturer's specifications,

$$u_{meas} = \pm 0.002\,\Omega \tag{6.6}$$

As with the electronic accuracy uncertainty, the measurement resolution (in ohms) is converted into a temperature uncertainty using the sensor sensitivity,

$$U_{meas} = \pm \left(\frac{0.002\Omega}{\frac{\partial R_{sensor}}{\partial T}} \right) \tag{6.7}$$

The uncertainty in the temperature measurement due to system-level issues can be sub-divided into an uncertainty due to power dissipation in the sensor that leads to a self-heating error and an uncertainty due to external heat loads on the sensor, primarily related to heat transfer through the sensor leads to the sensor. Both of these heat loads on the sensor are actually a bias rather than a randomly distributed error and both are strongly related to how well the sensor is mounted to the surface of interest. The specifications for the thermal potting and mounting of the PRT sensors are summarized in Table 6.2.

Table 6.2 – Temperature Measurement System Specifications

Sensor Mounting Specifications	Symbol	Nominal Value
Sensor Length[1], (mm)	L_{sensor}	12.2
Sensor Diameter[1], (mm)	D_{sensor}	1.6
Potted Surface Area, (mm^2)	A	0.0204
Thickness of Potting Grease, (mm)	L_{grease}	0.1
Length of Lead (Anchor to Sensor), (mm)	L_{lead}	304.8
Sensor Lead Diameter[1], (mm)	D_{lead}	0.127
Sensor Cross-Sectional Area, (mm^2)	A_{lead}	0.0127
Thermal Grease Conductivity[2], (W/m-K)	k_{grease}	0.144 (T=80K) 0.13 (T=20K)
Lead Wire Conductivity[1], (W/m-K)	k_{lead}	25 (T=80K) 10 (T=20K)

[1] Nominal value reported in the sensor literature [Lakeshore].
[2] Nominal value reported at temperature [SPI].

The uncertainty in the temperature measurement due to self-heating is related to the fact the PRT's are resistors that require excitation via a current source. The excitation current leads to power dissipation in the sensor that causes the sensor's temperature to rise relative to the temperature of the sample being measured. This uncertainty due to self heating can be expressed as,

$$U_{sh} = \pm\left(P\,R_{cond,sensor}\right) \tag{6.8}$$

where P is the power dissipation due to ohmic losses expressed as,

$$P = I^2\,R_{sensor} \tag{6.9}$$

I is the excitation current of the sensor and R_{sensor} is the electrical resistance of the sensor. The term $R_{cond,sensor}$ is the thermal resistance between the sensor and the sample being measured. In practice, this mounting thermal resistance is not easy to predict because it involves a contact resistance that is not well known at cryogenic temperatures. For this calculation, the mounting thermal resistance is estimated assuming that the dominant

resistance is conduction through the thermal grease that is applied between the sensor and the surface,

$$R_{cond,sensor} = \frac{L_{grease}}{k_{grease} A} \tag{6.10}$$

where L_{grease} is the thickness of thermal grease used to pot the sensor into the sample being measured, k_{grease} is the thermal conductivity of the thermal grease, and A is the surface area through which heat flows. Combining Eqns.(6.8), (6.9), and (6.10) yields the uncertainty in the temperature due to self heating in the sensor,

$$U_{sh} = +\left(I^2 R_{sensor} \frac{L_{grease}}{k_{grease} A} \right) \tag{6.11}$$

The uncertainty in the temperature measurement due to lead conduction is typically minimized in cryogenic system by thermally anchoring the sensor leads at a temperature that is close to the one being measured. However, for this system it is possible that a temperature difference between the sensor and the anchor point for the leads could approach 20-30 K because the leads are anchored to the cold-stage flange of the GM cryocooler, which is not immediately adjacent to the bus assembly. This temperature difference will provide the opportunity for conduction along the sensor leads to the sensor. The conduction heat transfer must be dissipated in the same manner as the sensor self heating power dissipation. The uncertainty in the temperature measurement due to the lead conduction is expressed as,

$$U_{lc} = +\left(Q R_{cond,sensor} \right) \tag{6.12}$$

where Q is the rate of heat transfer by conduction along the sensor leads, expressed as,

$$Q = 4\,k_{lead}\,A_{lead}\left(\frac{T_{sensor} - T_{lead,anchor}}{L_{lead}}\right) \tag{6.13}$$

where L_{lead} is the length of the sensor lead wire between the sensor and the thermal anchor point, k_{lead} is the thermal conductivity of the lead wire material, A_{lead} is the cross-sectional area of the lead wire, T_{sensor} is the temperature of the sample being measured, and $T_{lead,anchor}$ is the temperature of the lead anchor point. Combining Eqns. (6.10) and (6.13) yields the uncertainty in the temperature measurement, (U_{lc}), due to lead conduction,

$$U_{lc} = +\left[\left(\frac{L_{grease}}{k_{grease}\,A}\right)\left(4\,k_{lead}\,A_{lead}\left(\frac{T_{sensor} - T_{lead,anchor}}{L_{lead}}\right)\right)\right] \tag{6.14}$$

Using these individual uncertainty values for the temperature measurement, the total temperature uncertainty can be estimated by summing the randomly distributed errors (U_{cal}, U_{int}, U_{rep}, U_{elec}, and U_{meas}) in quadrature and adding the bias error related to U_{sh} and U_{lc},

$$U_T = \left(\pm\sqrt{U_{cal}^{\,2} + U_{int}^{\,2} + U_{rep}^{\,2} + U_{elec}^{\,2} + U_{meas}^{\,2}}\right) + \left(U_{sh} + U_{lc}\right) \tag{6.15}$$

The parameters listed in Tables 6.1 and 6.2 are utilized to arrive at the total uncertainty in the temperature measurement as well as the delineated uncertainty for each of the seven uncertainty terms discussed here. The results of this analysis are presented in Table 6.3 for two nominal operating temperatures.

Table 6.3 – Model PRT-103 Temperature Measurement Uncertainty

Delineated Sensor Uncertainty	**Symbol**	**Temperature (K)**	
		20	**77**
Calibration Uncertainty[1], (mK)	U_{cal}	±8	±10
Interpolation Uncertainty[2], (mK)	U_{int}	±0.9	±0.9
Reproducibility[3], (mK)	U_{rep}	unknown	±5
Measurement Resolution[3], (mK)	U_{elec}	±23	±4.8
Electronic Uncertainty[3], (mK)	U_{meas}	±51	±19
Self Heating, (mK)	U_{sh}	±0.008	±0.07
Lead Conduction, (mK)	U_{lc}	±0.13	±0.29
Total Temperature Uncertainty, (mK)	$\boldsymbol{U_T}$	**±56.24+0.135**	**±22.5+0.361**

[1] Nominal value reported by the manufacturer in the calibration reports for each of the PRT sensors [PRT].
[2] Average value of the three computed values for the three PRT sensors [PRT].
[3] Nominal value reported in the sensor literature [Lakeshore].

6.1.2 Pressure Measurement Uncertainty

Endevco Model 8510B-500 piezoresistive pressure transducers are utilized to measure large static (DC) and dynamic (AC) pressures in the experimental facility. PCB Electronics Model 112A22 piezoelectric transducers are utilized to measure small amplitude dynamic (AC) pressures. The piezoelectric transducer measures small amplitude AC pressure signals very precisely, whereas the piezoresistive transducer can accurately resolve the DC and large magnitude AC components of a pressure signal. While these transducers are utilized for different aspects of pressure measurement, the process of reducing the output signal is essentially the same; the output signal must be amplified/conditioned and then input into a Digital Signal Processing (DSP) Lock-in Amplifier manufactured by Stanford Research Systems for measurement of the pressure amplitude. Due to the difference in instrumentation and sensor style, the total uncertainty in the measurement of pressure using these two systems is analyzed separately in the following sections.

6.1.2.1 AC-DC Pressure Measurement Uncertainty

The specifications of the AC-DC pressure measurement system are summarized in Table 6.4 for the Endevco Model 8510B-500 piezoresistive pressure transducer.

Table 6.4 – AC-DC Pressure Measurement System Specifications

Measurement Specifications	Symbol	Nominal Value
Excitation Voltage[1], (VDC)	V_{PR}	10
Transducer Dead Volume[1], (cc)	$\forall_{PR}$	0.005
Full Scale Output[1], (mv)	FSO_{PR}	300
Sensor Sensitivity[1], (mv/Pa)	$\frac{\partial V_{PR}}{\partial P}$	8.70×10^{-5}
Sensor Noise[1], (μV)	$u_{PR,noise}$	5
Combined Hysteresis, Non-Linearity, and Non-Repeatability Uncertainty[1], (mV)	u_{PR}	0.5% FSO RSS Max
Cal. Pressure Meter Uncertainty[2], (Pa)	$U_{PR,cal}$	0.025% FS
Cal. Pressure Meter Full Scale[2], (Pa)	$FS_{cal,P}$	5.171×10^{6}
Strain-Gage Amp Output Noise[3,4], (μV)	$u_{PR,SGA}$	25.18
Lock-in Amplifier Noise[5], (μV)	$u_{PR,lockin}$	9.1

[1] Nominal value reported in the manufacturers literature for Model 8510B pressure transducer[Endevco 1].
[2] Nominal value reported by the manufacturers literature for Model 2102 digital pressure gage [Mensor].
[3] Nominal value reported by the manufacturers literature for Model SG-71 strain-gage amplifier and signal conditioning module [Validyne].
[4] Experimentally measured value using the lock-in amplifiers and a Model 8510B-500 pressure transducer.
[5] Experimentally measured value using the lock-in amplifiers.

The uncertainty in the pressure measurement that is inherent to the piezoresistive pressure transducer can be sub-divided into an uncertainty related to pressure hysteresis, non-repeatability, non-linearity, inherent sensor noise, and calibration accuracy. For the Endevco pressure transducer, the manufacturer reports a root sum squared maximum combined error for the pressure hysteresis, non-repeatability, and non-linearity, (u_{PR}), given by [Endevco],

$$u_{PR} = \pm 0.5\% \, FSO \tag{6.16}$$

where *FSO* is the full scale voltage output of the pressure transducer signal. The associated uncertainty in the pressure measurement due to the above mentioned combined effects, (U_{PR}), is defined as,

$$U_{PR} = \pm\left(\left(\frac{0.5}{100}\right)^2 \frac{FSO}{\frac{\partial V_{PR}}{\partial P}}\right) \tag{6.17}$$

where $\frac{\partial V_{PR}}{\partial P}$ is the sensitivity of the pressure transducer. The uncertainty related to the Endevco pressure transducers inherent random noise, ($u_{PR,noise}$), is given by [Endevco],

$$u_{PR,noise} = \pm 5x10^{-6} V \tag{6.18}$$

The associated pressure uncertainty, ($U_{PR,,noise}$), is given by,

$$U_{PR,noise} = \pm\left(\frac{5x10^{-6} V}{\frac{\partial V_{PR}}{\partial P}}\right) \tag{6.19}$$

The final source of sensor uncertainty, while not directly attributable to the pressure transducer itself, is related to the accuracy of the pressure gage that is utilized for the calibration of the Endevco pressure transducers. The error in the gage pressure will lead directly to an error in the pressure measurement using the Endevco transducer. The pressure gage that is utilized for calibration of the Endevco pressure transducers is a Mensor Model 2102 Digital Pressure Gage. The uncertainty of this pressure gage, ($U_{cal,P}$) is expressed as [Mensor],

$$U_{PR,cal} = \pm 0.025\% FS_{cal,P} \tag{6.20}$$

where $FS_{cal,P}$ is the full scale reading of the pressure gage.

The uncertainty due to the instrumentation equipment used to condition/amplify the pressure signal as well as measure the signal amplitude can be sub-divided into an uncertainty related to the output noise of the strain gage amplification as well as the input/internal noise of the lock-in amplifiers that are utilized to measure the pressure amplitude. The Validyne Model SG71 strain gage amplifier has an amplification noise ripple, ($u_{PR,SGA}$), at full scale amplification of 10 VDC given by [Validyne],

$$u_{PR,SGA} = 20\,mV\ RMS \tag{6.21}$$

Typically the output amplification is setup such that 1 V of output signal corresponds to 1 MPa of pressure for ease of reading. Since the full scale of the amplification stage is not used, but rather a much smaller one (0-3V), this reported uncertainty can be a significant source of error for measuring moderate amplitude pressure signals. However, the manufacturer does not indicate whether this noise is spectral or broadband in origin. In the case of broadband noise, the lock-in amplifier should filter this noise out of the signal as it eliminates noise harmonics away from the reference frequency. In the case of spectral noise this becomes more difficult if the maximum spectral power density is at or close to the desired pressure signal frequency as filtering can degrade the signal.

The uncertainty associated with the strain gage amplifier was experimentally quantified using a Model 8510B-500 pressure transducer and a Model SRS830 lock-in amplifier. This experiment was performed by charging a volume attached to the pressure transducer to a static pressure of 2.5 MPa. The resulting background AC noise was then measured and

recorded. The results from this experiment indicate that the actual noise due to the amplification of the pressure signal, assuming a signal frequency of 60 Hz, is given by,

$$u_{PR,SGA} = \pm 0.02518\, mV \tag{6.22}$$

The noise uncertainty is converted into an associated pressure uncertainty, ($U_{PR,,SGA}$), by the sensor sensitivity,

$$U_{PR,SGA} = \pm \frac{0.02518}{\frac{\partial V_{PR}}{\partial P}} \tag{6.23}$$

The uncertainty due to the Stanford Research System Model SRS830 DSP lock-in amplifier is a complex combination of parameters internal to this piece of instrumentation. Therefore, the input/internal noise of the lock-in amplifier was also measured experimentally. An internal function generator was used to generate a sinusoidal signal that was connected directly to the input of the lock-in amplifier. The error internal to the lock-in is then quantified in terms of the noise magnitude observed. Based upon the experimental measurements, the internal error of the lock-in amplifier, ($u_{PR,lockin}$), is given by,

$$u_{PR,lockin} = \pm 0.009\, mV \tag{6.24}$$

The uncertainty due to the lock-in amplifier is converted into an associated pressure uncertainty, ($U_{PR,,lockin}$), by the sensor sensitivity,

$$U_{PR,lockin} = \pm \frac{0.009}{\frac{\partial V_{PE}}{\partial P}} \tag{6.25}$$

The uncertainty in the AC-DC pressure measurement at the system-level manifests itself as a bias error that is related to signal attenuation associated with dead volume in the region

between the transducer and the flow that is being measured. The specifications for the nominal pressure port used in the apparatus are listed in Table 6.5.

Table 6.5 – Pressure Port Specifications

Sensor Mounting Specifications	Symbol	Nominal Value
Port Radius[1], (mm)	r_p	0.793
Port Length[1], (mm)	L_p	15.24
Effective Port Volume (including sensor dead volume), (cc)	$V_{P,eff}$	0.01253
Nominal Flow Pressure Amplitude[2], (Pa)	$\tilde{P}_f$	280000
Pressure Signal Frequency[2], (Hz)	ω	60

[1] Nominal machined value for the test flanges.
[2] Anticipated standard test condition.

Using the discussion presented in Holman (2001) regarding dynamic pressure signals, the uncertainty due to attenuation of the pressure signal can be expressed as,

$$U_{att} = -\frac{\tilde{P}_f}{\left[\left[1-\left(\frac{\omega}{\omega_n}\right)^2\right]^2 + 4h^2\left(\frac{\omega}{\omega_n}\right)^2\right]^{\frac{1}{2}}} \tag{6.26}$$

where $\tilde{P}_f$ is the magnitude of the flow pressure amplitude being measured, ω_n is the natural frequency of the pressure port, estimated according to,

$$\omega_n = \sqrt{\frac{3\pi r_p{}^2 c^2}{4 L_p V_{p,ef} f}} \tag{6.27}$$

where r_p is the radius of the pressure port tube, c is the speed of sound in the fluid, L_p is the length of the pressure measuring tube, and $V_{p,eff}$ is the effective volume between the flow being measured and the transducer inlet. A final term listed in Eqn. (6.26) is the damping ratio, h, which is defined as,

$$h = \frac{2\mu}{\rho c r_p^{\,3}} \sqrt{\frac{3 L_p V_{p,eff}}{\pi}} \tag{6.28}$$

where μ is the dynamic viscosity of the fluid and ρ is the density of the fluid.

The total pressure uncertainty is estimated by summing the randomly distributed errors (U_{PR}, $U_{PR,noise}$, $U_{PR,cal}$, $U_{PR,SGA}$, and U_{lockin}) in quadrature and adding the bias error due to U_{att},

$$U_{PR} = \left(\pm \sqrt{U_{PR}^{\,2} + U_{PR,noise}^{\,2} + U_{PR,cal}^{\,2} + U_{PR,SGA}^{\,2} + U_{lockin}^{\,2}} \right) - U_{att} \tag{6.29}$$

The parameters listed in Tables 6.4 and 6.5 are utilized to arrive at the total uncertainty in the AC-DC pressure measurement as well as the delineated uncertainty for each of the uncertainty terms discussed here. The results of this analysis are presented in Table 6.6.

Table 6.6 – Model 8510B-500 Pressure Transducer Uncertainty

Delineated Sensor Uncertainty	**Nominal Value (Pa)**
Combined Sensor Uncertainty, (Pa)	±86
Sensor Noise Uncertainty, (Pa)	±58
Calibration Gage Uncertainty, (Pa)	±1290
Strain Gage Noise Uncertainty, (Pa)	±290
Lock-in Amplifier Noise, (Pa)	±105
Attenuation Uncertainty, (Pa)	- 126
Total Pressure Uncertainty, (Pa)	**±1332-126**

6.1.2.2 Dynamic Pressure Measurement Uncertainty

The specifications of the small amplitude AC pressure measurement system are summarized in Table 6.7 for the PCB Model 112A22 piezoelectric pressure transducer. The uncertainty in the pressure measurement that is inherent to the piezoelectric pressure transducer can be sub-divided into an uncertainty related to transducer non-linearity, calibration accuracy, and

the resolution of the sensor. For the PCB pressure transducer, the manufacturer reports a non-linearity uncertainty ($U_{PE,nl}$) of [PCB 1],

$$U_{PE,nl} = \pm < 1\% \, RDG \tag{6.30}$$

The uncertainty due to the calibration of the pressure transducer, ($U_{PE,cal}$), is given by [PCB 1],

$$U_{PE,cal} = \pm 0.8\% RDG \tag{6.31}$$

The uncertainty due to the resolution of the pressure transducer, ($U_{PE,res}$), is defined as [PCB 1],

$$U_{PR,res} = \pm 6.895 \, Pa \tag{6.32}$$

The uncertainty due to the equipment that is used to condition/amplify the pressure signal as well as measure the amplitude of the signal can be sub-divided into an uncertainty related to the output noise of the transducer power supply/conditioner, output noise at the amplification stage, and the input/internal noise in the lock-in amplifiers. The PCB Model 482A20 ICP Power supply has two types of output noise; spectral noise and broadband noise [PCB 2]. The uncertainty in the pressure measurement due to spectral noise, ($u_{PR,sn}$), present in the output signal is given by [PCB 2],

$$u_{PE,sn} = \pm 0.18 \, \frac{nV}{\sqrt{Hz}} \tag{6.33}$$

Table 6.7 – AC Pressure Measurement System Specifications

Measurement Specifications	Symbol	Nominal Value
Excitation Voltage[1], (VDC)	V_{PR}	24
Full Scale Output[1], (Pa)	FS_{PE}	3447378
Sensor Sensitivity[1], (mv/Pa)	$\frac{\partial V_{PE}}{\partial P}$	0.0145
Sensor Non-Linearity[1], (Pa)	$U_{PE,nl}$	<1% FS
Sensor Resolution[1], (Pa)	$U_{PR,res}$	6.895
Calibration Uncertainty[2], (Pa)	$U_{PE,cal}$	0.8% FS
Conditioner Spectral Noise[3], $\left(nV/\sqrt{Hz}\right)$	$u_{PE,sn}$	0.18 at ω=10Hz
Conditioner Broadband Noise[3], $\left(nV/\sqrt{Hz}\right)$	$u_{PE,bn}$	10 at ω=1Hz-10kHz
Pre-Amp Output Noise[4], $\left(nV/\sqrt{Hz}\right)$	$u_{PE,an}$	4
Lock-in Amplifier Input Noise[5], (μV)	$u_{PR,lockin}$	9.1

[1] Nominal value reported in the manufacturers' literature for Model 112A22 pressure transducer [PCB 1].
[2] Nominal value reported via personal communication with PCB product engineer for Model 112A22 pressure transducer [PCB 2].
[3] Nominal value reported in the manufacturers' literature for Model 482A20 ICP power supply [PCB 3].
[4] Nominal value reported in the manufacturers' literature for Model 5113 pre-amplifier [EG&G].
[5] Experimentally measured value using the lock-in amplifiers.

Note that the value of $u_{PR,sn}$ is in units of volts-Hz$^{-0.5}$. This spectral noise uncertainty is converted into an associated pressure uncertainty, ($U_{PR,,sn}$), according to the sensor sensitivity and the frequency of the measured signal (ω),

$$U_{PE,sn} = \pm \frac{1000\ 0.18x10^{-9}\ \sqrt{\omega}}{\frac{\partial V_{PE}}{\partial P}} \tag{6.34}$$

where $\frac{\partial V_{PE}}{\partial P}$ is the sensitivity of the pressure transducer. The uncertainty due to the broadband noise, ($u_{PR,bn}$), present in the output signal can be expressed as [PCB 2],

$$u_{PE,bn} = \pm 10\ \frac{nV}{\sqrt{Hz}} \tag{6.35}$$

Note that the value of $u_{PR,bn}$ is in units of volts-Hz$^{-0.5}$. This broadband noise uncertainty is converted into an associated pressure uncertainty, ($U_{PR,,bn}$),

$$U_{PE,bn} = \pm \frac{1000\ 10x10^{-9}\ \sqrt{\omega}}{\frac{\partial V_{PE}}{\partial P}} \tag{6.36}$$

The uncertainty due to the noise in the output from the EG&G Model 5113 pre-amplifier, ($u_{PR,an}$), is given by [EG&G],

$$u_{PE,an} = \pm 4\ \frac{nV}{\sqrt{Hz}} \tag{6.37}$$

Note that the value of $u_{PR,an}$ is in units of volts-Hz$^{-0.5}$. The pre-amplifier output noise uncertainty is converted into an associated pressure uncertainty, ($U_{PR,,an}$),

$$U_{PE,bn} = \pm \frac{1000\ 4x10^{-9}\ \sqrt{\omega}}{\frac{\partial V_{PE}}{\partial P}} \tag{6.38}$$

The input/internal uncertainty in the lock-in amplifier is identical to that previously discussed and defined in Eqn. (6.25). For this pressure measurement there are no easily identifiable system-level uncertainty factors.

The total pressure uncertainty is estimated by summing the randomly distributed errors ($U_{PE,nl}$, $U_{PE,rep}$, $U_{PR,\ cal}$, $U_{PE,sn}$, $U_{PE,bn}$, $U_{PE,an}$, and U_{lockin}) in quadrature,

$$U_{PE} = \pm \sqrt{U_{PE,nl}^{\ 2} + U_{PE,res}^{\ 2} + U_{PE,cal}^{\ 2} + U_{PE,sn}^{\ 2} + U_{PE,bn}^{\ 2} + U_{PE,an}^{\ 2} + U_{lockin}^{\ 2}} \tag{6.39}$$

The parameters listed in Table 6.7 are utilized to arrive at the total uncertainty in the small amplitude AC pressure measurement as well as the delineated uncertainty for each of the uncertainty terms discussed here. The results of this analysis are presented in Table 6.8.

Table 6.8 – Model 112A22 Pressure Transducer Uncertainty[1]

Delineated Sensor Uncertainty	**Nominal Value**
Sensor Non-Linearity Uncertainty, (Pa)	±500
Sensor Resolution Uncertainty, (Pa)	±6.9
Sensor Calibration Uncertainty, (Pa)	±400
Spectral Noise Uncertainty, (Pa)	$\pm 9.6 \times 10^{-5}$
Broadband Noise Uncertainty, (Pa)	±0.005
Amplifier Noise Uncertainty, (Pa)	±0.002
Lock-in Amplifier Noise, (Pa)	±0.62
Total Pressure Uncertainty, (Pa)	**±640**

[1] Calculations performed assuming a pressure amplitude of 50 (kPa).

6.1.3 Heater Power Measurement Uncertainty

The measurement of the heat flow in the bus bar for determination of the energy flows requires precise knowledge of the applied heater power during calibration of the thermal bus assembly. In this test facility, the applied heater power is generated by thick-film metallic resistors. To accurately measure the power that is being dissipated in the heater, a Yokogowa Digital Power (Model WT1020) meter is utilized. Per the manufacturer's specifications, the uncertainty in the heater power measurement is given by [YOKO],

$$U_h = \pm\left(0.3\%\, RDG + 0.3\%\, RNG\right) \tag{6.40}$$

where *RDG* is the instrument reading (in W) and *RNG* is the instantaneous measurement range of the power meter (in W). Using this formula for the heater power uncertainty, the resulting error in the power measurement for six nominal input powers are listed in Table 6.9.

Table 6.9 – Model WT1020 Power Meter Uncertainty

Nominal Value	Instrument Range	Power Measurement Uncertainty
1 W	7.5 W	±0.0255 W
5 W	7.5 W	±0.0375 W
10 W	15 W	±0.075 W
25 W	30 W	±0.165 W
50 W	60 W	±0.33 W
100 W	150 W	±0.75 W

6.1.3 Phase Angle Measurement Uncertainty

The phase angle of each signal with respect to some reference is measured using a Stanford Research Systems SR-830/850 DSP lock in amplifier. Per the manufacturer's specifications, the error in this measurement has three components, corresponding to (1) phase noise, (2) phase drift, and (3) relative phase error.

The uncertainty in the phase measurement due to internal phase noise, ($U_{\phi,n}$), is given by [SRS],

$$U_{\phi,n} = \pm < 0.001° \tag{6.41}$$

The uncertainty in the phase angle measurement due to phase drift, ($u_{\phi,d}$), is defined as [SRS],

$$u_{\phi,d} = \pm < \frac{0.01°}{°C} \tag{6.42}$$

Assuming a maximum ambient temperature drift of five degrees centigrade, the uncertainty related to the phase drift, ($U_{\phi,d}$), is defined as,

$$U_{\phi,d} = \pm < 0.05° \tag{6.43}$$

The uncertainty in the phase angle measurement due to the relative phase error, ($U_{\phi,r\,s}$), is defined as [SRS],

$$U_{\phi,r} = \pm < 0.01° \tag{6.44}$$

Using these individual uncertainty values for the phase angle measurement, the total phase uncertainty can be determined by summing the randomly distributed errors ($U_{\phi,n}$, $U_{\phi,d}$, and $U_{\phi,r}$) in quadrature,

$$U_{\phi} = \pm\sqrt{U_{\phi,n}{}^2 + U_{\phi,d}{}^2 + U_{\phi,r}{}^2} \tag{6.45}$$

For all phase measurements, the total uncertainty is $U_{\phi} = \pm 0.051°$.

6.2 Measurement Uncertainty

To ensure that the test facility is capable of accurately measuring the quantities required to validate the CFD model, an uncertainty analysis is performed for the individual measurements that are required to determine each of the important energy terms. The uncertainty analysis is performed using a base case that corresponds to the performance predicted using the CFD model and the Regen 3.3 model. The goal of this analysis is to identify how the uncertainties in the individual instruments and measurements conspire to affect our ability to resolve these energy flows experimentally. The nominal parameters utilized for this analysis are presented in Table 6.10 and are reported for a cold end temperature of 80 K.

Table 6.10 – Model Predicted Energy Flows

Quantities to be Measured	Predicted Model Values
Regenerator energy flow, (W)	31
Pulse-tube energy flow, (W)	106
Net cooling power, (W)	75
Acoustic power flow, (W)	130

6.2.1 Regenerator Energy Flow, Net Cooling Power, and Pulse-Tube Energy Flow Measurement Uncertainty

The initial staring point for the regenerator energy flow measurement, the net cooling power measurement, and therefore the resulting calculation of the pulse-tube energy flow is the calibration of the conductive thermal pathway that links the cold end of the test facility to the cryocooler. The basic premise for this calibration is that the thermal characteristics of the bus bar and its associated joints will remain the same so long as none of these thermal joints are changed. As a result, if a known and precisely measured input power is applied at one end of the bar then the temperature difference that results can be measured and precisely correlated to the power (at a given cold end temperature). The calibration curve therefore correlates the measured temperature difference to the power passing through the bus bar; such a curve is illustrated in Figure 6.1. (Note that the data presented in Figure 6.1 are indicative of what the experimental data look like; these data are not actual test data but generated data based upon expected conditions.)

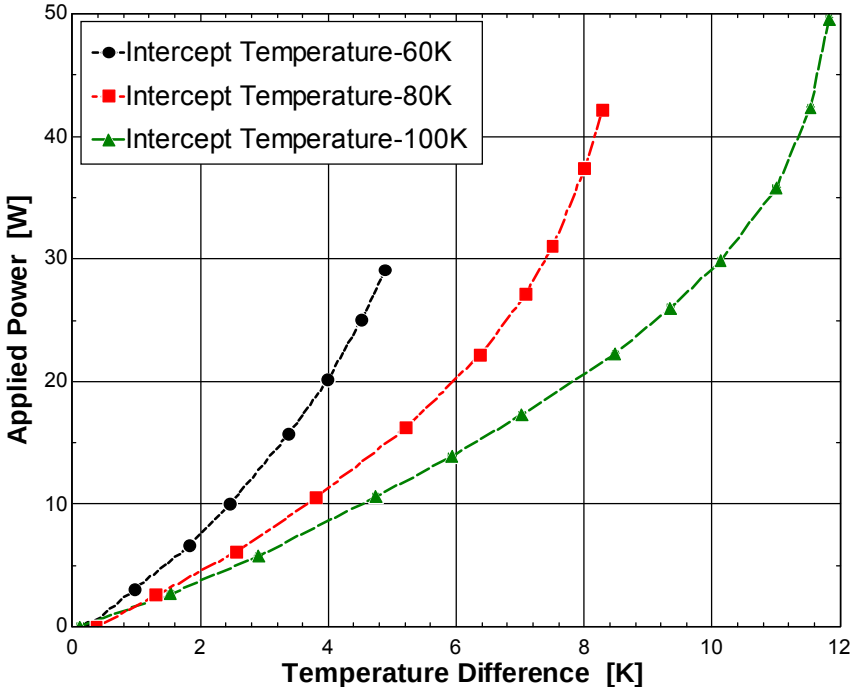

Figure 6.1: Plot illustrating the expected form of the calibration curve for the thermal bus bar assembly with anticipated errors bars; note the error values are very small, and thus the lack of visible error bars.

A regression analysis is carried out on the raw data in order to generate the calibration curve. A typical regression analysis assumes that the independent data (e.g., the temperature difference) are error free while the dependent data (e.g., the applied heater power) have some finite experimental error. However, in this case, both of the data (temperature difference and heater power) have some quantified uncertainty at each data point; this must be accounted for in the regression analysis. The commercial fitting software, LabFit, is utilized to fit the experimental data (Silva 2007). The regression analysis accomplished by LabFit is a bivariate regression and therefore includes the uncertainty in both axes via a weighting function that propagates the uncertainty from the independent variable into the prediction for the dependent variable (heater power). Using this program, the data presented in Figure 6.1 were fitted with a 3rd order polynomial. The results from this analysis yield an expression for

the heat flow through the bar (E) as a function of the measured temperature difference given by,

$$\dot{E} = A\Delta T + B\Delta T^2 + C\Delta T^3 \tag{6.46}$$

where, A, B, and C are the fitted coefficients with a finite uncertainty. The numerical values and the uncertainty in these coefficients are listed in Table 6.11.

Table 6.11 – Computed Fitting Parameters for an intercept temperature of 80K

Parameter	Nominal Values with Uncertainty
A	1.526 ± 0.028 W/K
B	0.047 ± 0.004 W/K^2
C	0.00085 ± 0.00013 W/K^3

Once the calibration curve has been generated, the total uncertainty in the measurement of either the regenerator energy flow or net cooling power can be determined via an uncertainty propagation analysis carried out on Eqn. (6.46) including the uncertainty in the coefficients generated by the calibration as well as the uncertainty in the temperature difference measurement itself. The uncertainty propagation is performed via partial differentiation of Eqn. (6.46) with respect to each of the variables and leads to:

$$U_{\dot{E}} = \left(\left(\frac{\partial \dot{E}}{\partial A} U_A \right)^2 + \left(\frac{\partial \dot{E}}{\partial B} U_B \right)^2 + \left(\frac{\partial \dot{E}}{\partial C} U_C \right)^2 + \left(\frac{\partial \dot{E}}{\partial \Delta T} U_{\Delta T} \right)^2 \right)^{\frac{1}{2}} \tag{6.47}$$

where U_A, U_B, U_c, and $U_{\Delta T}$ are the specific uncertainty values for each of the coefficients of the calibration curve (listed in Tables 6.11 and 6.12) and $U_{\Delta T}$ is the uncertainty in the measurement of the temperature difference. The partial differentials in Eqn. (6.47) are given by,

$$\frac{\partial \dot{E}}{\partial A} = \Delta T \tag{6.48}$$

$$\frac{\partial \dot{E}}{\partial B} = \Delta T^2 \tag{6.49}$$

$$\frac{\partial \dot{E}}{\partial C} = \Delta T^3 \tag{6.50}$$

$$\frac{\partial \dot{E}}{\partial \Delta T} = A + 2B\Delta T + 3C\Delta T^2 \tag{6.51}$$

The uncertainty in the regenerator energy flow and the net cooling power measurements is estimated using this approach; the "measured" temperature difference used for this estimate is obtained from the data presented in Figure 6.1. The results are summarized in Table 6.12.

Table 6.12 – Predicted Measurement Resolution for the Regenerator Energy Flow and Net Cooling Power using the Experimental PTC Test Facility.

Measurement	**Measured ΔT**	**Predicted**
Regen. Energy Flow, $\dot{E}_{REG,c}$	13.41 ± 0.046 K	30.9 ± 0.88(W
Net Cooling Power, $\dot{Q}_{net}$	24.06 ± 0.051 K	75 ± 3.01 W

The pulse-tube energy flow is the difference between the net cooling power and regenerator loss, each measured separately as previously discussed,

$$\dot{E}_{PT,c} = \dot{Q}_{net} - \dot{E}_{REG,c} \tag{6.52}$$

The expression for the uncertainty in the pulse-tube energy flow is determined by differentiating Eqn. (6.52) with respect to the regenerator energy flow and the net cooling power terms yielding,

$$U_{\dot{E}_{PT,c}} = \left(\left(\frac{\partial \dot{E}_{PT,c}}{\partial \dot{E}_{REG,c}} U_{\dot{E}_{REG,c}} \right)^2 + \left(\frac{\partial \dot{E}_{PT,c}}{\partial \dot{Q}_{net}} U_{\dot{Q}_{net}} \right)^2 \right)^{\frac{1}{2}} \tag{6.53}$$

where $U_{\dot{E}_{REG,c}}$ is the uncertainty in the regenerator energy flow measurement, and $U_{\dot{Q}_{net}}$ is the uncertainty in the net cooling power measurement. The partial differentials required by Eqn. (6.53) are given by,

$$\frac{\partial \dot{E}_{PT,c}}{\partial \dot{E}_{REG,c}} = 1 \tag{6.54}$$

$$\frac{\partial \dot{E}_{PT,c}}{\partial \dot{Q}_{net}} = 1 \tag{6.55}$$

The conditions presented in Table 6.12 are used with Eqns. (6.47), (6.52), and (6.53) to predict the uncertainty in the measurement of the pulse-tube energy flow as summarized in Table 6.13.

Table 6.13 – Predicted Measurement Resolution for the Pulse-Tube Energy Flow and Acoustic Power Flow

Measurement	Predicted Value
Pulse-Tube Energy Flow, $\dot{E}_{PT,c}$	107 ± 3.1 W
Acoustic Power Flow, $\dot{E}_{PT,c}$	130 ± 12.18 W

Based upon the results of this analysis, the predicted uncertainty in the measurements of the regenerator energy flow, the net cooling power, and the pulse-tube energy flow range from 2-4% of their nominal values.

6.2.2 Mass Flow Measurement Uncertainty

One of the critical measurements required for validation of the CFD model is the mass flow rate at the cold end of the system. This mass flow rate is a boundary condition for the model and is also used in the computation of the experimentally measured acoustic power flow. The measurement of the mass flow rate is accomplished by experimentally calibrating a flow sensor that is formed by a hydraulic resistance placed in the cold end heat exchanger (i.e., in the thermal resistance). The pressure drop across the sensor is correlated to the instantaneous mass flow rate.

The experimental calibration of the flow sensor proceeds by installing a reservoir directly to the cold end of the system and measuring the dynamic pressure and average temperature in the reservoir in order to infer the instantaneous mass flow rate. The expression for the mass flow rate into the reservoir volume is given by,

$$\left|\dot{m}_{res}\right| = \frac{\left|\tilde{P}\right| V_{res}}{\gamma T_{res} R} \tag{6.56}$$

where, $\left|\tilde{P}\right|$ is the magnitude of the measured dynamic pressure, V_{res} is the volume of the reservoir, γ is the ratio of specific heats for the working fluid, T_{res} is the temperature of the gas present in the reservoir volume, and R is the gas constant for the working fluid. Equation

(6.56) has some uncertainty that is related to the uncertainty in the fundamental measurements of temperature, pressure, and the volume of the reservoir.

$$U_{\dot{m}} = \left(\left(\frac{\partial \dot{m}}{\partial V_{res}} U_{V_{res}} \right)^2 + \left(\frac{\partial \dot{m}}{\partial T_{res}} U_{T_{res}} \right)^2 + \left(\frac{\partial \dot{m}}{\partial \left| \tilde{P} \right|} U_{\left| \tilde{P} \right|} \right)^2 \right)^{\frac{1}{2}} \tag{6.57}$$

where $U_{V_{res}}$ is the uncertainty in the reservoir volume measurement, $U_{T_{res}}$ is the uncertainty in the reservoir temperature measurement, and $U_{\left| \tilde{P} \right|}$ is the uncertainty in the dynamic pressure amplitude. The partial differential equations required by Eqn. (6.57) are obtained by differentiating Eqn. (6.56),

$$\frac{\partial \dot{m}}{\partial V_{res}} = \frac{\left| \tilde{P} \right|}{\gamma T_{res} R} \tag{6.58}$$

$$\frac{\partial \dot{m}}{\partial T_{res}} = -\frac{\left| \tilde{P} \right| V_{res}}{\gamma {T_{res}}^2 R} \tag{6.59}$$

$$\frac{\partial \dot{m}}{\partial \left| \tilde{P} \right|} = \frac{V_{res}}{\gamma T_{res} R} \tag{6.60}$$

The differential pressure across the flow sensor is also measured and correlated to the mass flow rate calculated by Eqn. (6.56). The differential pressure is,

$$\left| \Delta P \right| = P_1 - P_2 \tag{6.61}$$

where P_1 is the upstream pressure and P_2 is the downstream pressure. There is a fundamental uncertainty in the measurement of the pressure difference related to our ability to measure

small amplitude oscillating pressure, discussed earlier in the chapter. The expression for the uncertainty in the differential pressure is determined by differentiating Eqn. (6.61) with respect to the upstream and downstream pressure terms yielding,

$$U_{|\Delta P|} = \left(\left(\frac{\partial |\Delta P|}{\partial P_1} U_{P_1} \right)^2 + \left(\left(\frac{\partial |\Delta P|}{\partial P_2} U_{P_2} \right) \right)^2 \right)^{\frac{1}{2}} \tag{6.62}$$

where U_{P_1} is the uncertainty in the upstream pressure measurement, and U_{P_2} is the uncertainty in the downstream pressure measurement, while the partial differentials are given by,

$$\frac{\partial |\Delta P|}{\partial P_1} = 1 \tag{6.63}$$

$$\frac{\partial |\Delta P|}{\partial P_2} = 1 \tag{6.64}$$

The calibration curve therefore correlates the mass flow rate as a function of the differential pressure drop across the thermal intercept; such a curve is illustrated in Figure 6.2 with representative error bars.

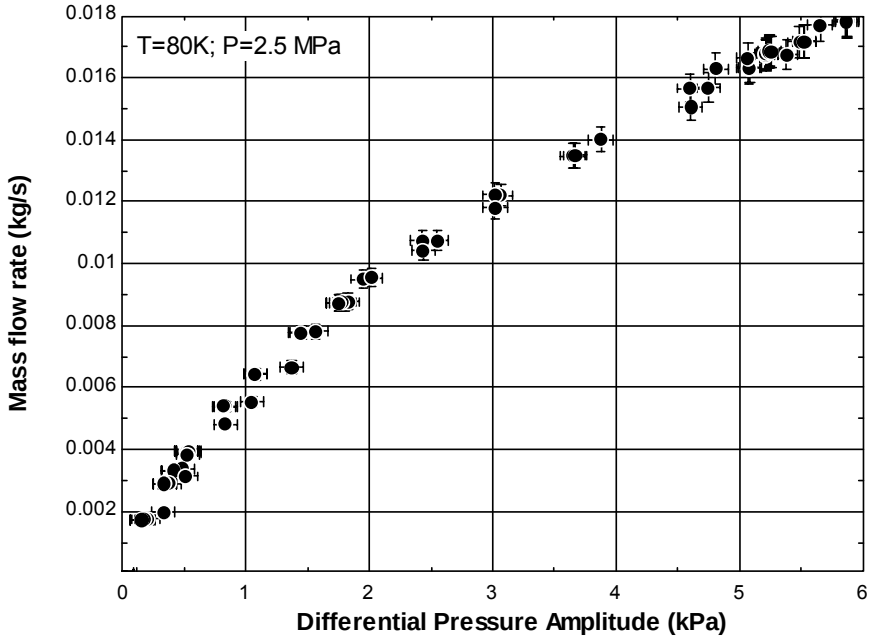

Figure 6.2: Plot illustrating the calibration curve for the mass flow rate with errors bars.

A regression analysis is carried out to generate the calibration curve from the raw data. The commercial fitting software, LabFit, is utilized to fit the experimental data (Silva 2007) because it is capable of taking into account the uncertainty in the independent and dependent variables. The results from this analysis yield an expression for the mass flow rate ($\dot{m}$) as a function of the measured pressure difference,

$$\dot{m} = A\,\Delta P + B\,\Delta P^2 + C\,\Delta P^3 \tag{6.65}$$

where, A, B, and C are the fitted coefficients with a finite uncertainty. The numerical values and the uncertainty in these coefficients are listed in Table 6.14.

Table 6.14 – Computed Fitting Parameters for the mass flow sensor data

Parameter	Nominal Values with Uncertainty
A	$0.744e^{-2} \pm 0.107e^{-3}$ (kg/s)/Pa
B	$-0.15e^{-2} \pm 0.542e^{-4}$ (kg/s)/Pa^2
C	$0.133e^{-3} \pm 0.701e^{-5}$ (kg/s)/Pa^3

6.2.3 Acoustic Power Flow Measurement Uncertainty

The experimentally measured acoustic power flow is defined as,

$$W_{pv} = \frac{1}{2} R T \left|\dot{m}\right| \frac{\left|\tilde{P}\right|}{\overline{P}} \cos\theta \tag{6.66}$$

where θ is the phase angle between mass flow and pressure, $\left|\tilde{P}\right|$ is the magnitude of the dynamic pressure, $\overline{P}$ is the mean pressure, T is the temperature of the gas, and $\left|\dot{m}\right|$ is the amplitude of the mass flow rate. The uncertainty in Eqn. (6.66) is determined from uncertainty propagation via partial differentiation of Eqn. (6.66) with respect to each of the variables; this process leads to:

$$U_{\dot{E}_{PT,\varepsilon}} = \left(\left(\frac{\partial W_{pv}}{\partial T} U_T \right)^2 + \left(\frac{\partial W_{pv}}{\partial \left|\dot{m}\right|} U_{|\dot{m}|} \right)^2 + \left(\frac{\partial W_{pv}}{\partial \left|\tilde{P}\right|} U_{|\tilde{P}|} \right)^2 + \left(\frac{\partial W_{pv}}{\partial \overline{P}} U_{\overline{P}} \right)^2 + \left(\frac{\partial W_{pv}}{\partial \theta} U_\theta \right)^2 \right)^{\frac{1}{2}} \tag{6.67}$$

where U_T, $U_{|\dot{m}|}$, $U_{|\tilde{P}|}$, $U_{\overline{P}}$,and U_θ are the specific uncertainty values for each of the fundamental measurements in the acoustic power expression. The partial differentials in Eqn. (6.67) are given by,

$$\frac{\partial W_{pv}}{\partial T} = \frac{1}{2} R \left|\dot{m}\right| \frac{\left|\tilde{P}\right|}{\overline{P}} \cos\theta \tag{6.68}$$

$$\frac{\partial W_{pv}}{\partial \left|\dot{m}\right|} = \frac{1}{2} R T \frac{\left|\tilde{P}\right|}{\overline{P}} \cos\theta \tag{6.69}$$

$$\frac{\partial W_{pv}}{\partial \left|\tilde{P}\right|} = \frac{1}{2} R T \left|\dot{m}\right| \frac{1}{\overline{P}} \cos\theta \tag{6.70}$$

$$\frac{\partial W_{pv}}{\partial \bar{P}} = -\frac{1}{2} R T \left|\dot{m}\right| \frac{\left|\tilde{P}\right|}{\bar{P}^2} \cos\theta \tag{6.71}$$

$$\frac{\partial W_{pv}}{\partial \theta} = -\frac{1}{2} R T \left|\dot{m}\right| \frac{\left|\tilde{P}\right|}{\bar{P}} \sin\theta \tag{6.72}$$

For this analysis, the uncertainty in the acoustic power measurement was estimated using the predicted temperature, pressure amplitudes, mean pressure, mass flow rate (differential pressure), and phase angle at the cold end that are consistent to those expected during experimental operation. The result of the analysis for the experimental error in the acoustic power flow measurement is presented in Table 6.13. Based upon the results of this analysis, the predicted experimental error for the experimental measurement of the acoustic power flow is approximately 10%.

7. Experimental Results

Experimental measurements were carried out in order to measure the regenerator loss as well as the pulse tube enthalpy flow for various pulse tube and flow transition permutations using the experimental test bed and methodology discussed in previous chapters. This chapter discusses the data reduction process. The measured regenerator loss data are compared to the predictions of REGEN3.3 and the measured pulse tube enthalpy flow data are compared to the enthalpy flow predicted by the CFD model.

7.1 Regenerator Experimental Results

This section discusses the data reduction process utilized for the raw experimental regenerator measurements and also presents the comparison between the measured regenerator loss and the predicted loss from the numerical regenerator code REGEN3.3.

7.1.1 Regenerator Data Reduction

One of the challenges with experimental measurements is that data must be post-processed in order to obtain usable information that can be compared in a meaningful way with modeling predictions. The data reduction process associated with the regenerator loss measurements involved four steps:

1) determine the regenerator loss via the calibration curves generated for the bus bar,
2) determine the cold end mass flow rate using the calibration curve for the mass flow sensor,

3) determine the cold end phase angle using the measured phase angles for mass flow and pressure, and

4) correction of the mass flow rate and phase angle at the thermal intercept to account for dead volume effects.

To determine the regenerator loss at a given set of operating conditions, the temperature difference generated across the thermal bus bar (which was interfaced with the cold end of system) was recorded. Using the measured temperature difference and the calibration curves for the bus bar, the rate of heat transfer through the bus bar (which is equal to the regenerator loss associated with that specific set of operating conditions) was determined. This process is illustrated in Figure 7.1. A measured temperature difference of 7.25 K at an intercept temperature of 80 K leads to a regenerator loss of 30 W.

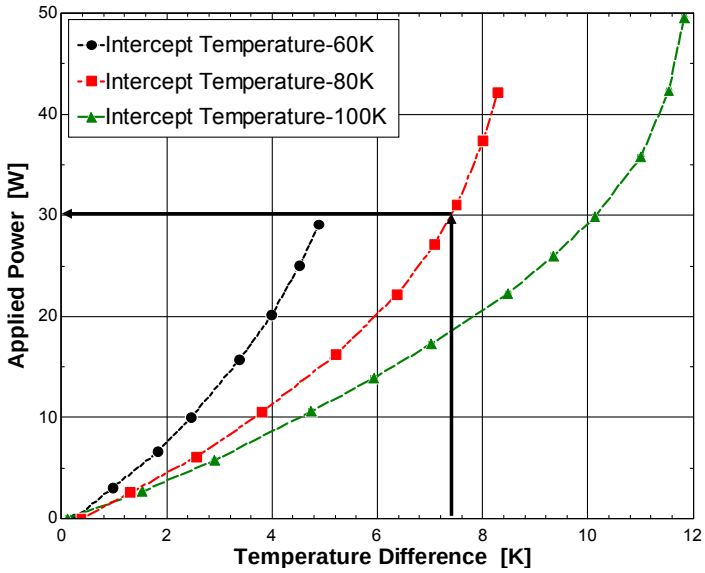

Figure 7.1: Plot showing the use of the bus bar calibration curve to determine the experimental regenerator loss using the measured temperature difference across the thermal bus bar.

Additional data is required in order to run the regenerator model and therefore compare the experimental measurement to the REGEN model predictions. These measurements include the mass flow rate at the cold end of the regenerator as well as the phase angle between the mass flow and the pressure at the cold end. The mass flow rate was determined via measurement of the pressure difference across the thermal intercept at the cold end of the regenerator. Using this pressure difference and the calibration curve for the mass flow meter, the mass flow amplitude in the thermal intercept was determined. This process is illustrated in Figure 7.2 - a measured differential pressure amplitude of 3.85 kPa for an intercept temperature of 80 K leads to a mass flow rate of 0.014 kg/s. The phase angle of the mass flow rate relative to the pressure at the cold end was determined via direct measurement of the mass flow phase angle and the pressure phase angle using lock-in amplifiers. The phase angle is the subtraction of these two quantities.

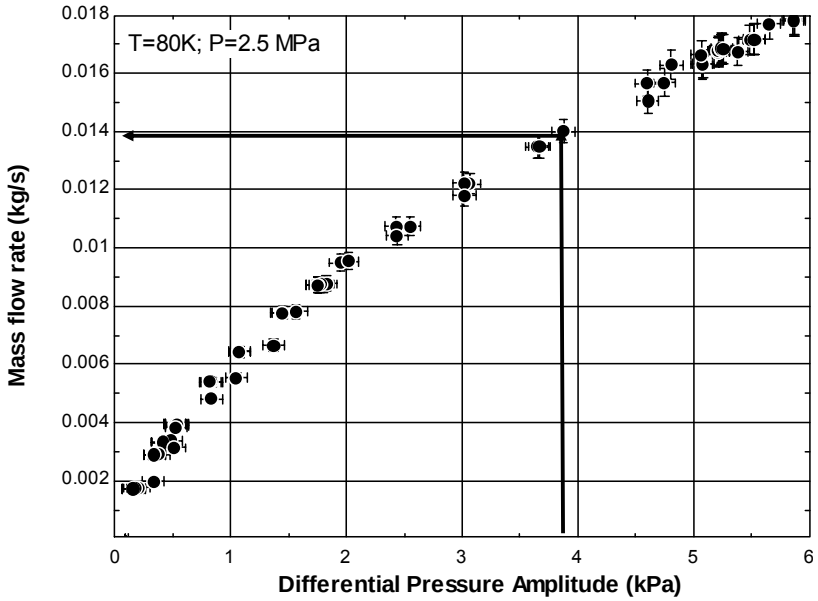

Figure 7.2: Plot showing the use of the mass flow calibration curve to determine the experimental cold end mass flow rate using the measured pressure difference across the thermal intercept.

The mass flow rate determined using the pressure differential and the phase angle both must be corrected slightly in order to account for dead volume present in the thermal intercept. The mass flow rate and phase angle determined using the raw experimental measurement represent the average mass flow rate and phase angle in the thermal intercept rather than the local mass flow rate and phase angle exiting the cold end of the regenerator (the inputs required by REGEN). Therefore, the experimental measurements were corrected using a phasor analysis (mass balance) applied to the thermal intercept, as shown in Figure 7.3. The MATLAB routine developed in order to perform the correction of the experimental data is located in Appendix E.

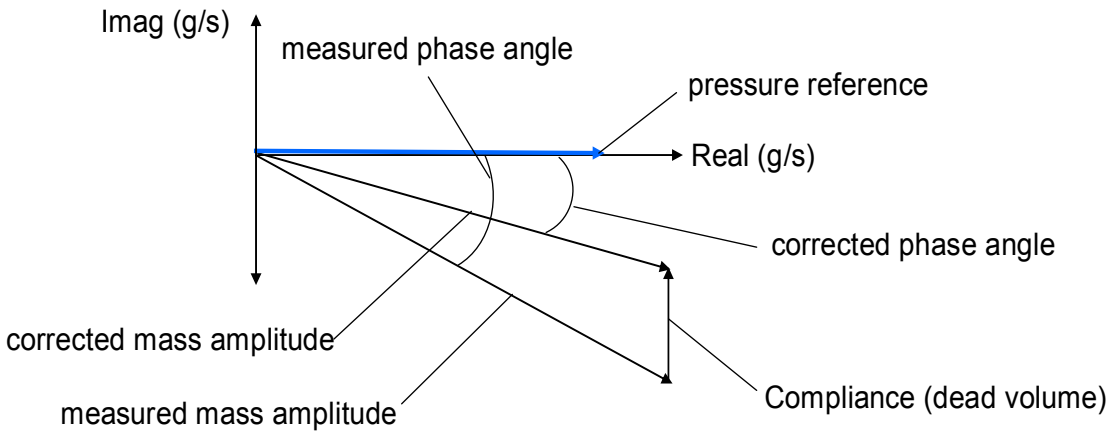

Figure 7.3: Plot showing the use of the bus bar calibration curve to determine the experimental regenerator loss using the measured temperature difference across the thermal bus bar.

The actual mass flow rate exiting the regenerator is determined via the vector addition of the measured mass flow amplitude vector and the dead volume (compliance) vector. The corrected phase angle is determined from the magnitude of the real and imaginary components of the corrected mass flow vector and then subtracted from the phase of pressure reference vector.

7.1.2 Regenerator Loss Results and Comparison

The regenerator designed for the experimental test facility was experimentally designed to allow parametric studies with two experimental parameters. The first parameter was the cold end phase angle between the mass flow and pressure; this was controlled via the use of two different inertance tubes. The two inertance tubes were designed using a distributed component model of the inertance tube developed by Schunk (2004). The second parameter that was experimentally varied was the cold end pressure ratio. The pressure ratio is directly related to the amplitude of the mass flow rate at the cold end and could be varied by adjusting the stroke of the compressor. The experimental test permutations are illustrated in Figure 7.4.

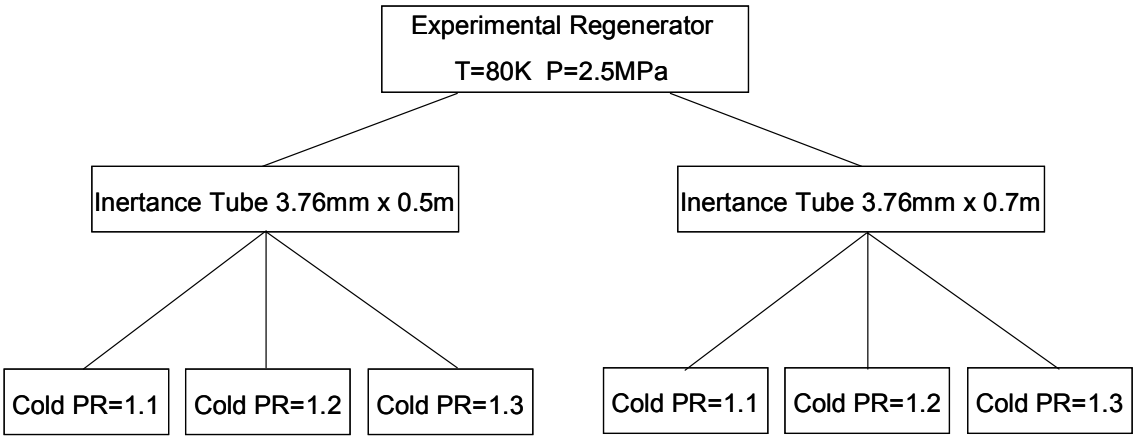

Figure 7.4: Flow chart illustrating the test permutations of the experimental regenerator for regenerator loss characterization.

For each of the permutations shown in Figure 7.4, the regenerator loss, mass flow rate, and cold end phase angle (between pressure and flow) were determined from the raw experimental measurements using the data reduction process discussed previously.

The experimental measurements were compared to the numerical model REGEN3.3. A numerical simulation was carried out using input conditions that corresponded to the measured mass flow rate, phase angle, and the cold end pressure ratio associated with each of the test conditions. Each model was run until a cycle steady state condition was achieved. The experimentally measured and predicted regenerator loss at each test permutation are summarized in Table 7.1.

Table 7.1 – Experimental and Modeling Results for Regenerator Loss

Inertance Tube	**Pressure Ratio**	**Measured Loss (W)**	**Predicted Loss (W)**
Inertance Tube 1 (0.505m x 3.46 mm)	1.3	29.3	27
	1.2	18.7	19
	1.1	6.6	10.7
Inertance Tube 2 (0.705m x 3.46 mm)	1.3	23.8	26.9
	1.2	13.2	16.5
	1.1	4.3	9.8

The comparison of the measured regenerator loss to the predicted regenerator loss is illustrated in Figures 7.5 and 7.6 which show the modeling predictions for the regenerator loss overlaid on the experimental measurements as a function of the cold end pressure ratio for each inertance tube.

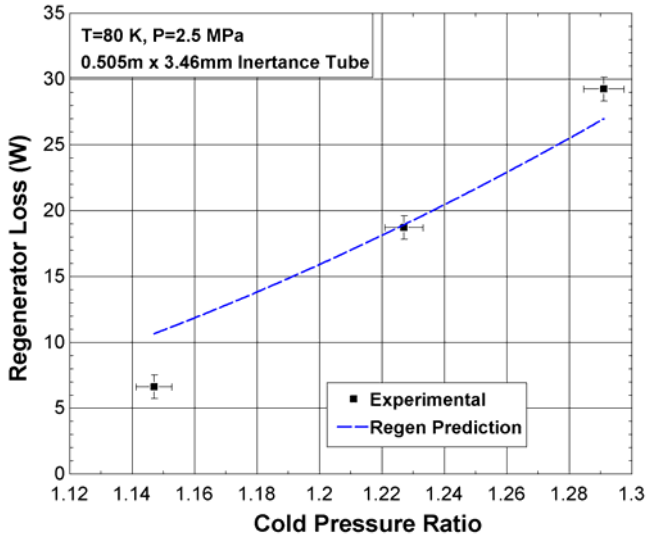

Figure 7.5: Plot showing the comparison between the measured regenerator loss and predicted loss for an inertance tube length and diameter of 0.505 m and 3.46 mm respectively.

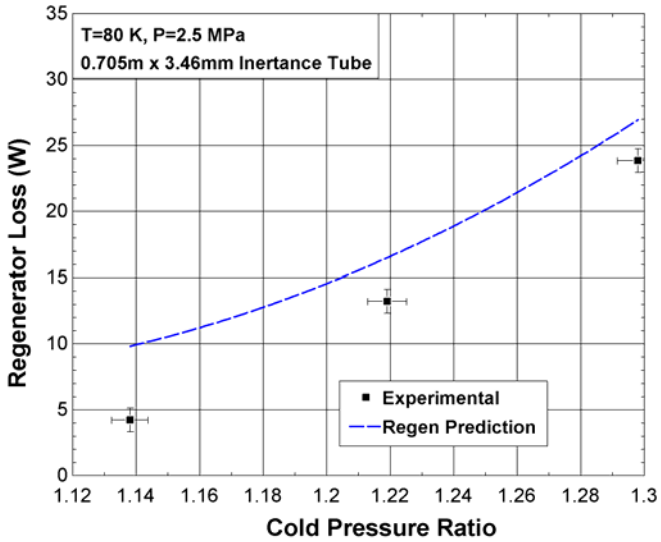

Figure 7.6: Plot showing the comparison between the measured regenerator loss and predicted loss for an inertance tube length and diameter of 0.705 m and 3.46 mm respectively.

Figures 7.5 and 7.6 show good agreement between the experimental measurements and the corresponding predictions obtained using REGEN3.3. The experimental results and model predictions clearly follow the same trends and the error between the measurements and

predictions at moderate to high pressure ratios is less than 20%. The error between the measurements and model predictions does grow as the pressure ratio is reduced; the error is approximately 50% at the lowest pressure ratio data points. This increase in error is due to three different effects. First, the error in the regenerator loss measurement is relatively constant over the range of tested pressure ratios. As the pressure ratio decreases so does the regenerator loss and therefore the error becomes a larger fraction of the loss. The reduction in the magnitude of the regenerator loss reduces the ability of the experiment to accurately resolve this quantity. Secondly, at low pressure ratios the mass flow rate is reduced and therefore the measurement of the pressure difference across the thermal intercept, from which the mass flow is determined, is difficult due to a low signal-to-noise ratio. This effect is likely the main source of the discrepancy between the experimental results and the model predictions at low pressure ratios. The mass flow rate is a primary input to the REGEN3.3 models and therefore any error in this measurement will have a large impact on the predicted regenerator loss. Third, some error between the model predictions and the experimental results is expected due to the nature of the REGEN3.3 model itself. REGEN3.3 is a one-dimensional model of the regenerator whereas the actual flow conditions are at least somewhat three-dimensional. Additionally, the correlations for friction factor and heat transfer coefficient utilized in this code are for steady flow whereas the actual flow conditions are oscillatory.

7.2 Pulse Tube Experimental Results

This section discusses the data reduction process used to obtain the pulse tube enthalpy flow from the raw experimental measurements and also presents the comparison between the

experimentally measured pulse tube enthalpy flow and the enthalpy flow predicted by the CFD model.

7.2.1 Pulse Tube Data Reduction

The data reduction process for the pulse tube measurements involved four steps,

1) determine the cold end mass flow rate using the calibration curve for the mass flow sensor,
2) determine the cold end phase angle using the measured phase angles for mass flow and pressure,
3) correct the mass flow rate at the thermal intercept to account for dead volume effects,
4) determine the pulse tube enthalpy flow using the measurements for the net cooling power together with the regenerator loss predicted using REGEN3.3, and
5) determine the acoustic power flow at the cold end of the pulse tube and the resulting figure of merit for the pulse tube component.

The first three steps listed above are identical to those performed for the regenerator loss measurements and are not discussed further. The enthalpy flow in the pulse tube component was determined using the experimentally measured cooling power as well as the regenerator loss predicted by REGEN3.3 under identical operating conditions. The regenerator loss was predicted using the same methodology discussed regarding previously for the regenerator loss. The reason for use of the predicted regenerator loss versus measuring it experimentally was adopted because it was not possible to exactly match the test conditions for the two

separate test configurations; this might have been possible for a single case, but not for each permutation of the pulse tube and flow transitions.

The sum of the predicted regenerator loss and the measured cooling power for a given set of operating conditions is the enthalpy flow in the pulse tube component. The acoustic power flow at the cold end of the pulse tube component was determined using the corrected mass flow rate, the corrected phase angle, and the pressure amplitude at the cold end in conjunction with Eqns. 5.4 and 5.5; these equations are described in Chapter 5. Finally, the figure of merit for the pulse tube component was determined via the ratio of the measured enthalpy flow and the measured acoustic power flow.

7.2.2 Pulse Tube Experimental Results

Two pulse tubes, each compatible with multiple flow transition configurations, were designed for the experimental test facility. Each pulse tube/flow transition configuration was experimentally characterized over a range of cold end pressure ratio (adjusted using the compressor stroke). The experimental test permutations are illustrated in Figure 7.7 in flow chart format with photos depicting the actual non-dimensional pulse tubes.

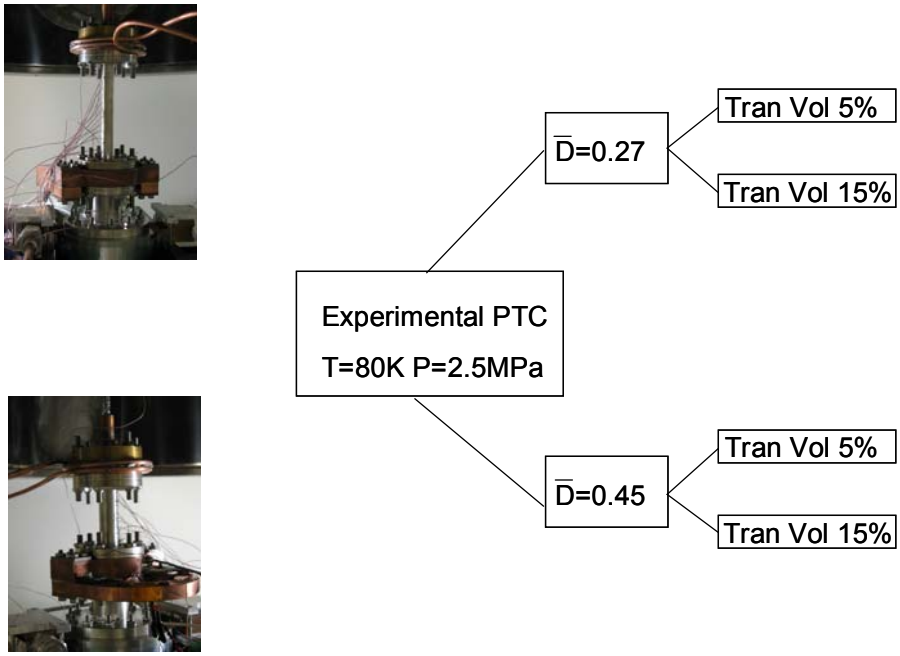

Figure 7.7: Flow chart illustrating the test permutations for the pulse tube experimental measurements.

One of the primary concerns related to comparing experimental data from the test facility to the CFD model predictions was the possibility of large three dimensional effects which would not be captured by the developed two-dimensional axisymmetric model. One technique that can be utilized in order to determine whether significant three-dimensional effects are present in a PTC is to instrument the pulse tube wall using thermocouples that are mounted around the cross section of the pulse tube component at specific axial locations along the pulse tube. In theory, this method is ideal and can be used to accurately map the temperature profile of the pulse tube component in three dimensions. However, this technique has an inherent problem related to accurate placement of all the thermocouples on exactly the same cross sectional plane. If the axial location of the thermocouples is not precise then the measured temperatures can deviate due to the axial temperature gradient in the pulse tube rather than an actual 3-D flow effect, thus yielding false results.

A much simpler, yet highly effective, method that can be used to qualitatively map the temperature profile within a pulse tube is to cool the system without installing the vacuum bell-jar. By cooling the system below the dew point, frost forms on the pulse tube component. One can then observe the frost line around the circumference of the pulse tube component in order to determine if there are significant three dimensional flow effects. This method was utilized for the short pulse tube component, which would experience the largest 3-D effects. The results of this experiment are shown in Figure 7.8 and show that the frost line was essentially constant in a given radial plane for the pulse tube component.

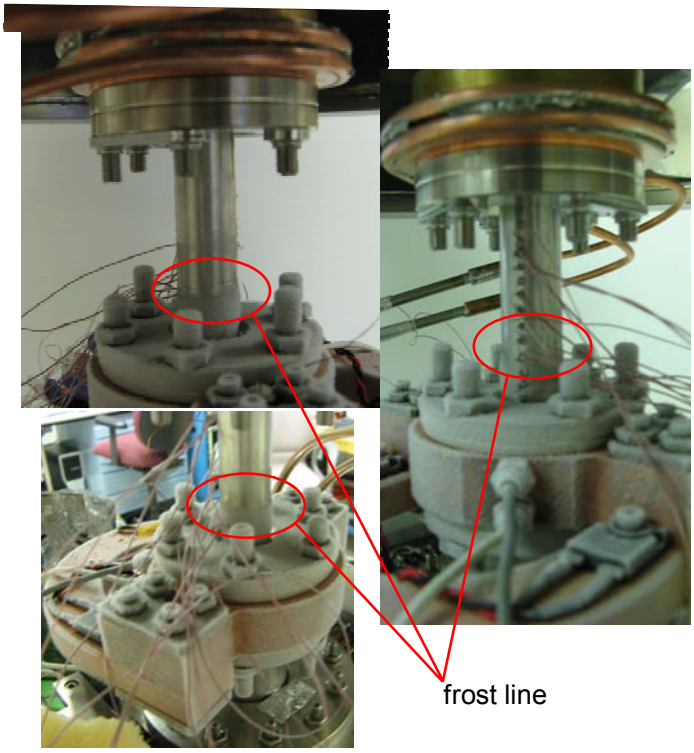

Figure 7.8: Illustration showing the results of the frost test in which the three camera angles are spaced ~120 deg apart radially.

For each of the permutations shown in Figure 7.7, the net cooling power, acoustic power, figure of merit, mass flow rate, and cold end phase angle (between pressure and flow) were

determined from the raw experimental measurements using the reduction process discussed previously. These results are summarized in Table 7.2.

A CFD model was developed that corresponded to each of the test permutations using the input conditions that correspond to the experimentally measured mass flow rate, phase angle, and cold end pressure ratio as inputs. Each model was run until a cycle steady state condition was achieved. The modeling predictions for the enthalpy flow, acoustic power, and figure of merit are also presented in Table 7.2.

Table 7.2 – Experimental and Modeling Results for Pulse Tube Enthalpy Flow, Acoustic Power, and Figure of Merit

Configuration	Pressure Ratio	Measured Enthalpy Flow (W)	Predicted Enthalpy Flow (W)	Predicted/Measured Acoustic Power (W)	FOM Exp / Pred
D_{ND} = 0.25 Flow Tran = 5%	1.249	97.7	113	147.1	0.66/0.77
	1.215	71	80.2	102	0.7/0.79
	1.173	48.4	47.6	61.6	0.78/0.77
	1.14	31.4	26.9	35.4	0.88/0.76
D_{ND} = 0.25 Flow Tran = 15%	1.251	102.3	112	148.6	0.69/0.75
	1.211	70	82.85	97.6	0.72/0.85
	1.178	44.2	56.2	62.7	0.7/0.89
	1.142	26.6	30.5	37.8	0.7/0.81
D_{ND}= 0.4 Flow Tran = 5%	1.257	102.1	109.1	152	0.67/0.72
	1.214	70.2	79.7	103	0.68/0.77
	1.17	38.9	42.1	56.1	0.69/0.75
	1.14	24.2	26.6	36.8	0.66/0.72
D_{ND} = 0.4 Flow Tran = 15%	1.251	91.6	99.3	124.1	0.74/0.8
	1.226	70.2	69.6	86.7	0.81/0.8
	1.192	46.8	43.8	53.7	0.87/0.82
	1.154	25.9	23.1	27	0.96/0.86

The comparison of the measured enthalpy flow and acoustic power in the pulse tube component to the predictions using the developed CFD model are illustrated in Figures 7.9, 7.10, 7.11, and 7.12, which show the modeling predictions overlaid on the experimental measurements as a function of the cold end pressure ratio.

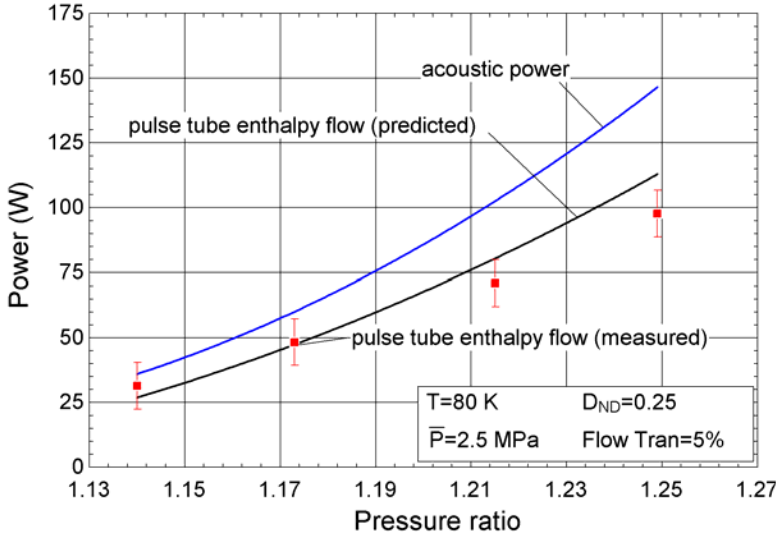

Figure 7.9: Plot showing the experimental measurements for the pulse tube enthalpy flow overlaid on the modeling predictions as a function of pressure ratio for a D_{ND}=0.25 and Tran Vol=5%.

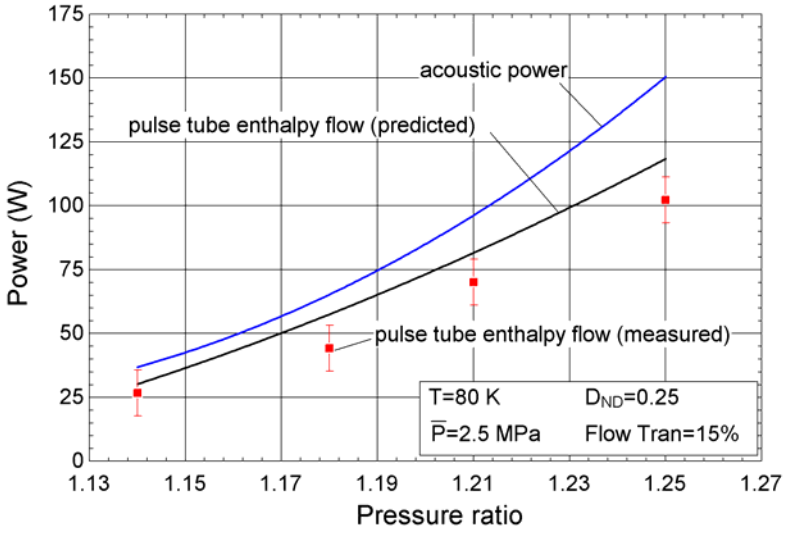

Figure 7.10: Plot showing the experimental measurements for the pulse tube enthalpy flow overlaid on the modeling predictions as a function of pressure ratio for a D_{ND}=0.25 and Tran Vol=15%.

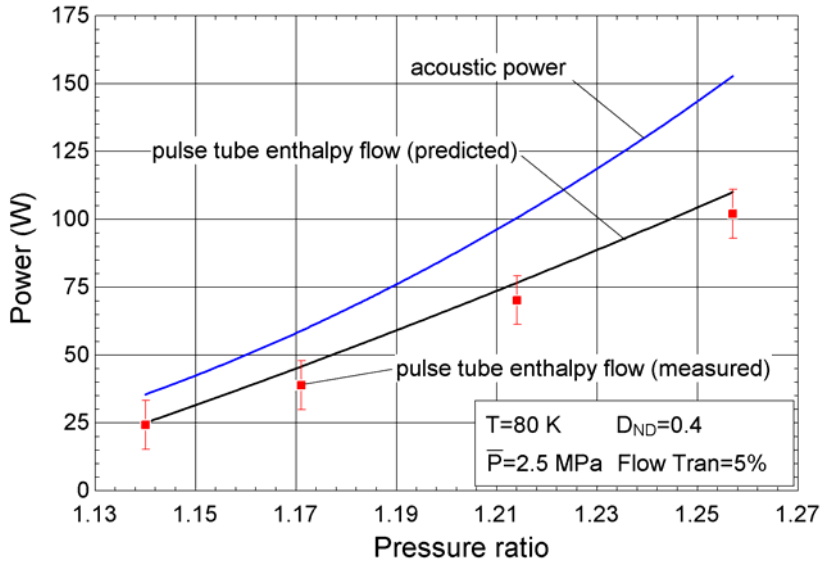

Figure 7.11: Plot showing the experimental measurements for the pulse tube enthalpy flow overlaid on the modeling predictions as a function of pressure ratio for a D_{ND}=0.4 and Tran Vol=5%.

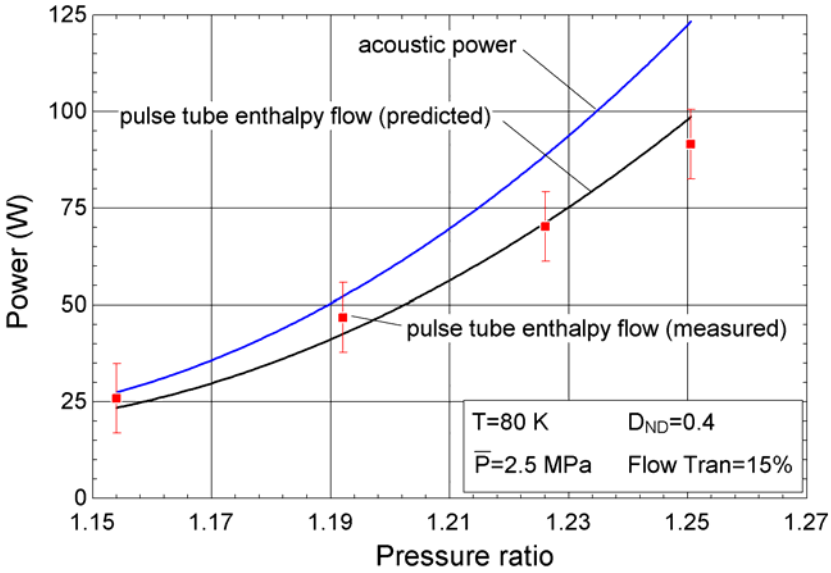

Figure 7.12: Plot showing the experimental measurements for the pulse tube enthalpy flow overlaid on the modeling predictions as a function of pressure ratio for a D_{ND}=0.4 and Tran Vol=15%.

Observing the results presented in Figures 7.9, 7.10, 7.11, and 7.12, there is excellent agreement between the experimental measurements and the corresponding predictions using the CFD model. Note that for all cases, the experimental acoustic power was essentially

identical to the predicted acoustic power (the quantities that dictate the acoustic power are used to setup the model input conditions) so only the experimental acoustic power is plotted. In all cases, the CFD model clearly predicts the correct enthalpy flow to within 15% of the measured value. For all data sets, the model seems to predict the correct value of the enthalpy flow (within experimental error) at low pressure ratios (1.1 to 1.2). There is some error at low pressure ratio that is attributed to the mass flow sensor resolution at low pressure ratios, as described for the regenerator loss measurements. At high pressure ratios, the model seems to be offset above the experimental predictions. This offset can be explained by the shuttle heat transfer loss which was not explicitly accounted for in the CFD model due to computational limits and the fact that this loss increases with pressure ratio.

One interesting conclusion from the experimental measurements and corresponding modeling predictions is that the dominant source of loss due to flow mal-distribution is at the warm end of the system. This was not an unexpected conclusion and further reinforces the results. The results indicate that the flow transition configuration of an open conical section at the warm end helps to radially equilibrate the flow before entering the pulse tube and the transition performance is independent of the volume, provided there is some finite volume such that the flow can expand sufficiently before entering the heat exchanger and pulse tube component. This is a highly useful result for the pulse tube designer as it identifies one optimum flow transition configuration for the flow ranges tested and validated herein.

Figure 7.13 illustrates the measured enthalpy flow as a function of the predicted enthalpy flow for all of the test data. Figure 7.13 includes error bands at 5% and 15%; note that all of the data is predicted to within 15%.

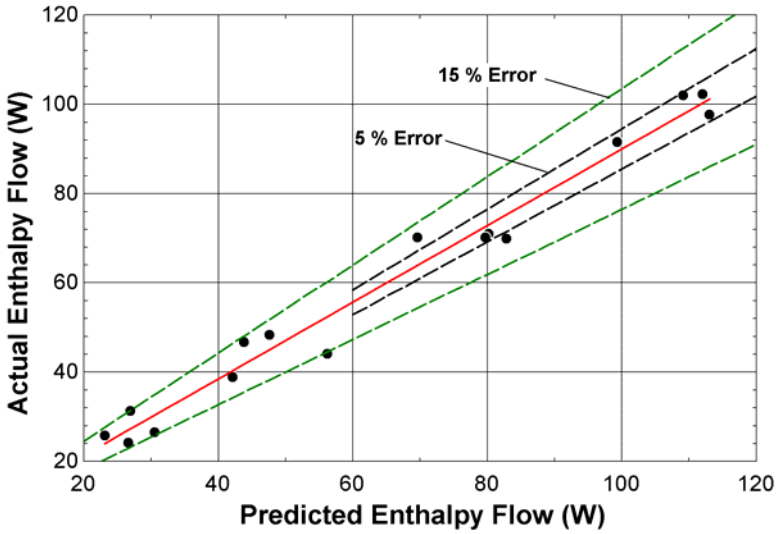

Figure 7.13: Plot showing the absolute error in the modeling prediction for the enthalpy flow. Error bands are illustrated at 5 and 15 percent.

From Figure 7.13, the error at lower pressure ratios (due to the difficult associated with measuring low mass flow rate) becomes more evident while the error is less at high pressure ratios. Figure 7.13 shows that the model is capable of capturing trends associated with changing the pulse tube aspect ratio and flow transitions. The model correctly predicts the trends that are observed experimentally and is capable of predicting the absolute value of the pulse tube enthalpy flow to within 5% at high pressure ratios and 15% over the entire range of operating conditions.

8. Model Extension for Simulations at 4K

One of the emerging areas of research related to PTC's is optimization for operation at 4K with sufficient cooling power for applications such as superconducting electronics (i.e., provides watts vs. milli-watts). Presently the only options that are available commercially for 4 K cooling are the GM cryocooler and the GM-type pulse tube cryocooler (both operate at a frequency of 1-2 Hz). To date, PTC's have not had substantial success achieving refrigeration at 4 K, except in specialized applications. The issues that have prevented 4 K PTC's are related to poor performance in the regenerator as well as the design of the pulse tube and flow transitioning components. This chapter presents the extension of the developed model discussed in Chapter 3 to allow for optimal design of the pulse tube and flow transitioning components. Initial modeling results are presented for a test case in order to demonstrate the ability of the model to simulate 4 K operation. Finally, a logical method for optimizing the pulse tube and flow transitioning components in a PTC for operation at 4 K is discussed.

8.1 CFD Model Extension for Operation at 4K

Several aspects of the numerical model and the post-processing routine that are discussed in Chapters 3 and 4 required modification in order to allow simulations at cold end temperatures near 4 K. These modifications are summarized in the following sections.

8.1.1 Solver Type and Algorithm

As discussed in Chapter 3, the choice of the segregated (pressure based) solver was a straightforward choice related to the size of the mach numbers present in the simulated models. More specifically, moderate temperature PTC's operate with a cold end temperature in the 50 to 100 K. In this temperature range, the typical Mach numbers encountered at the warm end of the pulse tube component rarely exceed values of 0.05-0.075. Under these conditions, the pressure based segregated solver is ideally suited, as it is designed for low Mach number flows. However, as the temperature of the helium gas approaches the critical point (5.5 K), the speed of sound decreases substantially while the density increases. Therefore, the local Mach number can reach values of 0.1-0.15. Initially it was believed that this could lead to numerical problems if the higher Mach number flow necessitates the use of a fully-coupled, density-based solver algorithm. Upon further investigation, it was found that while the increased Mach number approaches a range that in classical fluid mechanics would indicate strong coupling between pressure and density; for this application, the coupling is weak and temperature-driven. As a result, the pressure-based solution scheme was utilized. However, initial simulations using the standard conditions discussed in Chapter 3, showed divergence in the solution of the continuity equation. This indicated that the larger Mach numbers in this range of flows, while driven primarily by temperature effects, were posing problems for the standard segregated solver algorithm. To facilitate the convergence of the model, the pressure-velocity solution scheme utilized is a coupled pressure-velocity approach in which the continuity and momentum equations are solved simultaneously rather than iterating sequentially in order to arrive at the locally converged solution.

8.1.2 Material Properties

In the development of the CFD model discussed in Chapter 3, the ideal gas equation of state was utilized for computation of the density for the flow field while other thermophysical properties such as thermal conductivity and viscosity were specified according to piecewise polynomial fits to published data taken from the Engineering Equation Solver (EES, 2007). However, for simulations over the temperatures range of 4 to 40K, the material properties deviate substantially from the ideal gas approximation, as illustrated in Figure 8.1 in which the compressibility factor for helium at 2.5 MPa is plotted as function of the reduced temperature (i.e., the ratio of temperature to the critical temperature).

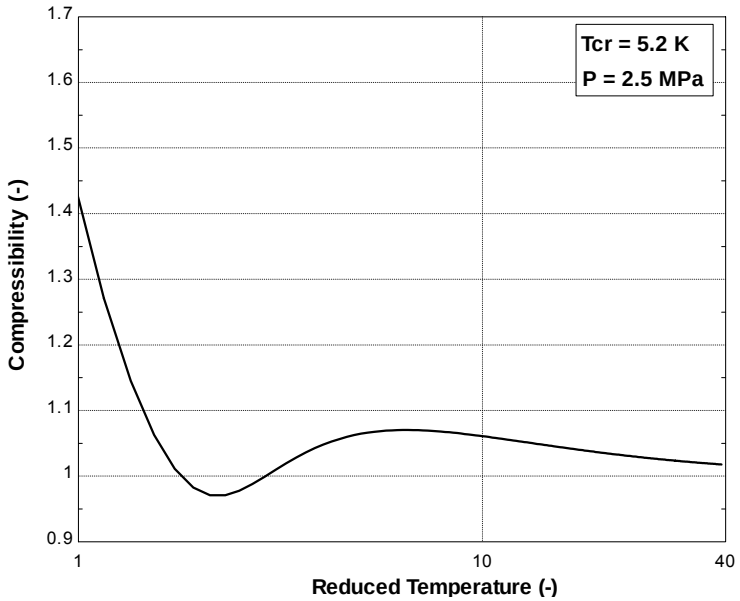

Figure 8.1: The compressibility factor of helium at 2.5 MPa as a function of reduced temperature; the deviation from unity illustrates the break-down of the ideal gas law over this temperature range.

It is necessary to utilize a more advanced equation of state that is capable of predicting the correct material properties over the temperature range of 4 to 40K. To facilitate the use of advanced equations of state with the FLUENT solver, the NIST REFPROP 8 real gas

property program was integrated with the FLUENT solver for low temperature simulations. By default, the use of real gas properties is not a normal option and this has only become available very recently in the latest software release (FLUENT 12 BETA, 2008); the use of real gas properties must be manually enabled by the user. The scope of this interface is that the FLUENT solver utilizes built-in subroutines that are compiled from source code and integrated with the solver in order to allow function calls to material property files available in REFPROP 8. Utilizing the real gas model allows all of the required thermophysical properties (density, thermal conductivity, enthalpy, and viscosity) required for the simulation to be determined via calls to this routine. The computational time increases substantially when these real gas subroutines are used.

8.1.3 Post-Processing

The use of an advanced equation of state required modification of the post-processing algorithm that was developed and discussed in Chapter 4. This modification was driven by the fact that it was no longer practical to export primitive variables and then post-process these quantities. The primary area of concern was related to the exported values for enthalpy with respect to the reference state being utilized. In practice this could be accounted for, but to do so would introduce some finite error in the trapezoidal integration of properties across a given cross sectional area. As a result, for all 4 K simulations, the quantities of interest to the user such as mass flow rates, enthalpy flow rates, temperatures, and pressures at any arbitrarily chosen cross-section of the model are the only quantities exported to the user. These quantities (exported at each time step) are then numerically integrated using a trapezoidal integration scheme in the MATLAB post-processing routine in order to compute

the energy balance for each cycle. Once this is accomplished, the quantities of interest are presented to the user in the same fashion described in Chapter 4.

8.2 4 K Model and Results

To illustrate the ability of the model to perform accurate simulations with cold end temperatures at 4 K, a simple test model was developed that is loosely based upon an anticipated design for a next generation PTC with a cooling power of approximately 4 watts at 4 K. This test model is simple in the fact that no wall-to-fluid heat transfer is accounted for and turbulent effects are neglected. While this does not account for all energy flows encountered in actual operation, it does illustrate the utility of the developed model. The parameters used for this test model are summarized in Table 8.1.

Table 8.1 – Nominal Model Parameters

Parameter	**Symbol**	**Nominal Value**
Diameter	D	0.4 in
Length	L	5.2 in
Aspect ratio	AR	16
Cold transition volume	V_c	10% of pulse tube
Warm transition volume	V_w	15% of pulse tube
Mean system pressure	$\overline{P}$	1 MPa
Pressure ratio (cold end)	PR	1.5
Frequency	f	30 Hz
Cold end temperature	T_c	4 K
Warm end temperature	T_h	20 K
Cold end acoustic power flow	PV_c	8.8 W
Cold end mass flow rate	$\dot{m}$	16 g/s
Cold end phase angle	θ	0 deg

This test simulation was run for 25 cycles, at which point the normalized global energy imbalance had reached ~3% and the model was deemed to have converged to a cyclic steady

state condition. The results of the model are presented qualitatively in Figure 8.2 as temperature contours at two times during the cycle and quantitatively in Table 8.2.

Table 8.2 – Model Results

Parameter	**Symbol**	**Nominal Value**
Enthalpy Flow	$\dot{H}$	7.7 W
Acoustic Power Flow	PV_c	8.8 W
Figure of Merit	FOM	0.88

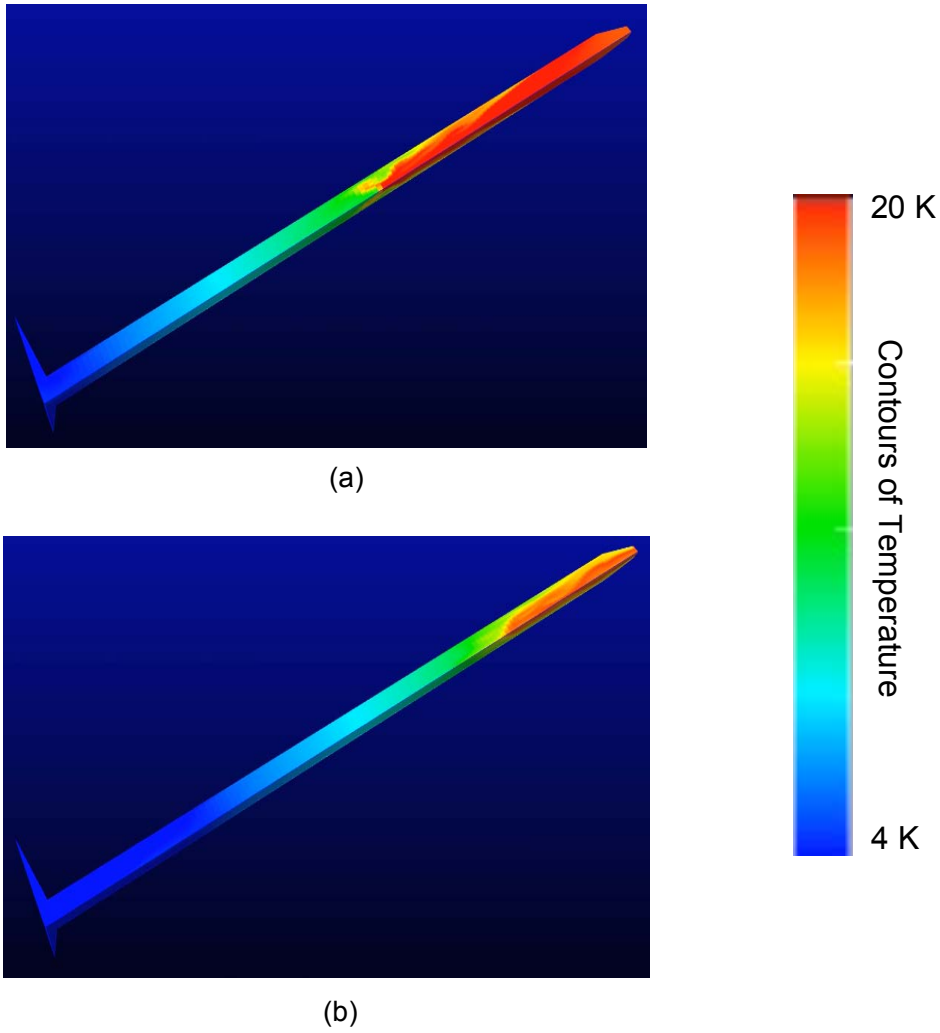

Figure 8.2: Plot illustrating the contours of temperature for the 4 K test case model at non-dimensional cycle times of (a) τ=0.25 and, (b) τ=0.75.

As the results shown in Figure 8.2 illustrate, the flow profiles predicted are consistent with and similar to those predicted by the higher temperature (ideal gas based) model. Qualitatively the flow profile can be considered accurate as certain effects which one would expect are clearly visible. For example, the flow entering the pulse tube component (shown in Figure 8.2(a)) is clearly perturbed due to jetting from the high velocity gas exiting the inertance tube, which is expected. Also, the flow at the cold end of the system shows negligible flow field disturbance which is expected for a pulse tube component with a large aspect ratio. The results in table 8.2 show that the gross cooling power available is 7.7 W (neglecting any associated regenerator losses). The acoustic power flow associated with the simulation conditions is 8.8 W which leads to a *FOM* for this pulse tube component of 0.88. Since turbulent effects and fluid to solid thermal interactions were not modeled, therefore it can be concluded that the loss in available cooling power is driven by the perturbed flow (mixing) at the warm end of the system.

8.3 Methodology for Optimizing Pulse-tube and Flow Transition Design for 4K

As discussed in Chapter 4, the developed CFD model can be used to perform parametric analyses of systems and or optimization based upon some defined design parameters. These types of analysis can be performed readily for pulse tubes operating at moderate temperatures where the ideal gas approximation is accurate and the simulations are not a large computational burden. However, in the case of 4 K simulations where the cold end temperature necessitates the use of real gas material properties, the computational burden associated with any single simulation increases substantially because of the real gas routines. For the test case presented in section 8.2, the solution required approximately 6 days

compared to less than 2 days for an equivalent ideal gas model. Clearly this is a significant increase in computational burden even without accounting for the additional time that would be required by the turbulence modeling and the interaction between the fluid and thermal solid material (wall). The addition of these parameters would likely increase the total computational time to at least 10 days for a single simulation. Without the use of dedicated computational resources such as a computational cluster, it is not practical to create a design chart that would encompass the entire logical operating range for 4 K PTC operation. This observation does not mean that it is not reasonable to use the model to optimally design the pulse tube and flow transitioning components in 4 K PTC's. However, the designer must be cognizant of these imitations and utilize the computational analysis in a directed manner for a given problem.

For a given 4K PTC design, it is proposed that the following steps be utilized in an effort to practically design the system while keeping computational requirements reasonable; these steps are illustrated in flowchart form in Figure 8.3.

1) Identify the operating envelope for the system that is required. This should include desired heat lift at temperature, the PTC configuration (co-axial, inline, or split). Use a basic zeroth order model of the pulse tube in order to estimate the relevant energy flows and phase angles.
2) Utilize the parameters identified in (1) to perform an iterative design of the regenerator using a 1-D transient simulation such as REGEN. This would involve maximizing the regenerator performance with a fixed set of parameters that are

dictated by the pressure wave generator, such as power input, acoustic power output, and impedance.

3) Utilize the parameters identified in (1) and (2) to design the inertance tube in order to give the desired phase relations in the system, as dictated by the phase angle present at the cold end of the regenerator.
4) Utilizing all the initial identified design constraints for the regenerator and inertance tube, develop a general PTC CFD model utilizing the known parameters such as cooling power, acoustic power flow, pressure ratio, etc. The numerical model will determine if the design is feasible and may suggest improvements/modifications to the pulse tube aspect ratio and flow transitions. Utilizing the results from this model, the inertance tube design can be modified, if necessary, in order to arrive at the correct phase relationships.
5) Utilize the finalized dimensions for the regenerator and inertance tube to perform a parametric analysis of the pulse tube and flow transitioning components. This includes variation of the volume and aspect ratio of the pulse tube component as well as design of the flow transiting components to include flow straightening material, location, and the volume as a function of the pulse tube volume.

Utilizing this design methodology for low temperature PTC's allows the designer to focus the largest computational task on a narrow band which will allow for the system performance to be maximized while minimizing computational burden.

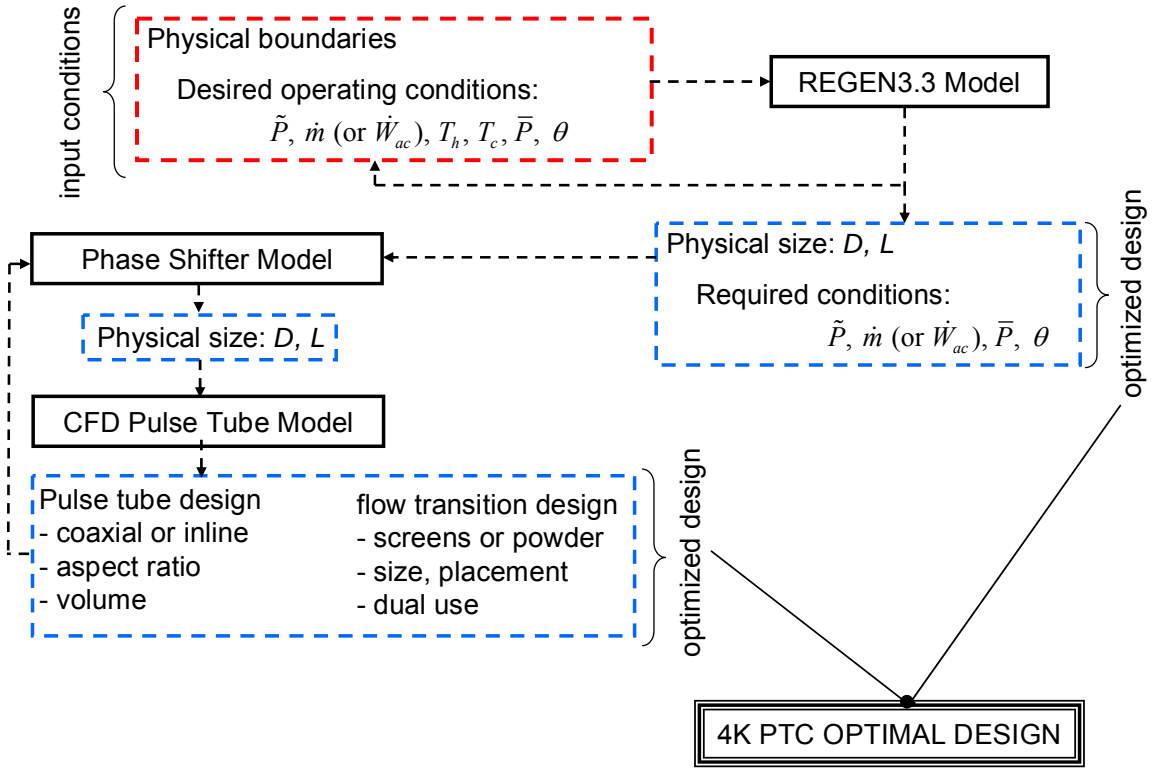

Figure 8.3: Plot illustrating the proposed methodology for optimally designing the pulse tube and flow transitioning components for a 4K PTC.

9. Conclusions

9.1 Research Conclusions

This dissertation has described the development of a two-dimensional (2-D) axisymmetric model of the pulse-tube and flow transitioning components in a PTC. The model is implemented in the commercial CFD solver package FLUENT. The notable advances associated with this model over others include:

1. use of a porous media model that employs empirical data to represent the inertial and viscous flow resistances in the axial and radial directions for packed wire mesh screens,
2. the simulation of turbulence that is present due to warm end high velocity gas flows,
3. the ability to model two working fluids, ^{4}He and ^{3}He, via the use of the ideal gas equation of state or by coupling the NIST REFPROP package to the CFD simulation Lemmon (2008), and
4. simulation times that range from 18 to 60 hours (i.e., days) compared to other models of the entire PTC that require simulation times on the order of weeks.

The inputs required for model simulation are the cold end mass flow rate, the phase angle between pressure and mass flow rate at the cold end of the pulse tube, and the mean pressure and pressure ratio at the cold end of the pulse tube. In addition to qualitative information about the characteristics of the flow and the presence of flow non-uniformities and recirculation, the outputs from the model are quantitative in nature. The quantities reported to the user include the pulse-tube energy flow, the acoustic power flow, and the figure of

merit for the pulse-tube component which characterizes its ability to convert acoustic power into useful cooling.

Post processing algorithms were developed in the mathematical programming language MATLAB. Two versions of the post-processing were developed: one for moderate temperature simulations (40-130 K) and one for low temperature simulations (4-40 K). Both of these codes read in the extensive set of CFD predictions that are exported at each time step during a given simulation and then perform the required computations to present the desired outputs to the user. The quantities that are output to the user are the enthalpy flow, acoustic power flow, phase angles, pressure ratios, and the figure of merit for the pulse tube component.

A state of the art test facility was designed and constructed in collaboration with the National Institute of Standards and Technology Cryogenic Technologies Group. This test facility was designed to allow for precise measurement of the regenerator loss (measured at the cold end during system operation) as well as measurement of the enthalpy flow and acoustic power flow at the cold of an operational pulse tube cryocooler. This set of measurements has not previously been carried out and the ability to separately resolve the regenerator loss and the pulse tube loss provides an unprecedented opportunity to verify these two, separate component models. A fundamental analysis of the experimental methodology and their associated measurement uncertainty was performed in order to guide the selection of the required instrumentation. The test facility was designed in a modular fashion in order to allow for flexibility with regard to experimental test set-ups while minimizing turn around

time between performance measurements. Experimental results from the test facility confirmed the fundamental analysis of the uncertainty and demonstrated our ability to resolve the quantities of interest for performance characterization of the regenerator and pulse tube components in a PTC.

The CFD model was verified in the limit of the known analytical solution of the Navier-Stokes equations for oscillating laminar flow in a long tube; this is a very limited verification as many of the more important aspects of pulse tube operation are not present in this situation. However, the analytical validation did demonstrate that the CFD model could capture the pertinent flow features associated with oscillatory gas flows (phase lag in the velocity at the wall compared to core flow due to viscous effects). The results of the analytical validation also showed that the model was capable of resolving the pertinent flow features for reasonable spatial and temporal discretization resolution.

The model was validated experimentally using the test facility at NIST by measuring for the pulse tube enthalpy flow and operating conditions for various pulse tube and flow transition configurations. The results were then compared to predictions generated by the CFD model using the experimental operating conditions to specify the mass flow rate, pressure ratio, and phase angle inputs to the CFD model. The agreement between the model and the experimental results was excellent, with an absolute error no larger than 15% for all cases and less than 5% for the cases with moderate to high pressure ratios

Finally, the model was extended to allow for simulations of pulse tube coolers that have cold end temperatures in the range of 4 K to 20 K. This process involved the integration of a real gas model for the working fluid in order to obtain the high accuracy thermophysical property data that is required for these simulations. An initial test case was simulated and the results indicated a proper flow profile and reasonable performance parameters.

The model developed in this dissertation has been shown to be useful as a design tool for the pulse tube and flow transitioning components in a PTC over a large range of temperatures. The model is capable of predicting the actual enthalpy flow of the pulse tube component with an error no larger than 15% for all of the experimental test cases. The model and the overall methodology are flexible and applicable to a wide range of pulse tube cooler applications and operating conditions. This work has illustrated that advanced computational analysis, when applied correctly to a specific component within a highly complex system such as a PTC, can be utilized in an efficient and useful manner in order to enhance the design and system level modeling required to deploy high efficiency PTCs.

9.2 Suggestions for Future Research

Due to the success of the work presented in this dissertation, there are many related research areas that could be explored. These areas range from relatively simple academic questions to more complex and practical issues related to design for specific applications in which a PTC must operate in stringent environments/envelopes. These areas are summarized briefly below.

Model Extension to Three Dimensions

One area of pulse tube cryocooler operation that should be investigated in detail is the effect of gravity on the flow profile in the pulse tube component and the resulting impact on system performance. In order to investigate the impact of gravity under off-axis configurations, it is necessary that the model be extended to three dimensions as the driving forces on the fluid are no longer axi-symmetric. One of the current areas of interest is off-axis performance and vibration effects for pulse tube coolers that will be utilized to cool superconducting A/D conversion electronics for next generation military communications deployed on mobile stations (e.g., in a Humvee). The model extension to three dimensions would allow for off-axis performance investigations and would be useful in identifying whether pulse tube coolers are well-suited to this type of application.

Investigation of the Shuttle Heat Transfer Effect/Loss

One of the more interesting aspects of pulse tube cryocooler hydrodynamics is the shuttle heat transfer effect. More specifically, the heat transfer interaction between the wall of the pulse tube and the oscillating working fluid. Many researchers have investigated this effect in the context of limiting analytical solutions or low order numerical models. The utility of the developed model allows for this analysis to be performed with much higher resolution and accuracy over a wide range of conditions. A specific area that should be investigated is the effect of shuttle heat transfer in 4 K pulse tube cryocoolers. At 4 K, the heat capacity of the wall is smaller than that of the working fluid which will likely increase the impact of the shuttle heat transfer effect.

Apply the Modeling Methodology to Other Pulse Tube Cryocooler Components

The success of this work relative to the development of a detailed component-level model of a specific component within a highly complex hydrodynamic/thermodynamic system suggests that the same approach could be used for other components. A logical extension of this research would be to apply the modeling methodology developed here to other components in a pulse tube cryocooler; for example, the regenerator, aftercooler, compressor, or inertance tube.

References

Baek, S. H., Jeong, E. S., and Jeong, S., "Two-dimensional model for tapered pulse tubes. Part 1: theoretical modeling and net enthalpy flow," *Cryogenics*, Vol. 40, pp. 379-385, (2000a).

Baek, S. H., Jeong, E. S., and Jeong, S., "Two-dimensional model for tapered pulse tubes. Part 2: mass streaming and streaming-driven enthalpy flow loss," *Cryogenics*, Vol. 40, pp. 387-392, (2000b).

Brereton, G.J., Mankbadi, R.R., "Review of recent advances in the study of unsteady turbulent internal flows," *Appl. Mech. Rev.,* Vol. 48, Num. 4, pp 189-212, 1995.

CEI, "Ensight 8.2 - Users Manual," Computational Engineering International., Apex, North Carolina, 2006.

Cha, J., "CFD Simulation of Multi-Dimensional Effects in Inertance Tube Pulse Tube Cryocoolers," *Masters Thesis – GA Tech*, 2004.

Cha, J.S., Ghiaasiaan, S.M., Desai, P.V., Harvey, J.P., and Kirkconnell, C.S., "CFD Simulation of Multi-Dimensional Effects in an Inertance Tube Pulse Tube Refrigerator," *Proc. 13th Cryocooler Conf.*, R. G. Ross, Jr., ed., Springer Science, New York, NY, pp. 285-292, (2005).

Cha, J.S., "Hydrodynamic parameters of microporous media for steady and oscillatory flow: application to cryocooler regenerators," PhD Thesis – Georgia Institute of Technology, Atlanta, Georgia, (2007).

David, M., Maréchal, J.C., and Encrenaz, P., "Measurements of Instantaneous Gas Velocity and Temperature in a Pulse Tube Refrigerator," *Adv. Cryogenic Eng.*, Vol. 37, pp. 939-946, (1992).

de Boer, P. C. T. "Analysis of basic pulse-tube refrigerator," *Cryogenics*, Vol. 35, pp. 547-553, (1995).

EES, "Engineering Equation Solver," F-Chart Software., Madison, Wisconsin, 2007.

Flake B. and Razani, A., "Modeling Pulse Tube Cryocoolers with CFD," *Adv. Cryogenic Eng.*, Vol. 49, pp. 1493-1499, (2004).

Fluent, "FLUENT 6.2 Users Manual," Fluent Inc., New Haven, Connecticut, January 2005.

Fluent12, "FLUENT 12.3 BETA Users Manual," Fluent Inc., New Haven, Connecticut, January 2008.

Garaway, I., Taylor, R., Lewis, M., Bradley, P., and Radebaugh, R.,, "Infrared Imaging as a Means of Characterizing Flow and Temperature Instabilities within Pulse Tube Cryocoolers," *Proc. 15th International Cryocooler Conference*, Vol. 15, in press, (2008).

Gary, J., Daney, D., and Radebaugh, R., "Computational Model for a Regenerator," *Proc. 3rd Cryocooler Conf.*, (1985).

Gary, J., O'Gallagher, A., Radebaugh, R., and Marquardt, E., *REGEN3.2 User Manual*, NIST, (2001).

Gedeon, D., "Sage: Object-oriented software for cryocooler design," *Proc. 8th Int. Cryocooler Conf.,* Plenum Press, New York, NY, pp. 281-292 (1995).

Grace, S., "Oscillatory motion of a viscous liquid in a long straight tube ", *London, Edinburgh, Dublin Philosophical Magazine and Journal of Science*, Vol. 5, Num. 31, pp 933-939, 1928.

Hagiwara, Y., Nara, K., Ito, S., and Saito, T., "Temperature Measurement in Pulse Tube with Rayleigh Scattering and Computation of Enthalpy Flow," *Cryogenics*, Vol. 39, No. 5, pp. 425-434, (1999).

Hozumi, Y., Murakami, M., and Iida, T., "Numerical Study of Pulse Tube Flow," *Proc. 10th Int. Cryocoolers Conf.*, R. G. Ross, Jr., ed., Kluwer Academic/Plenum Publishers, New York, NY, pp. 321-328, (1999).

Hozumi, Y., Murakami, M., and Shiraishi, M., "Numerical Study of Gas Dynamics Inside of a Pulse Tube Refrigerator," *Proc. 11th Int. Cryocooler Conf.*, R. G. Ross, Jr., ed., Kluwer Academic, Plenum Publishers, New York, NY, pp. 363-369, (2001).

Huang B.J. and Chuang, M.D., "System Design of Orifice Pulse-Tube Refrigerator using Linear Flow Network Analysis," *Cryogenics*, Vol. 36, pp. 889-902, (1996).

Ibrahim, M.B., Zhang, Z., Kembhavi, S., Simon, T.W., and Gedeon, D., "A 2-D Axisymmetric CFD Model of Oscillatory Flow with Separation," *37th Intersociety Energy Conversion Engineering Conf.-IEEE.*, pp. 549-555, (2002).

Jeong, E.S. and Smith Jr., J.L., "Secondary flow in reciprocating machinery," *Proc. ASME National Heat Transfer Conf.*, Vol. 24, pp. 97-104, (1992).

Jeong, S., Nam, K., Kim, M. G., Chang, H.-M., and Jeong, E. S., "Experimental Study of the Heat Transfer in Pulse Tubes," *Proc. 11th Int. Cryocoolers Conf.*, R. G. Ross, Jr., ed., Kluwer Academic/Plenum Publishers, New York, NY, pp. 345-351, (2001).

Kittel, P., Kashani, A., Lee, J. M., and Roach, P.R., "General pulse tube theory," *Cryogenics*, Vol. 36, pp. 849-857, (1996).

Koshimizu, T., Kubota, H., Takata, Y., and Ito, T., "Numercial simulation of heat and fluid flow in basic pulse tube refrigerator," *International Journal of Numerical Methods for Heat and Fluid Flow.*, Vol. 15, No. 7, pp. 617-630, (2005).

Kuriyama, F., and Radebaugh, R., "Analysis of mass and energy flow rates in an orifice pulse-tube refrigerator,"*Cryogenics*, Vol. 39, pp. 85-92, (1999).

Kuehl, H-D., and Shultz, S., "A 2nd Order Regenerator Model Including Flow Dispersion and Bypass Losses," *IEEE*, pp. 1343-1348, (1996).

Lakeshore, "Temperature Measurement and Control Catalog", Lakeshore Cryotronics, OH, pp. 58-60, 110-113, and 153-215, (2004).

Lee, J. M., Kittel, P., Timmerhaus, K.D., and Radebaugh,R., "Flow patterns intrinsic to the pulse tube refrigerator," *Proc. 7th Int. Cryocooler Conf.*, pp. 125-139, (1993).

Lee, J.M., Kittel, P., Timmerhaus, K.D., and Radebaugh, R., "Higher Order Pulse Tube Modeling," *Proc. 9th Int. Cryocooler Conf.,* R. G. Ross, Jr., ed., Plenum Press, New York, NY, pp. 345-353, (1997).

Lewis, M.A., and Radebaugh, R., "Measurement of Heat Conduction through Bonded Regenerator Matrix Materials," *Cryocoolers 12*, pp 517-522, 2003.

Lewis, M., Taylor, R., Bradley, P., Radebaugh, R, and Garaway, I., "Pulse-tube Cryocooler for Rapid Cooldown of a Superconducting Magnet," *Proc. 15th International Cryocooler Conference*, Vol. 15, in press, (2008).

Liang, J., Ravex, A., and Rolland, P., "Study on pulse tube refrigeration, Part 1: Thermodynamic nonsymmetry effect," *Cryogenics,* Vol. 36, pp. 87-93, (1996a).

Liang, J., Ravex, A., and Rolland, P., "Study on pulse tube refrigeration, Part 2: Theoretical modeling," *Cryogenics*, Vol. 36, pp. 95-99, (1996b).

Liang, W., and de Waele, A.T.A.M., "A new type of streaming," *Cryogenics*, Vol. 47, pp. 468-473, (2007).

Lyulina, I., "Numerical Simulation of Pulse tube Refrigerators," *Eindhoven, The Netherlands*, pp 92, (2004).

Mikulin, E.I. Tarasov, A.A., and Shrebyonock, M.P., "Low-temperature expansion pulse tube," *Adv. Cryogenic Eng.*, Vol. 29, R.W. Fast, ed., Plenum Press, New York, NY, pp. 629-637, (1984).

Miyabe, H., Takahashi, S., Hamaguchi, K., "An Approach To The Design Of Stirling Engine Regenerator Matrix Using Packs Of Wire Gauzes," *Proceedings of the 17th Intersociety Energy Conversion Engineering Conference,* pp 1839-1844, 1982.

Nakamura, N., Shiraishi, M., Seo, K., and Murakami, M., "Visualization Study of Oscillating Flow Inside a Pulse Tube Refrigerator," *Adv. Cryogenic Eng.*, Vol. 43, pp. 2023-2030, (1998).

Nara, K., Hagiwara, Y., and Ito, S., "Measurements of Gas Temperature in a Pulse Tube Using the Planar Laser Raleigh Scattering Method," *Proc. 10th Int. Cryocooler Conf.*, R. G. Ross, Jr., ed., Kluwer Academic/Plenum Publishers, New York, NY, pp. 395-404, (1999).

Olson, J.R. and Swift, G.W., "Acoustic Streaming in Pulse Tube Refrigerators: Tapered Pulse Tubes," *Cryogenics*, Vol. 37, pp. 769-776, (1997).

Olson, J.R. and Swift, G.W., "Suppression of Acoustic Streaming in Tapered Pulse Tubes," *Proc.10th Int. Cryocoolers Conf.*, R. G. Ross, Jr., ed., Kluwer Academic/Plenum Publishers, New York, NY, pp. 307-314, (1999).

Panton, R.L., "Incompressible Flow 3rd Edition," Wiley, New York, (2005).

Pfotenhauer, J.M, Bradley, P.E., Lewis, M.A, and Radebaugh, R., "Regenerator loss measurements at low temperatures and high frequencies" *Proc. 12th Int. Cryocooler Conf.*, R. G. Ross, Jr., ed., Kluwer Academic/Plenum Publishers, New York, NY, pp. 523-530, (2002).

Potratz, S. A., "Design and Test of a 300 W, 65 K Pulse Tube," *Masters Thesis – University of Wisconsin-Madison,* (2005).

PRT, Calibration Report, Serial Number – P14089., Lakeshore Cryotronics, OH, pp 1-12, (2007).

Radebaugh, R., Bradley, P., and Huang, Y., "Regenerators and He3" *Office of Naval Research Superconductive Electronics Program Review,* Panama City, FL, January 29-31, (2007).

Rawlins, W., Radebaugh, R., and Timmerhaus, K.D., "Thermal Anemometer for Mass Flow Measurement in Oscillating Cryogenic Gas Flows," *Rev. Sci. Instrum.*, Vol. 64, No. 11, pp. 3229-3235, (1993a).

Rawlins, W., Radebaugh, R., Brandly, P.E., and Timmerhaus, K.D., "Energy Flow in an Orifice Pulse Tube Refrigerator," *Adv. Cryogenic Eng.*, Vol. 39, pp. 1449-1456, (1993b).

Richardson, R.N., "Pulse tube refrigerator – An Alternative Cryocooler," *Cryogenics*, Vol. 26, No. 6, pp. 331-340, (1986).

Rott, N., "The Influence of Heat Conduction on Acoustic Streaming," *J. App. Math and Phys.*, Vol. 25, No. 3, pp. 417-421, (1974).

Rutland, C., Personal Communication – Discussion of Turbulence Modeling, January 16, (2007).

Schlichting, H., Gersten, K., "Boundary layer Theory," 8th Edition, Springer, Berlin, pp 131-141, (2003).

Seo, K., Shiraishi, M., Nakamura, N., and Murakami, M., "Investigation of Radial Temperature and Velocity Profiles in Oscillating Flows Inside a Pulse Tube Refrigerator,"*Proc.9th Int. Cryocoolers Conf.*, R. G. Ross, Jr., ed., Plenum Press, New York, NY, pp. 365-374, (1997).

Shiraishi, M., Nakamura, N., and Murakami, M., "Visualization Study of Velocity Profiles and Displacements of Working Gas Inside a Pulse Tube Refrigerator," *Proc. 9th Int. Cryocoolers Conf.,* R. G. Ross, Jr., ed., Plenum Press, New York, NY, pp. 355-364, (1997).

Shiraishi, M., Takamatsu, K., Murakami, M., Nakano, A., Iida, T., and Hozumi, Y., "Visualization of DC Gas Flows in a Double-Inlet Pulse Tube Refrigerator with a Second Orifice Valve," *Proc. 11th Int. Cryocoolers Conf.*, R. G. Ross, Jr., ed., Kluwer Academic/Plenum Publishers, New York, NY, pp. 371-379, (2001).

Shiraishi, M., Takamatsu, K., Murakami, M., and Nakano, A., "Dependence of convective secondary flow on inclination angle in an inclined pulse tube refrigerator revealed by visualization," *Cryogenics*, Vol. 44, pp. 101-107, (2004).

Silva, W.P. and Silva, Cleide M.D., "LAB Fit Curve Fitting Software (Nonlinear Regression and Treatment of Data Program) V 7.2.37", online - www.labfit.net, (2007).

Smith, W.R., "One-dimensional models for heat and mass transfer in pulse-tube refrigerators," *Cryogenics*, Vol. 41, pp. 573-582, (2001).

Storch P.J. and Radebaugh, R., "Development and Experimental Test of an Analytical Model of the Orifice Pulse Tube Refrigerator," *Adv. Cryogenic Eng.*, Vol. 33, pp. 851-859, (1988).

Tian, J., Kim, T., Lu, T.J., Hodson, H.P., Queheillalt, D.T., Sypeck, D.J., Wadley, H.N.G., "The effects of topology upon fluid-flow and heat-transfer within cellular copper sturctures," *International Journal of Heat and Mass Transfer,* Vol. 47, pp 3171-3186, 2004.

TSI, Personal Communication – Discussion of application of PIV and PLIF measurements to oscillatory cryogenic gas flows, (2008).

Uchida, S., "The Pulsating Viscous Flow Superposed on the Steady Laminar Motion of Incompressible Fluid in a Circular Pipe", *Zeitschrift für angewandte Mathematik und Physik*, Vol. 7, Num. 5, pp 403-422, 1956.

Wang, C., Wu, P., and Chen, Z., "Numerical modeling of an orifice pulse tube refrigerator," *Cryogenics*, Vol. 32, No. 9, pp. 785-790, (1992).

Wang, C., "Numerical Analysis of 4 K Pulse Tube Coolers: Part I. Numerical Simulation," *Cryogenics*, Vol. 37, pp. 207-213, (1997).

Ward B. and Swift, G., "*Design Environment for Low-Amplitude ThermoAcoustic Engines: DELTAE"*, Version 4.0, Los Alamos National Laboratory, (1996).

Wheatley, J., Hofler, T., Swift, G.W., and Migliori, A., "Understanding some simple phenomena in thermoacoustics with applications to heat engines," *Am. J. Physics*, Vol. 53, No. 2, pp. 147-162, (1985).

Willems D. W. J. and Dam, J. A. M., "Three-Dimensional Pulse Tube Simulations," *Adv. Cryogenic Eng.*, Vol. 47, pp. 934-941, (2002).

Yuan S.W.K. and Radebaugh, R., "A Blind Test on the Pulse Tube Refrigerator Model (PTRM)," *Cryogenics*, Vol. 41, p. 1383, (1996).

Yuan, S. W. K., "Validation of the Pulse Tube Refrigerator Model against a Lockheed pulse tube cooler," *Cryogenics*, Vol. 36, pp. 871-877, (1996).

Zhu S.W., and Chen, Z.Q., "Isothermal model of pulse tube refrigerator," *Cryogenics*, Vol. 34, No. 7, pp. 591-595, (1994).

Zhu S. and Matsubara, Y., "Numerical method of inertance tube pulse tube refrigerator," *Cryogenics*, Vol. 44, pp. 649-660, (2004).

Appendix A – Boundary Condition Code

Boundary Condition File Utilized for Simulations

```
#include "udf.h"
DEFINE_PROFILE(unsteady_pressure, thread, position)
{
face_t f;
real t = CURRENT_TIME;
begin_f_loop(f, thread)
 {
   F_PROFILE(f, thread, position)= 240967*sin(2*M_PI*60*t);
 }
end_f_loop(f, thread)
}

DEFINE_PROFILE(unsteady_massflow, thread, position)
{
face_t f;
real t = CURRENT_TIME;
begin_f_loop(f, thread)
 {
   F_PROFILE(f, thread, position)=( 0.013118*sin(2*M_PI*60*t +
                                    0.128))/( M_PI*0.000958*0.000958);
 }
end_f_loop(f, thread)
}
```

Appendix B – Post-Processing Codes

Post-Processing Code for Moderate Temperatures

```
%=========================================================================
% Code to Read in Fluent Data and Perform Energy Balance on the Pulse-tube
%=========================================================================
clear all;
%=========================================================================
%Model inputs for dimensional parameters
%=========================================================================
t_wall = 0.001;
R_inlet = 0.016637 ;%input('Enter the inlet radius\n');
R_outlet = 0.00287 ;%input('Enter the outlet radius\n');

%Pulse-tube Diameters
D_inlet = 2*R_inlet;
D_outlet = 2*R_outlet;
A_inlet = (pi*(D_inlet^2))/4;
A_outlet = (pi*(D_outlet^2))/4;
%=========================================================================
%Model inputs specified by user for material props
%=========================================================================
Cp = 5193;                  %specific heat at constant pressure
R_gas = 2077.14985;         %helium gas constant
%=========================================================================
%Model inputs for pulse-tube operating conditions
%=========================================================================
P_mean = 2500000 ;                  %input('Enter the mean pressure in Pa\n')
Freq = 60 ;                         %input('Input frequency in Hz\n')
T_ref = 298.15;                      %input('Input the reference temperature in K\n')
porosity_c=1;                       %input('Enter the inlet porosity\n');
porosity_h=1;                       %input('Enter the outlet porosity\n');
filenumberstart=input('Enter the min filenumber\n');
filenumberend=input('Enter the max filenumber\n');
%=========================================================================
%Model inputs based upon transient fluent simulation
%=========================================================================
deltat = 4.1666667e-5;
n =input('Enter the number of cycles to be evaluated\n');
tau = 1/Freq;                       %total cycle time in seconds
%=========================================================================
%User inputs filenames for analysis
%=========================================================================
cold = sprintf('coldend');
hot = sprintf('hotend');
avg = sprintf('avg_new.dat');
fidavg = fopen(avg, 'w');
cyc = sprintf('cyc_new.dat');
fidcyclic = fopen(cyc, 'w');
```

```
%=========================================================================
%Routine for reading in data which was exported from Fluent - all
%velocites, temperatures, density, ect for all surfaces selected
%=========================================================================
for i=filenumberstart:filenumberend

   if  i>=1000;
      filename1=sprintf('%s%i',cold, i);
      filename3=sprintf('%s%i',hot, i);
   else
      if i>=100;
         filename1=sprintf('%s0%i',cold, i);
         filename3=sprintf('%s0%i',hot, i);
         elseif i>=10;
            filename1=sprintf('%s00%i',cold, i);
            filename3=sprintf('%s00%i',hot, i);
            else
               filename1=sprintf('%s000%i',cold, i);
               filename3=sprintf('%s000%i',hot, i);
      end
   end
%=========================================================================
%Routine for computing the enthalpy flow, gas conduction, and wall
%conduction effects in the pulse-tube model using the exported data from
%Fluent at each timestep.  The data is written to user specified file which
%is read back in the follwing section so that the cyclic energy flows can
%be computed for the pulse-tube.
%=========================================================================
         Data_c = dlmread(filename1, '', 1, 0);                  %reads in the cold end data
         radial_c =  Data_c(:,3);                                %radial location data
         rho_c = Data_c(:,4);                                    % density
         ux_c = Data_c(:,5)*porosity_c;                          %average axial V
         ur_c = Data_c(:,6)*porosity_c;                          %average radial V
         P_static_c = Data_c(:,8);                               %static pressure
         T_static_c =  Data_c(:,9);                              %static temperature
         T_total_c =  Data_c(:,7);                               %total temperature
         P_avg_c = (trapz(radial_c, 2.*pi.*radial_c.*P_static_c))/(A_inlet);
         T_total_avg_c = (trapz(radial_c, 2.*pi.*radial_c.*T_total_c))/(A_inlet);
         DTDX_c = Data_c(:,10);                                   %temperature derivative in x-direction
         H_cold = trapz(radial_c, 2*pi.*radial_c.*rho_c.*ux_c.*Cp.*(T_total_c -298.15 ));
         h_cold = trapz(radial_c, 2*pi.*radial_c.*Cp.*(T_total_c -298.15 ));
         m_dot_cold = trapz(radial_c, 2*pi.*radial_c.*rho_c.*ux_c);
         q_gas_cold = -trapz(radial_c, 2*pi.*radial_c.*k_he(T_total_c).*DTDX_c); %
         V_dot_c=trapz(radial_c, 2*pi.*radial_c.*ux_c);
         Power_acoustic_cold = P_avg_c*V_dot_c;

         time = i*deltat ;                                        %sets the time which

         BB = dlmread(filename3, '', 1, 0);                      %reads in the hot end data
         Data_h = flipud(BB);
         radial_h = Data_h(:,3);                                 %radial location data
         rho_h = Data_h(:,4);                                    % density
         ux_h = Data_h(:,5)*porosity_h;                          %average axial V
         ur_h = Data_h(:,6)*porosity_h;                          %average radial V
```

```
        P_static_h = Data_h(:,8);                                   %static pressure
        T_static_h = Data_h(:,9);                                   %static temperature
        T_total_h = Data_h(:,7);                                    %total temperature
        P_avg_h = (trapz(radial_h, 2.*pi.*radial_h.*P_static_h))/(A_outlet);
        T_total_avg_h = (trapz(radial_h, 2.*pi.*radial_h.*T_total_h))/(A_outlet);
        DTDX_h = Data_h(:,10);                                      %temperature derivative in x-direction
        H_hot = trapz(radial_h, 2*pi.*radial_h.*(rho_h.*ux_h.*Cp.*(T_total_h-298.15)
        h_hot = trapz(radial_h, 2*pi.*radial_h.*Cp.*(T_total_h-298.15));
        m_dot_hot = trapz(radial_h, 2*pi.*radial_h.*rho_h.*ux_h);
        q_gas_hot = -trapz(radial_h, 2*pi.*radial_h.*k_he(T_total_h).*DTDX_h);
        V_dot_h=trapz(radial_h, 2*pi.*radial_h.*ux_h);
        Power_acoustic_hot = P_avg_h*V_dot_h;

        fprintf(fidavg,'%f\t    ', time);                           %prints the time to fidwrite
        fprintf(fidavg,'%f\t    ', H_cold);                         %prints the average enthalpy to fidwrite
        fprintf(fidavg,'%f\t    ', q_gas_cold);                     %prints the average enthalpy to fidwrite
        fprintf(fidavg,'%f\t    ', H_hot);                          %prints the average enthalpy to fidwrite
        fprintf(fidavg,'%f\t    ', q_gas_hot);                      %prints the average enthalpy to fidwrite
        fprintf(fidavg,'%f\t    ', Power_acoustic_cold);            %prints the average enthalpy
        fprintf(fidavg,'%f\t    ', Power_acoustic_hot);             %prints the average enthalpy
        fprintf(fidavg,'%f\t    ', T_total_avg_c);                  %prints the average enthalpy to fidwrite
        fprintf(fidavg,'%f\t    ', T_total_avg_h);                  %prints the average enthalpy to fidwrite
        fprintf(fidavg,'%f\t    ', m_dot_cold);                     %prints the average enthalpy to fidwrite
        fprintf(fidavg,'%f\t    ', m_dot_hot);                      %prints the average enthalpy to fidwrite
        fprintf(fidavg,'%f\t    ', h_cold);                         %prints the average enthalpy to fidwrite
        fprintf(fidavg,'%f\t    ', h_hot);                          %prints the average enthalpy to fidwrite
        fprintf(fidavg,'%f\t    ', P_avg_c);                        %prints the average enthalpy to fidwrite
        fprintf(fidavg,'%f\r    ', P_avg_h);                        %prints the average enthalpy to fidwrite
        i=i+1;                                                      %index advance
end
fclose(fidavg);                                                     %closes fidwrite
%=========================================================================
%Routine for performing the pulse-tube energy balance.  This reads in the file which was written
%previously which contains the energy terms at each temporal step.  This routine the performs a
%cyclic integral to compute the cyclic energy flows with emphasis on delineating the various loss
%mechanisms.
%=========================================================================
fid = fopen(avg, 'r');                                              %opens write - user input filename from above
filename5 = sprintf('%s',avg);
B = dlmread(filename5, '') ;                                        %puts data in fidwrite into matric form
increment = round((1/Freq)/(deltat));                               %increment which defines the integral bounds in
                                                                    matrix b

for k=1: n;
   time=k*deltat*increment;                                         %sets the time which is printed to fidcyclic
   Enthalpy_cold=Freq*trapz(B(1+(increment*(k-1)):(increment*k),1),B(1+(increment*(k-)):(increment*k),2));
   Enthalpy_hot=Freq*trapz(B(1+(increment*(k-1)):(increment*k),1),B(1+(increment*(k-1)):(increment*k),4));
   Power_acoustic_cyc_c=Freq*trapz(B(1+(increment*(k-1)):(increment*k),1),B(1+(increment*(k-)):
(increment*k),6));
   Power_acoustic_cyc_h=Freq*trapz(B(1+(increment*(k-1)):(increment*k),1),B(1+(increment*(k-
)):(increment*k),7));
   q_cold = Freq*trapz( B(1+(increment*(k-1)):(increment*k),1), B(1+(increment*(k-1)):(increment*k),3));
   q_hot = Freq*trapz( B(1+(increment*(k-1)):(increment*k),1), B(1+(increment*(k-1)):(increment*k),5));
   T_c_avg = Freq*trapz( B(1+(increment*(k-1)):(increment*k),1), B(1+(increment*(k-1)):(increment*k),8));
```

```
   T_h_avg = Freq*trapz( B(1+(increment*(k-1)):(increment*k),1), B(1+(increment*(k-1)):(increment*k),9));
   m_c_avg = Freq*trapz( B(1+(increment*(k-1)):(increment*k),1), B(1+(increment*(k-1)):(increment*k),10));
   m_h_avg = Freq*trapz( B(1+(increment*(k-1)):(increment*k),1), B(1+(increment*(k-1)):(increment*k),11));
   h_c_avg = Freq*trapz( B(1+(increment*(k-1)):(increment*k),1), B(1+(increment*(k-1)):(increment*k),12));
   h_h_avg = Freq*trapz( B(1+(increment*(k-1)):(increment*k),1), B(1+(increment*(k-1)):(increment*k),13));

   E_cold = Enthalpy_cold + q_cold;
   E_hot = Enthalpy_hot + q_hot;

   fprintf(fidcyclic,'%f\t    ', time);                          %prints the time to fidcyclic
   fprintf(fidcyclic,'%f\t    ', Enthalpy_cold);                 %prints the cyclic cold enthalpy flow
   fprintf(fidcyclic,'%f\t    ', Enthalpy_hot);                  %prints the cyclic hot enthalpy flow to fidcyclic
   fprintf(fidcyclic,'%f\t    ', Power_acoustic_cyc_c);          %prints the total cyclic heat transfer
   fprintf(fidcyclic,'%f\t    ', Power_acoustic_cyc_h);          %prints the total cyclic heat transfer
   fprintf(fidcyclic,'%f\t    ', E_cold);                        %prints the total cyclic heat transfer
   fprintf(fidcyclic,'%f\t    ', E_hot);                         %prints the total cyclic heat transfer
   fprintf(fidcyclic,'%f\t    ', T_c_avg);                       %prints the total cyclic heat transfer
   fprintf(fidcyclic,'%f\t    ', T_h_avg);                       %prints the total cyclic heat transfer
   fprintf(fidcyclic,'%12.9f\t    ', m_c_avg);                    %prints the total cyclic heat transfer
   fprintf(fidcyclic,'%12.9f\r', m_h_avg);                       %prints the total cyclic heat transfer
end
fclose('all');
%=========================================================================
% Code to Read in Fluent Data and Perform Energy Balance on the Pulse-tube
%=========================================================================
fid = fopen(avg, 'r');                                         %opens write - user input filename from above
filename5 = sprintf('%s',avg);
write = sprintf('phase.dat');
fidwrite = fopen(write, 'w');
C = dlmread(filename5, '') ;                                   %puts data in fidwrite into matric form

start= (increment*(n-1))+1  ;                                  %input('Enter the begin line\n');
ending=increment*n;                                            %input('Enter the end line\n');
time = C(start:ending,1);

coldmass = C(start:ending,10);
coldpressure = C(start:ending,14);
coldend = [time, coldmass, coldpressure] ;
hotmass = C(start:ending,11);
hotpressure = C(start:ending,15);
hotend = [time, hotmass, hotpressure]     ;

for i=2:(increment-1)
   if coldmass(i)>=coldmass(i-1) && coldmass(i)>coldmass(i+1);
       coldmass_max=i;
   end
end
for i=2:(increment-1)
   if coldpressure(i)>coldpressure(i-1) && coldpressure(i)>coldpressure(i+1);
      coldpressure_max=i;
   end
end
for i=2:(increment-1)
   if hotpressure(i)>hotpressure(i-1) && hotpressure(i)>hotpressure(i+1);
```

```
      hotpressure_max=i;
   end
end
for j=2:(increment-1)
   if coldpressure(j)<coldpressure(j-1) && coldpressure(j)<coldpressure(j+1);
      coldpressure_min=j;
   end
end
for j=2:(increment-1)
   if hotpressure(j)<hotpressure(j-1) && hotpressure(j)<hotpressure(j+1);
      hotpressure_min=j;
   end
end
for j=2:(increment-1)
   if hotmass(j)>=hotmass(j-1) && hotmass(j)>=hotmass(j+1);
      hotmass_max=j;
   end
end

t_coldmass_max = time(coldmass_max);
t_coldpressure_max = time(coldpressure_max);
P_maxc=coldpressure(coldpressure_max);
P_minc=coldpressure(coldpressure_min);
t_hotmass_max=time(hotmass_max);
t_hotpressure_max=time(hotpressure_max);
P_maxh=hotpressure(hotpressure_max);
P_minh=hotpressure(hotpressure_min);
phase_cold = ((t_coldpressure_max - t_coldmass_max)*2*pi*Freq)*(360/(2*pi));
phase_hot = ((t_hotpressure_max - t_hotmass_max)*2*pi*Freq)*(360/(2*pi));
phase_mass = ((t_coldmass_max - t_hotmass_max)*2*pi*Freq)*(360/(2*pi));
phase_pressure = ((t_coldpressure_max - t_hotpressure_max)*2*pi*Freq)*(360/(2*pi));
P_rc = (P_mean + P_maxc)/(P_mean + P_minc);
P_rh = (P_mean + P_maxh)/(P_mean + P_minh) ;

for k=1: n;
   time=k*deltat*increment;
   m_c_avg = Freq*trapz( coldend(1:increment,1), coldend(1:increment,2));
   m_h_avg = Freq*trapz( hotend(1:increment,1), hotend(1:increment,2));
end

fprintf(fidwrite,'The Cycle time is %f\r', time);
fprintf(fidwrite,'The cold end avg mass flux is %12.12f\r', m_c_avg);
fprintf(fidwrite,'The warm end avg mass flux is %12.12f\r', m_h_avg);
fprintf(fidwrite,'The cold end pressure ratio is %6.3f\r', P_rc);
fprintf(fidwrite,'The hot end pressure ratio is %6.3f\r', P_rh);
fprintf(fidwrite,'The cold end phase angle is %6.3f\r', phase_cold);
fprintf(fidwrite,'The warm end phase angle is %6.3f\r', phase_hot);
fprintf(fidwrite,'The mass flow phase angle is %6.3f\r', phase_mass);
fprintf(fidwrite,'The pressure phase angle is %6.3f\r', phase_pressure);
fclose('all');
```

Post-Processing Code for Low Temperatures

```
clear all;
Freq=60;
deltat = 4.166667e-5;
n =input('Enter the number of cycles to be evaluated\n');
tau = 1/Freq;
%=========================================================================
%User inputs filenames for analysis
%=========================================================================

cyc = sprintf('cyc_new.dat')  ;
fidcyclic = fopen(cyc, 'w')  ;
increment = round((1/Freq)/(deltat)) ;                    %increment which defines the integral bounds

% filename1 = sprintf('%s',Hdot_inlet.dat);
% filename2 = sprintf('%s',Hdot_outlet.dat);
A = dlmread('Hdot_in.dat', '',2,0) ;                      %puts data in fidwrite into matric form
B = dlmread('Hdot_out.dat', '',2,0) ;                     %puts data in fidwrite into matric form
C = dlmread('mdot_in.dat', '',2,0) ;                      %puts data in fidwrite into matric form
D = dlmread('mdot_out.dat', '',2,0) ;                     %puts data in fidwrite into matric form
E = dlmread('Vdot_in.dat', '',2,0) ;                      %puts data in fidwrite into matric form
F = dlmread('Vdot_out.dat', '',2,0) ;                     %puts data in fidwrite into matric form
G = dlmread('Press_in.dat', '',2,0) ;                     %puts data in fidwrite into matric form
H = dlmread('Press_out.dat', '',2,0) ;                    %puts data in fidwrite into matric form
for k=1: n;
   time=k*deltat*increment;                               %sets the time which is printed to fidcyclic
   Enthalpy_cold=Freq*trapz(A(1+(increment*(k-1)):(increment*k),1),A(1+(increment*(k-1)):(increment
                            t*k),2));
   Enthalpy_hot=Freq*trapz(B(1+(increment*(k-1)):(increment*k),1),-B(1+(increment*(k-
                              1)):(increment*k),2));
   mdot_cold = Freq*trapz( C(1+(increment*(k-1)):(increment*k),1), C(1+(increment*(k-1)):(increment*k),2));
   mdot_hot = Freq*trapz( D(1+(increment*(k-1)):(increment*k),1), D(1+(increment*(k-1)):(increment*k),2));
   Vdot_cold = Freq*trapz( E(1+(increment*(k-1)):(increment*k),1), E(1+(increment*(k-1)):(increment*k),2));
   Vdot_hot = Freq*trapz( F(1+(increment*(k-1)):(increment*k),1), F(1+(increment*(k-1)):(increment*k),2));
   Pdot_cold = Freq*trapz( G(1+(increment*(k-1)):(increment*k),1), G(1+(increment*(k-1)):(increment*k),2));
   Pdot_hot = Freq*trapz( H(1+(increment*(k-1)):(increment*k),1), H(1+(increment*(k-1)):(increment*k),2));
   PVdot_cold=Freq*trapz(G(1+(increment*(k-1)):(increment*k),1),(E(1+(increment*(k-
                              1)):(increment*k),2).*(G(1+(increment*(k-1)):(increment*k),2)-2.5e6)));
   PVdot_hot=Freq*trapz(H(1+(increment*(k-1)):(increment*k),1),(-F(1+(increment*(k-
                            1)):(increment*k),2).*(H(1+(increment*(k-1)):(increment*k),2)-2.5e6)));

   fprintf(fidcyclic,'%f\t    ', time);                  %prints the time to fidcyclic
   fprintf(fidcyclic,'%f\t    ', mdot_cold);             %prints the cyclic cold enthalpy flow
fprintf(fidcyclic,'%f\t    ', mdot_hot);                 %prints the cyclic hot enthalpy flow
   fprintf(fidcyclic,'%f\t    ', Enthalpy_cold);         %prints the cyclic cold enthalpy flow
   fprintf(fidcyclic,'%f\t    ', Enthalpy_hot);          %prints the cyclic hot enthalpy flow
   fprintf(fidcyclic,'%f\t    ', Vdot_cold);             %prints the cyclic cold enthalpy flow
   fprintf(fidcyclic,'%f\t    ', Vdot_hot);              %prints the cyclic hot enthalpy flow
   fprintf(fidcyclic,'%f\t    ', Pdot_cold);             %prints the cyclic cold enthalpy flow
   fprintf(fidcyclic,'%f\t    ', Pdot_hot);              %prints the cyclic hot enthalpy flow
   fprintf(fidcyclic,'%f\t    ', PVdot_cold);            %prints the cyclic cold enthalpy flow
   fprintf(fidcyclic,'%f\r    ', PVdot_hot);             %prints the cyclic hot enthalpy flow
end
```

```
write = sprintf('phase.dat')
fidwrite = fopen(write, 'w')

start= (increment*(n-1))+1  ;                                   %input('Enter the begin line\n');
ending=increment*n;                                             %input('Enter the end line\n');
time = A(start:ending,1);

coldmass = E(start:ending,2);
coldpressure = G(start:ending,2);
coldend = [time, coldmass, coldpressure] ;
hotmass = F(start:ending,2);
hotpressure = H(start:ending,2);
hotend = [time, hotmass, hotpressure]     ;

for i=2:(increment-1)
   if coldmass(i)>=coldmass(i-1) && coldmass(i)>coldmass(i+1);
       coldmass_max=i;
   end
end
for i=2:(increment-1)
   if coldpressure(i)>coldpressure(i-1) && coldpressure(i)>coldpressure(i+1);
      coldpressure_max=i;
   end
end
for i=2:(increment-1)
   if hotpressure(i)>hotpressure(i-1) && hotpressure(i)>hotpressure(i+1);
      hotpressure_max=i;
   end
end
for j=2:(increment-1)
   if coldpressure(j)<coldpressure(j-1) && coldpressure(j)<coldpressure(j+1);
      coldpressure_min=j;
   end
end
for j=2:(increment-1)
   if hotpressure(j)<hotpressure(j-1) && hotpressure(j)<hotpressure(j+1);
      hotpressure_min=j;
   end
end
for j=2:(increment-1)
   if hotmass(j)>=hotmass(j-1) && hotmass(j)>=hotmass(j+1);
      hotmass_max=j;
   end
end
P_mean=0
t_coldmass_max = time(coldmass_max);
t_coldpressure_max = time(coldpressure_max);
P_maxc=coldpressure(coldpressure_max);
P_minc=coldpressure(coldpressure_min);
t_hotmass_max=time(hotmass_max);
t_hotpressure_max=time(hotpressure_max);
P_maxh=hotpressure(hotpressure_max);
P_minh=hotpressure(hotpressure_min);
phase_cold = ((t_coldpressure_max - t_coldmass_max)*2*pi*Freq)*(360/(2*pi));
```

```
phase_hot = ((t_hotpressure_max - t_hotmass_max)*2*pi*Freq)*(360/(2*pi));
phase_mass = ((t_coldmass_max - t_hotmass_max)*2*pi*Freq)*(360/(2*pi));
phase_pressure = ((t_coldpressure_max - t_hotpressure_max)*2*pi*Freq)*(360/(2*pi));
P_rc = (P_mean + P_maxc)/(P_mean + P_minc);
P_rh = (P_mean + P_maxh)/(P_mean + P_minh) ;

fprintf(fidwrite,'The Cycle time is %f\r', time);                    %prints the time to fidcyclic
fprintf(fidwrite,'The cold end pressure ratio is %6.3f\r', P_rc);
fprintf(fidwrite,'The hot end pressure ratio is %6.3f\r', P_rh);     %prints the time to fidcyclic
fprintf(fidwrite,'The cold end phase angle is %6.3f\r', phase_cold);
fprintf(fidwrite,'The warm end phase angle is %6.3f\r', phase_hot);
fprintf(fidwrite,'The masGregs flow phase angle is %6.3f\r', phase_mass);
fprintf(fidwrite,'The pressure phase angle is %6.3f\r', phase_pressure);

fclose('all');
```

Appendix C – FLUENT Journal Code

Fluent Journal File for Automation

```
; ============================================================================================
; 2D Axisymmetric Pulse-tube Journal file
; Includes geometry of PTC between cold regenerator outlet and inlet to inertance tube
; Boundary conditions are defined via user-defined functions for mass flow and pressure
; Material properties are custom and input into FLUENT prop. routines for access in the
program.
;
; NOTE: Make changes at your own risk.  If changes are desired, it is advisable to do make
sure
; commands are correct in FLUENT command window based upon FLUENT TUI documentation.  Some
command
; options change depending upon which models are activated for solution.
;
; by Ryan Taylor
; Fall 2008
; ============================================================================================
;-------------------------------------------------------------
; Mesh is read in, scaled from inches to meters, and
; the domain is reordered for solution speed.
;-------------------------------------------------------------
rc Small_aspect_5percent.msh
grid/reorder/reorder-domain

;-------------------------------------------------------------
; This section is where the model is defined as being
; axisymmetric, the solver selected is the pressure based
; segregated solver, the energy equation is enabled and
; options selected, the transient solver is enabled with
; second order accuracy, the ke-realizable turbulence model
; is activated, and finally the operating pressure is set.
;-------------------------------------------------------------
define/models/axisymmetric/y
define/models/solver/pressure-based/y
define/models/energy/y n n y y
define/models/unsteady-2nd-order/y
define/models/viscous/ke-realizable/y
define/operating-conditions/operating-pressure/2.5e6
solve/set/numerics/n y y n n

define/user-defined/interpreted-functions "unsteady_inlets2.c" "cpp" 1000 n


;-------------------------------------------------------------
; This section is where all of the materials which are
; being utilized for the simulation are copied from the
; database to the simulation file at hand.  These properties
; include specific additions to the FLUENT "propdb.scm" and
; "thermodb.scm" files; note these files are located in the
; FLUENT program file folder under the specific version of
; software in the "cortex/lib" folder.  If you screw either of
; these files up you will start to have a bad day.
;-------------------------------------------------------------
define/materials/data-base/database-type/fluent-database
define/materials/copy/f/helium-cryo
define/materials/copy/s/copper
define/materials/copy/s/stainless-steel

;-------------------------------------------------------------
; This section defines the boundary conditions for the model to
; include specification of all paramters to define model to include
; UDF functions for pressure and mass flow, entering and exiting
```

```
; fluid temperature, walls, and axis.  Note that for turbulence
; at the hot trans, specific parameters are utilized for turbulent
; length scales and intensity.
;-------------------------------------------------------------
define/boundary-conditions/axis/CL_pt
define/boundary-conditions/axis/CL_hhx
define/boundary-conditions/axis/CL_htran
define/boundary-conditions/axis/CL_chx
define/boundary-conditions/axis/CL_chx_dv
define/boundary-conditions/axis/CL_chx_dvin
define/boundary-conditions/axis/CL_ctran

define/boundary-conditions/wall/pt_wall 0 n 0 y stainless-steel n n 0 n n n 0 n 0.5
define/boundary-conditions/wall/chx_wall_dvinb 0 n 0 y stainless-steel n n 0 n n n 0 n 0.5
define/boundary-conditions/wall/chx_wall_dvina 0 n 0 y stainless-steel n n 0 n n n 0 n 0.5
define/boundary-conditions/wall/chx_wall_dv 0 n 0 y stainless-steel n n 0 n n n 0 n 0.5
define/boundary-conditions/wall/ctran_wall 0 n 0 y stainless-steel n n 0 n n n 0 n 0.5
define/boundary-conditions/wall/chx_wall 0 n 0 y stainless-steel n n 0 n n n 0 n 0.5
define/boundary-conditions/wall/hhx_wall 0 n 0 y stainless-steel n n 0 n n n 0 n 0.5
define/boundary-conditions/wall/htran_wall 0 n 0 y stainless-steel n n 0 n n n 0 n 0.5

define/boundary-conditions/mass-flow-inlet/inlet n y y y "udf" "unsteady_massflow" n 80 n 0 y
y n 1 n 0 n y 0.01 0.003
define/boundary-conditions/pressure-outlet/outlet y y "udf" "unsteady_pressure" n 310 n y n y
40 6.85e-5 n

;-------------------------------------------------------------
; This section defines the fluid zones in the model to include
; specification of the material type as well as whether zone is
; porous medium with respective conditions for porous model.
;-------------------------------------------------------------
define/boundary-conditions/fluid/chx_dv y helium-cryo n n y n y n n
define/boundary-conditions/fluid/chx_in_dv y helium-cryo n n y n y n n

define/boundary-conditions/fluid/ctran y helium-cryo n n y n y n n
define/boundary-conditions/fluid/htran y helium-cryo n n y n y n n
define/boundary-conditions/fluid/pt y helium-cryo n n y n y n n

define/boundary-conditions/fluid chx_screen y helium-cryo n n y n y y y n 1 n 0 y n 7.5e8 n
2.98e9 n n 3526 n 14000 0 0 n 0.6 y copper
define/boundary-conditions/fluid/hhx y helium-cryo n n y n y y y n 1 n 0 y n 7.5e8 n 2.98e9 n
n 3526 n 14000 0 0 n 0.6 y copper

;-------------------------------------------------------------
; This section is where all of the numerical solver parameters
; are set.  These incldue customization of the numerical
; solution schemes for energy with tightened energy convergence.
; This makes the solver hunt harder for the correct energy terms.
; Also set are the local convergence parameter for all paramters.
;-------------------------------------------------------------
solve/set/discretization-scheme/mom/1
solve/set/discretization-scheme/pressure/14
solve/set/discretization-scheme/temperature/1
solve/set/p-v-coupling/22
solve/set/under-relaxation/pressure/0.6
solve/set/under-relaxation mom 0.7
solve/set/limits/1000000 4000000 4 400 1e-14 1e-20 100000
solve/set/multi-grid-controls/temperature/2 0.0001 0 0

;-------------------------------------------------------------
; This section is where the solution is initialized.  Once
; initialization has been performed, a custom written function
; for the initial temperature of the grid is patched to the
; domain.
;-------------------------------------------------------------
solve/set/expert/y n n y n
define/custom-field-functions/define "inittemp" 80+(230/0.1997)*x_coordinate
solve/initialize/initialize-flow
solve/patch chx_dv chx_in_dv chx_screen ctran hhx htran pt () temperature y inittemp
```

```
;-------------------------------------------------------------
; This section is where the data is exported.  There are two types
; of data being exported.  One is continously written files for
; pressure, mass flow, etc.  Second is primitive data at the inlet
; and outlet are exported at each time-step.
;-------------------------------------------------------------

solve/monitors/surface/set-monitor mdot_in "Mass Flow Rate" inlet () n n y "mdot_in.dat" 1 y
flow-time
solve/monitors/surface/set-monitor mdot_out "Mass Flow Rate" outlet () n n y "mdot_out.dat" 1
y flow-time

solve/monitors/surface/set-monitor Hdot_in "Flow Rate" enthalpy inlet () n n y "Hdot_in.dat"
1 y flow-time
solve/monitors/surface/set-monitor Hdot_out "Flow Rate" enthalpy outlet () n n y
"Hdot_out.dat" 1 y flow-time

solve/monitors/surface/set-monitor Vdot_in "Volume Flow Rate" inlet () n n y "Vdot_in.dat" 1
y flow-time
solve/monitors/surface/set-monitor Vdot_out "Volume Flow Rate" outlet () n n y "Vdot_out.dat"
1 y flow-time

solve/monitors/surface/set-monitor Press_in "Area-Weighted Average" absolute-pressure inlet
() n n y "Press_in.dat" 1 y flow-time
solve/monitors/surface/set-monitor Press_out "Area-Weighted Average" absolute-pressure outlet
() n n y "Press_out.dat" 1 y flow-time

solve/monitors/surface/set-monitor DTDX_in "Area-Weighted Average" dt-dx inlet () n n y
"DTDX_in.dat" 1 y flow-time
solve/monitors/surface/set-monitor DTDX_out "Area-Weighted Average" dt-dx outlet () n n y
"DTDX_out.dat" 1 y flow-time
;-------------------------------------------------------------
; This section is where the final solution parameters are set
; such as time step as will as local convergence values.
;-------------------------------------------------------------
solve/set/timestep/4.1666667e-5
solve/monitors/residual convergence-criteria 1.0e-6 1.0e-4 1.0e-4 1.0e-8 1.0e-3 1.0e-3
```

Appendix D – Mechanical Drawings

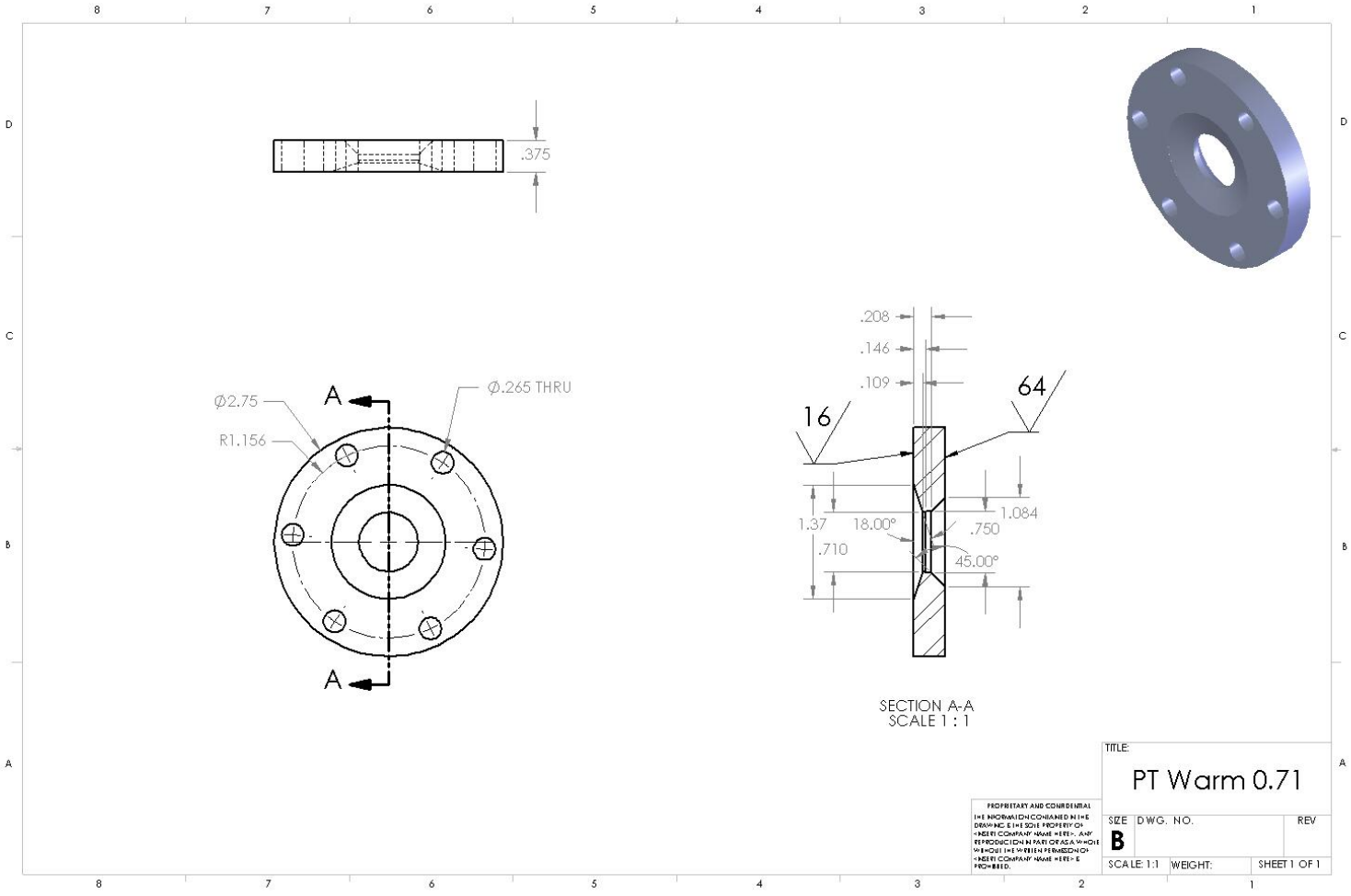

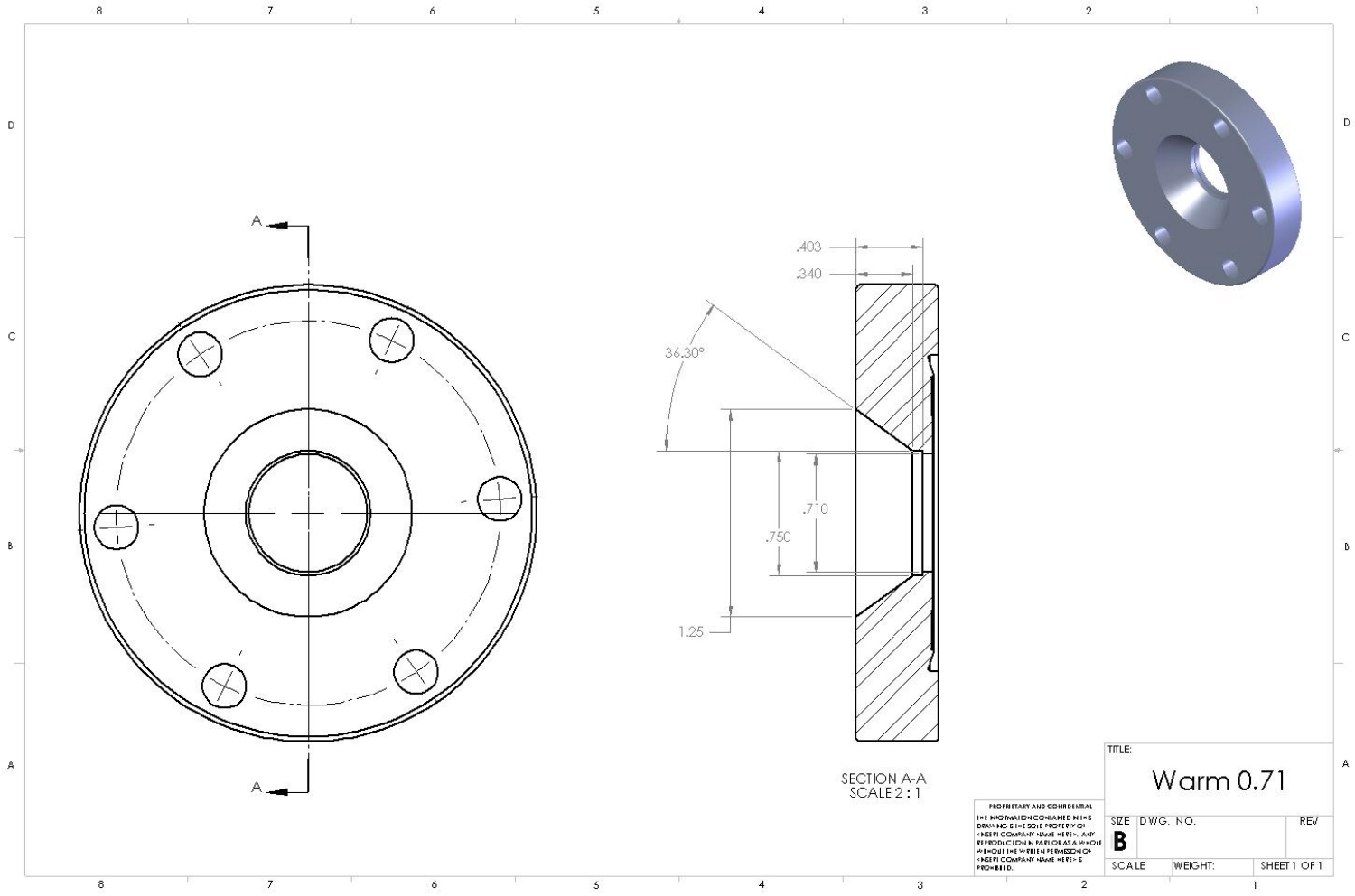
A
A
.403
.340
36.30°
.710
.750
1.25
SECTION A-A
SCALE 2 : 1
PROPRIETARY AND CONFIDENTIAL
THE INFORMATION CONTAINED IN THIS DRAWING IS THE SOLE PROPERTY OF <INSERT COMPANY NAME HERE>. ANY REPRODUCTION IN PART OR AS A WHOLE WITHOUT THE WRITTEN PERMISSION OF <INSERT COMPANY NAME HERE> IS PROHIBITED.
TITLE:
Warm 0.71
SIZE
B
DWG. NO.
REV
SCALE
WEIGHT:
SHEET 1 OF 1

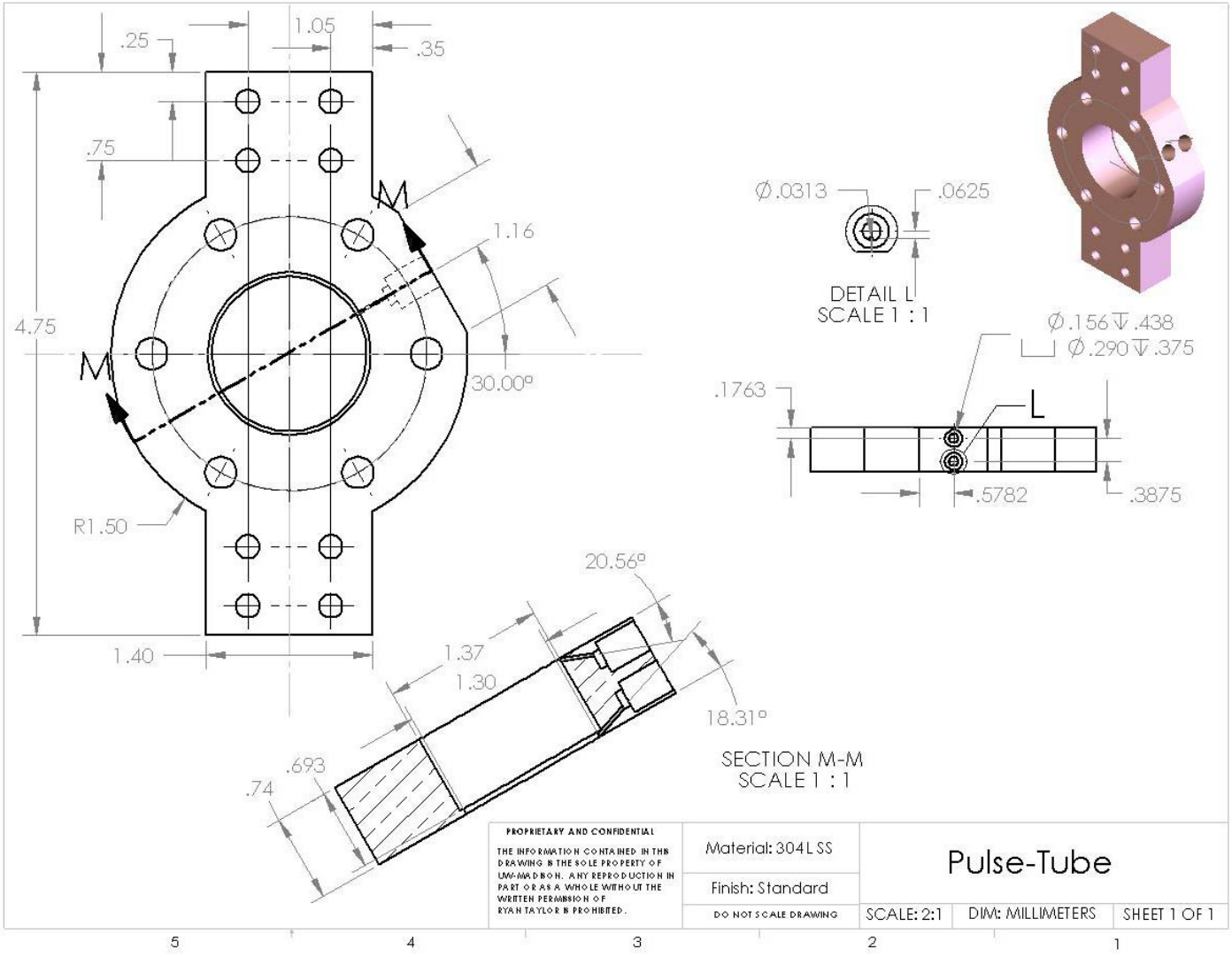
.25
1.05
.35
.75
M
1.16
4.75
M
30.00°
R1.50
1.40
Ø.0313
.0625
DETAIL L
SCALE 1 : 1
Ø.156 ↧ .438
Ø.290 ↧ .375
.1763
L
.5782
.3875
20.56°
1.37
1.30
18.31°
.693
.74
SECTION M-M
SCALE 1 : 1
PROPRIETARY AND CONFIDENTIAL
THE INFORMATION CONTAINED IN THIS DRAWING IS THE SOLE PROPERTY OF UW-MADISON. ANY REPRODUCTION IN PART OR AS A WHOLE WITHOUT THE WRITTEN PERMISSION OF RYAN TAYLOR IS PROHIBITED.
Material: 304 L SS
Finish: Standard
DO NOT SCALE DRAWING
Pulse-Tube
SCALE: 2:1
DIM: MILLIMETERS
SHEET 1 OF 1
5
4
3
2
1

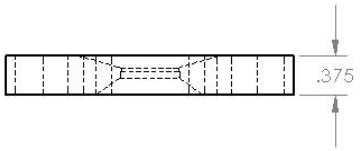

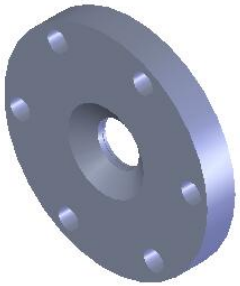

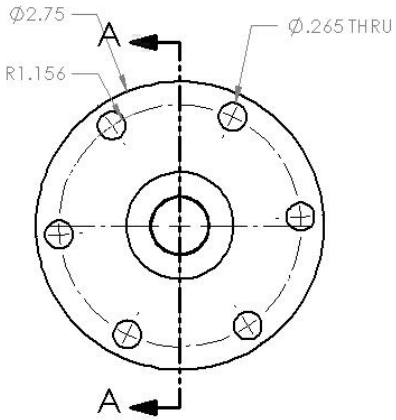

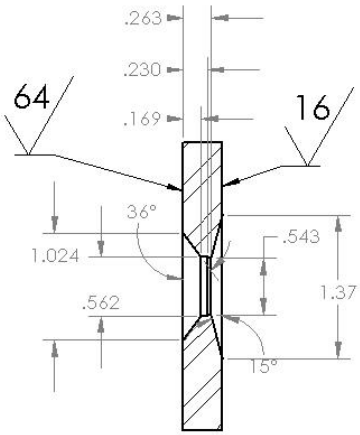

SECTION A-A
SCALE 1 : 1

TITLE:
PT Cold 0.543

SIZE	DWG. NO.	REV
B		
SCALE: 1:1	WEIGHT:	SHEET 1 OF 1

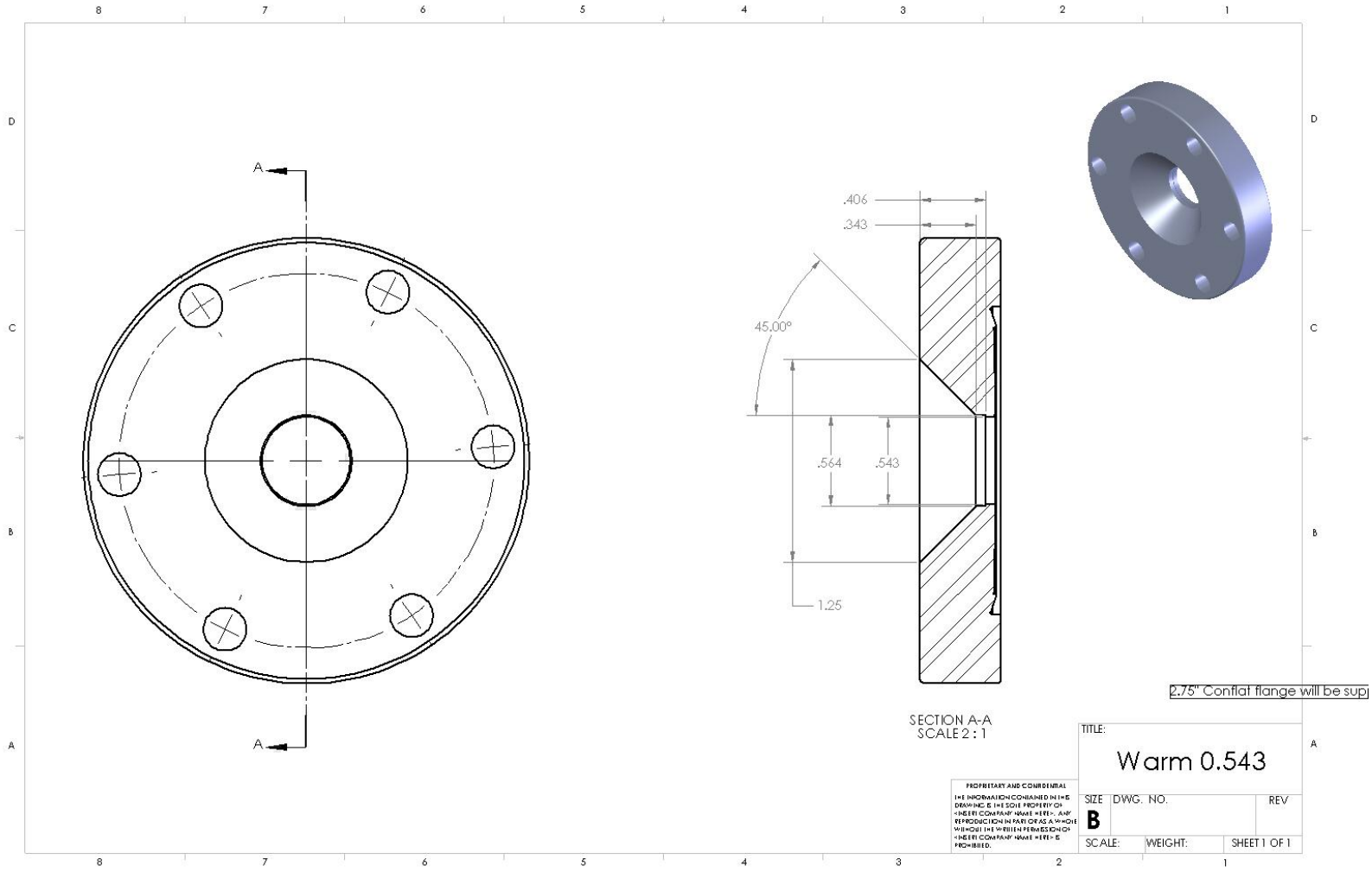
A
A
.406
.343
45.00°
.564
.543
1.25
SECTION A-A
SCALE 2 : 1
2.75" Conflat flange will be sup
TITLE:
Warm 0.543
SIZE
B
DWG. NO.
REV
SCALE:
WEIGHT:
SHEET 1 OF 1
PROPRIETARY AND CONFIDENTIAL
THE INFORMATION CONTAINED IN THIS DRAWING IS THE SOLE PROPERTY OF <INSERT COMPANY NAME HERE>. ANY REPRODUCTION IN PART OR AS A WHOLE WITHOUT THE WRITTEN PERMISSION OF <INSERT COMPANY NAME HERE> IS PROHIBITED.

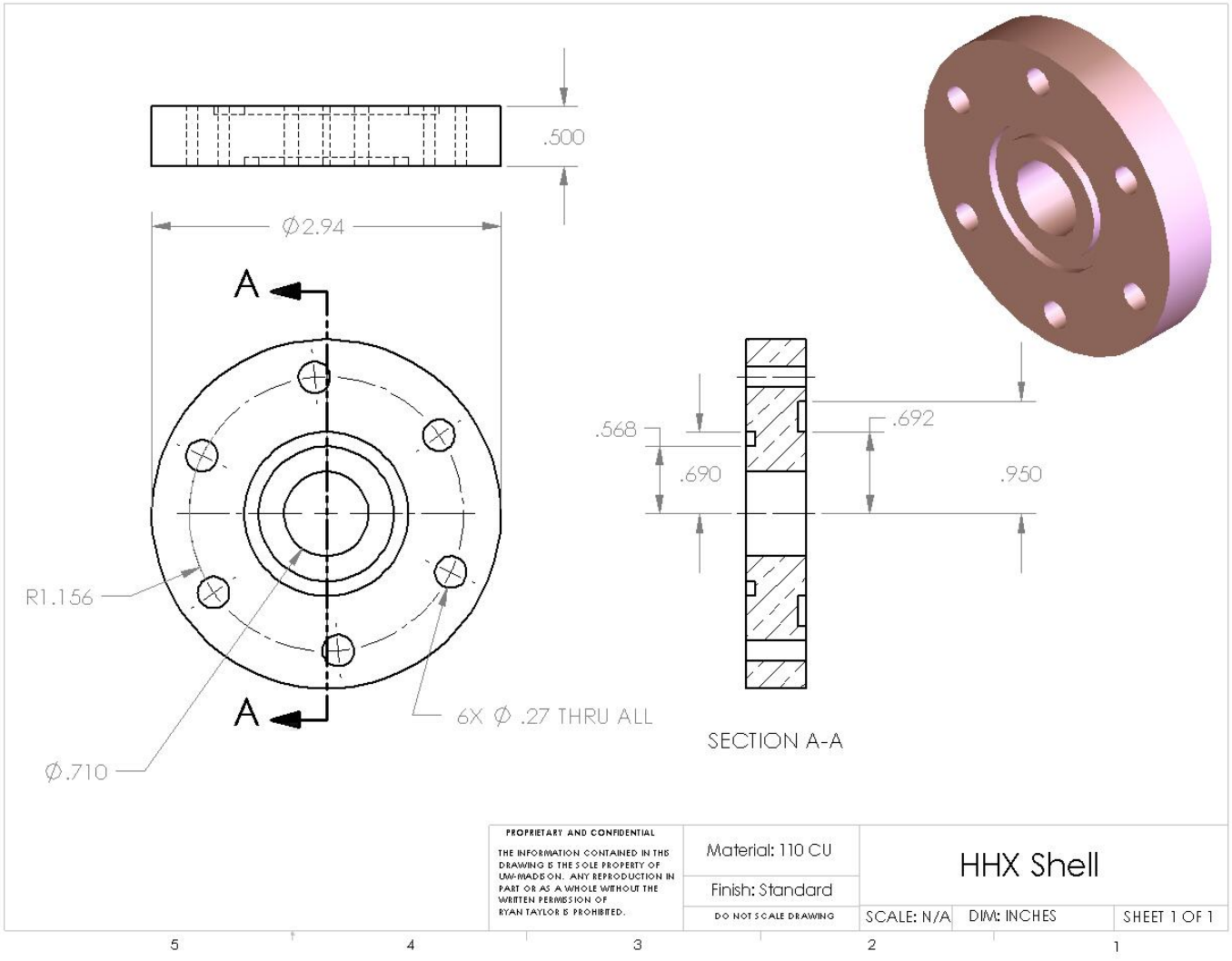
.500
Ø2.94
A
A
R1.156
Ø.710
6X Ø .27 THRU ALL
.568
.690
.692
.950
SECTION A-A
PROPRIETARY AND CONFIDENTIAL
THE INFORMATION CONTAINED IN THIS DRAWING IS THE SOLE PROPERTY OF UW-MADISON. ANY REPRODUCTION IN PART OR AS A WHOLE WITHOUT THE WRITTEN PERMISSION OF RYAN TAYLOR IS PROHIBITED.
Material: 110 CU
Finish: Standard
DO NOT SCALE DRAWING
HHX Shell
SCALE: N/A
DIM: INCHES
SHEET 1 OF 1
5
4
3
2
1

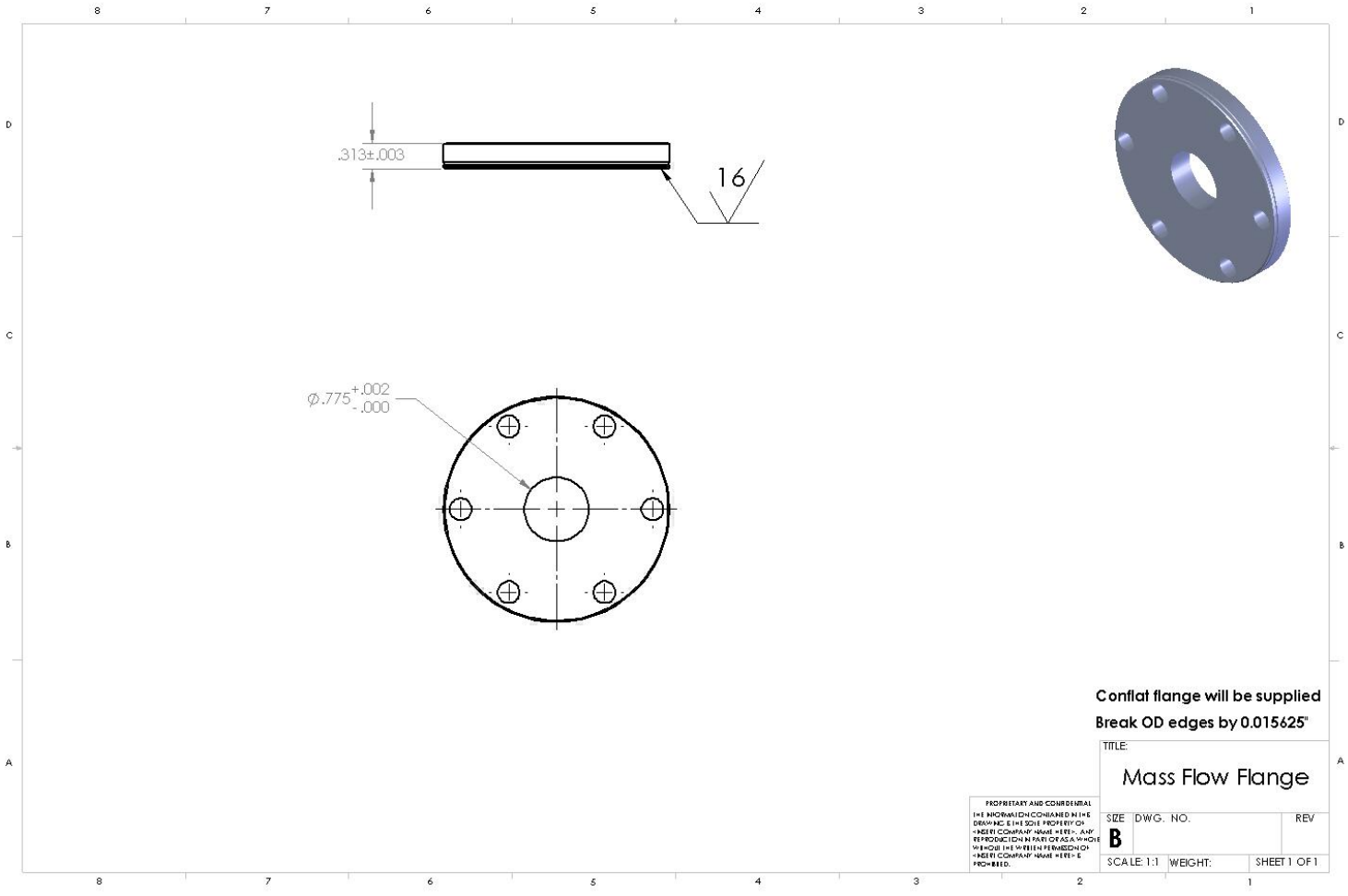
.313±.003
16
Ø.775 +.002 -.000
Conflat flange will be supplied
Break OD edges by 0.015625"
TITLE:
Mass Flow Flange
SIZE
B
DWG. NO.
REV
SCALE: 1:1
WEIGHT:
SHEET 1 OF 1
PROPRIETARY AND CONFIDENTIAL

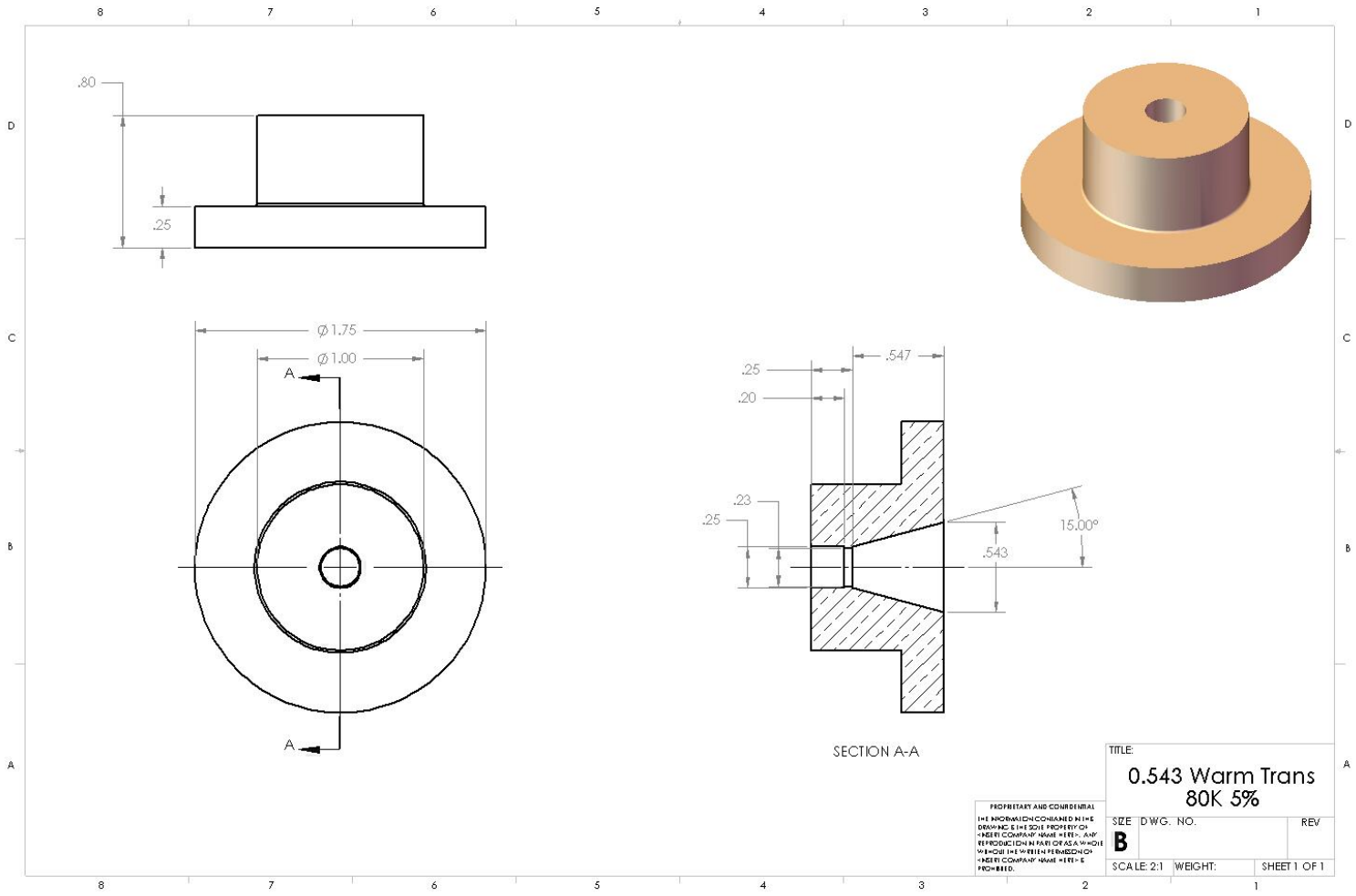
.80
.25
Ø1.75
Ø1.00
A
A
.25
.20
.547
.23
.25
15.00°
.543
SECTION A-A
PROPRIETARY AND CONFIDENTIAL
THE INFORMATION CONTAINED IN THIS DRAWING IS THE SOLE PROPERTY OF <INSERT COMPANY NAME HERE>. ANY REPRODUCTION IN PART OR AS A WHOLE WITHOUT THE WRITTEN PERMISSION OF <INSERT COMPANY NAME HERE> IS PROHIBITED.
TITLE:
0.543 Warm Trans
80K 5%
SIZE
B
DWG. NO.
REV
SCALE: 2:1
WEIGHT:
SHEET 1 OF 1

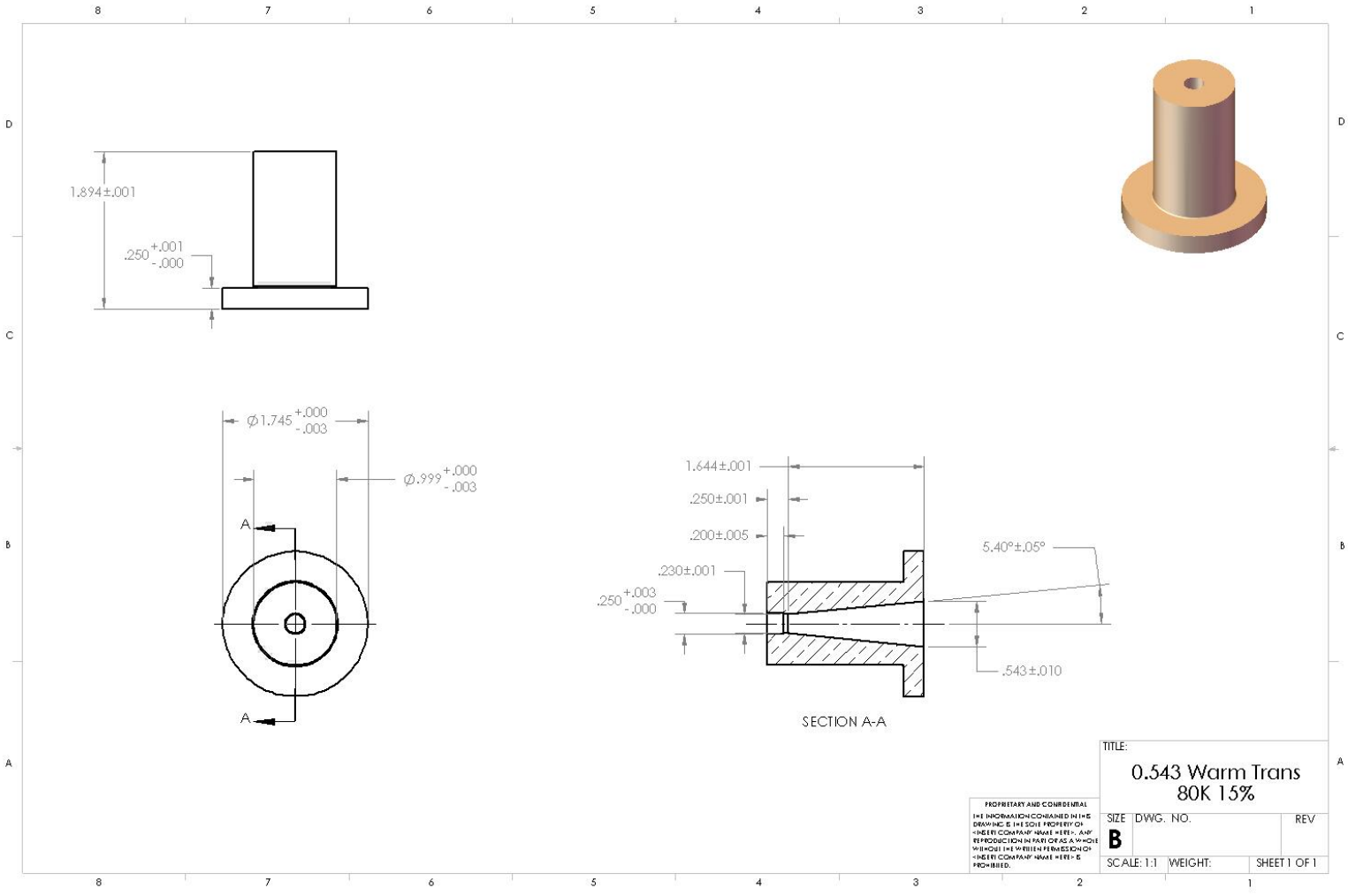
1.894±.001
.250 +.001 -.000
Ø1.745 +.000 -.003
Ø.999 +.000 -.003
A
A
1.644±.001
.250±.001
.200±.005
.230±.001
.250 +.003 -.000
5.40°±.05°
.543±.010
SECTION A-A
PROPRIETARY AND CONFIDENTIAL
THE INFORMATION CONTAINED IN THIS DRAWING IS THE SOLE PROPERTY OF <INSERT COMPANY NAME HERE>. ANY REPRODUCTION IN PART OR AS A WHOLE WITHOUT THE WRITTEN PERMISSION OF <INSERT COMPANY NAME HERE> IS PROHIBITED.
TITLE:
0.543 Warm Trans
80K 15%
SIZE
B
DWG. NO.
REV
SCALE: 1:1
WEIGHT:
SHEET 1 OF 1

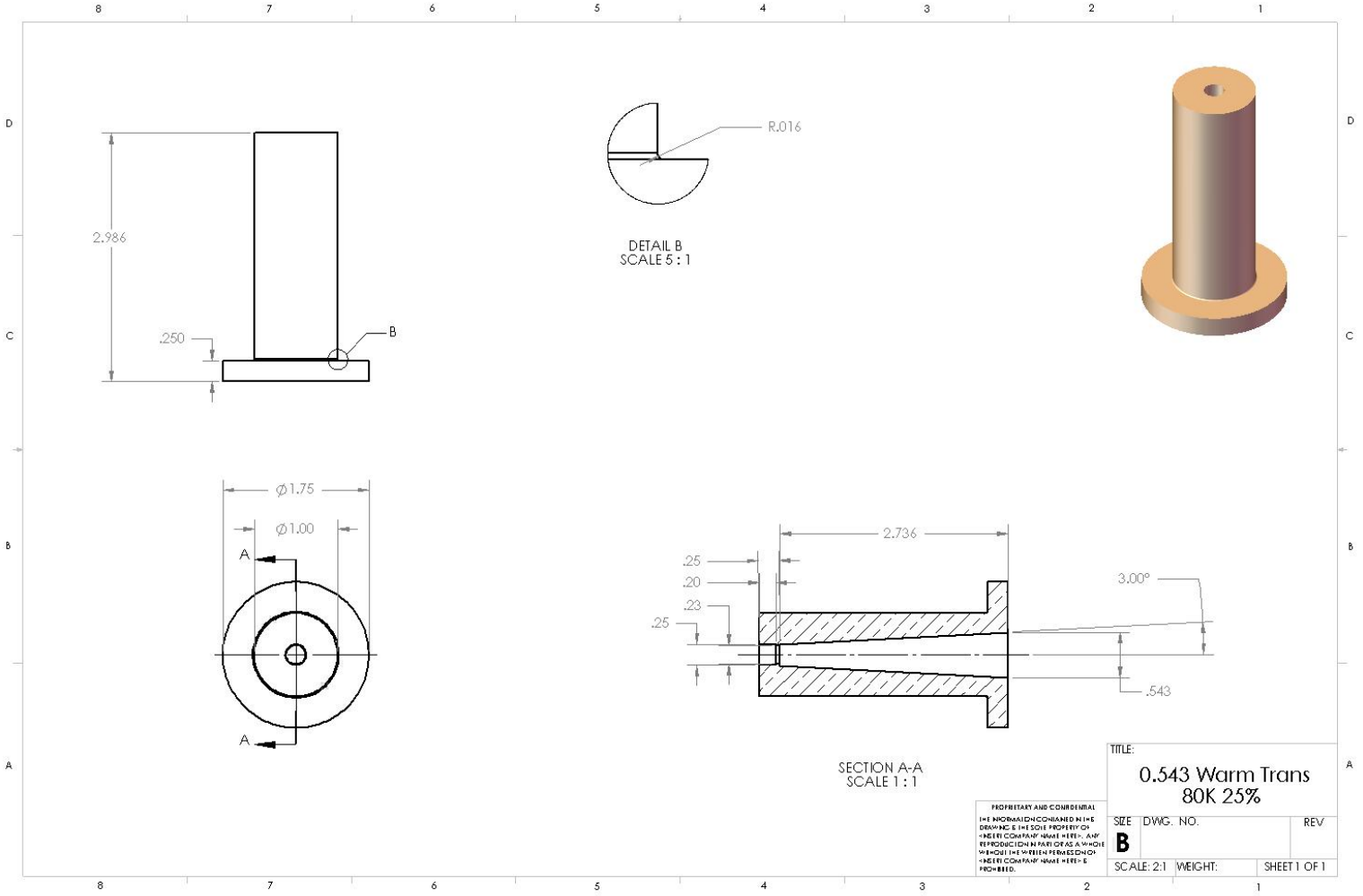
2.986
.250
B
R.016
DETAIL B
SCALE 5 : 1
Ø1.75
Ø1.00
A
A
2.736
.25
.20
.23
.25
3.00°
.543
SECTION A-A
SCALE 1 : 1
TITLE:
0.543 Warm Trans
80K 25%
SIZE
B
DWG. NO.
REV
SCALE: 2:1
WEIGHT:
SHEET 1 OF 1
PROPRIETARY AND CONFIDENTIAL

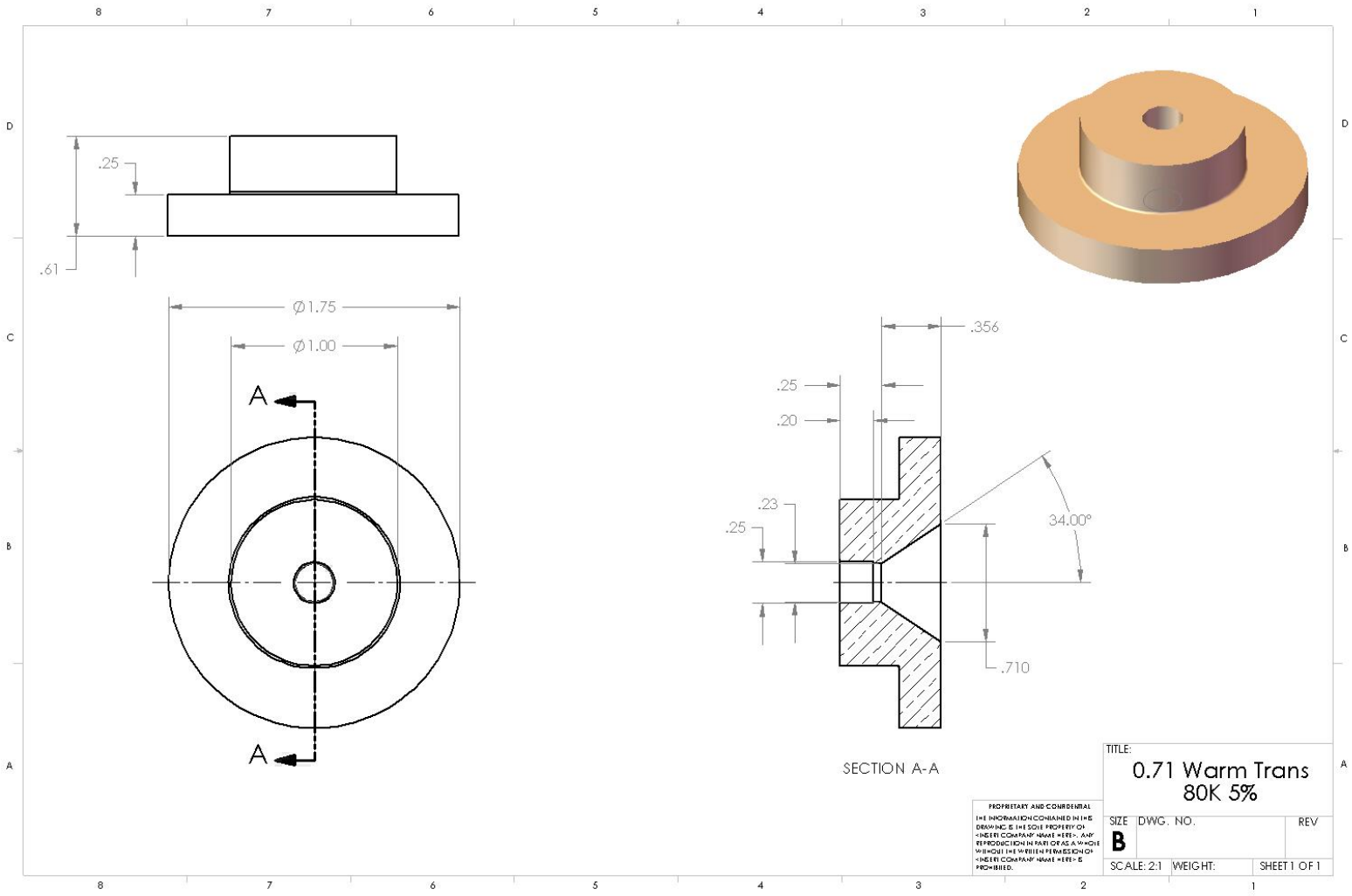
.25
.61
Ø1.75
Ø1.00
A
A
.356
.25
.20
.23
.25
34.00°
.710
SECTION A-A
TITLE:
0.71 Warm Trans
80K 5%
SIZE
B
DWG. NO.
REV
SCALE: 2:1
WEIGHT:
SHEET 1 OF 1
PROPRIETARY AND CONFIDENTIAL
THE INFORMATION CONTAINED IN THIS DRAWING IS THE SOLE PROPERTY OF <INSERT COMPANY NAME HERE>. ANY REPRODUCTION IN PART OR AS A WHOLE WITHOUT THE WRITTEN PERMISSION OF <INSERT COMPANY NAME HERE> IS PROHIBITED.

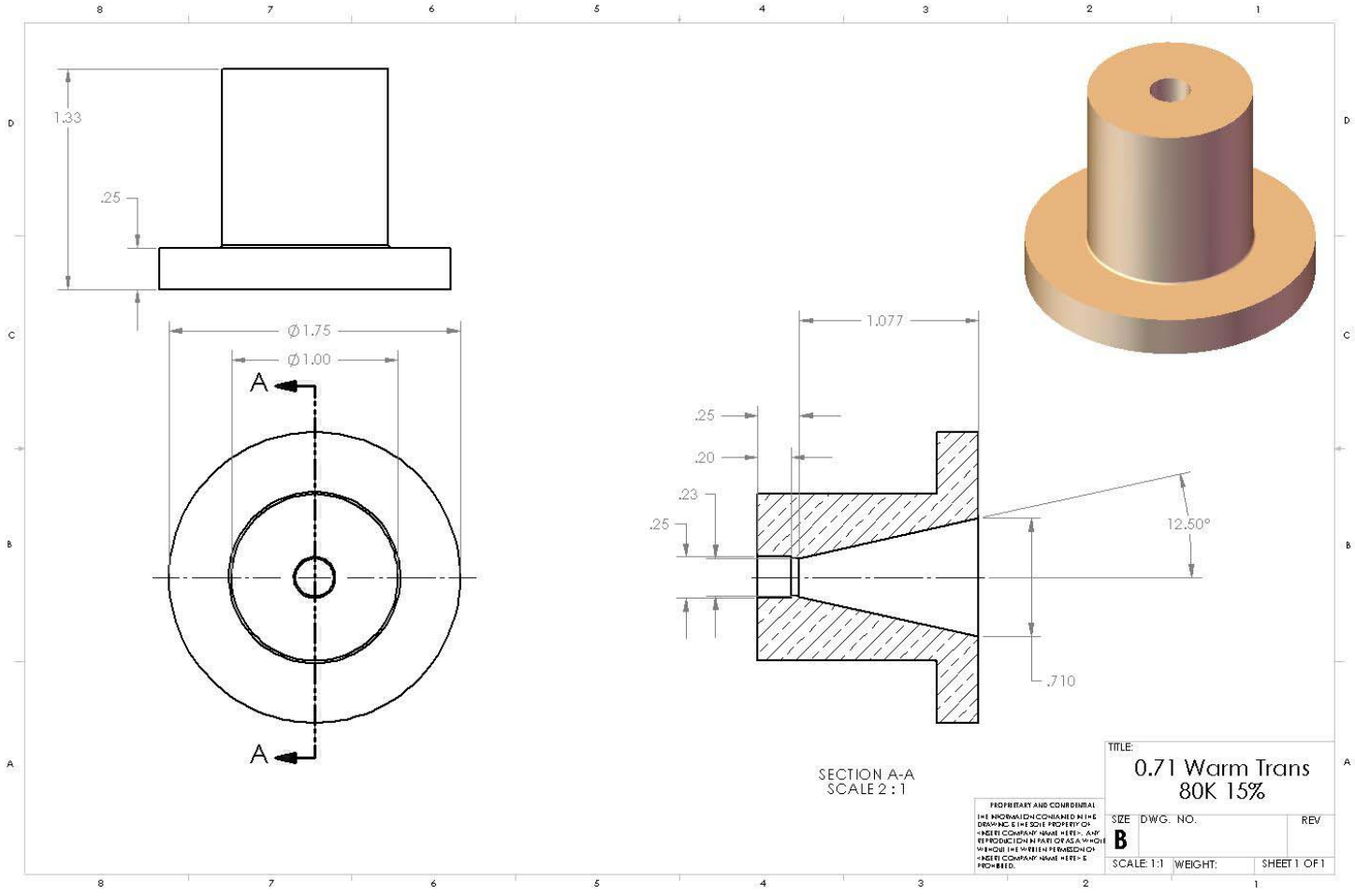
1.33
.25
Ø1.75
Ø1.00
A
A
1.077
.25
.20
.23
.25
12.50°
.710
SECTION A-A
SCALE 2 : 1
TITLE:
0.71 Warm Trans
80K 15%
SIZE
B
DWG. NO.
REV
SCALE: 1:1
WEIGHT:
SHEET 1 OF 1

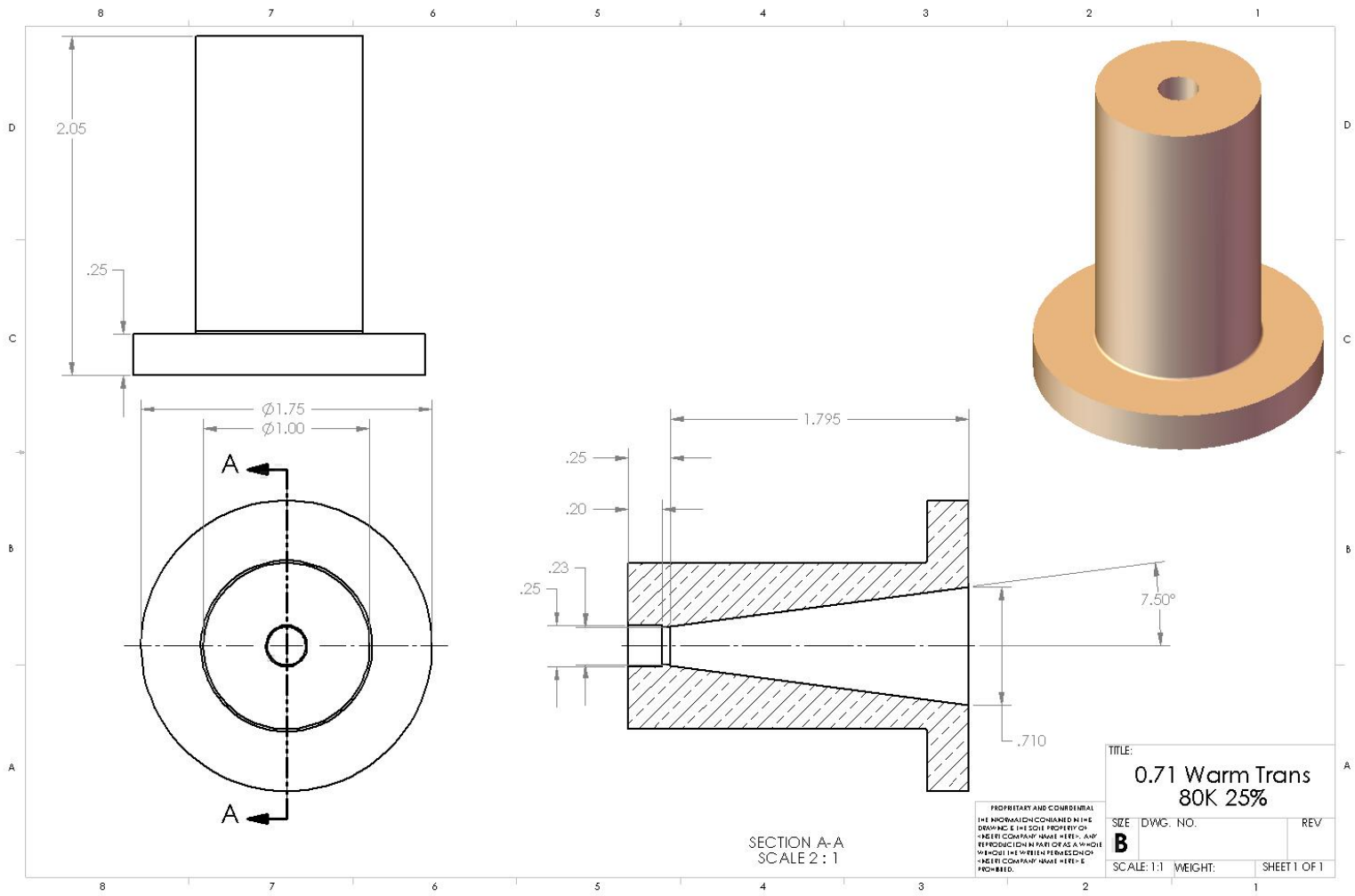
2.05
.25
Ø1.75
Ø1.00
A
A
1.795
.25
.20
.23
.25
7.50°
.710
SECTION A-A
SCALE 2 : 1
PROPRIETARY AND CONFIDENTIAL
TITLE:
0.71 Warm Trans
80K 25%
SIZE
B
DWG. NO.
REV
SCALE: 1:1
WEIGHT:
SHEET 1 OF 1

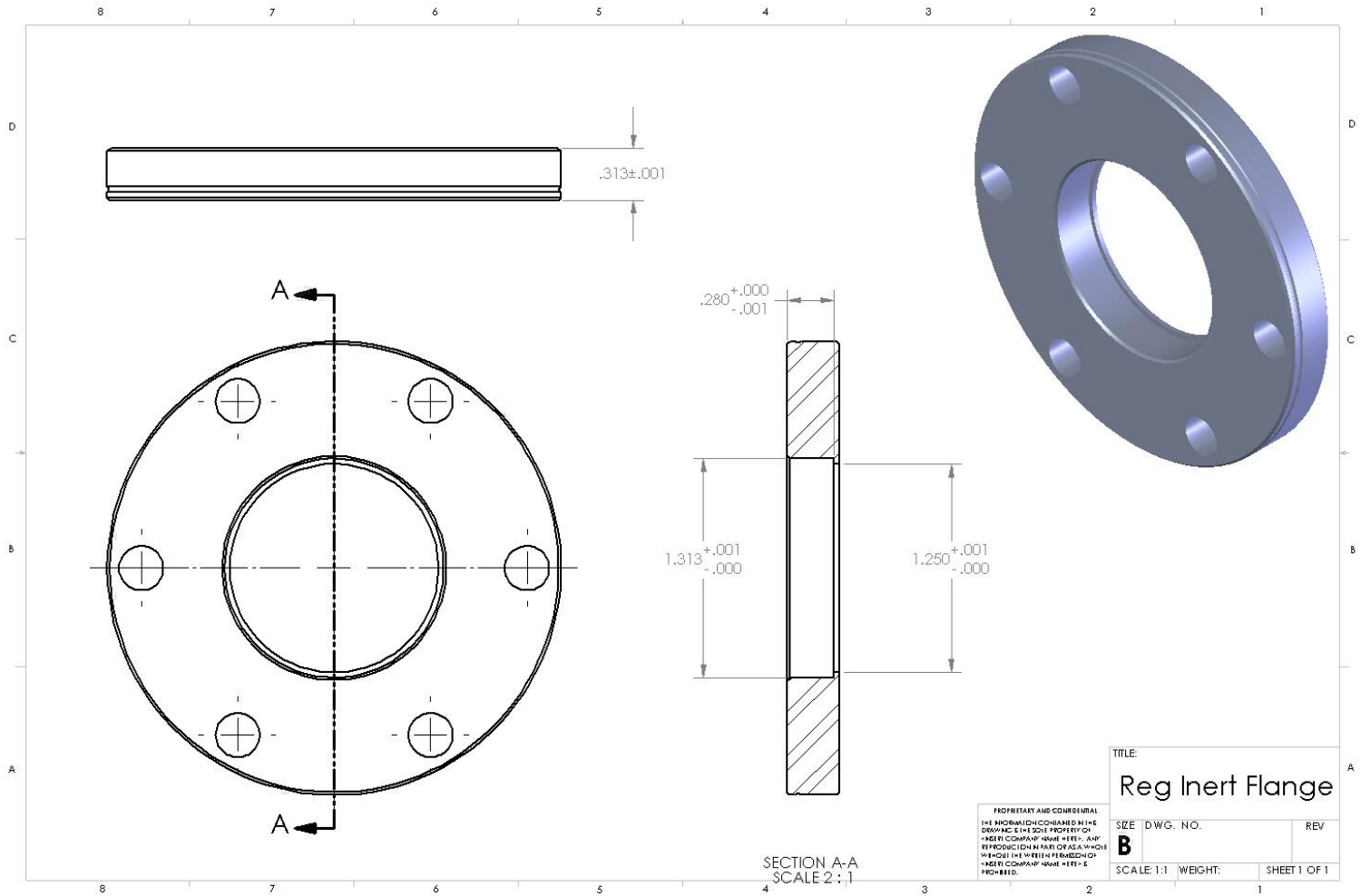
.313±.001
A
A
.280 +.000 -.001
1.313 +.001 -.000
1.250 +.001 -.000
SECTION A-A
SCALE 2 : 1
PROPRIETARY AND CONFIDENTIAL
TITLE:
Reg Inert Flange
SIZE
B
DWG. NO.
REV
SCALE: 1:1
WEIGHT:
SHEET 1 OF 1